UNIVERSITÀ DEGLI STUDI DI MILANO

DIPARTIMENTO DI FISICA

SCUOLA DI DOTTORATO IN FISICA, ASTROFISICA E FISICA APPLICATA

Ciclo XXIX

Probing mechanical interactions in cells and their microenvironment by Atomic Force Microscopy

Settore scientifico disciplinare FIS/03

Tesi di Dottorato di : Luca Puricelli

Coordinatore: Prof. Francesco Ragusa

Tutore: Prof. Alessandro Podestà

Co-tutore: Prof. Cristina Lenardi

A.A. 2015-2016

External referees:

Prof. Andrea Alessandrini,
Professore associato presso il Dipartimento di Fisica, Informatica e Matematica,
Università degli Studi di Modena e Reggio Emilia

Dr. Félix Rico,
Assistant Professor
Aix-Marseille Université – INSERM University Chair

Commission of the final examination:

President:
Prof. Daniel Navajas,
Full Professor of Physiology,
Facultat de Medicina i Ciències de la Salut - Universitat de Barcelona, Institut de Bioenginyeria de Catalunya

External Member:
Prof. Roberto Raiteri,
Professore associato presso il Dipartimento di Informatica, Bioingegneria, Robotica e Ingegneria dei Sistemi,
Università degli Studi di Genova

Internal Member:
Prof. Alessandro Podestà,
Professore associato presso il Dipartimento di Fisica,
Università degli Studi di Milano

Final examination:

23rd February, 2017
Dipartimento di Fisica, Università degli Studi di Milano
Milano, Italy

Ai miei zii, Daniele e Luciano

Ai miei nonni

A Davide & Eleonora

Alla mia famiglia

"Happiness is real only when shared"

Christopher McCandless

-Back to the Wild-

MIUR subjects:
FIS/03

PACS:
62.20.Dc
68.37.Ps
87.19.Rr
87.64.Dz
87.83.+a

PhD School in Physics, Astrophysics and Applied Physics
University of Milan
Cycle XXIX

PhD Candidate : Dr. Luca Puricelli

Conclusive report on three-year activity

EXPERIMENTAL ACTIVITY

The candidate has carried out research activity in the field of the characterization of cell mechanics and cellular interactions with specific environments by means of Atomic Force Microscopy (AFM) techniques.
Starting from the results obtained during the timespan of his Master Thesis, in the first year of his PhD course the candidate has completed the development of a comprehensive protocol on the combined topographic-mechanical imaging of single cells with *colloidal probes* [1], taking into account both theoretical and experimental issues. This work has proved to be very beneficial, providing on one side a first step towards the achievement of a robust and reliable protocol, which could be commonly adopted inside the scientific community, and a solid base for the analysis of the topographic-mechanical behavior of single cells and tissues, in correlation with specific biological processes, on the other side. Indeed, along with a continuous improvement and optimization of the procedure, the aforementioned protocol has been applied for the investigation of the relative importance and contribution of cellular elasticity to cells adhesion and migration processes in the framework of the so-called “molecular clutch” (MC) model [2].
In parallel with this activity, the candidate has contributed to scientific collaborations with national (S. Raffaele Hospital, Milan) and international (Weizmann Institute of Tel Aviv, COST Action TD1002) groups, aimed at the standardization of mechanical measurements [3] and at the understanding of the influence of cellular micro-environment on the progression of tumoral and inflammatory diseases [4], [5]. Specifically, the candidate has performed mechanical measurements at the microscale of ExtraCellular Matrices (ECMs) derived from tissues affected by a specific type of tumor or inflammatory disorder, adapting the experimental protocol previously developed to these specific cases. This kind of research pursues the goal of finding prognostic and therapeutic strategies alternative to the standard ones, overcoming the classic paradigm of targeting single cells alone, and thinking instead about the ECM-cells ensemble as a whole.
Eventually, a progressive shift of the focus from the properties of single cells to the interaction between cells and the outer environment has seen the candidate involved in a further project related to the differentiation of in vitro and ex-vivo neuronal stem cells induced by nanostructured biocompatible surfaces [6], [7]. The great versatility of the AFM, combined with the developed protocol involving the use of colloidal probes, has allowed the candidate to study both the morphological properties on the *nanoscale* of the nanostrustured surfaces and the mechanical response on the *microscale* of the cells cultured on these peculiar substrates, thus paving the way for a deep understanding of the biophysical triggers at the origin of the so-called “mechanotransductive” events, which in turn is essential to achieve the real reproducibility of the phenomenon and its exploitation in practical applications.

DIDACTIC AND FORMATIVE ACTIVITIES

Along with the experimental activity, the candidate has fulfilled several duties and parallel activities regulated by the guidelines of the PhD School, which can be summarized as follows:

PhD courses

Compulsory courses selected from a given list and followed by oral examination:

- *Experimental methods for the investigation of systems at the nanoscale*
- *Electronic Instrumentation*

Optional courses without final examination:

- *Training course on advanced machining techniques*
- *Training course on science communication*

Physics Colloquia and Seminars

The candidate has :

- attended six Physics Colloquia (seminars held by invited speakers) for each year
- held a public seminar at the end of each year, related to his own research activity.
- contributed to an internal Workshop with an oral presentation entitled: "*Nanomechanical and topographical imaging of living cells, extra-cellular matrices and tissues: a promising tool for the development of novel early-diagnostic and therapeutic strategies for cancer and inflammatory diseases*"

Stages in external laboratories or companies

The candidate has carried out a one-week internship at the facilities of Optics11 – Amsterdam, Netherlands – from 23 to 27 May 2016. In this instance the candidate has performed indentation measurements on a test PDMS sample through the "Piuma Nanoindenter" (supplied by Optics11) equipped with colloidal probes of various sizes, in order to compare the results obtained with preliminary measurements performed on the same sample by means of AFM. Interestingly, the comparison between AFM and Piuma Nanoindenter, based on an interferometric technique, has unveiled some critical issues related to the calibration of fundamental AFM parameters, such as the optical lever sensitivity and the cantilever force constant, particularly significant in connection to the use of colloidal probes. This has implied a deeper research and comprehension by the candidate about the limits and the accuracy of AFM-based mechanical measurements with colloidal probes.

External collaborations

National groups:

- S. Raffaele Hospital, Milan. *Measurements of nano-micromechanical properties of ECMs samples obtained from colon human tissues.* Contact person: Dr. Massimo Alfano

International groups:

- Weizmann Institute, Tel Aviv. *Characterization of the Young's Modulus of Extra-Cellular Matrices obtained from colon mice tissues by Atomic Force Microscopy.* Contact person: Prof. Irit Sagi
- COST Action TD1002. *Standardization of AFM-based mechanical measurements on soft and biological samples*.

Summer Schools

The candidate has attended the “AFMBioMed Summer School 2016” held in Marseille from 18 to 22 July 2016, where he had the opportunity to expand his knowledge of AFM-based techniques applied to the biomedical field. In detail, the school has been organized into lectures and practical sessions on the following topics:

- Single Molecule Force Spectroscopy
- High Resolution AFM
- Cell Mechanics
- High Speed AFM

Other activities

The candidate has dedicated part of his time to tutoring activities towards younger students and colleagues working in the same laboratories, as well as rewarded didactic support activities distributed as follows:

- A.A. 2013-2014: 25 hours for assistance in preparation and evaluation of oral and written tests. *Physics course at the Faculty of Agricultural and Food Sciences - University of Milan - held by Prof. Alessandro Podestà*
- A.A. 2014-2015: 30 hours for assistance in preparation and evaluation of oral and written tests. *Physics course at the Faculty of Agricultural and Food Sciences - University of Milan - held by Prof. Alessandro Podestà*
- A.A. 2015-2016: 60 hours for tutoring and assistance in preparation and evaluation of oral and written tests. *Physics course at the Faculty of Agricultural and Food Sciences - University of Milan - held by Prof. Alessandro Podestà*

Eventually, the candidate has performed the review of a paper for “Journal of Nanoparticle Research”.

LIST OF PUBLICATIONS

[1] L. Puricelli, M. Galluzzi, C. Schulte, A. Podestà and P. Milani, "Nanomechanical and topographical imaging of living cells by atomic force microscopy with colloidal probes" *Review of Scientific Instruments,* vol. 86, no. 033705, 2015.

[2] C. Schulte, G. M. Sarra Ferraris, A. Oldani, M. Galluzzi, A. Podestà, L. Puricelli, V. De Lorenzi, C. Lenardi, P. Milani and N. Sidenius, "Lamellipodial tension, not integrin/ligand binding, is the crucial factor to realise integrin activation and cell migration" *European Journal of Cell Biology,* vol. 95(1), pp. 1-14, 2015.

[3] H. Schillers, C. Rianna, J. Schäpe, T. Luque, H. Doschke, M. Wälte, J.J. Uriarte, N. Campillo, G. PA Michanetzis, J. Bobrowska, A. Dumitru, E.T. Herruzo, S. Bovio, P. Parot, M. Galluzzi, A. Podestà, L. Puricelli, S. Scheuring, Y. Missirlis, R. Garcia, M. Odorico, J.M. Teulon, F. Lafont, M. Lekka, F. Rico, A. Rigato, J.L. Pellequer , H. Oberleithner, D. Navajas and Manfred Radmacher, " Standardized Nanomechanical Atomic Force Microscopy Procedure (SNAP) for Measuring Soft and Biological Samples" *Submitted.*

[4] M. Nebuloni, L. Albarello, A. Andolfo, C. Magagnotti, L. Genovese, I. Locatelli, G. Tonon, E. Longhi, P. Zerbi, R. Allevi, A. Podestà, L. Puricelli, P. Milani, A. Soldarini, A. Salonia and M. Alfano, "Insight On Colorectal Carcinoma Infiltration by Studying Perilesional Extracellular Matrix" *Scientific Reports,* vol. 6, no. 22522, 2016.

[5] E. Shimshoni, R. Afik, A. Shenoy, M. Adler, L. Puricelli, A. Podestà, T. Geiger, P. Milani, U. Alon and I. Sagi, "Decoding omics: unsupervised tissue composition-to-structure translation reveals silent pathological states" *Submitted.*

[6] C. Schulte, S. Rodighiero, M. A. Cappelluti, L. Puricelli, E. Maffioli, F. Borghi, A. Negri, E. Sogne, M. Galluzzi, C. Piazzoni, M. Tamplenizza, A. Podestà, G. Tedeschi, C. Lenardi and P. Milani, "Conversion of nanoscale topographical information of cluster-assembled zirconia surfaces into mechanotransductive events promotes neuronal differentiation" *Journal of Nanobiotechnology,* vol. 14, no. 18, 2016.

[7] C. Schulte, M. Ripamonti, E. Maffioli, M. A. Cappelluti, S. Nonnis, L. Puricelli, J. Lamanna, C. Piazzoni, A. Podestà, C. Lenardi, G. Tedeschi, A. Malgaroli and P. Milani, "Scale invariant disordered nanotopography promotes hippocampal neuron development and maturation with involvement of mechanotransductive pathways" *Frontiers in Cellular Neuroscience,* vol. 10, no. 267, 2016.

Milano, 16/12/2016

The Supervisor

Prof. Alessandro Podestà

Alessandro Podestà

Contents

1 Introduction 11
1.1 AFM as a biomedical tool : state of the art 11
1.2 Thesis overview 12
1.3 Thesis outline 21

2 Characterization of mechanical properties of single living cells 23
2.1 Protocol development 23
2.1.1 Additional discussion 41
2.2 Mechanics of cell migration : the Molecular Clutch model 43
2.2.1 Additional discussion 62

3 Mechanics of the cellular microenvironment 65
3.1 Insight on colorectal carcinoma infiltration 65
3.2 Inflammatory bowel disease : a murine model 99
3.3 Additional discussion 110

4 Mimicking the ECM: engineering nanostructured biocompatible substrates 113
4.1 Differentiation of PC12 cells induced by nanostructured zirconia surfaces 113
4.1.1 Additional discussion 143

5 Conclusions and perspectives 145

A Calibration issues associated with large colloidal probes 151
A.1 Deflection sensitivity : the induced torque effect 151
A.2 Cantilever force constant : the added mass effect 159

B AFM & Piuma Nanoindenter **167**

C Photodetector nonlinearity **173**

Bibliography **174**

D Acknowledgments **187**

Chapter 1

Introduction

1.1 AFM as a biomedical tool : state of the art

One of the main reasons at the basis of the fast development of the Atomic Force Microscope (AFM) since its conception [1] has certainly been its great versatility. Indeed, the AFM has shown unprecedented potential compared to its ancestors in the field of scanning probe microscopy, being able on the one hand to operate in diverse environments (vacuum, air or liquid) or on different samples (conductive or insulating, organic or inorganic), and to map simultaneously the topography and various physico-chemical properties of the scanned sample at the *nanoscale*, like adhesion, friction or elasticity, on the other [2]. This, in parallel with an increasing demand for proper tools aimed at the nanomechanical characterization of biological specimens, able to support and integrate the information provided by biochemical techniques, has led to an intensive exploitation of AFM in the biomedical field and the subsequent production of a significant amount of scientific literature (for an exhaustive review, see e.g. refs [3, 4]).

Among all subfields, special attention has been reserved to the study of *cell mechanics* [5, 6], since a strong correlation between the mechanical properties of living cells and their fundamental biological functions, as well as the pathophysiological state, has been demonstrated [7, 8, 9]. In particular, the AFM potential in discriminating between healthy and cancer cells [10, 11, 12], along with the possibility of gaining a better understanding of the interplay between cells and the surrounding microenvironment [12, 13], has opened the way to practical biomedical applications, such as pre-diagnosis of cancer and other diseases, tissue engineering and regenerative medicine.

However, despite the great effort handed out in this direction, the actual scenario is still incomplete and fragmented, mainly *lacking a common point of view about the operational protocol* which prevents an effective comparison and validation of independent results obtained by different laboratories, thus severely hampering the concrete implementation of the AFM as a biomedical tool [14]. The main source of the problem can be traced back to the *intrinsic complexity* of biological specimens, with particular regard to *cells and tissues.* These samples stand far away from an easy interpretation and classification, showing instead a strong heterogeneity (fig. 1.1), which manifests itself on multiple levels and scales, from nano- to micro- : internal composition, structure and organization, local thickness and morphology, biophysical properties and susceptibility to external stimuli, as well as natural fluctuations inside the same specimen or population. This extreme variability raises difficulties on many steps of the experimental activity, from sample preparation to data analysis. The AFM itself, being originally conceived to probe samples on the nanoscale, is pushed to its limits in order to suit the micrometric dimensions typical of cells and tissues, thus forcing the operator to find adaptive solutions. Moreover, the overall tendency of theoretical models in physics towards universality and simplification hardly matches with the complexity of the biological world, often raising fundamental and interpretative issues; eventually, the analysis of bunches of heterogeneous data has to be faced from a computational point of view, requiring the development of complex algorithms. Therefore, it is not surprising to find still a plethora of experimental methods associated with AFM-based studies of cell and tissue mechanics.

1.2 Thesis overview

PROTOCOL DEVELOPMENT In the light of previous considerations, the first goal of my PhD activity has been the development of a comprehensive protocol for the combined topographic-mechanical imaging of living cells and soft samples, such as extracellular matrices or artificial gels (see section 2.1 and ref. [16]). Starting from a systematic review of the work already done in this field, the main open problems on both theoretical and experimental sides have been analyzed and consistent solutions have been proposed. Among many critical points, specific attention has been payed to the choice of AFM probe: compared to conventional and widely used sharp tips, micrometric spherical probes,

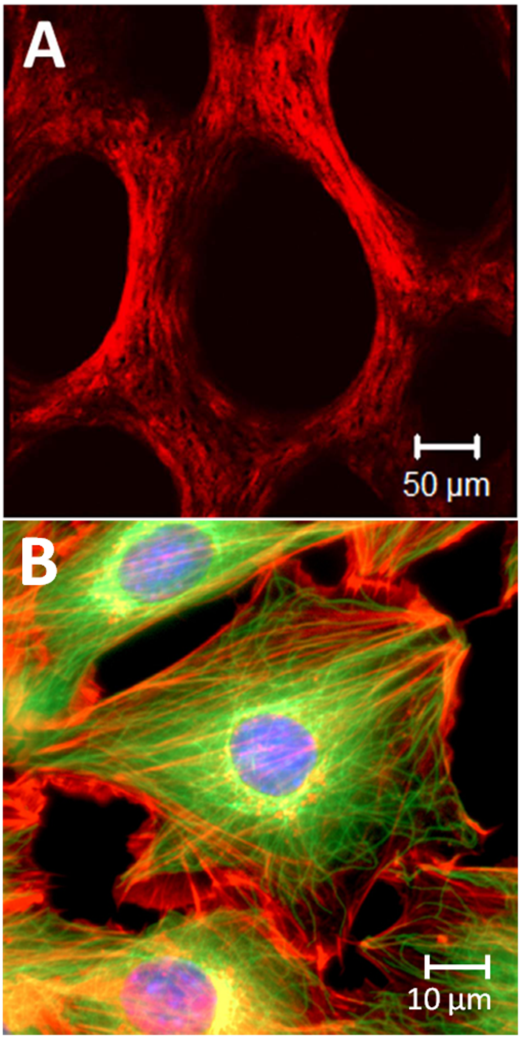

Figure 1.1: (A) Second-harmonic imaging of colon extracellular matrix derived from human biopsy. The holes represent cellular crypts. Reproduced from [15] (B) Immunofluorescence microscopy image of T3T mouse fibroblast cells. Major intracellular components are highlighted with different colors : nuclear DNA (blue), actin filaments (red), tubulin filaments (green). Adapted from [5].

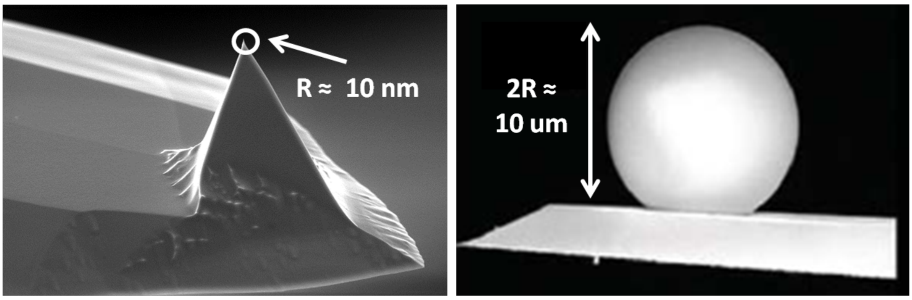

Figure 1.2: SEM images of a conventional sharp AFM tip (*left*) and a spherical micrometric probe, also known as colloidal probe (*right*). The typical radius of curvature (R) at the apex of the sharp tip and the diameter (2R) of the colloidal probe are reported. Despite sacrificing high-resolution on the nanoscale, colloidal probes clearly offer a well defined, smooth and simple geometry, better suited to probe the mechanics of soft and fragile samples.

also called *colloidal probes* (fig. 1.2), turn out to be superior in terms of reliability and accuracy of mechanical measurements on soft samples, overcoming on the one hand the technical issues concerning the calibration of the relevant geometrical probe parameters (and subsequently the accuracy of the related contact mechanics model), and identifying on the other hand a *mesoscopic* elasticity, representing the average collective contribution on the microscale of the cytoskeletal network and other cellular components, as the relevant biophysical observable for AFM-based clinical applications. This work has found its natural place in the framework of COST Action TD1002 (`http://www.afm4nanomedbio.eu/`), an European network aimed at the transferring of the AFM biophysical achievements to nanomedicine and clinical research. Among many activities, some efforts have been dedicated to the standardization of mechanical measurements on soft and biological samples by AFM [17]: this research, compared to the protocol presented in section 2.1, also involves more basic but nontrivial questions related to the calibration of fundamental AFM parameters such as the cantilever force constant and the optical lever sensitivity, and effectively compares mechanical measurements performed on test samples shared between different laboratories.

THE MOLECULAR CLUTCH MODEL The protocol I have developed has proved to be essential in the prosecution of the PhD activity, providing a solid background for the investigation of specific biophysical topics. A fundamental open field in biology concerns the intracellular mechanisms at the basis of cell adhesion and migration processes. The Molecular Clutch (MC) model, firstly proposed in 1988 by Mitchison and Kirschner [18], has been the subject of several studies. The term "clutch" refers to the complex, dynamic/adaptive linkage between the actin cytoskeleton and the "substrate" on which cells move, essential for the generation of the traction force needed by cells to migrate [19, 20, 21]. This coupling is effectively realized through the mediation of intracellular proteins (e.g. talin), interacting both with the actin cytoskeleton and trans-membrane proteins (e.g. integrin), which in turn can bind to the extracellular environment (see section 2.2 for details). Within this context, changes in cellular elasticity measured by AFM using the developed protocol turn out to be the manifestation of collective intracellular dynamics and cytoskeletal organization, proving again the correlation between cell mechanical properties and biological functions on the one hand, and helping to understand the relative importance of key MC proteins on the other, in combination with traditional optical and biochemical techniques (section 2.2 and ref. [22]).

PROBING THE CELLULAR MICROENVIRONMENT

A second quickly burgeoning field is represented by the interconnection between cells and their local microenvironment. One of the latter main component is represented by the extracellular matrix (ECM), a complex ensemble of proteins and other macromolecules sustaining multiple functions. Although it has been viewed for long time only as a *passive* constituent of living organisms, playing essentially a scaffolding role in tissue architecture and morphology, in the last decades several studies have led to the reversal of this idea. Indeed, ECM is now recognized to share a strong *reciprocal* interaction with cells, playing a fundamental role in the preservation of organs homeostasis (i.e. dynamic equilibrium and stability) and functions. ECM influences cellular behavior both from a biochemical and physical (mostly *mechanical*) point of view: through various signal transduction pathways the ECM can regulate cell growth, nuclear genetic expression and evolution; it offers anchorage points, where cells develop complex structures called focal adhesions which act as mechanosensors linking the ECM with the actin cytoskeleton, as in the case of the MC model; eventually, ECM spatial organization and orientation can determine its own *stiffness* and impact on cell migration, both favouring or constraining it : linearized collagen fibres are supposed to act as migration tracks, whereas a dense isotropic network of cross-linked proteins may work as a barrier [23, 24, 25]. A comprehensive overview of these processes can be found in fig. 1.3. Similarly, cells can modify the ECM chemical composition, influence the enzymatic activity or structurally reorganize its components, thus giving rise to a feedback loop by which cells and ECM transformation entail each other. A direct consequence of this interplay is that progression of cancers (or other diseases like inflammations) is strongly dependent on ECM deregulation, which in turn promotes cell abnormal behavior and metastasis, providing a proper tumorigenic microenvironment. In this framework, scientific collaborations with national and international groups, led respectively by Dr. Massimo Alfano (S. Raffaele hospital, Milan) and Prof. Irit Sagi (Weizmann Institute, Rehovot) have been carried out. These works aim at the quantification of changes in the biophysical properties of purified (i.e. decellularized) ECMs in association with human colorectal carcinoma infiltration (section 3.1 and ref. [26]) or inflammatory bowel disease progression based on a murine model (section 3.2 and ref.[27]). Again, we will see how AFM-based characterization of mechanical properties will provide a strong support to the evidence emerging from more traditional physical and biochemical techniques, or will even be able to discriminate between different pathological states when these techniques cannot detect significant differences (see refs. [26, 28] and section 3.1). The developed protocol for the combined topographic-mechanical imaging of living cells will supply the proper background also for the investigation of ECMs mechanics, with the exception of practical adjustments needed to match the characteristic dimensions of these samples (see fig. 1.1) and improvements in the statistical analysis, which in any case leave unaffected the core of the protocol. The choice of micrometric colloidal probes over sharp tips is once again done on the purpose of acquiring mesoscopically robust Young's modulus values which could be representative of the *collective* contributions of nanoscale molecular components organized in micrometer-sized structural and functional domains in the ECMs.

The rationale behind this kind of research is the attempt to gain a deep understanding of the complex relationship between cells and their local microenvironment. This, in turn, can prove to be beneficial on multiple sides. Indeed, the determination of ECM key components and biophysical features which are responsible for its deregulation during a specific disease progression, opens the way for the design of novel molecular agents targeting the ECM or the ensemble ECM-cells thought as an effective active entity, thus overcoming the classic paradigm according to which cells alone contribute to disease onset and development. This new kind of drugs can potentially bypass the difficulties experienced in delivery and uptake by conventional drugs, often associated to ECM hindrance effects.

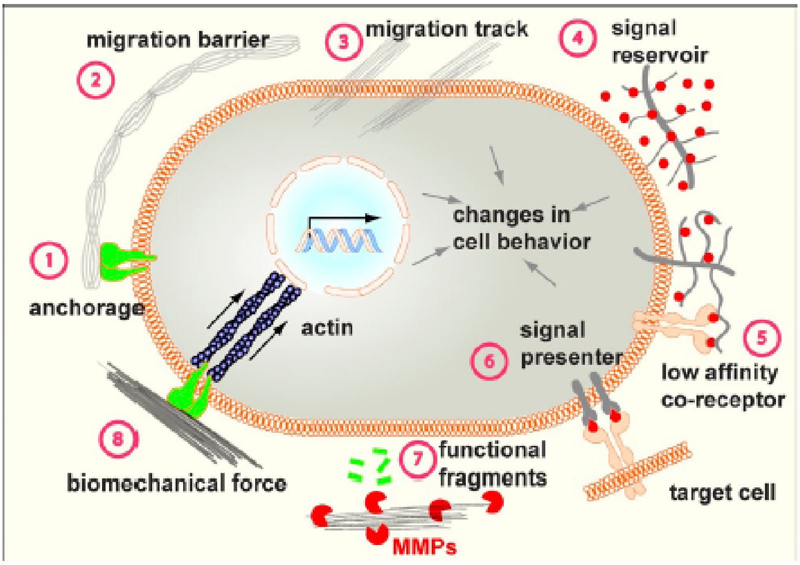

migration barrier
②
③ migration track
④ signal reservoir
changes in cell behavior
① anchorage
actin
signal presenter
⑥
⑤ low affinity co-receptor
⑧
biomechanical force
⑦ functional fragments
target cell
MMPs

Figure 1. **Mechanisms of ECM function.** The versatile functions of the ECM depend on its diverse physical, biochemical, and biomechanical properties. Anchorage to the basement membrane is essential for various biological processes, including asymmetric cell division in stem cell biology and maintenance of tissue polarity (stage 1). Depending on contexts, the ECM may serve to block or facilitate cell migration (stages 2 and 3). In addition, by binding to growth factor signaling molecules and preventing their otherwise free diffusion, the ECM acts as a sink for these signals and helps shape a concentration gradient (stage 4). Certain ECM components, including heparan sulfate proteoglycans and the hyaluronic acid receptor CD44, can selectively bind to different growth factors and function as a signal coreceptor (stage 5) or a presenter (stage 6) and help determine the direction of cell–cell communication (Lu et al., 2011). The ECM also direct signals to the cell by using its endogenous growth factor domains (not depicted) or functional fragment derivatives after being processed by proteases such as MMPs (stage 7). Finally, cells directly sense the biomechanical properties of the ECM, including its stiffness, and change a wide variety of behaviors accordingly (stage 8).

Figure 1.3: Schematics of ECM-cell interactions. Reproduced from [25]

MIMICKING THE ECM In a similar way, the identification of the ECM parameters relevant for cellular behavior and evolution can help in the improvement of conventional in-vitro culture systems, leading towards a new generation of engineered *active* biomaterials, able to stimulate specific cellular responses. Among many possible pathways, mechanotransduction is referred as the one by which cells capture and translate topographical and mechanical cues from the local microenvironment [29, 30]. From a structural point of view, natural tissue is well known to be nanostructured [30, 31]. Individual cell receptors and adhesion complexes also belong to the nanoworld, thus feeling local environment features on the nanoscale. In particular, many efforts have been dedicated so far to the investigation of the differentiation process induced on neuronal cells by *ordered nanostructured patterns* [32, 33, 34], produced by top-down techniques such as lithography and nanoimprinting. Yet, natural tissues typically appear to be quite *rough and disordered* on the nanoscale (fig. 1.4 A); moreover, the mechanisms underlying these mechanotransductive events are still only partially understood [32, 33, 34], thus providing a mainly *qualitative* picture of the overall process which hampers the practical use of these engineered substrates for biomedical applications, with particular regard to regenerative medicine. In this context, the possibility of exploiting a Supersonic Cluster Beam Deposition (SCBD) apparatus [35, 36, 37], which allows the production of biocompatible nanostructured surfaces (fig. 1.4 B) characterized by a *disordered topography, yet with accurately controllable and reproducible* morphological properties such as roughness, cluster size distribution and porosity [38], has provided the right input for a work aimed at a deep *quantitative* understanding of the mechanotransductive events promoting the differentiation of PC12 cells (a well-established neuron-like model cell line) cultured on zirconia nanostructured surfaces (section 4.1 and ref. [39]), thus moving a step forward the practical application of these devices in the biomedical field. Once again, AFM has proved to be a powerful tool, able to integrate the information provided on the biochemical side, thus contributing to build-up the global picture which links the nanoscopic topographical cues to the cellular fate in a causal way. In particular, its great versatility has allowed the investigation of both morphological properties of surfaces on the nanoscale, with traditional sharp tips and imaging modes, and the mechanical response of cells on the microscale, according to the developed protocol employing colloidal probes. Eventually, a similar approach has been applied to primary (ex-vivo) neuronal cells [40], though lacking the AFM-based mechanical characterization, mainly due to the increased physiological requirements of these cells, which are only partially achievable in the current AFM setting available in the laboratory (see e.g. Appendix C of the

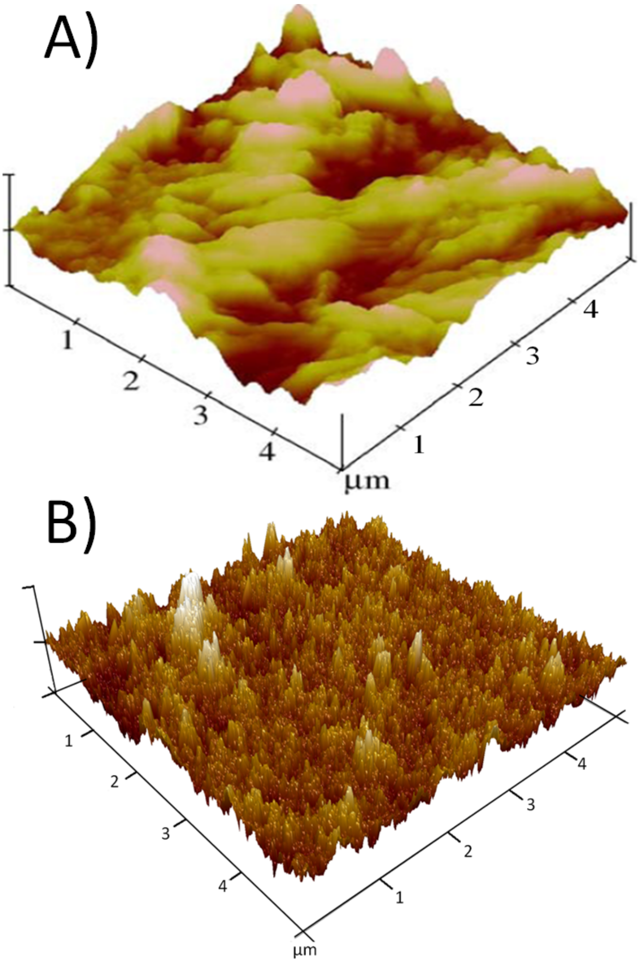

Figure 1.4: Mimicking the extracellular matrix : a qualitative comparison of the topography of natural tissues and engineered substrates on the nanoscale. A) AFM topography of porcine femur bone, adapted from [31] B) AFM topography of nanostructured carbon produced by SCBD. Vertical scale is 300 nm.

paper reported in section 2.1). Nevertheless, some improvements of the AFM experimental set-up will be soon realized (see also Chapter 5), together with topographical and mechanical measurements on human mesenchymal stem cells.

1.3 Thesis outline

In the next chapters, the Thesis will be organized as follows:

- In Chapter 2, the developed protocol for the AFM-based topographic and mechanical imaging on living cells with colloidal probes is reported [16], together with its application to a biological case of interest, i.e. cell migration [22];
- In Chapter 3 the aforementioned protocol is applied to the study of the influence of the cellular microenvironment on cell functions and behavior. In particular, the papers resulting from the collaboration with national and international groups, aimed at the study of progression and infiltration of Colorectal Carcinoma [26] and Inflammatory Bowel Disease [27], are reported;
- In Chapter 4 the possibility to reproduce in vitro the key features of the extracellular matrix (ECM) is discussed. In particular, the paper resulting from the investigation of neuron-like cells differentiation induced by nanostructured zirconia surfaces is reported [39];
- In Chapter 5 the main results obtained are briefly summarized, along with a discussion about potential improvements.

Eventually, some technical issues, mainly related to the calibration of fundamental parameters for AFM-based mechanics, are discussed in the Appendices:

- In Appendix A potential artefacts deriving from an inaccurate calibration of the deflection sensitivity and the cantilever force constant for the case of colloidal probes are extensively discussed, and possible solutions are proposed;
- In Appendix B a comparison between AFM and an interferometric nanoindenter [41] is performed through mechanical measurements on a PDMS sample;
- In Appendix C technical aspects about photodetector nonlinearity are briefly discussed.

Chapter 2

Characterization of mechanical properties of single living cells

2.1 Protocol development

Here below, my work concerning the building-up of a protocol for the combined topographic/mechanical imaging on living cells with colloidal probes is reported [16].

REVIEW OF SCIENTIFIC INSTRUMENTS **86**, 033705 (2015)

Nanomechanical and topographical imaging of living cells by atomic force microscopy with colloidal probes

Luca Puricelli, Massimiliano Galluzzi, Carsten Schulte, Alessandro Podestà,[a)]
and Paolo Milani
CIMaINa and Department of Physics, Università degli Studi di Milano, Via Celoria 16, 20133 Milano, Italy

(Received 16 September 2014; accepted 9 March 2015; published online 30 March 2015)

Atomic Force Microscopy (AFM) has a great potential as a tool to characterize mechanical and morphological properties of living cells; these properties have been shown to correlate with cells' fate and patho-physiological state in view of the development of novel early-diagnostic strategies. Although several reports have described experimental and technical approaches for the characterization of cellular elasticity by means of AFM, a robust and commonly accepted methodology is still lacking. Here, we show that micrometric spherical probes (also known as colloidal probes) are well suited for performing a combined topographic and mechanical analysis of living cells, with spatial resolution suitable for a complete and accurate mapping of cell morphological and elastic properties, and superior reliability and accuracy in the mechanical measurements with respect to conventional and widely used sharp AFM tips. We address a number of issues concerning the nanomechanical analysis, including the applicability of contact mechanical models and the impact of a constrained contact geometry on the measured Young's modulus (the finite-thickness effect). We have tested our protocol by imaging living PC12 and MDA-MB-231 cells, in order to demonstrate the importance of the correction of the finite-thickness effect and the change in Young's modulus induced by the action of a cytoskeleton-targeting drug. © *2015 AIP Publishing LLC.* [http://dx.doi.org/10.1063/1.4915896]

I. INTRODUCTION

In the last two decades, scientific interest is grown around the study of cells' mechanics,[1–4] as long as its close connection to several important cellular functions like adhesion, motility, proliferation, differentiation, internal molecular transport, or signal transmission, was being demonstrated. Indeed, cells can feel the outer environment and reorganize their cytoskeletal structure, an intricate network of cross-linked protein filaments,[3,5] in response to variations of their physico-chemical conditions. In general, the mechanical phenotype of cells is related to their own vital parameters.[2,3,6–13]

The Atomic Force Microscope[14,15] (AFM) has proved to be a valuable tool for the quantitative characterization of static and frequency-dependent mechanical properties of micro- and nanostructures, including biological specimens,[16–22] thanks to its ability to sense and apply nanoscale forces, and to capture the three-dimensional topography of samples in different environments, including physiological buffers. Several papers report on the measurement by AFM of modulations in cellular elasticity induced by variations in the environmental conditions, like drugs targeting specific cytoskeletal components,[23–25] by changes in the elasticity and surface energy of the substrate,[26–28] as well as by the correlation between cells' elasticity and their patho-physiological state, including cancer diseases.[29–34] In light of these considerations, it is not unreasonable to think about future applications of AFM in bio-nano-medicine, with particular regard to the pre-diagnosis of cancer diseases, drug testing, or regenerative medicine. However, despite the considerable results obtained so far, the application of AFM as an effective biomedical tool is still hampered by several practical and more fundamental issues, making difficult the comparison of independent experimental results obtained in different sessions or laboratories.

On one side, this is due to the extreme complexity of cellular systems. Indeed, cells are highly organized systems, characterized by a deep heterogeneity and diversity of their physico-chemical properties, even within the same specimen.

On the other side, the experimental methodology regarding both the measurements and the subsequent data-analysis of nanomechanical AFM-based tests is very complex. Artefacts can easily compromise the accuracy of the results. It is not surprising that the publication of (at least partially) methodological papers has always accompanied more biology-oriented publications (an interesting example, resulting from a recent networking effort within the EU, is represented by Ref. 35). The scenario, however, is still very fragmented, and a commonly accepted procedure is still missing. Our work represents an effort to contribute to the development of a common methodology.

A fundamental element of nanomechanical measurements of soft samples by AFM is the indenting probe. There is still debate about which are the best AFM probes for the nanomechanical investigation of cells, and the related issues about their spatial resolution limits and the applicability of the contact mechanics models. Commercial sharp tips, with their radius of curvature in the range 5-50 nm, are largely employed thanks to their low cost and their high resolution potential, which enables the concurrent topographical and

---

[a)]alessandro.podesta@mi.infn.it

© 2015 AIP Publishing LLC

Reuse of AIP Publishing content is subject to the terms at: https://publishing.aip.org/authors/rights-and-permissions. Download to IP: 159.149.46.47 On: Tue, 25 Oct 2016 11:25:43

mechanical investigation of nano-scale cellular components, like stress fibres, blebs, and other fine structures.[23,26,36–38] Micrometric spherical probes, also known as colloidal probes (CPs), obtained by attaching spherical microparticles to tipless cantilevers, are not very common, not only because of their much higher cost, but also because of their incompatibility with high spatial resolution. The limited spatial resolution in fact overshadows the great advantages of CPs, i.e., the well-defined geometry, the correspondingly well- (or better-) defined contact mechanics, as well as more subtle issues such as the more uniform strain and stress distribution induced in the sample upon contact, and the smoother averaged output generally provided in force measurements, as we will discuss in more detail in Sec. II.

A strong point of our work is that the commonly assumed incompatibility of lateral resolution with the use of CPs in combined AFM-based topographic and nanomechanical experiments is a false problem, provided one reconsiders the meaning of cellular elasticity and the technical requirements for accurately characterizing it. These aspects are introduced and discussed in detail in the manuscript. We show that CPs can provide enough resolution to accurately and simultaneously map topography and elasticity of living cells, with the ability of distinguishing among the biologically relevant cellular regions (body, nucleus, periphery, cellular extensions, etc.), and a number of advantages over sharp tips related to the interpretation of mechanical data.

Several aspects of the combined topographic and mechanical analysis are considered in this work, among which, the impact of the finite thickness of the cellular specimen on the measured Young's modulus; this leads typically to an overestimation of the elastic modulus,[39–41] due to the presence of the rigid substrate (typically, the plastic Petri dish bottom or a glass slide), acting as a spatial constraint to the strain and stress fields induced by the AFM probe in the cell body. We show that this effect is not negligible, and introduces artefacts depending on the local height of the cell and the intrinsic heterogeneity of its structure. We describe a strategy to take into account the finite-thickness effect, which is based on the recent work by Dimitriadis *et al.*[42] We also discuss other issues related to the rather complex data-analysis procedures for extracting quantitative information on cellular elasticity from the (typically huge) raw experimental data set, like the contact-point evaluation, the choice of the proper force (or indentation) interval on the single force curve for the Young's modulus estimation, and the estimation of the global error associated to the average Young's modulus of a population of cells. Noticeably, the accurate estimation of the contact point is an important step of the analysis, not only because it impacts directly on the fitting procedure leading to the Young's modulus estimation,[43,44] but also because this parameter is involved in the finite-thickness effect correction.

We therefore present a protocol for the combined topographical and mechanical analysis by AFM of living cells, as well as biological tissues and thin films, based on the use of micrometer-sized CPs. The protocol is meant to be an open framework within which single aspects of the topographic/nanomechanical characterization activity can be implemented, with the aim of converging towards a robust, accurate, shared methodology. The latter is essential for the quantitative comparison of independent results from different laboratories, and consequently for the effective exploitation of the AFM potential in the biomedical field. As a validation of the proposed procedure, we report on the characterization of the finite-thickness effect and of the modulation of cellular elasticity induced by Cytochalasin-D on living cells.

II. AFM TOPOGRAPHIC/MECHANICAL IMAGING OF LIVING CELLS BY COLLOIDAL PROBES

In this section, we outline the major points of our protocol, introducing the issues that characterize the different practices related to the topographical and mechanical analysis of cellular systems, as they have been developed in the last two decades by several authors. Here we discuss in detail three major points of nanomechanical analysis of soft samples, and in particular of living cells and tissues: the choice of the probe; the quantitative estimation of the impact of the constrained geometry (the finite-thickness effect) that characterizes the mechanical imaging of living cells; the complex data analysis procedure that aims at providing two numbers out of many AFM measurements, namely, the average value of the Young's modulus representative of a cell population, and its error. Meanwhile, we notice that when force and sample deformations must be measured by AFM, as in nanomechanical tests, force-distance curves are typically acquired by recording the cantilever deflection as a function of the distance travelled by the z-piezo during approaching/retracting cycles (details can be found in Ref. 17; latest developments can be found in Refs. 35 and 45). The acquisition of single force curves can be spatially resolved, by defining a grid of points spanning a finite area including the cell or the system under investigation and recording a set of curves, defining the so-called force volume.[46–48] The main advantage of force volume-like modes based on the vertical approach of the AFM probe is that the local height of the sample can be inferred by the force curves, so that the simultaneous acquisition of the topographic map and maps of other interfacial properties (elasticity among the others) in one-to-one correspondence is possible. The aforementioned vertical-approach modes have also been modified in order to perform variable-frequency experiments (typically in the 0-500 Hz range), to test the rheological response and viscoelasticity of the samples, including cells.[18,19,21,49,50]

A. Choosing the best probe

The choice of the probe for combined topographic and mechanical analysis of soft samples, living cells in particular, must be done considering different aspects, and will always represent a compromise where pros and cons are balanced with respect to the assumptions and aims of the experimental study one is willing to carry on. Depending on the requirements concerning the spatial resolution of topographic and mechanical maps, the contact mechanics model to adopt, as well as the physical properties that must be characterized, or better the meaning one attributes to them,

Reuse of AIP Publishing content is subject to the terms at: https://publishing.aip.org/authors/rights-and-permissions. Download to IP: 159.149.46.47 On: Tue, 25 Oct 2016 11:25:43

either standard sharp AFM tips or larger spherical beads can be preferred. The strong point we make in this work is that, provided one re-interprets the concept of cellular elasticity as an effective property, in the sense of averaged and mesoscopic, then large spherical beads represent the best choice for the AFM probe, in terms of reliability and accuracy of the mechanical results, adaptability to theoretical models, easiness of production and characterization, *as well* as spatial resolution. These points will be discussed in detail in Secs. II A 1–II A 4.

1. Sharp tips

The radius of curvature of the AFM probe determines the lateral resolution of the acquired maps. Despite the outstanding capability of resolving nanoscale mechanical (and morphological) heterogeneities of living cells demonstrated by conventional sharp AFM tips,[23,26,36–38] the applicability of hard sharp indenters against very soft and fragile samples like cells has been questioned.[21,40,42,51] For instance, a tendency by sharp tip to overestimate cells' rigidity has been reported and discussed,[39–41] and the applicability to sharp indenters of contact mechanics models has been addressed (the most commonly used non-adhesive models are introduced in Appendix A and Table III). Numerical simulations have also been performed to investigate and clarify these issues.[39,52] The critical points in using sharp AFM tips in mechanical measurements can be summarized as follows.

1. The nanometer-sized radius of curvature implies the application of high stress; the induced strain in soft samples like cells can be very large, even with very small applied forces.
2. Significant deviations from the nominal geometries are frequent; moreover, the evaluation of the relevant geometrical parameters can be difficult and inaccurate.
3. Cells are characterized by a heterogeneous and diverse structural complexity, and manifest strong dynamical nanoscale activity, so that the mechanical *nanoscale* properties are a rather poorly defined concept.

Concerning point 1, Dimitriadis and coworkers[42] have shown how probes with radii of curvature $R \leq 100$ nm can induce very high strains even for forces down to a few pN, which represents the lower limit of force detection for AFM optical beam deflection systems (see Figure 4 in Ref. 42). Under these conditions, damage of the cell's outer membrane or the underlying cytoskeletal structure is likely; moreover, and more fundamental, the small strain assumption, which is the basis of the most commonly used contact mechanics models, is not satisfied.

Concerning point 2, i.e., the tip geometry, it is well known that commercial tip shapes often exhibit departures from the ideal ones on which contact mechanics models rely, thus providing an ill-defined contact area and force-indentation response. Contact mechanics models apply therefore only approximately to the case of the contact between a hard sharp indenter and a soft sample. In particular, the actual geometry of the commercial probe is only partially accounted for by the existing models, therefore, for as good as one can characterize it (which can be rather time consuming and potentially destructive for the tip), there will always be a residual unaccountable uncertainty. Moreover, the difficulties related to the measurement of the relevant geometrical parameters (such as the tip opening angle) of sharp tips can lead to errors of the order of 15%-20%.[35]

In addition to technical issues, point 3 suggests that the cell structure, and in particular its peculiar nanoscale inhomogeneity, must also be considered when choosing the best probe for mechanical tests. Larger standard deviations are typically observed when using sharp indenters.[42] This feature can be a direct consequence of the high lateral resolution achievable with standard AFM sharp tips, because these probes are very sensitive to fine nanoscale inhomogeneities of the sample.[42,51] Moreover, the cells' dynamical activity on the nanoscale can introduce significant (time-dependent) fluctuations in the measured Young's modulus values. A higher spatial resolution, despite being an advantage from the topographic point of view, can turn into a disadvantage for the mechanical characterization, providing a less robust and less accurate estimation of the Young's modulus of the cell.

2. Colloidal spherical probes

Although several reports on the measurement of mechanical properties of living cells by AFM have been published so far, only a fraction of them is based on the use of CPs, among them, see Refs. 21, 40, 42, 51, and 53; as far as we know, the topographic imaging capabilities of CPs are typically not mentioned in such studies (with a few remarkable exceptions, as in Ref. 54). CPs represent, in our opinion, a better alternative to sharp tips whenever high resolution is not required, although, as we will show and discuss, they can provide satisfactory spatial resolution for the sake of cell topographic and mechanical characterization; CPs are the key feature of the AFM-based topographic/mechanical imaging protocol of the living cells we will describe in Secs. II B–II C 5. The main advantages of CPs versus sharp tips can be summarized as follows.

1. The applied force is distributed across a much wider (micrometric) area, thus, significantly reducing stress and strain in the cell.
2. CPs have a well-defined geometry, which can be easily characterized (see Appendix B 2 and Refs. 21, 55, and 56). The Hertz model (first in Table III) describes accurately the indentation of elastic bodies by spherical CPs.
3. CPs smear out nanoscale inhomogeneities, providing mesoscopic robust values of the Young's modulus of samples.[42,51]
4. CPs can be functionalized (thanks to their wide surface area) in order to study specific ligand/receptor interactions at the cell's surface.
5. CPs can be purchased, as well as produced directly in the laboratories, according to established protocols (see Appendix B and Refs. 55 and 57–60).

Micrometric CPs satisfy more easily the requirement of small strains at the basis of contact mechanics models (in the linear elastic regime), and at the same time, significantly

Reuse of AIP Publishing content is subject to the terms at: https://publishing.aip.org/authors/rights-and-permissions. Download to IP: 159.149.46.47 On: Tue, 25 Oct 2016 11:25:43

reduce the risk of cell's damage. In order to fully appreciate the advantages of CPs with respect to the applicability of contact mechanics models, we consider the commonly used model for spherical indenter, the Hertz model, first in the list of Table III. This model, first proposed by Hertz in 1881,[61] describes the local deformations related to the contact of two spheres of radius R_1 and R_2, characterized by a Young's modulus E_1 and E_2; the equation shown in Table III and commonly used represents the limiting case of a rigid sphere indenting an elastic half-space ($R_1 \rightarrow +\infty$, $E_1 \ll E_2$, or $E_2 \rightarrow +\infty$), which is not exactly the same situation for which the Hertz model had been originally developed (actually the opposite case, a soft indenter on a rigid surface[62]). Moreover, Hertz calculation is based on the assumption that the contact radius a (see the inset in Figure 2) is small compared to the radius of the sphere, that is $a \ll R$; this, in turn, implies that the deformation of the sample is much smaller than the radius of the sphere, $\delta \ll R$, knowing that contact radius and deformation are related by the equation $\delta = a^2/R$ (for more details, see Ref. 63). Using sharp tips, especially when indenting soft samples like cells, the hypotheses behind the Hertz model can be hardly satisfied.[62] The model developed by Sneddon, which can be applied to several geometries including the spherical one, does not suffer from the constraint $\delta \ll R$,[64] and more appropriately describes the case of a rigid indenter on a deformable surface (details in Appendix A). Unfortunately, Sneddon's equation for the spherical probe (Eq. (A2)) cannot be cast in an analytic closed form of the kind of Eq. (A1), but requires numerical methods to be solved.[62] Nevertheless, it is possible to prove that when the radius of the spherical indenter is larger than approximately 1-2 μm, the Hertz model, despite its more severe constraints, represents a very good approximation of the Sneddon model, therefore being appropriate to describe the force-indentation characteristics of soft samples, including living cells. Following Ref. 62, we show in Figure 1 the comparison of Hertz and Sneddon models describing the normal indentation of a soft sample as a function of the probe radius, for a Poisson coefficient $\nu = 0.5$ and three different force values (selected in the range typically observed during experiments). We see that for spheres with $R = 5$ μm even in extreme cases ($E = 200$ Pa, $F = 10$ nN), the relative discrepancy between the two models is well below 10%, and obviously decreases for milder conditions, so that for $F = 1$ nN, the relative discrepancy is only 1.7%, and further decreases for stiffer samples. Similarly, Figure 2 shows that when $R \gtrsim 5$ μm, the unphysical region where $a/R > 1$, in the same critical conditions, is never reached in Hertz model (Sneddon model has no such limitations like $a/R \ll 1$). In summary, the simple Hertz model represents always a good approximation for the contact mechanics of micrometric CPs, while its application to the case of sharp tips is questionable.

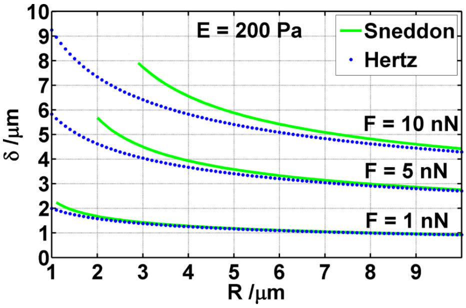

FIG. 1. Indentation vs tip radius for the case of a spherical micrometric probe according to the prediction of Hertz and Sneddon models; the Young's modulus (E = 200 Pa) and the selected forces are taken as fixed parameters.

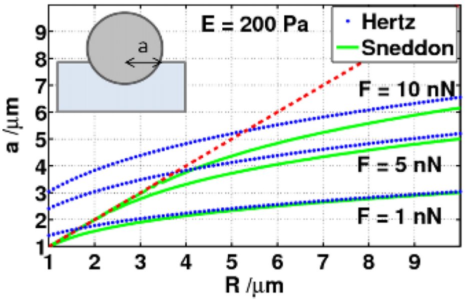

FIG. 2. Contact radius (shown in the inset) vs tip radius for the case of a spherical micrometric probe according to the prediction of Hertz and Sneddon models; the Young's modulus (E = 200 Pa) and the selected forces are taken as fixed parameters. The red dotted line marks the region for which the solutions of the Hertz model have physical meaning ($a \leq R$).

Concerning the other aspects, it has already been shown that micrometric spherical probes with different radii are able to provide comparable Young's modulus' values on both soft gels (Tables 1 and 2 in Ref. 42) and living cells (Figure 3 in Ref. 51): in the case of gels, they are also in good agreement with macroscopic measurements.[42] The contact geometry of CPs has been shown to be in excellent agreement to theoretical expectations by combined AFM and fluorescence microscopy analysis.[40] Moreover, it has been demonstrated that it is possible to detect length and grafting density of the brush layer on living cells,[65,66] or even to distinguish between cancerous and healthy cells' brushes,[67] thanks to the sensitivity of micrometric spherical probes provided by their wider surface area.

3. *Colloidal probes test an effective, yet biologically relevant elasticity*

It is clear that using micrometric spherical probes we must drop the idea of obtaining nano-scale lateral resolution in both topographic and mechanical maps, definitely losing information about fine structures like single stress fibres. As far as nanoscale heterogeneities at the membrane and close sub-membrane level are the object of the AFM investigation, sharp commercial tips have to be used; very remarkable results in coupling the nanoscale topographic imaging to the nanomechanical analysis have been obtained using this experimental configuration and published so far, as already pointed out. On the other hand, in light of the previous discussion, we must take into consideration that CPs can represent the best choice in order to obtain mesoscopic, statistically robust values of living cells' Young's modulus.

Reuse of AIP Publishing content is subject to the terms at: https://publishing.aip.org/authors/rights-and-permissions. Download to IP: 159.149.46.47 On: Tue, 25 Oct 2016 11:25:43

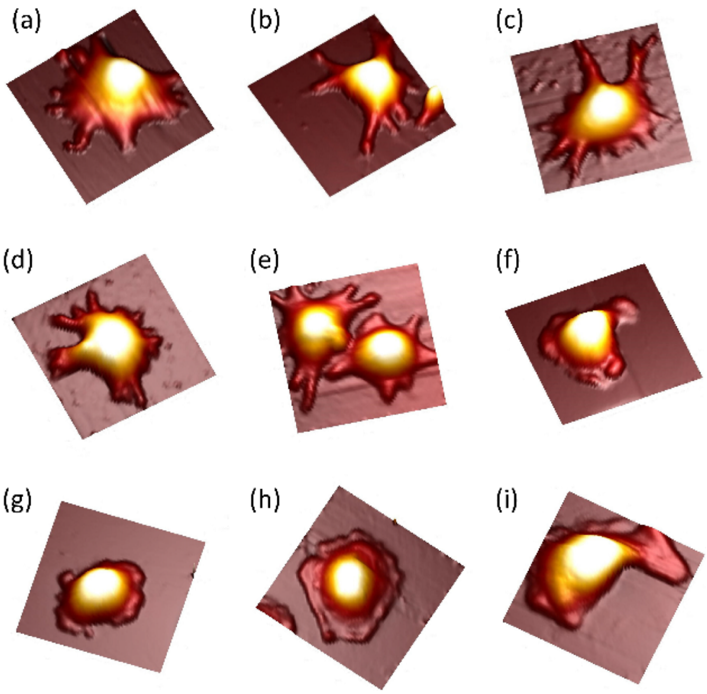

FIG. 3. Three-dimensional views of AFM topographic maps of living cells recorded in force volume mode using CPs with $R \simeq 5$ μm. Cells belong to the PC12 ((a)-(e)), and MDA-MB-231 ((f)-(i)) lines. The main parts of the cell are clearly resolved by the colloidal probe, despite its micrometric dimension. Scan sizes: (a) 65 μm; ((b),(c),(d),(f),(g)) 80 μm; (e) 75 μm; (h) 90 μm; (i) 50 μm. Vertical scale: (a) 4.5 μm; (b) 4.1 μm; (c) 2.4 μm; (d) 2.8 μm; (e) 3 μm; (f) 5.6 μm; (g) 6 μm; (h) 5 μm; and (i) 6 μm.

By mesoscopic, it is meant that the modulus should not reflect the mechanical properties of each single nanoscale entity of the complex cellular structure, such as an actin fibre, a microtubule, etc., but instead should represent the average combined collective action of several such entities, in numbers as well as typology. In other words, the effective elasticity of a cell in a given region is the result of the contributions of the membrane, the cytoskeleton and all its components, and possibly of other cellular elements, those that can be found in a reasonably large (mesoscopic) volume of the order of 1 μm^3. This effective mesoscopic elasticity is likely more relevant to clinical, pre-diagnostic applications of AFM nanomechanics than the elasticity of single nanoscale cellular components, as can be determined by using sharp tips. Once this point of view is accepted, then CPs represent the natural and optimal choice for carrying on a combined topographic and mechanical analysis.

4. *Lateral resolution of colloidal probes*

As long as one accepts that the effective mesoscopic Young's modulus is the relevant physical observable, the requirements on the lateral resolution of the topographic as well as of the nanomechanical analysis can be relaxed, the minimal resolution becoming the one allowing distinguishing among the major cellular regions, as the cell body, with the underlying nuclear region, and the cell periphery, with lamellipodia, cellular extensions, etc. A lateral resolution of a few microns is therefore more than enough to this purpose. Using CPs with radius up to 5 μm, an effective lateral resolution of 1–2 μm can be obtained, due to the fact that the contact radius a is typically only a fraction of the probe radius (with $R = 5$ μm and $\delta = 0.5$ μm, $a = \sqrt{\delta R} = 1.6$ μm; the sampling resolution of the force volume mapping can be comparable or even better). The lateral resolution can be appreciated in Figure 3, where several three-dimensional views of living cells belonging to the PC12 and MDA-MB-231 lines imaged in force volume mode using CPs with radius of approximately 5 μm are shown (images have not been corrected for the deformation, as explained in Sec. II C 4). By applying suitable masks to the force volume data set, built directly on the topographic map, it is possible to select the force curves corresponding to specific regions of the cell, and perform a site-resolved analysis of cellular elasticity; combining topographic to mechanical analysis is clearly an advantage from this point of view, with respect to performing only the mechanical analysis on pre-selected locations. The other great advantage of combining topographic and mechanical imaging is that the knowledge of the local height of the sample is crucial to implement the correction of the finite-thickness effect, as described in Sec. II B.

B. Finite-thickness effect

Besides the requirement of small strains, contact mechanics models are typically based on another important

Reuse of AIP Publishing content is subject to the terms at: https://publishing.aip.org/authors/rights-and-permissions. Download to IP: 159.149.46.47 On: Tue, 25 Oct 2016 11:25:43

assumption: the sample to be probed should be an elastic half-space, or at least its thickness should be much larger than the maximum indentation value ($h \gg \delta$). This is equivalent to ignoring the possible influence of the rigid substrate supporting the sample (i.e., the bottom of a Petri dish, in the case of living cells). For cells adherent to a substrate, this condition is not satisfied, since the cells' height typically varies from a few μm on the top (the nucleus region), to a few hundred nm on the peripheral regions, and indentation can easily exceed 1 μm. In the literature, this problem has been so far either poorly considered or addressed restricting, as a workaround, the mechanical analysis to the higher cells' areas (typically in the cell body), using small indentations. This solution keeps us from getting mechanical insights on all cellular regions and components, by limiting the mechanical analysis to the shallower regions as the outer membrane with the actin layer; in particular, it precludes the investigation of the thinner peripheral regions (as the cytoplasmic protrusions or lamellipodia), being responsible for the cells' motility and rich of focal adhesions points, which are potentially rich in information about cellular dynamics and interactions.

A few reports systematically investigate the influence of sample's thickness on the measured apparent Young's modulus, either experimentally or by means of numerical simulations.[21,39,44,68–72] Dimitriadis *et al.*[42] developed an analytic approximate correction for spherical probes in the limit of small indentation, to take into account the aforementioned effect due to the finite thickness of the sample (similar corrections have been reported for conical indenters;[72,73] for a study not limited to small indentation, see Ref. 71). Dimitriadis *et al.* analysed the two opposite conditions of a sample free to move (i.e., sliding) on the substrate, and of one that is well-bound to it:

$$F_{free} = \frac{16}{9} E R^{\frac{1}{2}} \delta^{\frac{3}{2}} \left[1 + 0.884\chi + 0.781\chi^2 + 0.386\chi^3 + 0.0048\chi^4\right] \tag{1}$$

for the case of free-to-move sample and

$$F_{bound} = \frac{16}{9} E R^{\frac{1}{2}} \delta^{\frac{3}{2}} \left[1 + 1.133\chi + 1.283\chi^2 + 0.769\chi^3 + 0.0975\chi^4\right] \tag{2}$$

for the case of the well-adherent sample. Here, $\chi = \frac{\sqrt{R\delta}}{h}$ is an adimensional variable that combines the critical lengths of the system. Noticeably, being $\delta = a^2/R$, we have $\chi = a/h$, i.e., the finite-thickness effect does not depend trivially on the ratio of vertical lengths δ and h, but rather on the ratio of the horizontal dimension of the contact (a) to the sample height h. The correction therefore takes into account the development of the strain and stress fields into the bulk volume of the sample, not only their vertical extension. As a consequence, we must expect stronger finite-thickness effects for colloidal probe with respect to sharp ones. The validity of Eqs. (1) and (2) is confirmed by the comparison with the numerical solutions for the system equations (as shown in Refs. 42 and 72), and the good agreement—especially for microspheres with $R = 5$ μm—with the macroscopic Young's modulus value measured on thin test samples of Poly(vinyl alcohol) gels. We can notice that the first term (outside the square brackets) is nothing but the Hertz model of Table III evaluated for $\nu = 0.5$, whereas the term in the square bracket is an adimensional factor, dependent on the local height and deformation of the sample, quantitatively describing the effect of the rigid substrate on which the cells are adhered, and vanishing as h becomes very large.

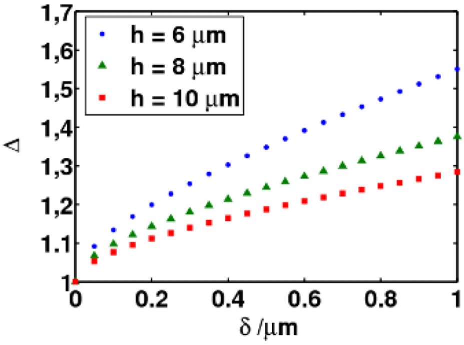

FIG. 4. Finite-thickness correction adimensional factor Δ vs indentations δ for typical cells' height values ($R = 5$ μm). For typical indentations of several hundreds nm, even in the limit of $h \simeq 10$ μm, Δ is not negligible.

A relevant question is whether cells should be considered free-to-move or well-adherent samples. Cells adhere to the underlying substrate through local dynamic structures named focal adhesions (which cells can destroy and rebuild depending on their necessities), therefore, they could be classified as inhomogeneously bound samples, i.e., as intermediate cases in between the two limiting conditions. Following the advice of Gavara and Chadwick,[73] we averaged Eqs. (1) and (2) calculating the arithmetical mean of the coefficients of the powers of the variable χ, obtaining

$$F = \frac{16}{9} E R^{\frac{1}{2}} \delta^{\frac{3}{2}} \left[1 + 1.009\chi + 1.032\chi^2 + 0.578\chi^3 + 0.051\chi^4\right]. \tag{3}$$

This is the effective equation for the correction of the finite-thickness effect that will be applied in Sec. III. Defining the correction factor, $\Delta(\chi) \equiv \Delta(\chi(R, \delta, h))$,

$$\Delta = 1 + 1.009\chi + 1.032\chi^2 + 0.578\chi^3 + 0.051\chi^4. \tag{4}$$

Equation (3) can be rewritten as

$$F = \frac{16}{9} E R^{\frac{1}{2}} \delta^{\frac{3}{2}} \Delta(\chi(R, \delta, h)). \tag{5}$$

Figure 4 shows that for a probe of radius $R = 5$ μm and indentations δ of several hundred nm, a typical situation in cell's mechanical analysis, the correction factor Δ is not negligible even for heights h as large as 10 μm.

C. Data analysis

Here, we describe and discuss the data-analysis procedures of the proposed protocol, aiming at defining a robust environment for the extraction of reliable and accurate results from nanomechanical data-sets. All data-analysis procedures

Reuse of AIP Publishing content is subject to the terms at: https://publishing.aip.org/authors/rights-and-permissions. Download to IP: 159.149.46.47 On: Tue, 25 Oct 2016 11:25:43

and algorithms have been implemented in Matlab environment.

Raw data must be pre-treated and converted so that force vs indentation curves in the proper units are obtained. These preliminary steps are described in Appendix D.

1. *Linearization of force curves*

Following Carl and Schillers,[51] we rewrite Eq. (5) in the linearized form

$$\delta - \delta_0 = \alpha F^*, \tag{6}$$

where δ_0 is explicitly introduced in order to account for the contact point, so that Eq. (6) holds for $\delta \geq \delta_0$, (δ_0 is implicitly assumed equal to zero in Table III); α is a constant containing the Young's modulus E, given by

$$\alpha = \left(\frac{9}{16}\frac{1}{ER^{\frac{1}{2}}}\right)^{\frac{2}{3}} \tag{7}$$

(with the assumption of Poisson ratio $\nu = 0.5$); F^* represents an effective pseudo-force, i.e., a variable with the dimensions of a force raised to the power of 2/3, given by

$$F^* = \left(\frac{F}{\Delta}\right)^{\frac{2}{3}}, \tag{8}$$

where Δ is the finite-thickness correction factor defined in Eq. (4). δ_0 and α are left as free parameters while fitting the experimental data.

From a technical point of view, linearization of Eq. (5) into Eq. (6) allows extracting the value of the Young's modulus from experimental data by means of a simple linear fit, which in turn can be done in parallel over a set of thousands of force curves by applying a matrix linear regression, drastically reducing the computational time with respect to a serial iterative fitting procedure.

2. *Multiple elastic regimes and their detection*

From the physical point of view, as already pointed out in Ref. 51, linearization of the force-indentation model allows performing a direct inspection on the cell's internal structure: indeed, the presence of multiple linear regimes in the linearized $F^*(\delta)$ curve can be the signature of different elastic regimes inside the cell, because the slope of the curve depends on the local elastic modulus. In Figure 5, the presence of several sloped portions of the curve (from a PC12 cell) is clearly visible, well beyond the noise level. It is also possible to notice a final non-linear region, where the force curve departs from a purely elastic behaviour, and/or where the finite-thickness correction model no longer holds. Trends like the one shown in Figure 5 represent an experimental evidence of the fact that cells are heterogeneous and complex systems, where different structural components contribute to the overall mesoscopic elasticity, and/or become active in a particular indentation range, depending also on their spatial distribution inside the cell's body.

When analyzing thousands of curves together and automatically, it would be useful to find a quick and automated way for identifying the different elastic ranges, or at least the region where the Hertz model (corrected for the finite thickness effect) can provide us with reliable mechanical information. The implementation of such automatic algorithm is very challenging for several reasons. First, cells are heterogeneous anisotropic specimens, so that we can observe a large variability of the value and the indentation range of different slopes from curve to curve; moreover, because of local different thickness, the range of each linear region can change moving from one region of the cell to the other. As a consequence, averaging different curves is not an option, because each curve is not in registry with the others. Second, the presence of noise further complicates the identification of different sloped regions. An interesting and robust solution to this problem was recently suggested by Polyakov *et al.*,[74] and it is based on a segmentation algorithm of force curves; the main drawback of the method, as highlighted by the authors themselves, is represented by the computational time required, which could reach several hours for the analysis of a single force volume set.

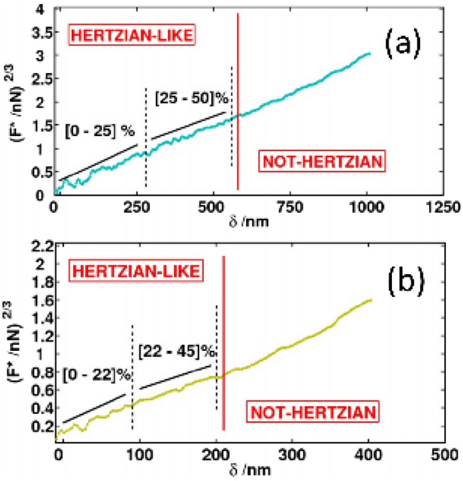

FIG. 5. Experimental force curves from a PC12 cell linearized according to Eq. (8): two different elastic regions are clearly visible, together with a non-linear region. The corresponding indentation percentages are reported. (a) Force curve taken over the cellular nucleus. (b) Force curve taken over the cellular peripheral regions or cytoplasmic extensions.

In light of these considerations, we decided to choose a semi-automatic approach based on the hypothesis that the relative amount of cytoskeletal components is approximately conserved in the cells, irrespective to the region, so that the absolute amount of each components is proportional to the local height of the sample. Under this simplified hypothesis, the relative width of each single elastic range is conserved in the force curves. The relative widths of different elastic regimes can be identified manually on a representative subset of force curves from different cell's regions and from different cells belonging to the same line and measured in the same experimental conditions, then set for all curves and the slopes evaluated by automatic parallel linear regression, as discussed above. The determination of linear ranges is the most time-consuming step of the procedure, but once the percentage

Reuse of AIP Publishing content is subject to the terms at: https://publishing.aip.org/authors/rights-and-permissions. Download to IP: 159.149.46.47 On: Tue, 25 Oct 2016 11:25:43

ranges are defined, it allows analysing automatically all the force volume sets from the same experiment.

3. Contact point evaluation

The absence of relevant adhesive interactions between the AFM probe and the cell surface represents an advantage when it allows using the simple Hertz model; the drawback is the lack of a clear jump-in structure in force curves, which helps identifying the contact point δ_0, which represents the origin of the indentation axis. In liquid, noise makes this identification even more difficult. Errors in the determination of the contact point may lead to poor estimation of the Young's modulus.[42,43] The accurate estimation of the contact point is also important for the correction of the finite-thickness effect, because δ_0 enters the definition of the χ parameter twice: through the indentation δ, which is calculated with respect to δ_0, and through the sample thickness h; indeed, the true height h of the sample is obtained adding the total elastic indentation to the apparent height, measured under compressive load in correspondence of the force setpoint (see Figure 3 of Ref. 42), and eventually subtracting the average height of the substrate.

It is commonly accepted that the best way to determine the contact point is by means of a fitting procedure.[42–44,75]

Our strategy for the determination of the contact point δ_0 is the following.

1. The distribution of all force values for each force curve is evaluated (Figures 6(a) and 6(b)). Force curves are baseline-subtracted (see Appendix D), therefore, a well-shaped peak is typically present, representing force values of the non-contact region fluctuating around an average value, typically close to zero. This small residual offset is subtracted to the data. Notice that in the presence of a well-shaped distribution, the Gaussian fit can be easily automatized. The width of the distribution, i.e., the standard deviation of the Gaussian curve, is taken as the representative noise level of the force curve.
2. A noise threshold is set N standard deviations (usually N = 1 is enough) above the baseline level previously determined (Figure 6(b)). The region of the curve above threshold (the contact part) is considered for fitting.
3. The first 20% of the contact part of the linearized force curve (i.e., the region closest to the contact point) is fitted by the Hertzian model, according to Eq. (6) with δ_0 as free parameter (Figure 6(c)). The finite-thickness correction can be neglected in this small-indentation region.

The width of the fitting region is arbitrary. Empirically, analyzing a significant set of curves selected among different cellular regions and cellular samples, we found an optimal percentage equal to 20% and 30% for the higher cellular regions (above and near the nucleus) and the thinner ones (cytoplasmic extensions), respectively. By repeating the fitting procedure varying the percentage width of the fitting interval between 20% and 30%, and by averaging the standard deviation of the mean of the obtained δ_0 values on different cells, we have estimated the error associated to the contact point as $\epsilon_{\delta_0} \approx 10$ nm; a smaller value would be unreasonable, considered the complexity of the probe/cell contact interface.

4. Calculation of corrected topographic and elastic maps

Once the contact point δ_0 has been determined with its error, the uncompressed topographic map is calculated, and the finite-thickness effect correction is implemented on force curves. The following actions are performed.

1. For each force curve, a new indentation axis $\delta' = \delta - \delta_0$ is calculated, so that the contact point is re-located at $\delta' = 0$. Force curves are now horizontally aligned with respect to the point of first contact.
2. The deformation map δ_{max} is calculated as $\delta_{max} = \delta_{stp} - \delta_0$, where δ_{stp} is the indentation value on the original axis in correspondence of the force setpoint.
3. The uncompressed topographic map h is calculated by adding the total deformation to the compressed topographic map, then subtracting the average height of the substrate.
4. The sample thickness h and total indentation δ_{max} are used to calculate the correction factor Δ (Eq. (4)) and the effective pseudo-force F^* (Eq. (8)).
5. The values of Young's modulus are extracted via linear regression of linearized curves on the selected indentation range, and the corresponding map is built.

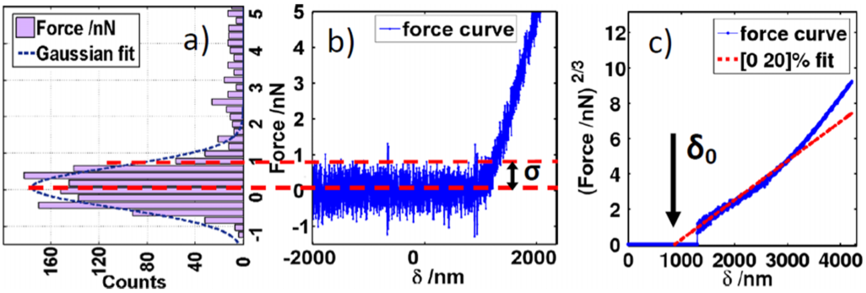

FIG. 6. Strategy for identifying the region of the force curve to fit with Hertzian model to determine accurately the contact point δ_0. The center and the width σ of the main peak in the histogram of all force values of the force curve are determined by a Gaussian fit (a), and used to set a force threshold on the force curve (a magnified view of the force curve close to the contact point is shown in (b)); the first 20% of the portion of the linearized force curve lying above this threshold is fit by the linearized Hertz model (Eq. (6)), with δ_0 as free parameter (c).

Reuse of AIP Publishing content is subject to the terms at: https://publishing.aip.org/authors/rights-and-permissions. Download to IP: 159.149.46.47 On: Tue, 25 Oct 2016 11:25:43

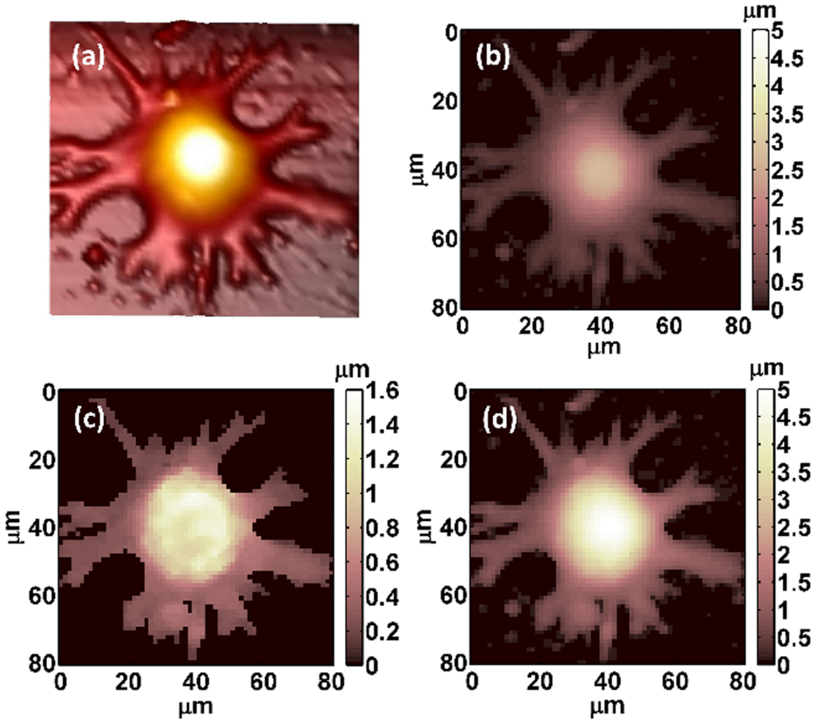

FIG. 7. Topographic maps for a cell from the line PC12. The maps were acquired using a colloidal probe with radius $R = 5008 \pm 51$ nm, attached to a cantilever with elastic constant $k = 0.32 \pm 0.03$ N/m. (a) 3D view of the compressed height map; (b) 2D compressed height map; (c) Indentation map: the substrate's height was arbitrarily set to zero; (d) Real height map given by the sum of (b) and (c).

When the distance axis of force curves is built using the absolute z-piezo position (z-sensor signal), the uncompressed topographic map h simply corresponds to δ_0 and step 3 can be skipped.

It is important to note that the z-piezo displacement signal is usually not reliable for accurate measurements of distances, therefore, the z-piezo should be operated in close-loop, or its absolute position (z-sensor signal) should be recorded while ramping. Non-linearities in vertical distances can lead to large errors in Young's modulus determination (see, for example, Ref. 76).

In Figure 7, we can see an overview of the different steps needed to build the final uncompressed topographic map: starting from the compressed topographic map (Figures 7(a) and 7(b)), we add the deformation map resulting from the local sample indentation (Figure 7(c)) in order to obtain the real height map of the cell (Figure 7(d)).

When indenting soft samples as living cells, deformation can be as large as a few microns, as seen in Figure 7, and the correction of the compressed topographic map is mandatory in order to accomplish the finite-thickness correction of the Young's modulus.

Not considering the identification of the multiple elastic ranges, the method discussed here allows obtaining the combined topographic/mechanical maps of a living cell from a force volume set of $64 \times 64 = 4096$ force curves in a few minutes using a 64 bit personal computer: the key is represented by the use of Hertz-like linearized expressions like Eq. (6), which allows analyzing in parallel, by means of matrix linear regression, the whole set of several thousands of curves.

5. Estimation of the error associated to the Young's modulus

Several sources of error, as well as the intrinsic variability of the biological specimens, affect the estimation of the Young's modulus E_{Cells} representative of a population of cells, N_{Cells} of which are actually imaged by AFM (typically $N_{Cells} \simeq 10$). The intrinsic cell-to-cell variability is significant even within the same cellular population. Then, at the single-cell level, we must consider several other contributions: the intrinsic variability arising from the heterogeneity of cellular structure (different cellular regions may have different elasticity, the local elasticity itself being the result of several different contributions from different parts of the cytoskeleton); the experimental error related to the mechanical measurement. Experimental errors can be due to uncertainties in the calibration of the AFM probe (cantilever elastic constant, probe radius) and the optical beam detection system (deflection sensitivity), as well as in the evaluation of physical parameters, like the contact point.

In Appendix E, we describe in detail our strategy to take into account all these uncertainties and estimate the total error, so that the result of the nanomechanical measurement can be expressed as $E_{Cells} \pm \sigma_{Cells}$.

Reuse of AIP Publishing content is subject to the terms at: https://publishing.aip.org/authors/rights-and-permissions. Download to IP: 159.149.46.47 On: Tue, 25 Oct 2016 11:25:43

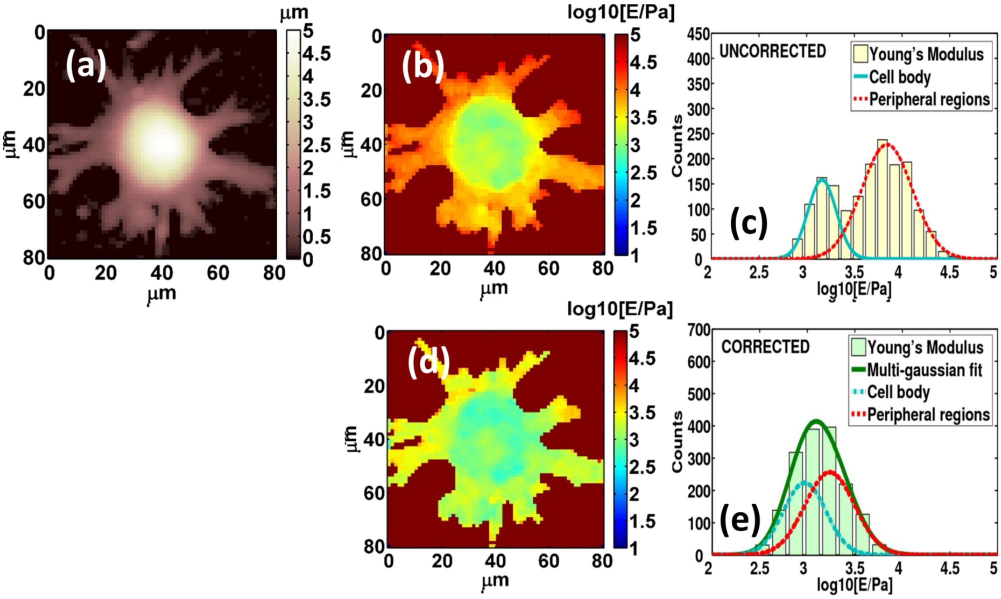

FIG. 8. The effect of finite thickness of sample in the determination of the Young's modulus. Topographic and elastic maps of a PC12 cell, and corresponding histograms of Young's modulus values (fitted on the 0%–40% indentation range), are shown. The value of the Young's modulus of the substrate has been arbitrarily set to 10 GPa. (a) Undeformed topographic map. (b) Young's modulus map without finite-thickness correction and (c) corresponding histogram of the Young's modulus values. (d) Young's modulus map with finite-thickness correction, and (e) corresponding histogram of the Young's modulus values. Young's modulus values are shown in semilog10 scale, with multi-Gaussian fit (details in Appendix C 3). Mean values, standard deviations, and the overall error associated to the force volume measurement (Sec. II C 5) are reported in Table I.

III. APPLICATION OF THE PROTOCOL TO LIVE CELL IMAGING

We have tested our protocol for topographic/mechanical imaging by CPs on living cells from the lines PC12 (pheochromocytoma of the rat adrenal medulla) and MDA-MB-231 (human breast adenocarcinoma), which have been cultured *in vitro* and then transferred into the thermostatic AFM fluid cell and kept for a few hours at 37 °C (recently, we have also applied our protocol to characterise lamellipodial membrane tension in the newly discovered phenomenon of ligand-independent adhesion signalling by integrins[77]). We have first investigated the effect of the finite-thickness correction on the determination of the elastic modulus, then we have studied the action of Cytochalasin-D, a cytoskeleton-targeting drug, on cellular elasticity.

A. Evidence of the finite-thickness effect in nanomechanical imaging of living cells

Figure 8 shows topographic and elastic maps, as well as the corresponding Young's modulus histograms, obtained on PC12 cells before and after the application of the finite-thickness correction. The Hertz model has been fitted to the 0%–40% indentation range; indentation was therefore enough deep to sense the presence of the underlying substrate, yet not exceedingly deep, so that Dimitriadis correction could apply with reasonable accuracy.

As previously discussed, cells usually appear more rigid because of their finite thickness and the presence of a rigid substrate underneath: for this reason, when the finite thickness correction is applied, we notice, in accordance to Eq. (3), an overall decrease of the cell's Young's modulus, and a relative decrease of the rigidity of the thinner peripheral regions with respect to the higher cell body. Young's modulus values (Figures 8(b) and 8(d)) can be represented in a semilog scale, in order to obtain more compact distributions (Figures 8(c) and 8(e)). Mean values and standard deviations corresponding to the different modes of the distributions (extracted by a multi-Gaussian fit on the semilog10 scale, then converted to the linear scale), and the overall error associated to the force volume measurement, are reported in Table I. When the correction is not applied (Figure 8(c)), a bimodal distribution is clearly observed, where the dominant peak represents mainly the contribution of the cell body and the other represents the contribution of the cellular extension; when the correction is applied (Figure 8(e)), the two different modes overlap, almost equally weighted, and are thus difficult to identify. Nevertheless, the peripheral, thinner, cellular region remain more rigid even after the finite-thickness correction, as can

TABLE I. The Young's modulus of a PC12 cell (Figure 8) calculated with and without the finite-thickness correction. Results are presented in the form: $E \pm \sigma_E(\pm\sigma_{FV}^{Cell})$/Pa (see Appendix E).

	Cell body	Peripheral region
Uncorrected	1706 ± 671(±69)	8165 ± 3212(±1062)
Corrected	976 ± 194(±30)	2108 ± 901(±169)

Reuse of AIP Publishing content is subject to the terms at: https://publishing.aip.org/authors/rights-and-permissions. Download to IP: 159.149.46.47 On: Tue, 25 Oct 2016 11:25:43

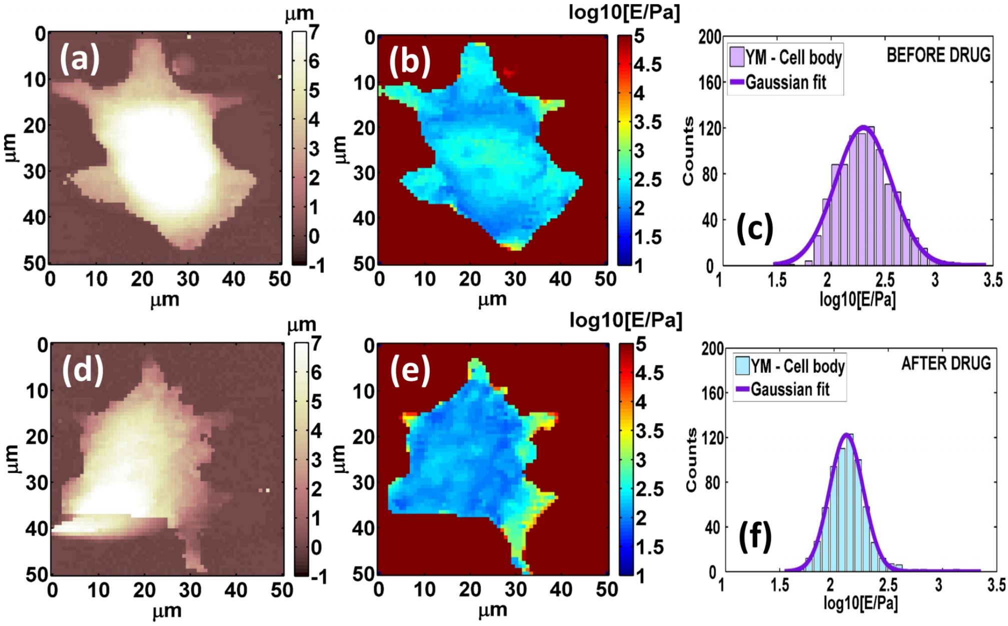

FIG. 9. Combined topographic/mechanical imaging of a cell from the MDA-MB-231 line before and after the introduction of Cytochalasin-D in the cell buffer. The value of the Young's modulus of the substrate has been arbitrarily set to 10 GPa; experimental artefacts have been properly masked when evaluating the Young's modulus histograms, from the cellular body region. (a) Topographic map. (b) Young's modulus map. (c) Histogram of the Young's modulus values before the drug's introduction. (d) Topographic map. (e) Young's modulus map. (f) Histogram of the Young's modulus values after the drug's introduction. Young's modulus values are reported in histograms in semilog10 scale, with multi-Gaussian fit (details in Appendix C 3). Mean values, standard deviations, and the overall error associated to the force volume measurement (Sec. II C 5) are reported in Table II.

be concluded by crossing the data from Figures 8(c) and 8(e). This is not surprising, as in the thinner cytoplasmic extensions is concentrated the majority of focal adhesion points, which allow the cell to anchor itself to the underlying substrate; it is therefore reasonable that the actin network, the principal cytoskeletal component involved in adhesion processes, possesses higher local density and rigidity.

B. The effect of Cytochalasin-D on the Young's modulus of living cells

In order to test the validity of the developed protocol to highlight structural changes in the cell's cytoskeleton, we have investigated the effect of a cytoskeleton-targeting drug, Cytochalasin-D, a complex molecule belonging to the class of micotoxins, which is able to penetrate the cell and depolimerize the actin network, binding itself to the active site of the free proteins or breaking the bondings between two consecutive proteins along a filament.[78] Therefore, a decrease in the cell's rigidity after the introduction of the drug in the culture medium has to be expected; this effect has been demonstrated by several authors thanks to AFM-based nanomechanical studies.[23–25] In Figure 9 are shown the results of the interaction of Cytochalasin-D with cells from the MDA-MB-231 line; the topographic and elastic maps (corrected for the finite-thickness effect) are shown, as well as the histograms of the Young's modulus values (the corresponding mean values and standard deviations are reported in Table II) measured on a single cell. The Hertz model has been fitted to the 0%–40% indentation range; a relatively shallow indentation range was chosen so as to capture the contribution of the actin network that is coupled to the cell membrane.

In this case, the exposure of the cell to the drug has produced not only a significant change in the Young's modulus (compare Figures 9(b) to 9(e)), but also a morphological change, especially in the thin cytoplasmic protrusions (compare Figures 9(a) to 9(d)); these regions are particularly rich in actin filaments and focal adhesions, which tend to be destroyed, reshaped, and pulled back by the drug. For this reason, the histograms and the mean values reported in Table II are related only to the cell's body, which undergo minor morphological changes upon drug exposure. The results obtained without applying the finite-thickness correction are qualitatively similar (the cell softens upon interacting with Cytochalasin D), although quantitatively different. When the correction is not applied, the difference between the average values of the Young's modulus before and after the treatment is larger; the standard deviations of data are larger as well, as the apparent modulus depends on the local height of

TABLE II. The Young's modulus of the cellular body of an MDA cell (Figure 9) before and after exposure to Cytochalasin-D. Results are presented in the form: $E \pm \sigma_E(\pm\sigma_{FV}^{Cell})$/Pa (see Appendix E).

	Uncorrected	Corrected
Before Cyto D	378 ± 226(±19)	235 ± 93(±5)
After Cyto D	254 ± 128(±13)	142 ± 42(±5)

Reuse of AIP Publishing content is subject to the terms at: https://publishing.aip.org/authors/rights-and-permissions. Download to IP: 159.149.46.47 On: Tue, 25 Oct 2016 11:25:43

the cell, which is far from being constant. It is worthwhile mentioning that, in principle, the percentage intervals related to the different slopes in the force curves (see Sec. II C 2) could change after the exposure to the drug; we actually observe this effect, since the percentage interval corresponding to the linear region changed from [0%–40%] to about [0%-60%] (in order to allow a better comparison, we have used a common indentation range, i.e., [0%–40%]).

IV. CONCLUSIONS

We have developed an experimental protocol for the combined topographic and nanomechanical imaging by AFM of soft samples, and in particular of cellular systems, based on the use of micrometric colloidal probes. Once it is accepted that the average mesoscopic Young's modulus of cells is the relevant physical quantity, a reasonable assumption in view of clinical and pre-diagnostic applications, as well as for studying the cell's response to external stimuli, it turns out that CPs represent a better alternative in terms of accuracy and reliability of mechanical measurements than sharp AFM tips. Moreover, we have shown that despite the common belief, CPs provide more-than-enough lateral resolution to carry out a spatially resolved analysis of the mechanical properties of living cells, where all the important components of the cellular system (the cell body with the nuclear region, the peripheral region, with the cellular extensions, protrusions and/or lapellipodia, etc.) can be clearly identified.

We have implemented a correction of finite-thickness effects in the determination of the Young's modulus, a necessary step in the protocol, due to the softness and limited thickness of the cellular samples. This allows measuring mechanical properties across the whole cellular surface, included the thinnest regions like lamellipodia, cellular extensions, or other cytoplasmic extensions, whose importance is justified by their role in cells' motility and richness in focal adhesions. Without the implementation of the finite-thickness effect, nanomechanical analyses should be limited to the highest cellular regions, so as to minimize the impact of the constrained contact geometry.

The protocol has been tested by performing combined topographic and mechanical imaging of living cells, from the PC12 and MDA-MB-231 lines. These experiments proved the reliability of the general protocol, and confirmed on one side the importance of the correction of the finite-thickness effect, on the other that CPs not only provide robust estimation of the Young's modulus of soft matter, but also a satisfactory lateral resolution in mechanical mapping of cellular systems.

Summarizing, in view of the standardization process for the extensive application of the AFM in the nano-biomedical field, and considering the many advantages related to the employment of CPs, we think that the ambition of performing a truly nanoscale mapping could be dropped in favour of a decent micrometric resolution, provided by CPs, which is appropriate to map even the smallest cells. The combined use of micrometric spherical probes and vertical approach modes like the Force Volume mode, together with the development and refinement of suitable algorithmic tools for the automation of data analysis and the improvement of AFM probe calibration methods, seems to us the best way towards the optimization of the combined topographic/mechanical imaging on living cells, and the effective exploitation of the potential of AFM in biology and medicine.

ACKNOWLEDGMENTS

A.P. thanks the COST Action TD1002 for providing a stimulating scientific environment for the discussion of AFM-based nanomechanics of cells and soft matter, and for supporting his networking activities. The authors thank M. Indrieri, D. Piotti, R. Simonetta, F. Fanalista for support in the development and test of the nanomechanical protocol, and C. Lenardi for support in the cell-biology laboratory of CIMaINa.

APPENDIX A: FORCE-INDENTATION MODELS

It is useful to recall the most important contact mechanics models and briefly discuss the physical conditions on which they rely. These models, under the hypothesis of negligible or null adhesion, can be cast (following the outline of Ref. 75) in a simple and generalized equation linking the force F applied by the AFM probe to the deformation (or indentation) δ of the sample

$$F = \lambda\delta^{\beta}, \qquad \text{(A1)}$$

where λ is a parameter containing the relevant mechanical information, i.e., the sample's Young's modulus E and the Poisson ratio ν, as well as the indenter properties, such as R, the radius of curvature, or the tip angle α. In Table III, the commonly used AFM probe shapes and the corresponding expressions and values for λ and β are listed.

TABLE III. Summary of the most common AFM tips' geometries and the corresponding parameters for Eq. (A1) (notice that the formula for the conical punch is reported incorrectly in Ref. 64).

λ	β	Probe shape
$\frac{4}{3}\frac{ER^{\frac{1}{2}}}{(1-\nu^2)}$	$\frac{3}{2}$	Sphere, or paraboloid, of radius R (Hertz[61])
$\frac{2}{\pi}\frac{E\tan\alpha}{(1-\nu^2)}$	2	Conical punch of tip angle 2α (Sneddon[80])
$0.7453\frac{E\tan\alpha}{(1-\nu^2)}$	2	Four-sided pyramidal punch of tip angle 2α (Bilodeau[79])
$0.7071\frac{E\tan\alpha}{(1-\nu^2)}$	2	Blunted four-sided pyramidal punch of tip angle 2α (Rico[49])
$2\frac{ER}{(1-\nu^2)}$	1	Flat-ended cylindrical punch of radius R (Sneddon[64])

Reuse of AIP Publishing content is subject to the terms at: https://publishing.aip.org/authors/rights-and-permissions. Download to IP: 159.149.46.47 On: Tue, 25 Oct 2016 11:25:43

Sharp tips belong to the last four rows of Table III; in particular, Bilodeau[79] and Rico[49] solutions for pyramidal tips are approximations derived from the Sneddon solution for the conical shape.[80] Sneddon solved the Boussinesq axisymmetric problem, calculating the solution for the case of the indentation of an elastic half-space by a solid of revolution whose axis is normal to the sample surface: equations for special shapes like sphere, cone, cylinder, and paraboloid of revolution have been derived. Sneddon calculations are developed in the framework of the classical theory of elasticity, which assumes a linear relationship between stress and strain, which in turn is based on the assumption of small strains; even if the strain upper limit for the validity of linear elasticity is not well defined (cells are sometimes described as elastomers,[81] which can bear high strains if compared with other materials) and could change from one cell type to another, it is clear that strains as high as those induced by sharp tips (Figure 4, Ref. 42) can easily exceed the boundaries of linear elasticity, thus depriving the Young's modulus of physical meaning.

Sneddon model for the indentation δ of an elastic flat surface by a rigid spherical punch is the following:[62,64]

$$F = \frac{E}{2(1-\nu^2)}\left[(a^2+R^2)\ln\left(\frac{R+a}{R-a}\right) - 2aR\right] \qquad \text{(A2)}$$

$$\delta = \frac{1}{2}a\ln\left(\frac{R+a}{R-a}\right), \qquad \text{(A3)}$$

where F is the force, a is the contact radius, R is the sphere radius, E and ν are the Young's modulus and the Poisson coefficient of the surface, accordingly. Equations (A2) and (A3) provide the Hertz model (the first in Table III) in the limit of small deformations and large tip radii ($a/R \ll 1$).[62] Noticeably, while the contact mechanical models in Table III and the Sneddon model have been derived under the assumption that the stress-strain relation is linear (purely elastic behaviour), i.e., under the hypothesis of small strains, the sphere-on-flat model by Sneddon (Eqs. (A2) and (A3)) does not rely on the additional constraint that also the indentation δ is small compared to the probe radius; the price to pay is the lack of an analytical form for the force vs indentation equation, which makes the Sneddon solution hard to implement in a real experiment. However, it can be shown (Sec. II A 2) that the Hertz model represents a very good approximation of the Sneddon model for colloidal probe, while this is not the case for sharp tips.

APPENDIX B: PRODUCTION AND CHARACTERIZATION OF COLLOIDAL PROBES

1. Production of colloidal probes

We have developed a protocol for the production and characterization of monolithic borosilicate glass CPs, which is described in detail in Ref. 55. Probes with similar characteristics can be produced by sintering methods also according to the procedures reported in Refs. 57 and 58. The most important highlights of the protocol and the advantages of the probes that can be produced are reported below.

1. Borosilicate glass microspheres are attached to tipless silicon cantilevers exploiting only adhesive capillary forces, thus avoiding using epoxy-based adhesives and other chemicals, which may either contaminate the probe and/or the imaging buffer, or keep from cleaning them in aggressive media.
2. Glass spheres are attached to silicon cantilevers by thermal annealing at high temperature (≃800 °C). The resulting *monolithic* borosilicate glass CPs can be washed/cleaned aggressively after use in order to remove contaminants (probes get readily contaminated upon indenting very soft samples like cells). Considering that the actual geometry and dimensions of the probes can be characterized accurately (more details in Appendix B 2), it follows that the same probe can be used many times, for the sake of comparability of data and reproducibility of experiments, on one side, and saving of money on the other.

2. Characterization of colloidal probe radius

The characterization of the radius of CPs is based on reverse AFM imaging of the probe, which is obtained by imaging a spiked grating (like the TGT1 from NT/MDT) (Figure 10), as described in detail in Ref. 55.

A collection of hundreds of independent replicas of the probe apical geometry is typically obtained; once the geometrical parameters of each probe replica have been calculated (volume, projected area, height), calibration curves

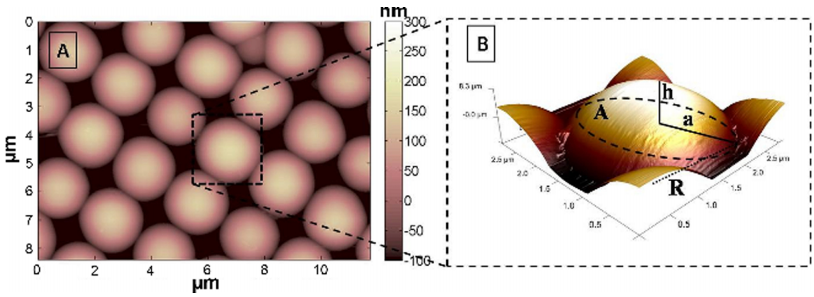

FIG. 10. Section of a topographic image acquired by a micrometric spherical probe over an array of spikes. (b) Detail of the single spherical cap with the relevant geometrical parameters.

Reuse of AIP Publishing content is subject to the terms at: https://publishing.aip.org/authors/rights-and-permissions. Download to IP: 159.149.46.47 On: Tue, 25 Oct 2016 11:25:43

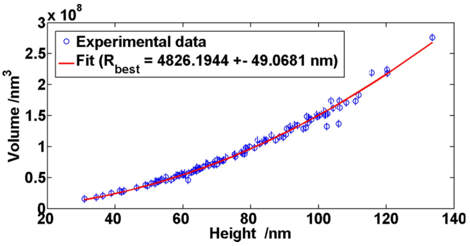

FIG. 11. Fit of the Volume vs Height relation obtained by a set of spherical caps (see Figure 10), which provides the radius R of the underlying sphere.

are built (the volume versus height curve is shown in Figure 11), and the probe radius R is extracted by fitting data to the appropriate spherical cap model, in this case $V = (\pi/3)h^2(3R - h)$. The overall accuracy of the probe radius evaluation can be as good as 1%.

Noticeably, this characterization approach also allows determining the three-dimensional shape of the apical region of the probe, before any spherical cap approximation, which can be useful, for instance, to test the hypothesis of spherical geometry or the contamination level of the probe.

APPENDIX C: EXPERIMENTAL SETUP AND IMAGING PARAMETERS

1. Thermostatic AFM liquid cell

Cells need the right environment to live and proliferate, i.e., a proper culture medium, a temperature $T = 37\,^\circ\mathrm{C}$, and an atmosphere with a 5% concentration of CO_2; in particular, temperature is the most relevant parameter for the stability of cells' conditions, so it should be addressed as a critical aspect for AFM measurements on living cells. In order to be able to run nanomechanical experiments for several hours (to collect a reasonable number of force volume maps, for the sake of statistics), we have built a thermostatic fluid cell, schematically represented in Figure 12.

The fluid cell is composed of two nested Petri dishes, the outer one working as a thermal bath (distilled water fills the gap between the two), and the innermost one containing the cells and the culture medium. Thermalization is obtained by means of an electrical resistor (inserted into a thin transparent plastic stripe), fixed on the internal surface of the outer Petri dish and properly calibrated in order to get the correct relation between the system temperature and the applied voltage. The two Petri dishes are fixed one to the other and to the AFM stage using magnets.

A direct consequence of thermalization is the evaporation of the culture medium, which can be harmful for both the AFM optical components and cells, leading to their apoptosis. It is possible to partially solve this problem covering the system with a plastic cap, with a proper hole for the insertion of the AFM head: this expedient suffers from the drawback of limiting the lateral range of the piezoelectric actuators, but on the other side, it creates a nearly closed system, characterized by a locally vapour-saturated atmosphere. This device does not compromise the eyesight of the integrated optical microscope and lets us to measure the cells' properties in their physiological conditions for an overall time of about 4-5 h, before they show clear suffering signals.

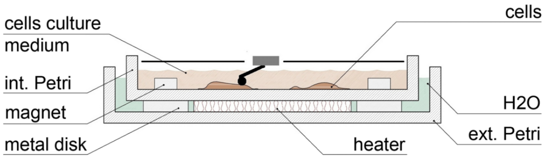

FIG. 12. Schematic representation of the custom thermostatic AFM cell.

2. Cell culture conditions

PC12 cells were maintained in RPMI-1640 Medium (Sigma-Aldrich), supplemented with 10% horse serum (HS; Sigma-Aldrich), 5% fetal bovine serum (FBS; Sigma-Aldrich), L-glutamine 2 mM, 100 units/ml penicillin, 100 g/ml streptomycin, 1 mM pyruvic acid (sodium salt), and 10 mM Hepes in 5% CO2, 98% air-humidified incubator (Galaxy S, RS Biotech, Irvine, California, USA) at 37 °C. Cells were detached from culture dishes using a solution 1 mM EDTA in HBSS (Sigma-Aldrich), centrifuged at 1000 rpm for 5 min, and resuspended in culture medium. Subcultures or culture medium exchanges were routinely established every 2nd to 3rd day into Petri dishes ($\Phi = 10$ cm).

The MDA-MB-231 cells were cultured in Dulbecco's modified eagle medium (DMEM; Lonza) supplemented with 10% fetal bovine serum (FBS; Sigma-Aldrich), L-glutamine 5 mM, 100 units/ml penicillin, and 100 units/ml streptomycin in 5% CO_2, 98% air-humidified incubator (Galaxy S, RS Biotech, Irvine, California, USA) at 37 °C. Cells were detached from culture dishes using a 0.25% Trypsin-EDTA in HBSS (Sigma-Aldrich), centrifuged at 1000 rpm for 5 min, and resuspended in culture medium. Subcultures or culture medium exchanges were routinely established every 2nd to 3rd day into Petri dishes ($\phi = 10$ cm).

3. Mechanical measurements and imaging parameters

All the topographic/mechanical maps were acquired with a Bioscope Catalyst AFM (Bruker) equipped with a Nanoscope V controller, by means of the force volume technique, with the following parameters: 64×64 force curves, each of them characterized by 2048 points, a ramp length $L = 5$ μm, a maximum applied force $F \approx$10–15 nN, a global ramp frequency $f = 7.10$ Hz composed by an approaching velocity $v_{appr} = 43.4$ μm/s, and a retracting velocity $v_{retr} = 195$ $\mu m/s$; this last choice is suggested by the effort to minimize the total time required for the acquisition of a single force volume map and the restriction of data analysis to the approaching force curves only. We employed spherical probes with radius $R \approx 5$ μm and cantilevers with elastic constants $k \approx 0.2$–0.3 N/m (thermal noise calibration), produced and characterized according to the procedures described in Appendix B. Living cells have been imaged

Reuse of AIP Publishing content is subject to the terms at: https://publishing.aip.org/authors/rights-and-permissions. Download to IP: 159.149.46.47 On: Tue, 25 Oct 2016 11:25:43

using a home-built thermostatic fluid cell set at $T = 37\,°\mathrm{C}$ (see Appendix C 1) in their own culture buffer, with the addition of 25 mM HEPES to keep the pH at the physiological value.

The logarithmic scale is well suited to represent the distribution of Young's modulus values from a single cell, considered the heterogeneity of cell's structure and the scattering of measured values. In semilog10 scale, the Young's modulus distributions are approximately Gaussian, which suggests that Young's modulus values are distributed lognormally. Peak values and corresponding widths are extracted by applying multi-Gaussian fits to Young's modulus histograms in semilog10 scale (the center of the Gaussian corresponds to the $\log_{10}$ of the median value of the Young's modulus). Under the assumption that the distribution is approximately lognormal, the fitting procedure allows getting rid of outliers and noise effectively, while a direct calculation of average values on linear scale would be more strongly affected by their presence. Logarithmic values are then transformed to linear values according to the theory of lognormal distributions; in particular, the mean Young's modulus value E and its standard deviation σ_E are calculated as: $E = 10^{\mu_{10}+(0.5\ln 10)\sigma_{10}^2}$ and $\sigma_E = E\sqrt{10^{\sigma_{10}^2} - 1}$, where μ_{10} and σ_{10} are the center and standard deviation of the Gaussian curve in semilog10 scale. Alternatively, the median value and the median absolute deviation (MAD) from the median value can be used to represent average and deviation of Young's modulus values.

APPENDIX D: DATA ANALYSIS: PRELIMINARY OPERATIONS

Force vs indentation $F(\delta)$ data must be prepared from raw data in order to extract Young's modulus data by suitable fitting procedures. The standard data pre-processing procedures are listed below (see also Ref. 17).

- All curves belonging to a force volume data set are processed simultaneously, in order to remove linear or sinusoidal baselines, which are often evident in the non-contact region, and are due to laser/cantilever/detector non-ideal alignment, laser interference etc. After baseline subtraction, the non-contact part of the force curve must appear flat. The baseline is fitted to the non-contact part of the curve, but is subtracted from the whole curve.
- Conversion of the raw cantilever deflection ΔV measured in Volts by the photodiode to the true deflection Δd in nanometers, through the equation $\Delta d = zsens \cdot \Delta V$, where $zsens$ is the deflection sensitivity in nm/V. $zsens$ is calculated as the inverse slope of the contact region of force curve acquired on a rigid substrate, or better averaged from those force curves in the Force Volume map belonging to the rigid substrate. Determination of $zsens$ parameter is critical, especially with CPs, due to non trivial bending of the cantilever/sphere assembly in the initial part of the contact region,[82] and care must be taken when fitting the linear region (an alternative strategy has been recently proposed[35]).
- Conversion of the horizontal axis from the piezoelectric displacement z_p (the typical abscissa of force curves as recorded by the AFM software) to the effective tip-sample distance d (which on the negative semi-axis corresponds, with the sign reverted, to the indentation δ, once the abscissa of the contact point has been set to zero): $d = z_p + \Delta d$, where Δd is positive or negative depending whether the cantilever is deflected upwards or downwards (see Figure 3 in Ref. 42, as well as Ref. 17).
- Calculation of the force F in nN: $F = k \cdot \Delta d$, where k is the cantilever vertical force constant, in N/m (as calibrated, for instance, by the thermal noise or Sader methods;[83,84] an alternative strategy has been recently proposed[35]). Details on the calibration procedure (as, for example, on the distinction between intrinsic and effective force constant[85]) can be found here: http://www.physics.uwo.ca/~hutter/calibration/afmcal.html.

APPENDIX E: DATA ANALYSIS: CALCULATION OF ERRORS

The uncertainties related to the cantilever elastic constant and the deflection sensitivity can be reasonably assumed to be of the order of 10% and 5%,[86] respectively. The absolute error on the contact point is about 10 nm, as discussed previously; the error on the probe radius (Appendix B 2) is about ≃1% and can be neglected.

A reliable method for estimating the global error on the Young's modulus deriving by the uncertainties in the calibration of experimental parameters is represented by a Monte Carlo simulation:[87] starting from a single experimental force curve (bearing its own noise level) in the original form (i.e., neither linearized nor corrected for the finite-thickness effect), a family of noisy curves is generated by adding a suitable noise to the original force curve. To each force value of the original curve, a random noise term randomly taken from a Gaussian distribution with zero mean and standard deviation δF is added. δF is calculated by propagating the experimental uncertainties through the equation $F = k \cdot zsens \cdot \Delta V$,

$$\delta F = \sqrt{(\Delta V \cdot zsens)^2 \delta_k^2 + (k \cdot \Delta V)^2 \delta_{zsens}^2}, \qquad \text{(E1)}$$

where ΔV represents the cantilever deflection detected in Volts by the photodiode and δ_k and δ_{zsens} stand for the aforementioned uncertainties on the cantilever elastic constant and the deflection sensitivity. Concerning the error on the contact point, this is accounted for in a similar way, by shifting the indentation axis of the original force curve by a random offset taken from a Gaussian distribution with zero mean and standard deviation $\epsilon_{\delta_0} = 10$ nm. For each noisy curve, the correction factor Δ (Eq. (4)) is calculated, as well as the effective force F^* (Eq. (8)). Typically, $N = 10^4$ force curves are generated according to this procedure, and fitted in order to obtain N independent values of the Young's modulus, which are expected to be distributed around the best value obtained by fitting the original rescaled curve. From the corresponding statistical distribution, we extract the 68% confidence interval σ_{fit}, symmetrically evaluated around the mean value, which

Reuse of AIP Publishing content is subject to the terms at: https://publishing.aip.org/authors/rights-and-permissions. Download to IP: 159.149.46.47 On: Tue, 25 Oct 2016 11:25:43

represents the global systematic error of the fitting procedure due to uncertainties in the calibration of the experimental parameters, including the contact point.

Restricting the analysis to those points belonging to a nearly homogeneous region of the cell (like the area above the nucleus, or the cell's periphery, with the cellular extensions), so as to exclude variability due to the intrinsic structural differences between different regions of the cell, we can calculate the global error for the single force volume set as

$$\sigma_{FV}^{Cell} = \sqrt{\sigma_{stat}^2 + \sigma_{fit}^2}, \tag{E2}$$

where $\sigma_{stat} = \frac{\sigma_E}{\sqrt{N}}$ is the standard deviation of the mean of the N Young moduli E (from N force curves) measured on the cellular region, which are distributed with standard deviation σ_E.

As a final step, the average value of the Young's modulus that is representative of the whole cellular population is calculated as $E_{Cells} = (\sum(E_i))/N_{Cells}$, N_{Cells} being the number of acquired force volume maps (each related to a different cell), and E_i being the Young moduli of single cells. The associated error must take into account both the error associated to the single force volume and that arising from the variability within the population. To this purpose, first of all, we propagate the error associated to the single force volume measurement σ_{FV}^{Cell} through the equation for the arithmetic mean, obtaining the total force volume error σ_{FV},

$$\sigma_{FV} = \frac{1}{N_{Cells}} \sqrt{\sum_i (\sigma_{FV}^{Cell})^2}, \tag{E3}$$

then, we add this error in quadrature to the standard deviation of the mean, $\sigma_{E_{Cells}}^{mean} = \frac{\sigma_{E_{Cells}}}{\sqrt{N_{Cells}}}$, of single-cell moduli E_i, which are distributed with standard deviation $\sigma_{E_{Cells}}$, in order to take into account the cell-to-cell variability as well. The final total error σ_{Cells} associated to the population mean value E_{Cells} is

$$\sigma_{Cells} = \sqrt{(\sigma_{E_{Cells}}^{mean})^2 + \sigma_{FV}^2}. \tag{E4}$$

The final output of the experimental procedure is therefore given as $E_{Cells} \pm \sigma_{Cells}$ (this typically refers to a specific region of the cell, although, in principle, an average value representing the cell as a whole can be determined in the same way, and also to a specific indentation range, i.e., to a specific elastic regime of the normalized force curve).

[1] C. Zhu, G. Bao, and N. Wang, Annu. Rev. Biomed. Eng. **2**, 189 (2000).
[2] S. Suresh, Acta Biomater. **3**, 413 (2007).
[3] D. A. Fletcher and D. Mullins, Nature **463**, 485 (2010).
[4] C. Lim, E. Zhou, and S. Quek, J. Biomech. **39**, 195 (2006).
[5] B. Alberts, A. Johnson, J. Lewis, M. Raff, K. Roberts, and P. Walter, *Molecular Biology of the Cell* (Garland Science, Taylor and Francis Group, 2008).
[6] D. E. Jaalouk and J. Lammerding, Nat. Rev. Mol. Cell Biol. **10**, 63 (2009).
[7] A. Diz-Munoz, D. A. Fletcher, and O. D. Weiner, Trends Cell Biol. **23**, 47 (2013).
[8] G. Lamour, A. Eftekhari-Bafrooei, E. Borguet, S. Soues, and A. Hamraoui, Biomaterials **31**, 3762 (2010).
[9] G. Bao and S. Suresh, Nat. Mater. **2**, 715 (2003).
[10] D. E. Discher, P. Janmey, and Y. L. Wang, Science **310**, 1139 (2005).
[11] M. J. Paszek, N. Zahir, K. R. Johnson, J. N. Lakins, G. I. Rozenberg, A. Gefen, C. A. Reinhart-King, S. S. Margulies, M. Dembo, D. Boettiger, D. A. Hammer, and V. M. Weaver, Cancer Cell **8**, 241 (2005).
[12] E. Elson, Annu. Rev. Biophys. Biophys. Chem. **17**, 397 (1988).
[13] J. Stricker, T. Falzone, and M. L. Gardel, J. Biomech. **43**, 9 (2010).
[14] D. J. Muller and Y. F. Dufrene, Nat. Nanotechnol. **3**, 261 (2008).
[15] A. Alessandrini and P. Facci, Meas. Sci. Technol. **16**, R65 (2005).
[16] A. L. Weisenhorn, M. Khorsandi, S. Kasas, V. Gotzos, and H.-J. Butt, Nanotechnology **4**, 106 (1993).
[17] H.-J. Butt, B. Cappella, and M. Kappl, Surf. Sci. Rep. **59**, 1 (2005).
[18] M. Radmacher, R. Tillmann, and H. Gaub, Biophys. J. **64**, 735 (1993).
[19] J. Alcaraz, L. Buscemi, M. Grabulosa, X. Trepat, B. Fabry, R. Farre, and D. Navajas, Biophys. J. **84**, 2071 (2003).
[20] S. Kasas and G. Dietler, Pfluegers Arch. - Eur. J. of Physiol. **456**, 13 (2008).
[21] R. E. Mahaffy, S. Park, E. Gerde, J. Kas, and C. K. Shih, Biophys. J. **86**, 1777 (2004).
[22] H. T. Nia, I. S. Bozchalooi, Y. Li, L. Han, H.-H. Hung, E. Frank, K. Youcef-Toumi, C. Ortiz, and A. Grodzinsky, Biophys. J. **104**, 1529 (2013).
[23] C. Rotsch and M. Radmacher, Biophys. J. **78**, 520 (2000).
[24] S. Kasas, X. Wang, H. Hirling, R. Marsault, B. Huni, A. Yersin, R. Regazzi, G. Grenningloh, B. Riederer, L. Forro, G. Dietler, and S. Catsicas, Cell Motil. Cytoskeleton **62**, 124 (2005).
[25] H. Oberleithner, C. Riethmuller, T. Ludwig, V. Shahin, C. Stock, A. Schwab, M. Hausberg, K. Kusche, and H. Schillers, J. Cell Sci. **119**, 1926 (2006).
[26] J. Domke, S. Dannohl, W. J. Parak, O. Muller, W. K. Aicher, and M. Radmacher, Colloids Surf., B **19**, 367 (2000).
[27] S. Y. Tee, J. Fu, C. S. Chen, and P. A. Janmey, Biophys. J. **100**, L25 (2011).
[28] A. Engler, L. Bacakova, C. Newman, A. Hategan, M. Griffin, and D. Discher, Biophys. J. **86**, 617 (2004).
[29] S. C. Lieber, N. Aubry, J. Pain, G. Diaz, S.-J. Kim, and S. F. Vatner, Am. J. Physiol.: Heart Circ. Physiol. **287**, H645 (2004).
[30] T. K. Berdyyeva, C. D. Woodworth, and I. Sokolov, Phys. Med. Biol. **50**, 81 (2005).
[31] M. Lekka, P. Laidler, D. Gil, J. Lekki, Z. Stachura, and A. Z. Hrynkiewicz, Eur. Biophys. J. **28**, 312 (1999).
[32] M. Lekka, K. Pogoda, J. Gostek, O. Klymenko, S. Prauzner-Bechcicki, J. Wiltowska-Zuber, J. Jaczewska, J. Lekki, and Z. Stachura, Micron **43**, 1259 (2012).
[33] S. E. Cross, Y. S. Jin, J. Rao, and J. K. Gimzewski, Nat. Nanotechnol. **2**, 780 (2007).
[34] M. Plodinec, M. Loparic, C. A. Monnier, E. C. Obermann, R. Zanetti-Dallenbach, P. Oertle, J. T. Hyotyla, U. Aebi, M. Bentires-Alj, R. Y. H. Lim, and C. A. Schoenenberger, Nat. Nanotechnol. **7**, 757 (2012).
[35] J. Schäpe *et al.*, "Standardized atomic force microscopy method for measuring mechanical properties of soft samples: The Dubrovnik procedure" (unpublished).
[36] G. Pletikapic, A. Berquand, T. M. Radic, and V. Svetlicic, J. Phycol. **48**, 174 (2011).
[37] C. Braunsmann, J. Seifert, J. Rheinlaender, and T. E. Schäffer, Rev. Sci. Instrum. **85**, 073703 (2014).
[38] A. Cartagena and A. Raman, Biophys. J. **106**, 1033 (2014).
[39] K. D. Costa and F. C. Yin, J. Biomech. Eng. **121**, 462 (1999).
[40] A. R. Harris and G. T. Charras, Nanotechnology **22**, 345102 (2011).
[41] C. T. McKee, J. A. Last, P. Russell, and C. J. Murphy, Tissue Eng., Part B **17**, 155 (2011).
[42] E. K. Dimitriadis, F. Horkay, J. Maresca, B. Kachar, and R. S. Chadwick, Biophys. J. **82**, 2798 (2002).
[43] S. L. Crick and F. C.-P. Yin, Biomech. Model. Mechanobiol. **6**, 199 (2006).
[44] J. Domke and M. Radmacher, Langmuir **14**, 3320 (1998).
[45] See http://www.cost.eu/domains_actions/bmbs/Actions/TD1002 for COST Action TD1002, European network on applications of atomic force microscopy to nanomedicine and life sciences (AFM4NanoMed&Bio (2014)).
[46] K. O. van der Werf, C. A. J. Putman, B. G. de Groot, and J. Greve, Appl. Phys. Lett. **65**, 1195 (1994).
[47] M. Radmacher, M. Fritz, C. M. Kacher, J. P. Cleveland, and P. K. Hansma, Biophys. J. **70**, 556 (1996).
[48] W. F. Heinz and J. H. Hoh, Trends Biotechnol. **17**, 143 (1999).
[49] F. Rico, P. Roca-Cusachs, N. Gavara, R. Farre, M. Rotger, and D. Navajas, Phys. Rev. E **72**, 021914 (2005).
[50] J. Rother, H. Nöding, I. Mey, and A. Janshoff, Open Biol. **4**, 140046 (2014).
[51] P. Carl and H. Schillers, Pfluegers Arch. - Eur. J. of Physiol. **457**, 551 (2008).
[52] D. C. Lin, D. I. Shreiber, E. K. Dimitriadis, and F. Horkay, Biomech. Model. Mechanobiol. **8**, 345 (2008).

Reuse of AIP Publishing content is subject to the terms at: https://publishing.aip.org/authors/rights-and-permissions. Download to IP: 159.149.46.47 On: Tue, 25 Oct 2016 11:25:43

[53] W. A. Ducker, T. J. Senden, and R. M. Pashley, Nature **353**, 239 (1991).
[54] I. Alesutan, J. Seifert, T. Pakladok, J. Rheinlaender, A. Lebedeva, S. T. Towhid, C. Stournaras, J. Voelkl, T. E. Schäffer, and F. Lang, Cell Physiol. Biochem. **32**, 728 (2013).
[55] M. Indrieri, A. Podesta, G. Bongiorno, D. Marchesi, and P. Milani, Rev. Sci. Instrum. **82**, 023708 (2011).
[56] C. Neto and V. S. J. Craig, Langmuir **17**, 2097 (2001).
[57] E. Bonaccurso, "Investigation of electrokinetic forces on single particles," Ph.D. thesis (Universitat-Gesamthochschule Siegen, Siegen, Germany, 2001).
[58] V. Kuznetsov and G. Papastavrou, Rev. Sci. Instrum. **83**, 116103 (2012).
[59] Y. Gan, Rev. Sci. Instrum. **78**, 081101 (2007).
[60] L. H. Mak, M. Knoll, D. Weiner, A. Gorschluter, A. Schirmeisen, and H. Fuchs, Rev. Sci. Instrum. **77**, 046104 (2006).
[61] H. Hertz, J. Reine Ang. Math. **92**, 156 (1881).
[62] M. Heuberger, G. Dietler, and L. Schlapbach, *8th International Conference on Scanning Tunneling Microscopy and Related Methods (STM 95)*, *Snowmass, CO*, *July 25-29, 1995* [J. Vac. Sci. Technol., B **14**, 1250 (1996)].
[63] K. L. Johnson, *Contact Mechanics* (Cambridge University Press, 1985).
[64] I. N. Sneddon, Int. J. Eng. Sci. **3**, 47 (1965).
[65] R. O'Callaghan, K. M. Job, R. O. Dull, and V. Hlady, Am. J. Physiol. Lung Cell Mol. Physiol. **301**, L353 (2011).
[66] I. Sokolov, S. Iyer, V. Subba-Rao, R. M. Gaikwad, and C. D. Woodworth, Appl. Phys. Lett. **91**, 023902 (2007).
[67] S. Iyer, R. M. Gaikwad, V. Subba-Rao, C. D. Woodworth, and I. Sokolov, Nat. Nanotechnol. **4**, 389 (2009).
[68] B. B. Akhremitchev and G. C. Walker, Langmuir **15**, 5630 (1999).
[69] B. Oommen and K. Van Vliet, Thin Solid Films **513**, 235 (2006).
[70] Y. Sun, T. Bell, and S. Zheng, Thin Solid Films **258**, 198 (1995).
[71] R. Long, M. S. Hall, M. Wu, and C.-Y. Hui, Biophys. J. **101**, 643 (2011).
[72] J. A. C. Santos, L. M. Rebelo, A. C. Araujo, E. B. Barros, and J. S. de Sousa, Soft Matter **8**, 4441 (2012).
[73] N. Gavara and R. S. Chadwick, Nat. Nanotechnol. **7**, 733 (2012).
[74] P. Polyakov, C. Soussen, J. Duan, J. F. L. Duval, D. Brie, and G. Francius, PLoS One **6**, e18887 (2011).
[75] D. C. Lin, E. K. Dimitriadis, and F. Horkay, J. Biomech. Eng. **129**, 430 (2007).
[76] C. Braunsmann, V. Prucker, and T. E. Schäffer, Appl. Phys. Lett. **104**, 103101 (2014).
[77] G. M. S. Ferraris, C. Schulte, V. Buttiglione, V. De Lorenzi, A. Piontini, M. Galluzzi, A. Podesta, C. D. Madsen, and N. Sidenius, EMBO J. **33**, 2458 (2014).
[78] U. B. Nair, P. B. Joel, Q. Wan, S. Lowey, M. A. Rould, and K. M. Trybus, J. Mol. Biol. **384**, 848 (2008).
[79] G. G. Bilodeau, J. Appl. Mech. **59**, 519 (1992).
[80] J. W. Harding and I. N. Sneddon, Math. Proc. Cambridge Philos. Soc. **41**, 16 (1945).
[81] X. Zeng and S. Li, J. Eng. Mech. **140**, 04013003 (2013).
[82] P. P. Weafer, J. P. McGarry, M. H. van Es, J. I. Kilpatrick, W. Ronan, D. R. Nolan, and S. P. Jarvis, Rev. Sci. Instrum. **83**, 093709 (2012).
[83] H. J. Butt and M. Jaschke, Nanotechnology **6**, 1 (1995).
[84] J. E. Sader, J. W. M. Chon, and P. Mulvaney, Rev. Sci. Instrum. **70**, 3967 (1999).
[85] J. L. Hutter, Langmuir **21**, 2630 (2005).
[86] While the statistical error associated to the deflection sensitivity can be rather small, provided several force curves acquired in different locations are used, and the corresponding values of the sensitivity averaged, there are subtle and rather poorly accountable systematic errors which can make the total error larger,[82] so that a 5% estimation is more reasonable (if not optimistic; this issue is discussed in detail in a forthcoming publication[35]).
[87] M. Lybanon, Comput. Geosci. **11**, 501 (1985).

Reuse of AIP Publishing content is subject to the terms at: https://publishing.aip.org/authors/rights-and-permissions. Download to IP: 159.149.46.47 On: Tue, 25 Oct 2016 11:25:43

2.1.1 Additional discussion

As previously outlined in section 1.2, the developed protocol does not offer a complete and definitive answer to the entire landscape of AFM-related issues for the investigation of soft and biological samples, even if providing a robust starting point towards the standardization of this kind of measurements. In particular, some technical matters show residual but remarkable uncertainties:

- The calibration of cantilever force constant k and deflection sensitivity *invOLS*, is not such an easy task as it may appear at a first glance. Both parameters are fundamental for AFM-based mechanical experiments, since they are needed to transform the original voltage signals into the proper units, as explained in Appendix D of the paper reported above (ref. [16]). The *invOLS* parameter is the most critical, since it affects both the indentation and the force axes; moreover, is it significantly involved also in the calibration of k, which is usually performed according to the thermal noise method [42, 43]. Micrometric spherical probes unfortunately can further complicate both the calibration of *invOLS* and k, due to non trivial bending of the cantilever, which influences its local shape and slope, probed by the optical lever system, and to the increase of the probe-to-cantilever mass ratio, which would eventually require correction factors for the "standard" thermal noise equation. All these problems are discussed in detail in Appendix A.

- "Dimitriadis correction" [44] for the finite thickness effect becomes less and less accurate as the local thickness of the sample decreases, since the Taylor series expansion is based on the assumption $\delta/h \ll 1$, where δ represents the local deformation or indentation and h the local sample thickness, respectively; moreover, the series diverges if $h \leq 0.1\,R$, where R stands for the radius of the indenting probe. Therefore, Young's modulus values obtained on peripheral regions like lamellipodia or other kinds of cellular protrusions are typically affected by a greater error, not easy to evaluate, compared to higher regions like the cellular body.

- The measured Young's modulus must be interpreted as an effective elastic property, since the Hertz model describes purely elastic mediums; on the contrary, biological samples often show a viscoelastic behavior [45, 46], dependent on the frequency of the approaching/retracting cycle as well as on the specific type of sample analyzed. Therefore, the use of a suitable viscoelastic model could improve further the accuracy of the obtained results, and provide better insights about the physics of biological samples (see also Chapter 5).

- The transition region between nuclear and peripheral areas is characterized by more or less steep slopes, depending on cell type (see fig. 3 in the paper reported above, ref. [16]). This can potentially lead to marked artefacts in the measured force curves, mainly due to multiple false contacts (e.g. touching the cell by the lateral edge or an inner part of the cantilever, meanwhile the probe is squeezing the cell at a lower position), and/or to deviations from the predicted hertzian contact radius $a = \sqrt{\delta R}$, which assumes local orthogonality between the surface and the indenting probe.

In light of these considerations, the quantification of an *absolute* Young's modulus map turns out to be quite difficult and questionable, despite the better accuracy demonstrated by colloidal probes with respect to conventional sharp tips. Nevertheless, it is not strictly necessary: in many (if not all) biophysical experiments, variations in the Young's modulus *relative* to control conditions, or reference samples, are measured. This allows to preserve the general trend and get rid of systematic errors, if the same experimental conditions (e.g. the same probe) are kept fixed[1]. In any case, an effective reproducibility and validation of independent results obtained by different laboratories cannot be achieved outside the borders of a standardized operational protocol [17].

---

[1] To notice, the estimated uncertainty mainly due to systematic errors (the term σ_{FV} in equation E4 inside the paper reported in section 2.1) typically turns out to be two-four times smaller than the fluctuations arising from natural cell-to-cell variability (σ^{mean}_{Ecells}), depending on the specific cellular type. The same is true also for the case of Extracellular matrices analyzed in Chapter 3. This assumes that the errors related to the calibration of the force constant K and the deflection sensitivity $invOLS$ are on the order of 10% and 5% respectively, as discussed in the paper above. If large colloidal probes ($R \gtrsim 30\,\mu m$) are used, proper corrections must be applied (see Appendices A, B), otherwise the overall systematic error may become comparable to or even greater than the intrinsic population variability.

2.2 Mechanics of cell migration : the Molecular Clutch model

The Molecular Clutch (MC) hypothesis [18] is the mainstream theory adopted by biologists to describe the mechanisms underlying cellular migration. This model suggests that the force/traction necessary for the protrusion of the membrane and the cellular translocation with respect to the substrate is provided by the retrograde actin flow. Basically, the actin meshwork undergoes a dynamic process by which it is continuously assembled, rearranged and locally disassembled depending on cell needs. The polymerization of actin filaments at the front edge of the lamellipodium should provide the force needed to push the membrane forward, but it is actually counterbalanced by a retrograde flow of the same filaments driven by mechanical passive resistance of the plasma membrane and the activity of Myosin II, which contracts filaments back in order to disassemble and reorganize them [19]. The equilibrium unbalance can happen if a "clutch" between the retrograde-moving actin filaments and transmembrane proteins binding to the extracellular matrix (ECM), properly mediated by intracellular adaptor proteins, is effectively realized. This ECM-cytoskeleton coupling in turn leads to a slowing of the retrograde flow and the subsequent generation of a net protrusion force (fig. 2.1). In detail, sufficient force generation can lead to the stretching and unfolding of talin, an essential protein which provides the initial linkage between the integrins and the cytoskeleton in the nascent adhesions, enabling the binding of vinculin and a further reinforcement of the molecular clutch. Vinculin, in turn, initiates the recruitment of additional integrin adhesion complex proteins potentially leading to the maturation of a macromolecular assembly, so-called focal adhesions, and stress fiber formation. Various parameters at different levels influence the dynamics and the extent of the molecular clutch engagement (fig. 2.2); i.e. the substrate stiffness and topography, the loading time of the MC, the breaking strength (slip bond, catch bond) and lifetime of the different molecular clutch linkages, the generated traction force [20, 21]. All these factors can either favor the maturation of the structure or cause its disassembly.The status and composition of these adhesion complexes impacts furthermore on the cytoskeletal organization and the cellular mechanics and signaling, determining therewith the response of the cell to its microenvironment. The whole process is defined as mechanotransduction and is not only essentially involved in the regulation of cell migration but in many processes, in particular in development and tissue homeostasis (see also Chapters 3 and 4).

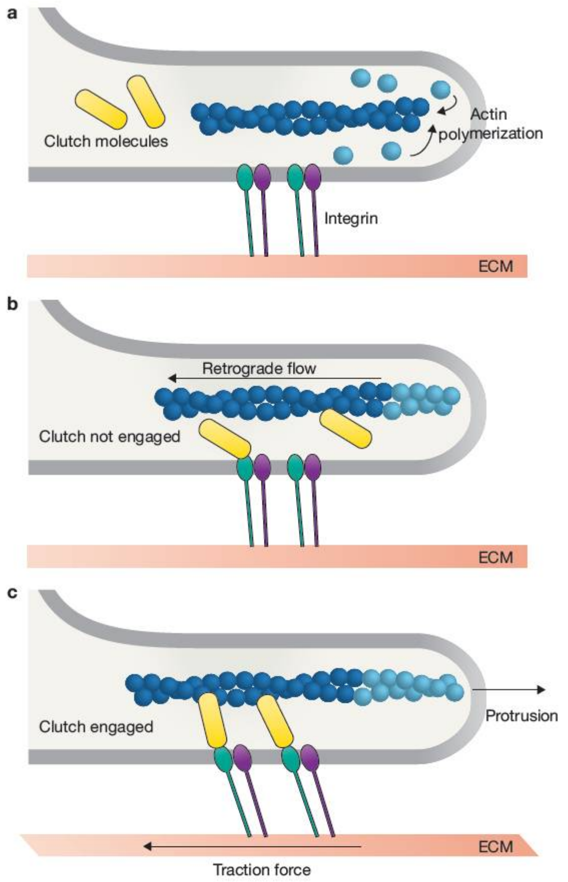
a
Clutch molecules
Actin polymerization
Integrin
ECM
b
Retrograde flow
Clutch not engaged
ECM
c
Clutch engaged
Protrusion
ECM
Traction force

Figure 1 The molecular clutch hypothesis. (**a**) New actin monomers (light blue) are incorporated on to the barbed end of a pre-existing actin filament (dark blue) facing the leading edge of the lamellipodia. Transmembrane integrin dimers (green and purple) are bound to the extracellular matrix (ECM). (**b**) If the clutch (yellow) is not engaged to connect actin to the ECM, then actin polymerization results in rapid retrograde cytoskeletal flow, no net leading edge protrusion and no traction force on the ECM. (**c**) If the clutch is engaged, the forces generated by polymerization of the actin cytoskeleton are physically transmitted to the ECM, resulting in slowing of retrograde flow, traction force on the ECM and a net edge protrusion.

Figure 2.1: Simple schematic capturing the main steps involved in the MC model for cell migration. Reproduced from [19]

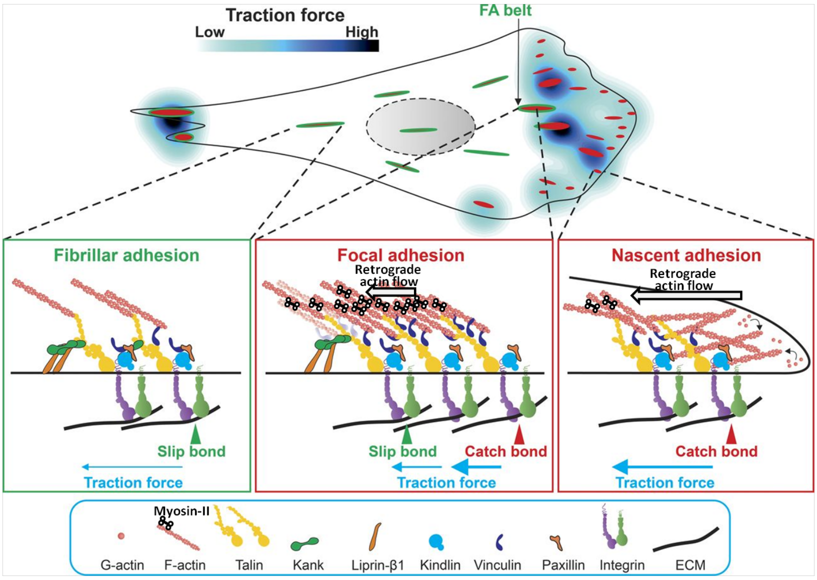
Traction force
Low
High
FA belt
Fibrillar adhesion
Slip bond
Traction force
Focal adhesion
Retrograde actin flow
Slip bond
Catch bond
Traction force
Nascent adhesion
Retrograde actin flow
Catch bond
Traction force
Myosin-II
G-actin
F-actin
Talin
Kank
Liprin-β1
Kindlin
Vinculin
Paxillin
Integrin
ECM

Figure 2.2: Detailed picture of the MC model, highlighting various proteins involved in the mediated integrin-cytoskeleton linkage, as well as diverse integrin-based adhesion structures which transmit different levels of traction forces to the ECM. Adapted from [20].

In the following, a paper by Schulte et al. [22], to which I contributed as a coauthor, is reported. This interdisciplinary work aims at investigating the different substeps of the MC model, trying to discriminate among the crucial and the dispensable ingredients. The work includes a recently discovered non-canonical integrin/ligand binding-independent condition [47], in which an indirect connection between non-integrin adhesion receptors and integrins is mediated by membrane tension (fig. 2.3).This work thus focuses on the intracellular linkage between integrins and the actin cytoskeleton, testing the effect of several talin variants on both mechanical and dynamical properties of HEK293 (Human Embryonic Kidney) cells. For sake of clarity, the main experimental conditions used throughout the paper are summarized in table 2.1.

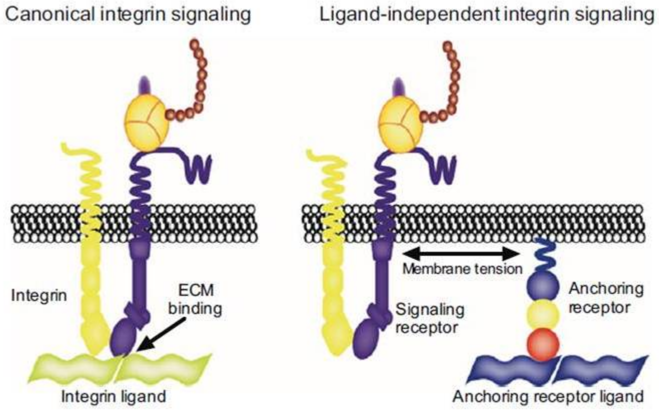
Canonical integrin signaling
Ligand-independent integrin signaling
Integrin
ECM binding
Integrin ligand
Membrane tension
Signaling receptor
Anchoring receptor
Anchoring receptor ligand

Figure 2.3: Schematic of two alternative ways to clutch the ECM with the inner cytoskeleton. Even in the case of a non-canonical binding, the "terminal" connection with the actin cytoskeleton is provided by the interaction between intracellular proteins (e.g. talin) and integrin, but integrin activation is mediated by membrane tension. Reported from [47].

In this framework, the AFM-based topographic/mechanical measurements, performed according to the protocol reported in section 2.1, allowed to detect changes in cell elasticity which turn out to be a biophysical marker of hidden molecular processes, i.e. the MC engagement status. This, in combination with other optical or biochemical experimental techniques, quantifying in particular lamellipodia spreading, integrin activation and clustering, and retrograde flow velocity, has provided a more complete picture of the phenomenon, eventually identifying the talin-mediated linkage between integrins and the actin cytoskeleton as a key feature for cell migration capability.

Substrate type	**Description**
VN^{RGD}	Vitronectin-coated substrate allowing integrin and uPAR binding
VN^{RAD}	Vitronectin-coated substrate permissive only for uPAR binding but not for integrin binding

(a) Vitronectin-coated substrates offering different adhesion pathways (see also fig. 2.3)

Talin variant	**Description**
TLN endogenous	Talin endogenously produced by cells
TLN WT-overexpressed	Induced overexpression of exogenous talin
TLN ΔABS	Talin able to bind to the integrins, but not to the actin cytoskeleton
TLN ΔABS/W359A	Talin unable to bind both to the integrins and the actin cytoskeleton

(b) Different types of talin with specific potential in mediating the integrins-cytoskeleton connection

Table 2.1: Overview of the different experimental conditions employed for the investigation of the MC model. A graphical illustration can be found in Figure 1A of the publication reported here below.

European Journal of Cell Biology 95 (2016) 1–14

Contents lists available at ScienceDirect

European Journal of Cell Biology

journal homepage: www.elsevier.com/locate/ejcb

Research paper

Lamellipodial tension, not integrin/ligand binding, is the crucial factor to realise integrin activation and cell migration

Carsten Schulte[a,c,*], Gian Maria Sarra Ferraris[a], Amanda Oldani[b], Massimiliano Galluzzi[c], Alessandro Podestà[c], Luca Puricelli[c], Valentina de Lorenzi[a], Cristina Lenardi[c], Paolo Milani[c], Nicolai Sidenius[a]

[a] Unit of Cell Matrix Signalling, IFOM, The FIRC Institute of Molecular Oncology, Via Adamello 16, 20139 Milan, Italy
[b] Imaging Unit, IFOM, The FIRC Institute of Molecular Oncology, Via Adamello 16, 20139 Milan, Italy
[c] CIMaINa (Interdisciplinary Centre for Nanostructured Material and Interfaces) and Department of Physics, Università degli Studi di Milano, Via Celoria 16, 20133 Milano, Italy

ARTICLE INFO

Article history:
Received 18 May 2015
Received in revised form 5 October 2015
Accepted 13 October 2015

Keywords:
Talin
PIP_2
uPAR
Focal adhesion
Molecular clutch
Mechanotransduction
AFM

ABSTRACT

The molecular clutch (MC) model proposes that actomyosin-driven force transmission permits integrin-dependent cell migration. To investigate the MC, we introduced diverse talin (TLN) and integrin variants into Flp-In^{TM} T-Rex^{TM} HEK293 cells stably expressing uPAR. Vitronectin variants served as substrate providing uPAR-mediated cell adhesion and optionally integrin binding. This particular system allowed us to selectively analyse key MC proteins and interactions, effectively from the extracellular matrix substrate to intracellular f-actin, and to therewith study mechanobiological aspects of MC engagement also uncoupled from integrin/ligand binding. With this experimental approach, we found that for the initial PIP_2-dependent membrane/TLN/f-actin linkage and persistent lamellipodia formation the C-terminal TLN actin binding site (ABS) is dispensable. The establishment of an adequate MC-mediated lamellipodial tension instead depends predominantly on the coupling of this C-terminal TLN ABS to the actomyosin-driven retrograde actin flow force. This lamellipodial tension is crucial for full integrin activation eventually determining integrin-dependent cell migration. In the integrin/ligand-independent condition the frictional membrane resistance participates to these processes. Integrin/ligand binding can also contribute but is not necessarily required.

© 2015 Elsevier GmbH. All rights reserved.

1. Introduction

Integrin-dependent cell migration is important in many biological processes like embryo- and tissue-morphogenesis, wound healing and immune defence, or pathological situations such as metastasis. It requires morphological changes regulated and effected by complex intracellular events.

The cell polarises and forms membrane protrusions like filopodia and lamellipodia. Lamellipodia are generated by an actin polymerisation machinery that pushes forward membrane protrusions (Ridley, 2011). Myosin II then contracts the filamentous actin (f-actin) network contributing to its retrograde flow (Svitkina et al., 1997). To protrude the front membrane efficiently, these actomyosin-driven forces are linked to the integrins in the cell membrane by the assembly of the “molecular clutch” (MC) (Mitchison and Kirschner, 1988). Various studies revealed that the MC comprises an elaborated mechanosensitive network of interacting cytoskeletal, scaffolding and signalling components realising a highly adaptive coupling of the cellular outside with the actomyosin network (Giannone et al., 2009; Renkawitz et al., 2009; Vicente-Manzanares et al., 2009; Ciobanasu et al., 2013, 2014).

Integrins are heterodimeric transmembrane adhesion receptors capable of bidirectional signalling and mechanical force transduction across the membrane (Hynes, 2002; Luo and Springer, 2006; Ciobanasu et al., 2013). Different integrin activation states can be implemented by cytoplasmic tail separation and swing-out of the

---

Abbreviations: ABS, actin-binding site; ΔABS, actin-binding site deletion; ECM, extracellular matrix; FA(s), focal adhesion(s); f-Actin, filamentous actin; FC(s), focal complex(es); FERM, 4.1 protein, ezrin, radixin, moesin; FN, fibronectin; (k)Pa, (kilo)Pascal; mAb, monoclonal antibody; MC, molecular clutch; MCBD, methyl-β-cyclodextrin; MIDAS, metal ion-dependent adhesion sites; pN, pico Newton; TLN, talin; uPA, urokinase plasminogen activator; uPAR, urokinase plasminogen activator receptor; VN, vitronectin; WT, wildtype; SD, standard deviation; CI, 95% confidence interval; DIC, differential interference contrast.

[*] Corresponding author. Current address: CIMaINa (Interdisciplinary Centre for Nanostructured Materials and Interfaces) and Department of Physics, University of Milan, Via Celoria, 16, 20133 Milan, Italy.

E-mail address: carsten.schulte@unimi.it (C. Schulte).

http://dx.doi.org/10.1016/j.ejcb.2015.10.002
0171-9335/© 2015 Elsevier GmbH. All rights reserved.

flexible extracellular hybrid domain. In inside-out signalling, intracellular signals induce binding of activators to the tails. This leads to conformational changes of the extracellular integrin domain influencing also its ligand affinity. In outside-in signalling integrin/ligand binding triggers the integrin activation and signalling (Hynes, 2002; Arnaout et al., 2005; Luo and Springer, 2006; Askari et al., 2009; Shattil et al., 2010; Chen et al., 2010, p. 2; Kim et al., 2012; Ciobanasu et al., 2013). Also non-integrin adhesion receptors, such as the urokinase-type plasminogen activator receptor (uPAR), can initiate integrin-dependent signalling by increasing membrane tension, even independently of direct interaction of the integrins with the extracellular matrix (ECM) (Ferraris et al., 2014).

Talin (TLN) is recruited to the lamellipodial cell membrane and activated by PIP_2 (Goksoy et al., 2008; Legate et al., 2011). There it mediates the initial connection between the β-integrin tail and the retrograde actin flow. This controls furthermore the focal adhesion (FA) nanoarchitecture (Liu et al., 2015). TLN consists of a N-terminal head and a C-terminal flexible rod domain. The head FERM domain binds membrane-proximal motifs of the β-integrin tail which activates the integrin (Vinogradova et al., 2002; Jiang et al., 2003; Tadokoro et al., 2003; Wegener et al., 2007; Critchley, 2009; Moser et al., 2009; Kim et al., 2012; Pinon et al., 2014). The rod provides the major part of actin binding via actin binding sites (ABS), in particular the C-terminal ABS3 (Hemmings et al., 1996; Giannone et al., 2003; Jiang et al., 2003; Gingras et al., 2008).

The initial connection between integrins and f-actin in nascent adhesions can mature to focal complexes (FC) or eventually FA. Therefore many components must be recruited which transform the structures into signalling hubs (Hu et al., 2007; Moser et al., 2009; Kanchanawong et al., 2010; Ciobanasu et al., 2013; Schiller and Fässler, 2013; Pinon et al., 2014). Their proper spatiotemporal organisation is critical for optimal migration (Gupton and Waterman-Storer, 2006) as they integrate biochemical and mechanical signals regulating the cell behaviour (Schwartz and Horwitz, 2006; Ciobanasu et al., 2013; Lieber et al., 2013). Tension is essential and keeps the signals confined (Houk et al., 2012) and controls the lamellipodial organisation, polarity, spreading and migration (Raucher and Sheetz, 2000; Fletcher and Mullins, 2010; Batchelder et al., 2011; Diz-Muñoz et al., 2013; Ferraris et al., 2014). However, these mechanobiological aspects are only partially understood.

In this context we here addressed the following questions:

> Does integrin-dependent cell migration require strictly integrin/ligand binding and if not, what are the essentials? How are talin and integrin activated in ligand-independent integrin signalling? Are PIP_2, the integrin/TLN/f-actin linkage and actomyosin pulling forces required? What is the exact importance of C-terminal TLN/f-actin linkage and integrin/ligand binding for migration-related processes; in particular for retrograde actin flow force coupling, the build-up of lamellipodial tension, and integrin activation?

2. Results

2.1. Cells induced by uPAR/VN-mediated adhesion are capable of establishing persistent lamellipodia despite interference with the C-terminal TLN/f-actin linkage

In a previous work (Ferraris et al., 2014), we showed that uPAR-mediated VN adhesion triggers a novel kind of ligand-independent integrin signalling. This signalling does not require direct integrin binding to VN whereas it is dependent on the increase of plasma membrane tension generated by the uPAR/VN interaction.

To study structure/function requirements of the MC, we benefited from the same cell system of Flp-In^{TM} T-Rex^{TM} HEK293, which stably expressed an inducible uPAR variant, seeded on VN substrates that allowed either uPAR/VN and integrin (VN^{RGD}) or only uPAR/VN (VN^{RAD}) binding, and employed the cells with different variants of principal MC proteins (TLN, β1 or β3 integrins) (detailed description in Section 4). An illustration of the experimental approach can be found in Fig. 1A. The experimental approach enabled us to interfere selectively with key MC interactions/functions practically from the substrate to f-actin. In particular, and uniquely compared to many other approaches, this system permits the analysis of important aspects of MC engagement and migration even in the absence of direct integrin/ECM contact.

The first parameter we assayed in our system was the lamellipodia formation of cells expressing different TLN-1 variants (expressed at comparable levels, Fig. S1). Pro-uPA stimulation induced uPAR/VN binding and the formation of persistent lamellipodia on both substrates (VN^{RGD} and VN^{RAD}) in the control cells. Overexpression of TLN^{WT} resulted in a significant increase of cell spreading compared to the one mediated by endogenous TLN alone. If instead the C-terminal ABS 3 of TLN was deleted ($TLN^{\Delta ABS}$), there was a partial, but still evident spreading. Most of the cells presented persistent lamellipodia formation (Fig. 1B, Movie S2). The effect on lamellipodia formation was specific for the $TLN^{\Delta ABS}$ variant and relied on $TLN^{\Delta ABS}$/integrin interaction because the partial spreading returned towards control levels (endogenous TLN condition) when a mutation (W359A (Tadokoro et al., 2003)) was introduced, that impedes binding to the β-integrin tail. Indeed, the $TLN^{\Delta ABS/W359A}$ variant was almost absent from the lamellipodia (Fig. S2A) and did not colocalise with essential MC proteins (Fig. S2B–D). It was biologically inactive and these cells behaved like the control cells with endogenous TLN in all following experiments.

In summary, despite the interference with the C-terminal TLN/f-actin binding the cells are still able to form persistent lamellipodia (see also Movie S2).

2.2. Molecular clutch reinforcement is possible even in the absence of direct integrin/ligand binding, but requires C-terminal TLN ABS/f-actin binding

To examine the impact of this interference with C-terminal TLN/f-actin binding on the retrograde actin flow inside the lamellipodia, the actin dynamics were visualised transfecting the cells with lifeact^{TM}-Cherry (Riedl et al., 2008; Renkawitz et al., 2009) and imaged by spinning disc confocal microscopy.

Control cells showed a clearly visible retrograde actin flow in the lamellipodia (Fig. 2, Movie S1). This flow was mostly dependent on actomyosin contractility (Fig. S3A and B). Both, on VN^{RGD} and VN^{RAD}, the actin backflow was heavily slowed down by TLN^{WT} overexpression, with the strongest reduction of the flow rate on VN^{RGD} (Fig. 2, Fig. S3C, Movie S1). The increase in MC engagement caused by the exogenous TLN^{WT} led also to increased integrin clustering (Fig. S3D). Expression of $TLN^{\Delta ABS}$ instead resulted in a significantly increased retrograde flow velocity compared to the control cells expressing only endogenous TLN, with the fastest velocity flow observed on VN^{RAD} (Fig. 2, Fig. S3C, Movie S1). This effect was reversed towards control levels in the $TLN^{\Delta ABS/W359A}$-expressing cells. In general, the retrograde flow rates were faster in all VN^{RAD} conditions compared to their correspondent VN^{RGD} counterparts (Fig. 2).

The data indicate that both reduced internal ($TLN^{\Delta ABS}$) or external MC engagement (VN^{RAD}) affect the retrograde actin flow force coupling. The impact of $TLN^{\Delta ABS}$ on the retrograde actin flow was expected and confirmed what was reported before (Giannone et al., 2003). The result that intracellular MC engagement on its own in the absence of integrin/ECM binding (in particular in the presence

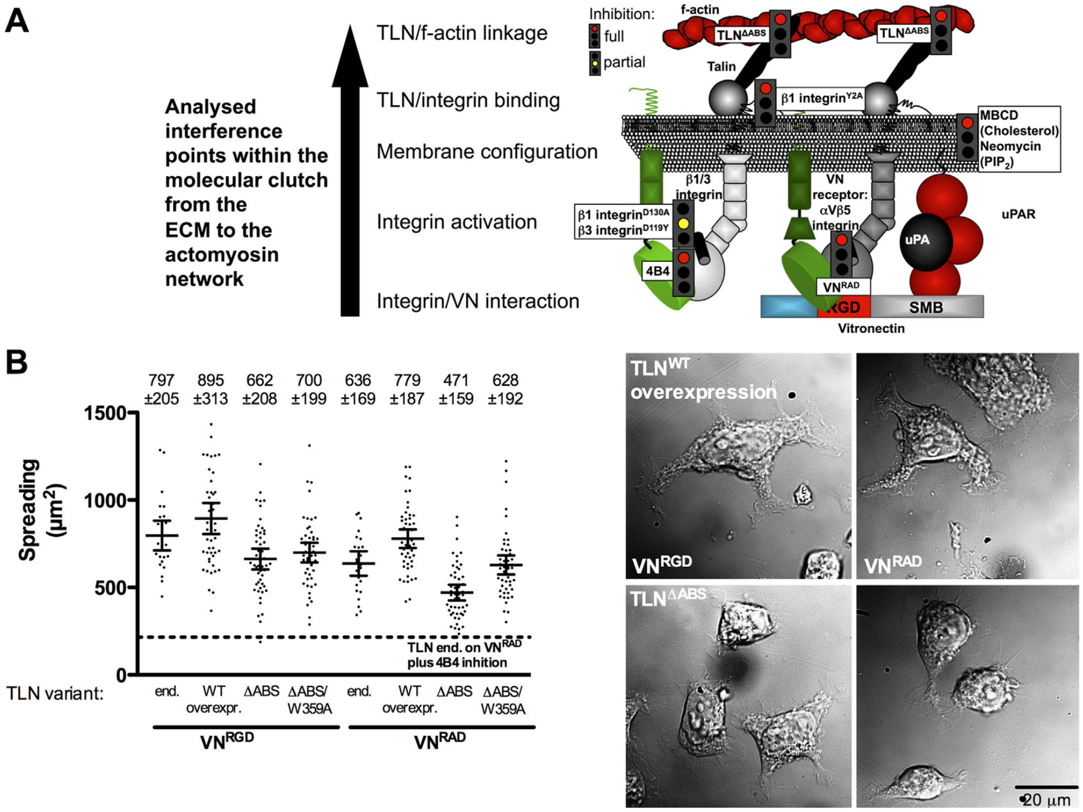
A
Analysed interference points within the molecular clutch from the ECM to the actomyosin network
TLN/f-actin linkage
TLN/integrin binding
Membrane configuration
Integrin activation
Integrin/VN interaction
Inhibition:
full
partial
f-actin
TLNΔABS
TLNΔABS
Talin
β1 integrinY2A
MBCD (Cholesterol) Neomycin (PIP2)
β1/3 integrin
VN receptor: αVβ5 integrin
β1 integrinD130A
β3 integrinD119Y
4B4
VNRAD
uPA
uPAR
RGD
SMB
Vitronectin
B
797 ±205
895 ±313
662 ±208
700 ±199
636 ±169
779 ±187
471 ±159
628 ±192
Spreading (µm2)
1500
1000
500
0
TLN end. on VNRAD plus 4B4 inhition
TLN variant:
end.
WT overexpr.
ΔABS
ΔABS/ W359A
end.
WT overexpr.
ΔABS
ΔABS/ W359A
VNRGD
VNRAD
TLNWT overexpression
VNRGD
VNRAD
TLNΔABS
20 µm

Fig. 1. (A) Experimental approach; (B) lamellipodia formation despite interference with TLN/f-actin binding: (A) The scheme illustrates the experimental set-up and highlights the interference points in the membrane, the TLN, β1/3 integrin and vitronectin (VN) variants studied in this work (for a detailed description of the cell system see Section 4). In the baseline condition, uPAR mediates adhesion to VN through the N-terminal SMB domain, whereas (αVβ5) integrins engages the RGD motif (if present). uPAR/VN interaction has been shown to induce migration and integrin signalling (Madsen et al., 2007; Pirazzoli et al., 2013; Ferraris et al., 2014) mediated by a Src/FAK/p130cas/Doc180/Rac1 signalling axis (Smith et al., 2008). The particularity of the presented experimental approach lies in the possibility that integrin signalling can be induced also independently of direct integrin/ligand binding. In a few words, this occurs via an increase of membrane tension generated by cell adhesion, which is mediated by an anchoring receptor (in this case uPAR). Further details on this non-canonical ligand-independent integrin signalling can be found in a recently published work by Ferraris et al. (2014) where it has been analysed profoundly. In the present work we exploited the unique opportunity offered by this system to study especially mechanobiological aspects of MC engagement, spreading and cell migration also uncoupled from integrin-mediated cell adhesion. (B) The HEK293 uPAR T54A cells were plated in serum-free medium on VN^{RGD} or VN^{RAD} (10 µg/ml) and then induced with pro-uPA for 30 min. After the fixation of the cells with 4% PFA, DIC images (representative examples of some conditions on the right) were taken and the cell area of in total 50 cells from 2 independent experiments was quantified via ImageJ. The mean is flanked by ±95% CI, the values are indicated with ±SD. The graphs on the right show the quantification of spreading and representative DIC images of some conditions are shown on the left. The dashed line represents the minimum baseline value of unspread, round control cells on VN^{RAD} with 4B4 mAb inhibition (for a representative image of this condition see Fig. 7A).

of an excess of TLN^{WT}) suffices for substantial retrograde flow force coupling was surprising.

2.3. PIP_2/TLN binding is a prerequisite for molecular clutch engagement and independent of C-terminal TLN/f-actin binding

In our previous work we showed that the membrane and its tensional state play an important role for the induction of integrin/ligand binding-independent spreading and signalling (Ferraris et al., 2014). In addition, membrane tension and phosphoinositides have been found to regulate actin polymerisation, cell membrane remodelling and leading edge formation (Gallop et al., 2013; Suetsugu et al., 2014; Tsujita et al., 2015). In particular, locally synthesised PIP_2 is pivotal for the recruitment of TLN to the lamellipodial cell membrane and its activation, which hence controls integrin clustering, FA formation and force coupling (Cluzel et al., 2005; Goksoy et al., 2008; Legate et al., 2011). We therefore addressed this aspect of the PIP_2/TLN interaction by analysing the impact of the PIP_2-masking agent neomycin (which inhibits the binding of PIP_2 effectors) on the retrograde actin flows in cells expressing the different TLN variants.

Neomycin treatment did not disturb the general cellular competence for lamellipodial actin polymerisation, but rather significantly accelerated the retrograde actin flow rates on both substrates and for all TLN variants, independently of whether the C-terminal ABS was present or not (Fig. 3A).

The PIP_2/TLN binding is an essential prerequisite for the subsequent integrin-dependent MC engagement, but the C-terminal ABS of TLN is dispensable for this initial TLN-mediated f-actin/membrane linkage.

2.4. Frictional resistance caused by membrane viscosity contributes to the retrograde flow deceleration

The finding that the initial TLN/membrane interaction is independent of the C-terminal TLN ABS/f-actin binding prompts the

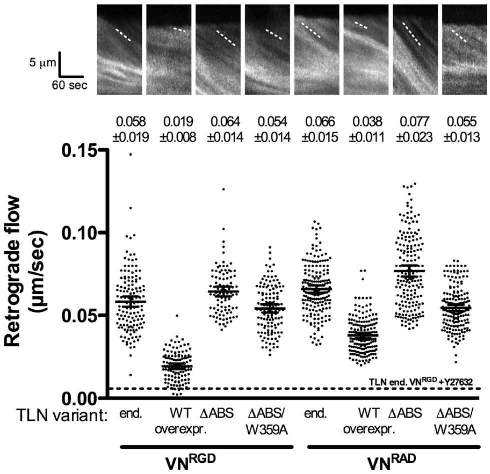

Fig. 2. TLN/f-actin linkage is predominantly responsible for actin retrograde flow force transmission and MC reinforcement: The cells were plated on VN^{RGD} or VN^{RAD} (10 μg/ml) in serum-free medium and after spreading the retrograde actin flow (visualised by $lifeact^{TM}$) was recorded with a spinning disc confocal microscope (1 image/s). From the movies kymographs were derived and quantified using ImageJ. The graph shows the results of 70–186 retrograde velocities, which were analysed. The mean is flanked by ±95% CI, the values are indicated with ±SD. The dashed line represents the baseline value for retrograde flow measured in lamellipodia treated with the inhibitor Y27632 (see Fig. S3A).

question how the membrane is involved in the observed integrin/ligand binding-independent MC reinforcement (Fig. 2). We therefore analysed the possibility that the biomechanical viscous cell membrane properties contribute to the retrograde actin flow force coupling in the integrin/ligand binding-independent condition by providing frictional resistance. In general, resistance measurements have revealed that the resistive barrier force of the membrane against lateral movements is in the range of pN/(μm/s) (Suzuki et al., 2000). In HEK293 cells, treatment with methyl-β-cyclodextrin (MBCD) has been demonstrated to be an efficient way to modulate the nanomechanical properties (in particular membrane viscosity) of cell membranes by cholesterol depletion (Khatibzadeh et al., 2012) and that these properties contribute to the mechanics of cell protrusions (Khatibzadeh et al., 2013).

Consistently, the data in Fig. 3B demonstrate that on VN^{RAD} the retrograde actin flow rates raised significantly after MBCD incubation in the cells with TLN^{WT} (endogenous and overexpressed). In the lamellipodia of cells expressing $TLN^{\Delta ABS}$ (where the actomyosin network is not effectively coupled to the integrins, Fig. 2) the retrograde flow velocity instead remained unaffected by the MBCD treatment (Fig. 3B). On VN^{RGD} where αVβ5 integrin can bind the substrate no effect is visible.

The nanomechanical properties of the membrane, namely its frictional resistance as a viscous fluid, may provide the counterforce needed for the coupling of retrograde actin flow force in the absence of integrin/ECM binding.

2.5. Manipulating membrane viscosity or C-terminal TLN/f-actin binding lowers the lamellipodial tension

To investigate the importance of the membrane viscosity and the C-terminal TLN linkage to the actomyosin network for the general nanomechanical properties of the lamellipodia, we performed live cell atomic force microscopy measurements (Figs. 4 and 5) on cells grown in serum-containing medium (serving also as a source of VN^{RGD}). Under these conditions the effect of the $TLN^{\Delta ABS}$ variant on retrograde actin flow was comparable (Fig. S3C) to what was observed for the VN^{RGD} coating (Fig. 2).

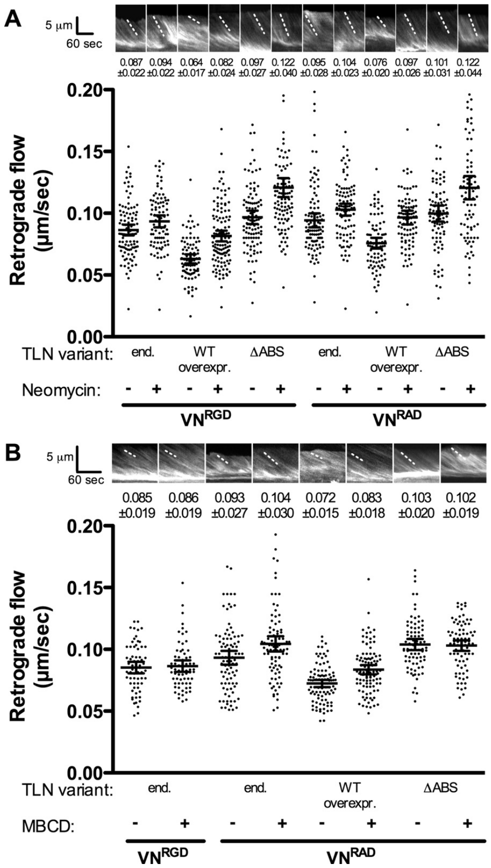

Fig. 3. PIP_2/TLN interaction is a prerequisite for MC reinforcement and frictional resistance of the membrane can contribute to the force coupling, especially in the non-canonical ligand binding-independent condition: The experimental set-up is the same as in Fig. 2 but the actin retrograde flow of the cells was recorded (A) in the absence or presence of 3 mM neomycin or (B) before and after 30 min incubation with 5 mM methyl-β-cyclodextrin. The graph summarises the data of (A) 84–120 analysed retrograde velocities (to improve the clarity of the graph, the data for the cells expressing $TLN^{\Delta ABS/W359A}$ has not been included because, as before, they behaved like the control cells) or (B) 66–100 analysed retrograde velocities. The mean is flanked by ±95% CI, the values are indicated with ±SD.

The control cells expressing only endogenous TLN had young's modulus values (low indentation range representing the membrane/cytoskeletal layer) in the lamellipodial zones corresponding to an average rigidity of ~4 kPa (Fig. 4A and F) and also the lamellipodial tension in the TLN^{WT}-overexpressing cells (Fig. 4D) was in the same range. $TLN^{\Delta ABS}$-expressing cells instead showed a significant reduction of lamellipodial rigidity to ~2.76 kPa (Fig. 4B and F), whereas the value returned to control range in the $TLN^{\Delta ABS/W359A}$-expressing cells (Fig. 4E). The cell body had a much lower rigidity compared to the lamellipodia with no significant differences between the conditions (Fig. 4G). As negative control we treated the control cells with 10 μM cytochalasin D for ≥15 min, which caused a drastic decrease of rigidity in the lamellipodia towards the value of the cell body (Fig. 4C and F). The treatment of control cells with MBCD also caused a considerable lowering of the lamellipodial rigidity to ~3 kPa (Fig. 5A and B).

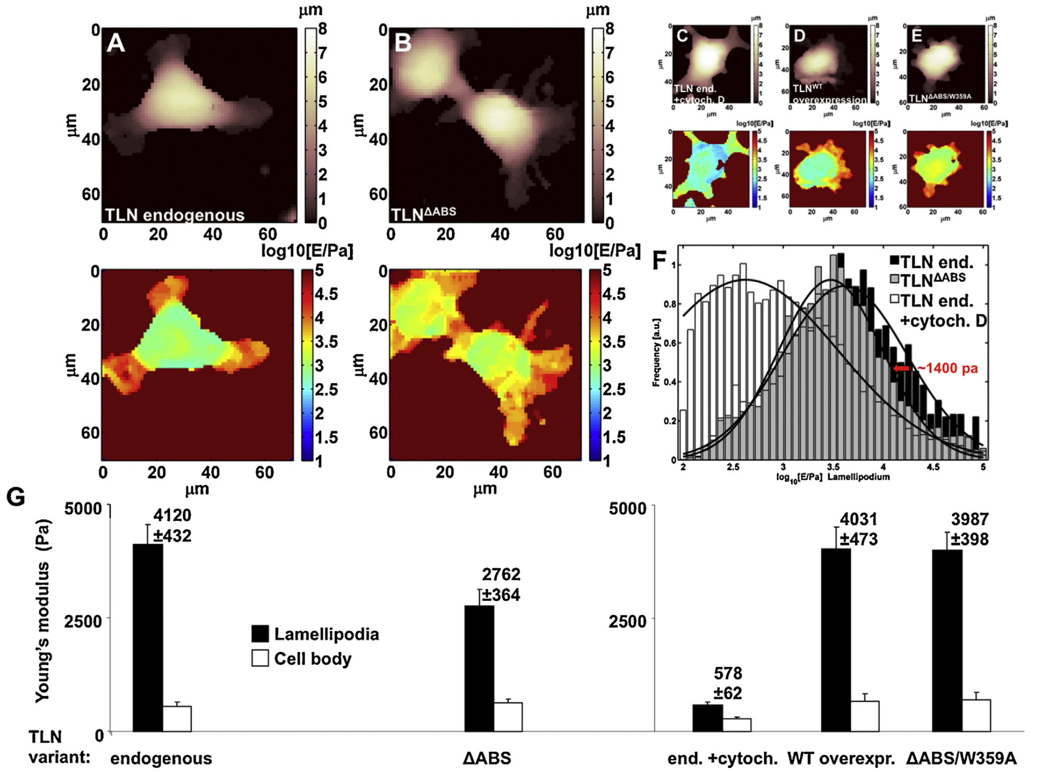

Fig. 4. Impaired TLN/f-actin interaction changes nanomechanical properties of the lamellipodia: The cells were plated in serum-containing medium (serves also as source for VN^{RGD} in this case) on glass-bottomed plates one day before the experiment. For the live cell atomic force measurements, the spreading was induced by addition of pro-uPA >30 min before transferring the plates to the atomic force microscope. (A, B) On the top morphological images (height) of representative cells with (A) endogenous TLN and (B) TLN$^{\Delta ABS}$ are shown. On the bottom the corresponding elasticity/rigidity (Young modulus) maps of these cells are displayed with a colour code representing the values of the low indentation range young modules calculated from each individual force curve measurement (4096 force curves per image). (C–E) Morphology and elasticity maps for further conditions representing cells with (C) endogenous TLN plus cytochalasin D treatment (≥10 min), with (D) overexpressed TLN^{WT} and with (E) TLN$^{\Delta ABS/W359A}$ are displayed. (F) The graph shows the distribution of frequency of low indentation range young's modulus values (lines are corresponding gaussian fits) from the lamellipodial zone of cells with endogenous TLN with (white bars) or without (black bars) cytochalasin D treatment and with TLN$^{\Delta ABS}$ (grey bars). Consider that the logarithmic scale values are presented in this graph; indeed, the highlighted shift (red arrow) between the curves of endogenous TLN and TLN$^{\Delta ABS}$ corresponds to a highly significant difference of almost 1400 Pa in linear scale (see also Graph G). (G) The bars represent the mean value of the cell rigidity measurements of the lamellipodial zone (black bars) and the cell body zone (white bars) with the error propagated from the Gaussian distribution. The values above the bar display the mean value in the lamellipodial zones in linear scale (7–14 cells were measured).

Disturbing the membrane viscosity by cholesterol depletion or an insufficient MC engagement (in the TLN$^{\Delta ABS}$ cells) leads to a change in the nanomechanical properties within the lamellipodial cytoskeletal/membrane layer, resulting in a lowering of the lamellipodial tension.

2.6. β1 integrin activation is diminished in TLN$^{\Delta ABS}$-expressing cells

Our experiments demonstrate that C-terminal TLN binding to f-actin is crucial for accurate MC engagement and the consequent build-up of lamellipodial tension. Another essential event for MC function is TLN-dependent integrin activation (Wegener et al., 2007; Shattil et al., 2010). Thus, we probed the β1 integrin activation level in dependency of the TLN variants. This was achieved by measuring the ratio between activated β1 integrin (9EG7 mAb)/total β1 integrin (K20 mAb) signal using an Olympus Scan^R Screening Station. The 9EG7 mAb binds to the I-EGF like repeats of highly activated, extended β1 integrin (Bazzoni et al., 1995; Askari et al., 2010).

The activation state of the β1 integrin in TLN$^{\Delta ABS/W359A}$ cells seeded on VN^{RGD} was used for reference, as these cells behave like control cells. On VN^{RGD} and VN^{RAD}, the β1 integrin activation levels of TLN$^{\Delta ABS}$ cells were significantly diminished, while cells overexpressing TLN^{WT} instead displayed an augmented activation on both substrates (Fig. 6A).

We conclude that the TLN/f-actin linkage-dependent MC engagement status impacts on integrin activation. The capacity of TLN$^{\Delta ABS}$ to fully activate β1 integrin is reduced.

2.7. Impairing TLN/f-actin coupling strongly compromises the migration capacity despite lamellipodia formation

The effects of the TLN C-terminal ABS deletion on cell spreading, actin retrograde flow, lamellipodial tension and integrin activation beg the question how these changes eventually affect cell migration.

Control cells showed strong migration capacity on VN^{RGD} and VN^{RAD} (Fig. 6B, Movie S2). TLN^{WT}-overexpressing cells on the contrary displayed – on both substrates – a reduced migration compared to cells with endogenous TLN alone possibly due to

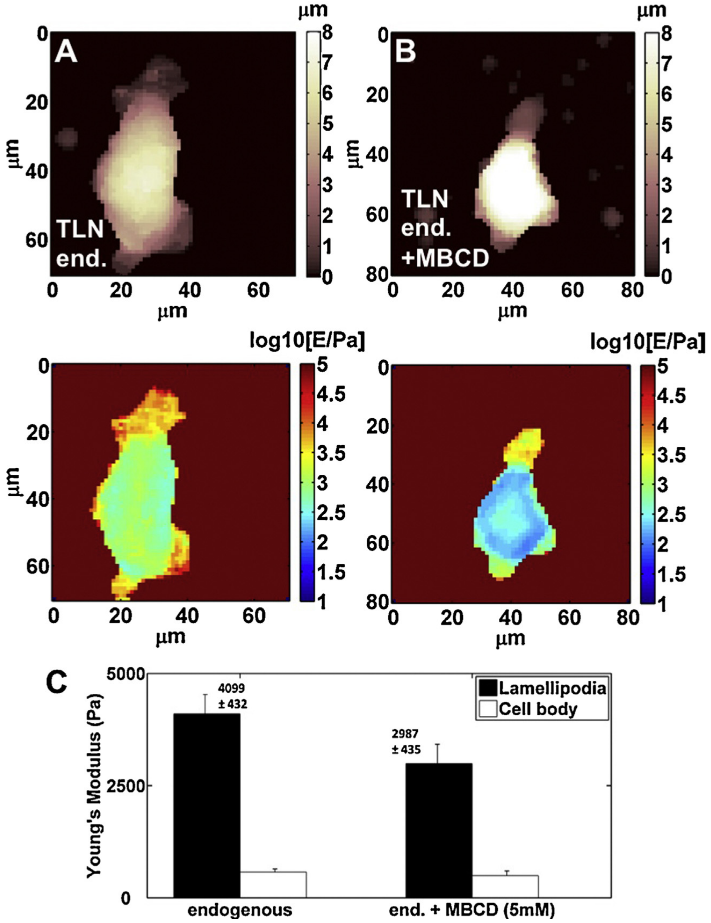

Fig. 5. Changing membrane viscosity by cholesterol depletion lowers the lamellipodial tension: The experimental set-up is the same as in Fig. 4 but here the control cells with endogenous TLN were measured in the (A) absence or (B) presence of 5 mM methyl-β-cyclodextrin (≥30 min incubation). (C) The graph summarises the data obtain in the measurements. The bars display the mean value of the cell rigidity measurements in the lamellipodial zone (black bars) and the cell body zone (white bars). The error was propagated from the Gaussian distribution. The values above the bar show the mean value of the lamellipodial zones in linear scale (7–8 cells were measured).

the enhanced integrin clustering/signalling and retrograde flow force coupling observed in these cells (Fig. 6A and Fig. S2D). Also the migration of the TLN$^{\Delta ABS}$ cells was diminished on VN^{RGD} and strongly impaired on VN^{RAD} (Fig. 6B, Movie S2), while for the TLN$^{\Delta ABS/W359A}$ cells the migration instead was in the range of the control cells.

The observation that cells expressing TLN$^{\Delta ABS}$, despite their capability of establishing a migratory-like phenotype, have a strong defect in migration (especially on VN^{RAD}) indicates that the functionality of this TLN variant is sufficient for persistent lamellipodia formation, but much less so for the realisation of cell migration.

2.8. Compromising full activation of integrins causes comparable effects as perturbing TLN/f-actin linkage

The critical role of integrin activation in migration-related processes is widely studied (Huttenlocher et al., 1996; Gupton and Waterman-Storer, 2006; Vicente-Manzanares et al., 2009; Shattil et al., 2010). Based on the demonstration of an impaired β1 integrin activation in TLN$^{\Delta ABS}$ cells (Fig. 6A), we further investigated the relevance of the integrin activation status to the process.

First, we employed a β1 integrin variant carrying a D130A substitution in the MIDAS motif of the I-domain. This substitution inhibits ligand binding and full integrin head piece extension keeping the integrin in an intermediate activation status (Takada et al., 1992; Chen et al., 2006, p. 2; Ferraris et al., 2014). An additional K218A substitution was employed to make the β1 integrin variants refractory to inhibition by the 4B4 mAb (Luo et al., 2004; Ferraris et al., 2014).

Cells expressing the β1 integrin$^{K218A/D130A}$ displayed comparable characteristics to those observed for TLN$^{\Delta ABS}$ cells. The majority of cells established smaller, but persistent lamellipodia on both substrates (Fig. 7A, Movie S3). The migration instead was strongly diminished on VN^{RGD} and almost completely abolished on VN^{RAD} (Fig. 7B, Movie S3). The residual activity on VN^{RGD} was dependent on αVβ5 integrin engagement because β1 integrin$^{K218A/Y2A}$ cells (with mutated β1 integrin binding sites for TLN and kindlin) showed the same effects on migration (Fig. 7B, Movie S3).

The same phenomenon could be provoked in the control cells by a gradual, titrated inhibition of the endogenous β1 integrin activation by the 4B4 mAb (in particular 4B4 mAb concentration of 0.1 µg/ml in Fig. S4).

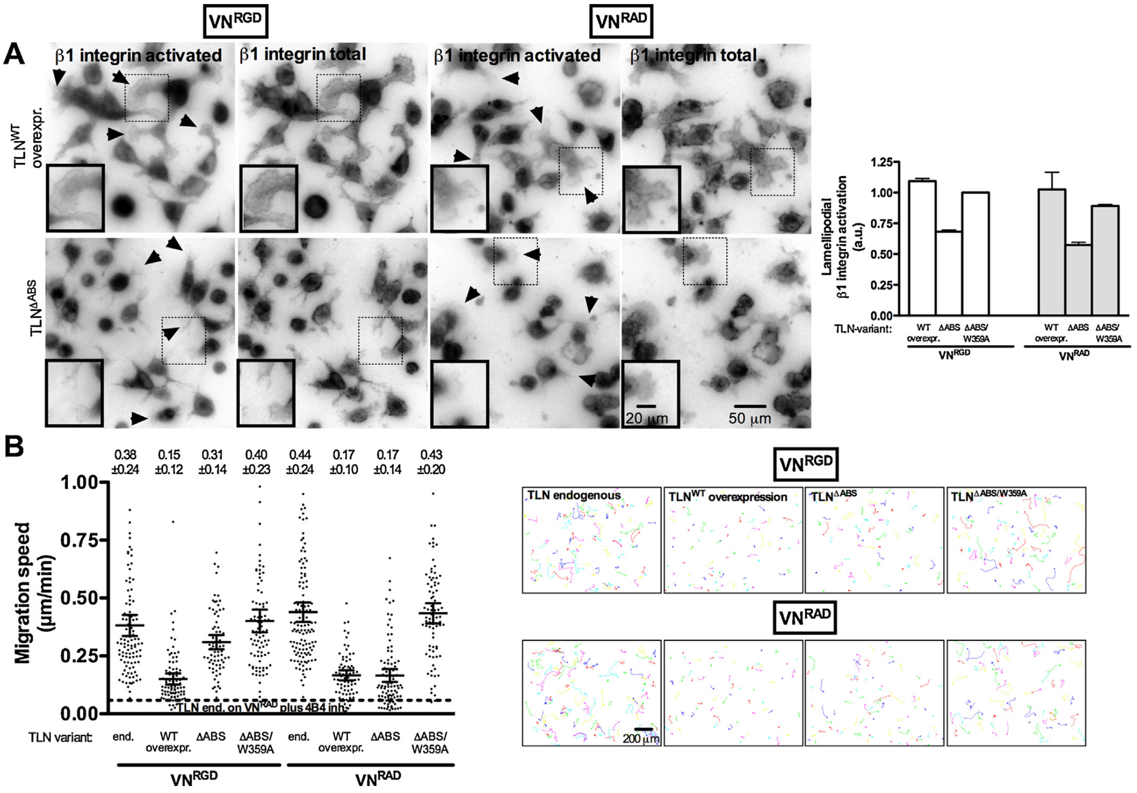

Fig. 6. (A) Impaired β1 integrin activation in lamellipodial zones upon interference with TLN/f-actin binding and (B) diminished cell migration capacity despite lamellipodia formation: The cells were plated on VN^{RGD} or VN^{RAD} (10 µg/ml) and induced with 10 nM pro-uPA. After attachment and spreading the cells were incubated for 15 min on ice with the 9EG7 mAb (activated β1 integrin) and then fixed with 4% PFA and stained for total β1 integrin (K20 mAb). An additional DAPI staining was used to facilitate autofocussing of the Olympus ScanR̂ Screening Station which then automatically took images. From these images quantifications were performed calculating the ratio of the lamellipodial 9EG7 signal relative to the total K20 mAb signal. For better illustration the whole images of the figure were inverted and enhanced in contrast using ImageJ – Enhance Contrast plugin. Arrows highlight representative areas and magnifications display lamellipodial zones in detail. The bars (white: VN^{RGD}, and grey: VN^{RAD}) in the graph represent the average of 2 independent experiments (+SD) (in total 85–181 cells were analysed). The value of the $TLN^{\Delta ABS/W359A}$ on VN^{RGD} condition was set as 1 (arbitrary units). (B) The cells were plated on VN^{RGD} or VN^{RAD} (10 µg/ml) in serum-free medium and the time lapse microscope recording was started after attachment of the cells (>30 min). The migration speed was quantified using the ImageJ plug-in "Particle Analysis" (results are shown for one experiment but in total 73–147 cells were analysed from 2 independent experiments with comparable outcome). The mean is flanked by ±95% CI, the values are indicated with ±SD. On the right typical examples of migration tracks are shown. The dashed line represents the minimum baseline value observed for unspread, round control cells with 4B4 inhibition on VN^{RAD} (see Fig. 7A,B).

Disturbing the equilibrium between active and inactivate β1 integrin apparently at a certain point causes this particular effect allowing lamellipodia formation, but not cell migration.

The observed effects were not specific for the β1 integrin. Expression of β3 $integrin^{D119Y}$ (equivalent to the D130A variant in β1 integrin) led to comparable consequences for the cells and in particular migration deficiency despite lamellipodia formation (Fig. S5A and D, Movie S5). Furthermore, the retrograde actin flow was accelerated and the FC/As smaller compared to β3 $integrin^{WT}$-expressing cells (Fig. S5B and C). The partial spreading, FA size, and the retrograde flow velocity of the β3 $integrin^{D119Y}$-expressing cells were restored to β3 $integrin^{WT}$ cell levels when a D723A mutation was introduced into the D119Y variant (Fig. S5A–C, Movie S4). This mutation constitutively activates intracellularly the β3 integrin by separating the integrin tails (Hughes et al., 1996). Yet, even these cells were still incapable of migrating (Fig. S5D, Movie S5).

These results resemble those seen with β1 integrin and further underscore that full extracellular activatibility of the integrin is essential for cell migration. Even a constitutive intracellular activation of the integrin (at least the one mediated by the D723A mutation) cannot rescue migration if the extracellular integrin domain cannot achieve its fully activated conformation. Hence, the interference with the integrin activatibility has very similar consequences for migration-related events as the deletion of the C-terminal ABS of TLN.

3. Discussion

In this study we selectively interfered with MC engagement processes from the ECM to f-actin and analysed the consequences on diverse migration-related parameters. Uniquely compared to other studies in this context, our specific approach allowed us to integrate also a condition where integrins are activated but not bound to the ECM (details in Fig. 1A and Ferraris et al. 2014).

The C-terminal interaction of TLN with the actomyosin network was determined to be a key event for MC engagement, build-up of lamellipodial tension, retrograde actin flow force coupling, full integrin activation and cell migration. For the retrograde actin flow, our data showed that the slow down is a consequence of the TLN-mediated MC engagement, which again is partly dependent on extracellular engagement (integrin/ECM) and also partly

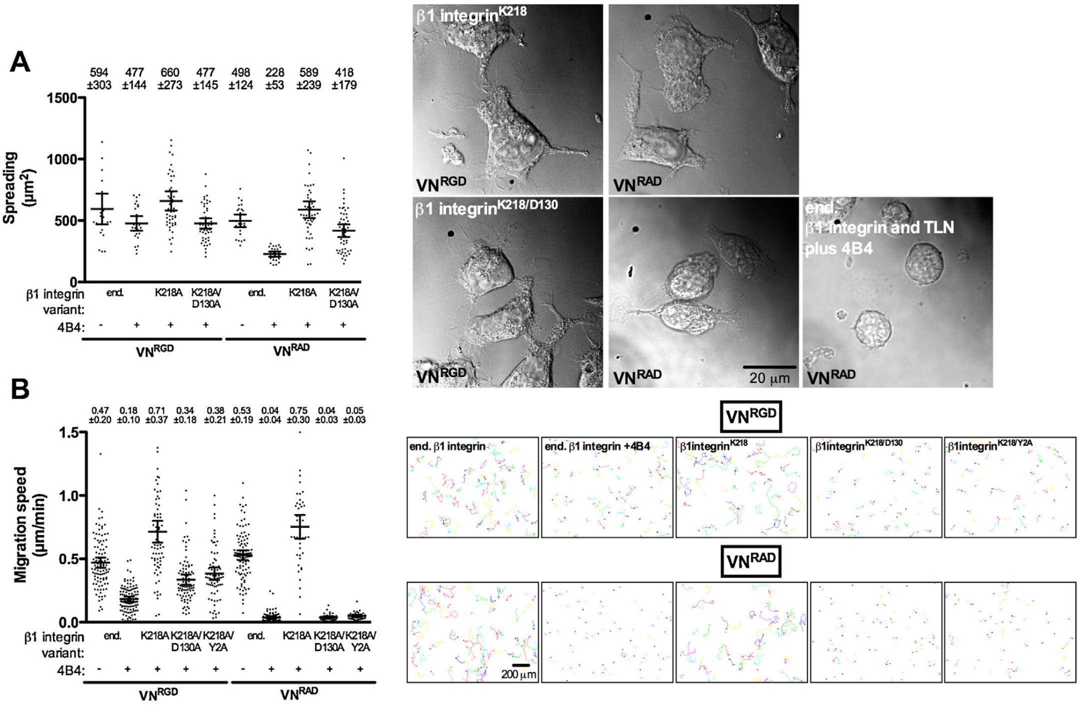

Fig. 7. Impairing the full activatibility of β1 integrin has similar effects on (A) lamellipodia formation and (B) migration as the C-terminal actin binding site deletion in TLN: The experiments were done as described in Figs. 1B and 6B but the cells expressing β1 integrin variants were pre-incubated with the 4B4 mAb to block endogenous β1 integrin activity if indicated so (the overexpressed β1 integrin variants were insensitive to 4B4 mAb inhibition due to the K218 mutation). (A) The quantification of two independent experiments is shown. (B) The graph shows the results of migration track analysis of one experiment. In total two independent experiments with reproducible outcome were performed and 58–130 cells were analysed. The mean is flanked by ±95% CI and the values are indicated with ±SD. On the right typical examples of migration tracks are shown.

on intracellular engagement (integrin/TLN/actin). The observation that even intracellular MC engagement alone, without actual integrin/ligand binding (VN^{RAD} condition) causes a notable deceleration of the retrograde actin flow is intriguing.

In our previous experiments we learned that membrane tension is essential for signalling and spreading in the absence of direct integrin/ECM ligation (Ferraris et al., 2014). Interestingly in this context are the recent findings that membrane tension/curvature can activate and regulate polarised actin polymerisation and consequentially leading edge formation via membrane-bending proteins (e.g. FBP17) (Suetsugu et al., 2014; Tsujita et al., 2015; Simunovic and Voth, 2015).

Also phosphoinositides play a complex role in the initial phase of cell membrane remodelling and f-actin/membrane linkage (Gallop et al., 2013; Suetsugu et al., 2014). Local lamellipodial PIP_2 synthesis has been found to be important for TLN recruitment to the MC and subsequent force coupling (Legate et al., 2011) and both PIP_2 and TLN are necessary to implement integrin clustering and activation (Cluzel et al., 2005; Goksoy et al., 2008; Orłowski et al., 2015, p. 2) In our system, blocking effector binding to PIP_2 by neomycin did not compromise the general cellular capacity for actin polymerisation, but raised the retrograde actin flow rates independently of the presence of the C-terminal ABS in TLN. Two other, more N-terminal ABS domains have been reported in TLN but their impact on retrograde actin flow force coupling to the integrins has been found to be negligible (Hemmings et al., 1996; Jiang et al., 2003; Giannone et al., 2003). Also in our system these ABS cannot compensate for the deletion of the ABS3 regarding this aspect. Considering the data from the neomycin treatment it can be speculated, though, that they might be involved in the PIP_2-dependent f-actin/membrane linkage in the initial phase of lamellipodia formation, but further experiments are necessary to address this point. It is particularly intriguing in this context, that the TLN head FERM domain, which contains the ABS1, can bind to f-actin and phosphatidylinositol 4-phosphate 5-kinase (Lee et al., 2004).

Furthermore, it has been shown that the membrane viscosity participates to the mechanics of cell protrusions (Khatibzadeh et al., 2012, 2013). The frictional resistance to lateral movement caused by the cell membrane viscosity has been measured to be in the range of pN/(µm/s) (Suzuki et al., 2000). In the cells expressing TLN^{WT} the retrograde actin flow rates accelerated and the lamellipodial tension decreased after cholesterol depletion obtained with MBCD treatment, while in $TLN^{\Delta ABS}$-expressing cells (with impaired integrin/actomyosin linkage) MBCD did not affect retrograde actin flow rates. It has to be considered that uPAR dimers are anchored in the membrane by GPI and are recruited to lipid rafts where they mediate VN binding, which makes them susceptible to changes of the cholesterol concentration (Cunningham et al., 2003; Caiolfa et al., 2007). This could contribute to the observed effects.

However, the results highlight that the frictional resistance of the viscoelastic membrane fluid can contribute to realise efficient coupling of actin retrograde flow force, in particular in the absence of integrin/ECM ligation. This could represent a part of the yet undefined membrane-parallel tension counterforce component inside the integrin/TLN/actin module suggested in a FA force transmission model. This model was derived upon theoretical considerations, based on geometric FA nanoarchitecture data published recently (Liu et al., 2015).

Indeed, our study pinpoints tension as the striking factor for the realisation of integrin-dependent migration. Despite its undisputed significance the exact role of tension in migration-related processes is still quite controversial (Gauthier et al., 2012; Diz-Muñoz et al., 2013), but the general recent view is that reduction of tension leads to impaired lamellipodial organisation/polarisation, leading edge signal confinement and migration (Batchelder et al., 2011; Houk et al., 2012).

Our data accentuate specific mechanobiological aspects, extending the picture also by the non-canonical integrin/ligand binding-independent scenario. An accurate membrane configuration and C-terminal TLN/f-actin linkage are essential for the build-up of tension in the lamellipodial cytoskeletal/membrane layer, which proves to be predominantly important for full integrin activation and migration, whereas direct integrin/ECM interaction is not an indispensible prerequisite.

For thorough cell migration both, the linkage of TLN to the β-integrin tail and f-actin, turned out to be crucial. If the TLN binding site of the β-integrin tail is mutated, no lamellipodia formation (and apparently also no correlated biological events) can be observed in our system (Ferraris et al., 2014). An excess of intracellular engagement (TLN^{WT} overexpression), though, connects the actomyosin network immoderately to the integrins in the membrane and leads to a surplus of integrin clustering and activation (Fig. S3D) that eventually reduces migration.

On the other hand, cells expressing the TLN variant without the C-terminal ABS display quite particular characteristics and various mutation-specific effects. $TLN^{\Delta ABS}$ shows specific colocalisation with β1 integrin (Fig. S2D) and is more prominent in the lamellipodia than $TLN^{\Delta ABS/W359A}$ (which interacts neither with f-actin nor with β-integrin, Fig. S2), though it shows a somewhat diminished accumulation at the lamellipodial edge compared to TLN^{WT} (Fig. S2A). However, $TLN^{\Delta ABS}$ cells are sensitive to neomycin inhibition, meaning that this TLN variant is recruited to the membrane via PIP_2.

Consequently, $TLN^{\Delta ABS}$ cells establish persistent lamellipodia but they are characterised by a faster retrograde actin flow and lower tension, resulting in an impaired capacity to fully activate integrins and to migrate. Similar to this, Zhang et al. (2008) found that initial but unstable spreading in TLN−/− cells on FN could be restored to a partial, but stable spreading with persistent lamellipodia by the expression of the TLN head alone, whereas the retrograde flow was still accelerated.

The binding of the TLN head F2F3 domain to the integrin NPxY motif is fundamental for integrin activation and cell spreading (Calderwood et al., 1999; Vinogradova et al., 2002; Wegener et al., 2007; Anthis et al., 2010; Ye et al., 2010; Pinon et al., 2014) but also the IBS-2 domain contributes to a constitutive, low affinity level integrin binding (Himmel et al., 2009). In $TLN^{\Delta ABS}$ these two domains are functional, which enables the initial interaction with the membrane and the β-integrin tails. What $TLN^{\Delta ABS}$ apparently is not capable to perform, is the final switch to high affinity interactions with integrins and f-actin. To create an initial 2 pN slip bond, this switch needs conformational changes of the helix bundles of the domains IBS-2A/B and exactly the ABS-3/DS (Giannone et al., 2003; Jiang et al., 2003; Himmel et al., 2009), which is missing. A stretch of the TLN rod is necessary to complete vinculin recruitment and MC reinforcement. This step requires strong interaction with the actomyosin-network (Ciobanasu et al., 2014), with a threshold of required force formation of around 5 pN to unlock TLN in an unfolded conformation (Yao et al., 2014) and 12 pN to expose further cryptic vinculin binding sites (del Rio et al., 2009). Super-resolution microscopy has determined a polarised TLN orientation in adhesion complexes, with the N-terminus of TLN in the integrin signalling layer and the C-terminus directed towards the actin regulatory layer (Kanchanawong et al., 2010), which is crucial for the control of the FA nanoarchitecture and function (Liu et al., 2015). Vinculin plays an important role in the advancement of these processes by creating a positive feedback that keeps TLN vertically extended, reinforces the MC, and regulates the FA composition (Giannone et al., 2003; Humphries et al., 2007; Carisey et al., 2013; Thievessen et al., 2013; Ciobanasu et al., 2014; Case et al., 2015). Simulations of the molecular dynamics propose that the TLN orientation is determined by mechanical force, representing thus a further potential mode of mechanosensing (Golji and Mofrad, 2014). Also the dimerisation of TLN has a significant importance for actin binding. However, TLN C-termini with mutations that impede dimerisation but are otherwise intact, still maintain a notable actin binding capacity (Gingras et al., 2008).

Our observed lower correlation coefficients with vinculin and f-actin and the reduced lamellipodial tension, as well as the faster retrograde actin flow in $TLN^{\Delta ABS}$ cells compared to TLN^{WT} are all in congruency with these characteristics. Altogether, $TLN^{\Delta ABS}$ functionality suffices – at least partly – for the induction of MC-correlated events until persistent lamellipodia formation. We here demonstrate, though, that the C-terminal TLN/f-actin binding-implemented force transmission and lamellipodial tension (but not necessarily integrin/ligand binding) represent an indispensable limiting factor for proper integrin activation and migration.

Indeed, full integrin activation is of decisive relevance for the realisation of cell migration. Interestingly, the phenotypes of $TLN^{\Delta ABS}$ and β1 $integrin^{D130A}$, respectively β3 $integrin^{D119Y}$ cells are very similar in our system. This mutation was shown to cause a somehow intermediate active conformation, allowing FA recruitment but not integrin/ligand binding (Takada et al., 1992; Chen et al., 2006, p. 2). Congruently, in our system the induction of canonical integrin/ligand binding-dependent signalling is completely abolished by this mutation. However, after uPAR/VN binding these integrins can still trigger the Src/FAK/p130cas/Doc180/Rac1 signalling axis and spreading in the integrin/ligand binding-independent scenario (Ferraris et al., 2014).

Vice versa, in this study $TLN^{\Delta ABS}$ cells show a significantly reduced β1 integrin activation. The lamellipodial tension and force transmission attainable by $TLN^{\Delta ABS}$ apparently are insufficient for the implementation of this integrin conformation. Similar effects were seen in equivalent experiments with β3 integrin variants (Fig. S5). Additionally these experiments accentuate that not even an intracellular constitutive salt bridge separation (by D723A mutation) can rescue cell migration if the active integrin conformation cannot be implemented completely (because of the block by the D119Y substitution in the MIDAS motif).

It can be speculated about the possibility that activated, but unligated integrins could participate to the migratory or, in case of cancer cells, metastatic capacity of cells, which might have biomedical relevance for therapeutic approaches based on e.g. inhibitory integrin antibodies or molecules (Desgrosellier and Cheresh, 2010; Seguin et al., 2015). Indeed, a contribution of ligand-independent integrin signalling to biological processes *in vivo* has already been demonstrated, i.e. for tumour progression (Desgrosellier et al., 2009; Seguin et al., 2015). This anchorage-independent growth of tumour cells depends on an association of TLN, phosphatidylinositol 4-phosphate 5-kinase and src (Thapa et al., 2013), which is in line with our presented data regarding the role of PIP_2, TLN and integrin signalling. The aforementioned molecular processes are also in accordance with the presence of conformationally activated, but unligated integrins in lamellipodia and growth cones demonstrated by Galbraith et al. (2007) and might provide a first insight on how their activation is actually established (Fig. 8B). Furthermore, it proposes a more fluent transition between amoeboid and mesenchymal migration by the addition of a potential integrin/ligand binding-independent but integrin signalling-dependent migration condition.

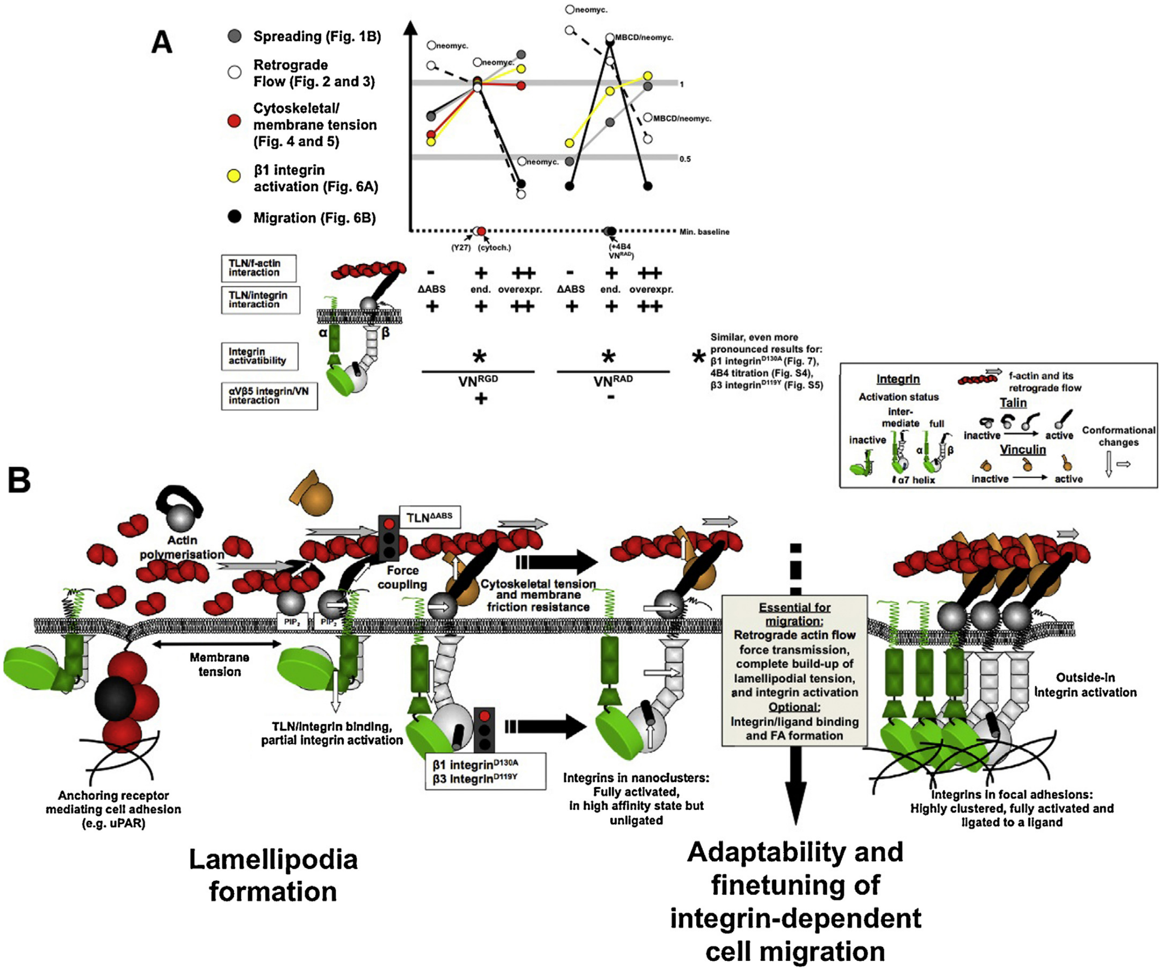
A
Spreading (Fig. 1B)
Retrograde Flow (Fig. 2 and 3)
Cytoskeletal/ membrane tension (Fig. 4 and 5)
β1 integrin activation (Fig. 6A)
Migration (Fig. 6B)
neomyc.
neomyc.
neomyc.
neomyc.
MBCD/neomyc.
MBCD/neomyc.
1
0.5
Min. baseline
(Y27)
(cytoch.)
(+4B4 VNRAD)
TLN/f-actin interaction
TLN/integrin interaction
Integrin activatibility
αVβ5 integrin/VN interaction
α
β
- + ++ - + ++
ΔABS end. overexpr. ΔABS end. overexpr.
+ + ++ + + ++
* *
VNRGD
+
VNRAD
-
* Similar, even more pronounced results for: β1 integrinD130A (Fig. 7), 4B4 titration (Fig. S4), β3 integrinD119Y (Fig. S5)
Integrin
Activation status
inactive
inter-mediate
full
α
β
α7 helix
f-actin and its retrograde flow
Talin
inactive
active
Vinculin
inactive
active
Conformational changes
B
Actin polymerisation
PIP2
PIP2
TLNΔABS
Force coupling
Cytoskeletal tension and membrane friction resistance
Membrane tension
Anchoring receptor mediating cell adhesion (e.g. uPAR)
TLN/integrin binding, partial integrin activation
β1 integrinD130A
β3 integrinD119Y
Integrins in nanoclusters: Fully activated, in high affinity state but unligated
Essential for migration: Retrograde actin flow force transmission, complete build-up of lamellipodial tension, and integrin activation
Optional: Integrin/ligand binding and FA formation
Outside-in integrin activation
Integrins in focal adhesions: Highly clustered, fully activated and ligated to a ligand
Lamellipodia formation
Adaptability and finetuning of integrin-dependent cell migration

Fig. 8. Summary (A) and model (B) for the role of C-terminal TLN/f-actin binding and full β-integrin activation in molecular clutch engagement and its importance for mesenchymal migration: (A) This figure summarises the data presented in this study and sets them graphically in relation to each other. The black circles represent the migration, the grey circles the lamellipodia formation/spreading, the white ones the retrograde actin flow, the yellow ones β1 integrin activation and the red ones the cytoskeletal/membrane tension. For simplicity reasons TLN is displayed as monomer not as dimer. The dashed line represents the baseline of the minimal values found in the control condition with endogenous TLN with the indicated treatments on VN^{RGD} : cytoch. = cytochalasin-D (see. Fig. 4C,F,G), Y27 = Y27632 (Fig. S2A); or on VN^{RAD}: +4B4 = control cells on plus 4B4 mAb inhibition (spreading: 228 ± 53 μm^2, migration: 0.04 ± 0.04 μm/min, see Fig. 7A and B). Remarkably, the results demonstrate that the system needs a balanced fine-tuning but allows also a high adaptability of the cell and a rather smooth transition between the two formerly exclusive migration modes – amoeboid (no or weak substrate interaction) and mesenchymal (high integrin-ECM attachment) (Friedl and Wolf, 2010). This has also been proposed by Renkawitz et al. (2009). Unexpectedly, our data suggest the existence of a new hybrid migration mode somewhere in between these two conditions; that is integrin/ligand binding-independent but integrin signalling-dependent (if cell adhesion is realised elsewhere, e.g. by uPAR/VN interaction). (B) The figure integrates the data presented in this paper into a potential mechanism (considering also data from other publications discussed throughout the manuscript). Summing up, $TLN^{\Delta ABS}$ and the not fully activatable integrin variants are sufficient for persistent lamellipodia formation. To achieve accurate integrin activation and cell migration, an adequate build-up of lamellipodial tension and retrograde flow force transmission has to be realised whose implementation is predominantly regulated by C-terminal TLN/f-actin linkage. Integrin/ligand binding can contribute to these processes but is not necessarily required.

4. Materials and methods

4.1. Cell system and culture

As basis cell line for all experiments Flp-In^{TM} T-Rex^{TM} HEK293 cells (Life Technologies, Carlsbad, USA) constitutively expressing $uPAR^{T54A}$ were used (further details in Ferraris et al., 2014 and Fig. 1A). The indicated TLN and integrin variants were integrated into the Flp-In^{TM} target site. The uPAR variant permits conditional induction of uPAR/VN binding for cell adhesion. The cells were plated either on (αVβ5) integrin binding-susceptible wildtype VN (VN^{RGD}), or a VN variant (VN^{RAD}), which only allows uPAR but no integrin binding.

For regular cell culture, the cells were cultured in DMEM (Lonza, Basel, Switzerland) supplemented with 10% FBS (GE Healthcare Life Sciences, Chalfont St. Giles, UK), penicillin (100 U/ml), streptomycin (100 U/ml), glutamine (5 mM) (all Euroclone, Pero, Italy), blasticidin (15 μg/ml) and zeocin (100 μg/ml) (Life Technologies) at 37 °C in 5% CO_2 with addition of 0.8 mg/ml G418 (EuroClone). Flp-In transfections were performed with a 1:10 ratio of pcDNA5/FRT/TO-based expression vector and pOG44 (Life Technologies) using Fugene 6 (Roche, Basel, Switzerland) and the selection was done in medium containing 150 μg/ml hygromycin (Roche) instead of the zeocin. Expression of recombinant cDNAs in the HEK293 cells introduced by the Flp-In transfection was induced by addition of tetracycline (1 μg/ml) (Sigma–Aldrich, St. Louis, USA) for 24–48 h. Further cell culture reagents PBS and trypsin were from EuroClone, plasticware for cell culture from Becton Dickinson (Franklin Lakes, USA). All TLN and integrin variants were expressed efficiently and with comparable expression levels analysed by FACS (FACSCalibur, BD Biosciences) (see Fig. S1, respectively Fig. SI5B and SI6A in Ferraris et al., 2014).

4.2. Expression vector construction, clonings and mutations

4.2.1. Talin-1:

To clone the TLN$^{\text{WT}}$ human talin-1 cDNA (OpenBiosystems, Cat# MHS1010-9204676) was amplified with Tln1upA and Tln1dwN oligos (product digested with Kpn1/Not1) and assembled into Kpn1/Not1 digested pcDNA5/FRT/TO (Life Technologies). The product was called pFRT/TO-TLN1$^{\text{WT}}$. To achieve the C-terminal ABS deletion (TLN$^{\Delta\text{ABS}}$ → 2229 aa) amplifications of the pFRT/TO-TLN1$^{\text{WT}}$ with Tln1upA and TlnABSr oligos were performed and the products were reintroduced into the parental vector. For TLN$^{\Delta\text{ABS/W359A}}$ the single amino acid substitution Tln$^{\text{W359A}}$ was realised with the TlnW359A oligo and the Tln1upA and TlnABSr oligos.

Tln1upA	5′-ggaccggtggaatggttgcactttcactgaagatca-3′
Tln1dwN	5′-tgcgcggccgcttagtgctcatctcgaagctctgaa-3′
TlnABSr	5′-tgcgcggccgcttaggccacttctgggtggtaagc-3′
TlnW359A	5′-tttgggagacgcagccgcgcgtttgatgttggt-3′

4.2.2. Lifeact™ mCherry

The lifeact™ leader peptide (Riedl et al., 2008) was generated by annealing oligos LAU/LAL and cloned Kpn1/Age1 in front of an expression vector containing the mCherry cDNA.

LAU	5′-catgggcgtggccgacctgatcaagaagttcgagagcatcagcaaggaggagggcgaccca-3′
LAL	5′-ccggtgggtcgccctcctccttgctgatgctctcgaacttcttgatcaggtcggccacgcccatggtac-3′

4.2.3. β1 integrin, β3 integrin, Vitronectin

The cloning strategy was done as described in detail in Ferraris et al. (2014). The double mutation β3 integrin$^{\text{D119Y}}$ β3 integrin$^{\text{D723A}}$ was generated taking benefit from a cDNA carrying already the β3 integrin$^{\text{D723A}}$ mutation (kind gift from Dr. Bernhard Wehrle-Haller) and the B3119Yf/B3119Yr oligos.

4.3. Expression and purification of recombinant VN

For the expression of the recombinant VN semi-confluent CHO-Flp-In cells were used that were stably transfected with the vectors encoding for the VN variants. The cells were washed with PBS and incubated for one or two weeks in CHO protein-free medium (Sigma–Aldrich). The collected supernatants were purified by immobilised metal-affinity chromatography and dialysed extensively against PBS.

4.4. Coating of wells

The coatings of the plates for the experiments were done overnight at 4 °C with the following concentrations: Vitronectin (RGD and RAD) 10 μg/ml, fibronectin 10 μg/ml. At the day of the experiment the coated wells were blocked with 5% BSA/PBS at 37 °C for at least 3 h.

4.5. Antibodies, immunofluorescence and other reagents

The following antibodies were used in this work: β1 integrin 4B4 mAb (Beckman Coulter, Pasadena, USA) (this antibody is an allosteric inhibitor binding to the K218 in the β1 integrin I-like domain and preventing the shift of the α7 helix and the swing-out of the hybrid domain (Luo et al., 2004), β1 integrin antibody K20 mAb (Santa Cruz Biotechnology, Dallas, USA), β1 integrin antibody 9EG7 mAb (BD Biosciences), vinculin hVIN-1 (Sigma–Aldrich). Other fluorescence reagents: Phalloidin (TRITC or FITC conjugated) and DAPI from Sigma–Aldrich. The inhibitors blebbistatin, latrunculin and Y27632 were from Calbiochem (Merck Millipore, Billerica, USA). Cytochalasin D, neomycin and methyl-β-cyclodextrin (MBCD) were from Sigma–Aldrich.

The expression vector for Paxillin-GFP was kindly provided by Dr. Alan F. Horwitz.

4.6. Cell preparation for spreading and cell migration assays and imaging

The tetracycline-induced cells were trypsinised and counted with a Beckmann Coulter counter (Beckman Coulter). The cells were washed with serum-free DMEM medium and the cell pellet resuspended in serum-free DMEM medium to achieve a cell concentration of 250.000 cells/ml. If the cells were treated with antibodies or inhibitors the cells were incubated with the reagent (with the indicated concentrations) for 10 min in suspension at room temperature before plating. Exceptions were the treatment with methyl-β-cyclodextrin and the combined application of latrunculin and blebbistatin, which were performed as indicated in the figure legends. Directly before plating, the cells were eventually induced by addition of 10 nM pro-uPA (if not indicated differently). Then the cells were subjected to the dedicated wells of a glass-bottomed plate (single or 12 well, MatTek, Ashland, USA) coated with the indicated substrates.

4.7. Immunofluorescence imaging

For immunofluorescence imaging (except the integrin activation assay) the cells were fixed with 4% PFA/PBS for 10 min, permeabilised with 0.2% Triton X-100/PBS for 3 min and blocked with 3% BSA/PBS for 10 min. The primary and secondary antibodies (in 0.3% BSA/PBS) were incubated in humid environment for 1 h at room temperature. Optionally phalloidin to stain the actin cytoskeleton was added to the secondary antibody solution. After the staining the cells were postfixed with 4% PFA/PBS for 10 min and mounted with Mowiol or ProLong® Gold antifade (Molecular Probes). Images were taken with a Nikon Ti inverted microscope (Nikon, Tokyo, Japan) equipped with a Perkin Elmer Ultraview Vox spinning disc confocal system (Perkin Elmer, Waltham, USA) controlled by Volocity software (Perkin Elmer) (Objectives used: 60x Plan Apo VC, NA 1.4 Oil (Nikon) or 100x Apo TIRF, NA 1.49 Oil (Nikon)) or with a Leica TCS SP2 (AOBS) confocal microscope (Leica, Wetzlar, Germany) with a 63x HCX Pl Apo, NA 1.4 Oil objective (Leica).

4.8. Microscopy for spreading and migration assays

For the spreading assay the cells were fixed with 4% PFA after 30 min adhesion time. To quantify the cell spreading differential interference contrast (DIC) microscopic images were taken with an Olympus IX81 inverted microscope (Olympus, Tokyo, Japan) controlled by Metamorph software (Molecular Devices, Sunnyvale, USA) and equipped with a DIC prism. A 60× Plan Apo, NA 1.4 Oil, DIC objective (Olympus) was used. The cell area was quantified using ImageJ (National Institute of Health, Bethesda, USA).

For the migration assays the plates were transfer to an Olympus IX70 microscope with a 10x PlanC N, NA 0.25 Dry, controlled by ScanR̂ (all Olympus) and equipped with an incubator to sustain humid 37 °C and 5% CO_2. For a total period of at least 2 h (or longer) every 5 min phase contrast images were taken and later assembled and quantified by ImageJ (particle analysis).

4.9. *Confocal spinning disc live cell imaging to analyse retrograde actin flow*

To perform the live cell imaging experiments examining the retrograde actin flow, the cells were transiently transfected with 1:3 ratio of lifeact^{TM}-Cherry encoding vector and Fugene6 24–48 h before the recording day (the same transfection strategy was used for the Paxillin-GFP vector). On the recording day, the cells were prepared as described for the migration assays. The transfected cells were plated on 35 mm glass-bottomed MatTek plates (MatTek) coated with the indicated substrates. After attachment/spreading of the cells, lifeact^{TM}-Cherry transfection-positive cells were recorded using a spinning disc confocal microscope (Nikon and Perkin Elmer) with a C9100-50 electron-multiplying CCD (charge-coupled device) camera (Hamamatsu Photonics, Hamamatsu, Japan). The system was controlled by Volocity software (Perkin Elmer). The conditions necessary for live cell imaging were kept stable by an incubator chamber at humid 37 °C and 5% CO_2. The objective used for this approach was a 100× Apo TIRF, NA 1.49 Oil (Nikon). The cells were recorded with an image frequence of 0.2, 0.5 or 1 image(s)/s (as indicated in the experiments). The image sequences were assembled with ImageJ and quantified with the kymograph plug-in.

4.10. *Measurement of β1 integrin activation*

For the β1 integrin activation measurement a different immunofluorescence staining protocol was used. The indicated cells (125.000 cells/well) were plated in an 8 well chamber slide (Lab-Tek II Chamber Slide System from Sigma–Aldrich). 30 min after pro uPA-induced spreading, the cells were put on ice and incubated for 15 min with the 9EG7 mAb (5 μg/ml) (as described in Asperti et al., 2009). After washing the staining of the total β1 integrin was done with the K20 mAb (5 μg/ml). Additionally the cells were stained with DAPI to allow easy autofocussing. The images were then recorded by automated microscopic screening with an Olympus ScanR̂ Screening Station (Olympus) (Objective used: 10× Plan Apo, NA 0.4 Dry (Olympus)).

The quantification was done as described by Rantala et al. (2011). The images were processed with ImageJ setting fixed thresholds so that the background was masked. For the 9EG7 signal only the lamellipodial signal was considered whereas for the K20 signal the whole cell signal was taken into account. From the obtained signal values a 9EG7/K20 ratio of single cells was calculated.

4.11. *Measurement of β1 integrin clustering*

The clustering of β1 integrin (visualised by K20 mAb staining, see Fig. S2D) was analysed following the procedure described in Cluzel et al. (2005) with the only difference that the clustering was quantified for the lamellipodial zones and not for the whole cell area.

4.12. *Correlation analysis*

The correlation analysis (Fig. S2) of TLN construct-GFP and lifeact^{TM}-Cherry, vinculin or β1 integrin stainings were done using the ImageJ plug-in Colocalisation Analysis–Manders Coefficient, determining the Pearson's Correlation Coefficient r. Before analysis, the background was subtracted via the plug-in ImageJ Background Substraction from ROI (same ROI in both channels). Zero/Zero pixel pairs were not taken into account and negative coefficients were not included into the statistics. For the TLN/lifeact^{TM} correlation the region of the leading edge of the lamellipodium (approximate first 5 μm) and a region towards the lamellum were analysed separately. For vinculin and β1 integrin stainings the total lamellipodium was quantified.

4.13. *Atomic force microscopy measurements on live cells*

For the atomic force microscopy characterisation the indicated cells were plated in sparse concentration (100.000 cells per ml) onto glass-bottomed dishes (Willco Wells, Amsterdam, Netherlands) in fully supplemented DMEM (serum as VN^{RGD} source) the day before the actual AFM measurement. At least 30 min before the measurements the cells were induced with 10 nM pro-uPA and after microscopic control of the spreading the plates were transferred to the atomic force microscope sample holder. Treatments with reagents were applied as indicated in the figure legends.

During the AFM measurements the temperature of the medium (25 mM HEPES buffer was added to keep physiological pH) was maintained at 37 °C by a homemade heating system. For combined topographical/mechanical measurements, a Bioscope Catalyst AFM (Bruker, Billerica, USA) was operated in *force volume* mode (Butt et al., 2005) using custom spherical probes attached to silicon cantilevers (elastic constant 0.22 N/m, measured radius of curvature of the tip 4850 nm). AFM probes were manufactured and characterised in the laboratory using an established method (Indrieri et al., 2011). Each force volume consists in an array of 64 × 64 force versus distance curves recorded across the region occupied by a single cell from which the local height of the sample and the local elastic modulus can be extracted. By these means topographic and elastic maps of the sample can therefore be acquired in one-to-one correspondence. All the measurements were performed with the following parameters: ramp length for each force curve: 5 μm; approaching speed 43.4 μm/s; scan rate 7.1 Hz; 2048 points per curve. The lateral scan size varied between 60 μm × 60 μm and 100 μm × 100 μm, depending on the cell's dimension. Data processing of force volumes was carried out in Matlab^{TM} (Mathworks, Natick, USA) environment using custom routines. Using the Hertz model (Butt et al., 2005) enhanced by finite thickness correction (Dimitriadis et al., 2002), each force curve was fitted on the small indentation regime (up to 30% of the total local indentation) to highlight the contribution to the cell's elasticity of the membrane and actin cytoskeleton. Further information on this AFM live cell imaging and details of the corresponding analysis can be found in the recently published work of Puricelli et al. (2015). Potential treatments with reagents were performed as indicated in the figure legends.

Conflict of interest

The authors declare to have no conflict of interests.

Author contributions

CS, GMSF and NS conceived the project.
CS wrote the manuscript and designed the figures.
CS did the cell biological and light microscopy experiments and their statistical analysis (except AFM data and FACS), the second with significant support from AM. GMSF produced the cell lines used in this study and did the FACS analysis. GMSF and NS realised the cloning work and VdL the VN purification.

MG, LP, AP, and CS conceived and performed the AFM part of the study.

CL and PM provided important materials, equipment and information.

Acknowledgements

This work was supported by research grants from the Italian Association for Cancer Research (AIRC) and the Cariplo foundation hold by NS. VDL was supported by a fellowship from the AIRC. Furthermore, this project has been supported by the Italian Ministry of University and Research, MIUR, through the “National Funding for Basic Research” (FIRB) hold by CL. COST Action TD1002 is acknowledged for providing a stimulating scientific environment for the discussion of AFM-based nanomechanics of cells and soft matter.

We are very grateful for critical reading of the manuscript by Giorgio Scita and provided suggestions. We thank all the staff of the Imaging Unit of IFOM (The FIRC Institute of Molecular Oncology), in particular Sara Barozzi, Massimiliano Garrè and Dario Parazzoli, for support in experiments involving imaging.

Appendix A. Supplementary data

Supplementary data associated with this article can be found, in the online version, at http://dx.doi.org/10.1016/j.ejcb.2015.10.002.

References

Anthis, N.J., Wegener, K.L., Critchley, D.R., Campbell, I.D., 2010. Structural diversity in integrin/talin interactions. Structure 18 (12), 1654–1666, http://dx.doi.org/10.1016/j.str.2010.09.018.

Arnaout, M.A., Mahalingam, B., Xiong, J.-P., 2005. Integrin structure, allostery, and bidirectional signaling. Annu. Rev. Cell Dev. Biol. 21, 381–410, http://dx.doi.org/10.1146/annurev.cellbio.21.090704.151217.

Askari, J.A., Patrick, A., Buckley, A., Mould, P., Humphries, M.J., 2009. Linking integrin conformation to function. J. Cell Sci. 122 (Pt 2), 165–170, http://dx.doi.org/10.1242/jcs.018556.

Askari, J.A., Tynan, C.J., Webb, S.E.D., Martin-Fernandez, M.L., Ballestrem, C., Humphries, M.J., 2010. Focal adhesions are sites of integrin extension. J. Cell Biol. 188 (6), 891–903, http://dx.doi.org/10.1083/jcb.200907174.

Asperti, C., Astro, V., Totaro, A., Paris, S., de Curtis, I., 2009. Liprin-alpha1 promotes cell spreading on the extracellular matrix by affecting the distribution of activated integrins. J. Cell Sci. 122 (Pt 18), 3225–3232, http://dx.doi.org/10.1242/jcs.054155.

Batchelder, E.L., Hollopeter, G., Campillo, C., Mezanges, X., Jorgensen, E.M., Nassoy, P., Sens, P., Plastino, J., 2011. Membrane tension regulates motility by controlling lamellipodium organization. Proc. Natl. Acad. Sci. U. S. A. 108 (28), 11429–11434, http://dx.doi.org/10.1073/pnas.1010481108.

Bazzoni, G., Shih, D.T., Buck, C.A., Hemler, M.E., 1995. Monoclonal antibody 9EG7 defines a novel beta 1 integrin epitope induced by soluble ligand and manganese, but inhibited by calcium. J. Biol. Chem. 270 (43), 25570–25577.

Butt, H.-J., Cappella, B., Kappl, M., 2005. Force measurements with the atomic force microscope: technique, interpretation and applications. Surf. Sci. Rep. 59 (1–6), 1–152, http://dx.doi.org/10.1016/j.surfrep.2005.08.003.

Caiolfa, V.R., Zamai, M., Malengo, G., Andolfo, A., Madsen, C.D., Sutin, J., Digman, M.A., Gratton, E., Blasi, F., Sidenius, N., 2007. Monomer dimer dynamics and distribution of GPI-anchored uPAR are determined by cell surface protein assemblies. J. Cell Biol. 179 (5), 1067–1082, http://dx.doi.org/10.1083/jcb.200702151.

Calderwood, D.A., Zent, R., Grant, R., Rees, D.J., Hynes, R.O., Ginsberg, M.H., 1999. The talin head domain binds to integrin beta subunit cytoplasmic tails and regulates integrin activation. J. Biol. Chem. 274 (40), 28071–28074.

Carisey, A., Tsang, R., Greiner, A.M., Nijenhuis, N., Heath, N., Nazgiewicz, A., Kemkemer, R., Derby, B., Spatz, J., Ballestrem, C., 2013. Vinculin regulates the recruitment and release of core focal adhesion proteins in a force-dependent manner. Curr. Biol. 23 (4), 271–281, http://dx.doi.org/10.1016/j.cub.2013.01.009.

Case, L.B., Baird, M.A., Shtengel, G., Campbell, S.L., Hess, H.F., Davidson, M.W., Waterman, C.M., 2015. Molecular mechanism of vinculin activation and nanoscale spatial organization in focal adhesions. Nat. Cell Biol. 17 (7), 880–892, http://dx.doi.org/10.1038/ncb3180.

Chen, JianFeng, Yang, Wei, Kim, Minsoo, Carman, C.V., Springer, T.A., 2006. Regulation of outside-in signaling and affinity by the beta2 I domain of integrin alphaLbeta2. Proc. Natl. Acad. Sci. U. S. A. 103 (35), 13062–13067, http://dx.doi.org/10.1073/pnas.0605666103.

Chen, Xing, Xie, Can, Nishida, Noritaka, Li, Zongli, Walz, T., Springer, T.A., 2010. Requirement of open headpiece conformation for activation of leukocyte integrin alphaXbeta2. Proc. Natl. Acad. Sci. U. S. A. 107 (33), 14727–14732, http://dx.doi.org/10.1073/pnas.1008663107.

Ciobanasu, C., Faivre, B., Le Clainche, C., 2013. Integrating actin dynamics, mechanotransduction and integrin activation: the multiple functions of actin binding proteins in focal adhesions. Eur. J. Cell Biol. 92 (10–11), 339–348, http://dx.doi.org/10.1016/j.ejcb.2013.10.009, SPP 1464:Actin Dynamics – Part I.

Ciobanasu, C., Faivre, B., Le Clainche, C., 2014. Actomyosin-dependent formation of the mechanosensitive talin–vinculin complex reinforces actin anchoring. Nat. Commun. 5 (January), 3095, http://dx.doi.org/10.1038/ncomms4095.

Cluzel, C., Saltel, F., Lussi, J., Paulhe, F., Imhof, B.A., Wehrle-Haller, B., 2005. The mechanisms and dynamics of (alpha)v(beta)3 integrin clustering in living cells. J. Cell Biol. 171 (2), 383–392, http://dx.doi.org/10.1083/jcb.200503017.

Critchley, D.R., 2009. Biochemical and structural properties of the integrin-associated cytoskeletal protein talin. Annu. Rev. Biophys. 38, 235–254, http://dx.doi.org/10.1146/annurev.biophys.050708.133744.

Cunningham, O., Andolfo, A., Santovito, M.L., Iuzzolino, L., Blasi, F., Sidenius, N., 2003. Dimerization controls the lipid raft partitioning of uPAR/CD87 and regulates its biological functions. EMBO J. 22 (22), 5994–6003, http://dx.doi.org/10.1093/emboj/cdg588.

del Rio, A., Perez-Jimenez, R., Liu, R., Roca-Cusachs, P., Fernandez, J.M., Sheetz, M.P., 2009. Stretching single talin rod molecules activates vinculin binding. Science (New York, NY) 323 (5914), 638–641, http://dx.doi.org/10.1126/science.1162912.

Desgrosellier, J.S., Barnes, L.A., Shields, D.J., Huang, M., Lau, S.K., Prévost, N., Tarin, D., Shattil, S.J., Cheresh, D.A., 2009. An Integrin alpha(v)beta(3)-c-Src oncogenic unit promotes anchorage-independence and tumor progression. Nat. Med. 15 (10), 1163–1169, http://dx.doi.org/10.1038/nm.2009.

Desgrosellier, J.S., Cheresh, D.A., 2010. Integrins in cancer: biological implications and therapeutic opportunities. Nat. Rev. Cancer 10 (1), 9–22, http://dx.doi.org/10.1038/nrc2748.

Dimitriadis, E.K., Horkay, F., Maresca, J., Kachar, B., Chadwick, R.S., 2002. Determination of elastic moduli of thin layers of soft material using the atomic force microscope. Biophys. J. 82 (5), 2798–2810, http://dx.doi.org/10.1016/S0006-3495(02)75620-8.

Diz-Muñoz, A., Fletcher, D.A., Weiner, O.D., 2013. Use the force: membrane tension as an organizer of cell shape and motility. Trends Cell Biol. 23 (2), 47–53, http://dx.doi.org/10.1016/j.tcb.2012.09.006.

Ferraris, G.M.S., Schulte, C., Buttiglione, V., De Lorenzi, V., Piontini, A., Galluzzi, M., Podestà, A., Madsen, C.D., Sidenius, N., 2014, August. The interaction between uPAR and vitronectin triggers ligand-independent adhesion signalling by integrins. EMBO J., e201387611, http://dx.doi.org/10.15252/embj.201387611.

Fletcher, D.A., Mullins, D.R., 2010. Cell mechanics and the cytoskeleton. Nature 463 (7280), 485–492, http://dx.doi.org/10.1038/nature08908.

Friedl, P., Wolf, K., 2010. Plasticity of cell migration: a multiscale tuning model. J. Cell Biol. 188 (1), 11–19, http://dx.doi.org/10.1083/jcb.200909003.

Galbraith, C.G., Yamada, K.M., Galbraith, J.A., 2007. Polymerizing actin fibers position integrins primed to probe for adhesion sites. Science (New York, NY) 315 (5814), 992–995, http://dx.doi.org/10.1126/science.1137904.

Gallop, Jennifer L., Walrant, Astrid, Cantley, Lewis C., Kirschner, Marc W., 2013. Phosphoinositides and membrane curvature switch the mode of actin polymerization via selective recruitment of Toca-1 and Snx9. Proc. Natl. Acad. Sci. U. S. A. 110 (18), 7193–7198, http://dx.doi.org/10.1073/pnas.1305286110.

Gauthier, N.C., Masters, T.A., Sheetz, M.P., 2012. Mechanical feedback between membrane tension and dynamics. Trends Cell Biol. 22 (10), 527–535, http://dx.doi.org/10.1016/j.tcb.2012.07.005.

Giannone, G., Jiang, G., Sutton, D.H., Critchley, D.R., Sheetz, M.P., 2003. Talin1 is critical for force-dependent reinforcement of initial integrin-cytoskeleton bonds but not tyrosine kinase activation. J. Cell Biol. 163 (2), 409–419, http://dx.doi.org/10.1083/jcb.200302001.

Giannone, G., Mège, R.-M., Thoumine, O., 2009. Multi-level molecular clutches in motile cell processes. Trends Cell Biol. 19 (9), 475–486, http://dx.doi.org/10.1016/j.tcb.2009.07.001.

Gingras, A.R., Bate, N., Goult, B.T., Hazelwood, L., Ilona Canestrelli, J., Grossmann, G., Liu, H.J., et al., 2008. The structure of the C-terminal actin-binding domain of talin. EMBO J. 27 (2), 458–469, http://dx.doi.org/10.1038/sj.emboj.7601965.

Goksoy, E., Ma, Y.-Q., Wang, X., Kong, X., Perera, D., Plow, E.F., Jun, Q., 2008. Structural basis for the autoinhibition of talin in regulating integrin activation. Mol. Cell 31 (1), 124–133, http://dx.doi.org/10.1016/j.molcel.2008.06.011.

Golji, J., Mofrad, M.R.K., 2014. The talin dimer structure orientation is mechanically regulated. Biophys. J. 107 (8), 1802–1809, http://dx.doi.org/10.1016/j.bpj.2014.08.038.

Gupton, S.L., Waterman-Storer, C.M., 2006. Spatiotemporal feedback between actomyosin and focal-adhesion systems optimizes rapid cell migration. Cell 125 (7), 1361–1374, http://dx.doi.org/10.1016/j.cell.2006.05.029.

Hemmings, L., Rees, D.J., Ohanian, V., Bolton, S.J., Gilmore, A.P., Patel, B., Priddle, H., Trevithick, J.E., Hynes, R.O., Critchley, D.R., 1996. Talin contains three actin-binding sites each of which is adjacent to a vinculin-binding site. J. Cell Sci. 109 (November (Pt 11)), 2715–2726.

Himmel, M., Ritter, A., Rothemund, S., Pauling, B.V., Rottner, K., Gingras, A.R., Ziegler, W.H., 2009. Control of high affinity interactions in the talin C terminus: how talin domains coordinate protein dynamics in cell adhesions. J. Biol. Chem. 284 (20), 13832–13842, http://dx.doi.org/10.1074/jbc.M900266200.

Houk, A.R., Jilkine, A., Mejean, C.O., Boltyanskiy, R., Dufresne, E.R., Angenent, S.B., Altschuler, S.J., Wu, L.F., Weiner, O.D., 2012. Membrane tension maintains cell polarity by confining signals to the leading edge during neutrophil migration. Cell 148 (1–2), 175–188, http://dx.doi.org/10.1016/j.cell.2011.10.050.

Hughes, P.E., Diaz-Gonzalez, F., Leong, L., Wu, C., McDonald, J.A., Shattil, S.J., Ginsberg, M.H., 1996. Breaking the integrin hinge. A defined structural constraint regulates integrin signaling. J. Biol. Chem. 271 (12), 6571–6574.

Hu, K., Ji, L., Applegate, K.T., Danuser, G., Waterman-Storer, C.M., 2007. Differential transmission of actin motion within focal adhesions. Science (New York, NY) 315 (5808), 111–115, http://dx.doi.org/10.1126/science.1135085.

Humphries, J.D., Wang, P., Streuli, C., Geiger, B., Humphries, M.J., Ballestrem, C., 2007. Vinculin controls focal adhesion formation by direct interactions with talin and actin. J. Cell Biol. 179 (5), 1043–1057, http://dx.doi.org/10.1083/jcb.200703036.

Huttenlocher, A., Ginsberg, M.H., Horwitz, A.F., 1996. Modulation of cell migration by integrin-mediated cytoskeletal linkages and ligand-binding affinity. J. Cell Biol. 134 (6), 1551–1562, http://dx.doi.org/10.1083/jcb.134.6.1551.

Hynes, R.O., 2002. Integrins: bidirectional, allosteric signaling machines. Cell 110 (6), 673–687.

Indrieri, M., Podestà, A., Bongiorno, G., Marchesi, D., Milani, P., 2011. Adhesive-free colloidal probes for nanoscale force measurements: production and characterization. Rev. Sci. Instrum. 82 (2), 023708, http://dx.doi.org/10.1063/1.3553499.

Jiang, G., Giannone, G., Critchley, D.R., Fukumoto, E., Sheetz, M.P., 2003. Two-piconewton slip bond between fibronectin and the cytoskeleton depends on talin. Nature 424 (6946), 334–337, http://dx.doi.org/10.1038/nature01805.

Kanchanawong, P., Shtengel, G., Pasapera, A.M., Ramko, E.B., Davidson, M.W., Hess, H.F., Waterman, C.M., 2010. Nanoscale architecture of integrin-based cell adhesions. Nature 468 (7323), 580–584, http://dx.doi.org/10.1038/nature09621.

Khatibzadeh, N., Gupta, S., Farrell, B., Brownell, W.E., Anvari, B., 2012. Effects of cholesterol on nano-mechanical properties of the living cell plasma membrane. Soft Matter 8 (32), 8350–8360, http://dx.doi.org/10.1039/C2SM25263E.

Khatibzadeh, N., Spector, A.A., Brownell, W.E., Anvari, B., 2013. Effects of plasma membrane cholesterol level and cytoskeleton F-actin on cell protrusion mechanics. PLoS ONE 8 (2), e57147, http://dx.doi.org/10.1371/journal.pone.0057147.

Kim, C., Ye, F., Hu, X., Ginsberg, M.H., 2012. Talin activates integrins by altering the topology of the β transmembrane domain. J. Cell Biol. 197 (5), 605–611, http://dx.doi.org/10.1083/jcb.201112141.

Lee, H.-S., Bellin, R.M., Walker, D.L., Patel, B., Powers, P., Liu, H., Garcia-Alvarez, B., et al., 2004. Characterization of an actin-binding site within the talin FERM domain. J. Mol. Biol. 343 (3), 771–784, http://dx.doi.org/10.1016/j.jmb.2004.08.069.

Legate, K.R., Takahashi, S., Bonakdar, N., Fabry, B., Boettiger, D., Zent, R., Fässler, R., 2011. Integrin adhesion and force coupling are independently regulated by localized PtdIns(4,5)2 synthesis. EMBO J. 30 (22), 4539–4553, http://dx.doi.org/10.1038/emboj.2011.332.

Lieber, A.D., Yehudai-Resheff, S., Barnhart, E.L., Theriot, J.A., Keren, K., 2013. Membrane tension in rapidly moving cells is determined by cytoskeletal forces. Curr. Biol. 23 (15), 1409–1417, http://dx.doi.org/10.1016/j.cub.2013.05.063.

Liu, J., Wang, Y., Goh, W.I., Goh, H., Baird, M.A., Ruehland, S., Teo, S., et al., 2015, August. Talin determines the nanoscale architecture of focal adhesions. Proc. Natl. Acad. Sci. U. S. A., http://dx.doi.org/10.1073/pnas.1512025112.

Luo, B.-H., Springer, T.A., 2006. Integrin structures and conformational signaling. Curr. Opin. Cell Biol. 18 (5), 579–586, http://dx.doi.org/10.1016/j.ceb.2006.08.005.

Luo, B.-H., Strokovich, K., Walz, T., Springer, T.A., Takagi, J., 2004. Allosteric beta1 integrin antibodies that stabilize the low affinity state by preventing the swing-out of the hybrid domain. J. Biol. Chem. 279 (26), 27466–27471, http://dx.doi.org/10.1074/jbc.M404354200.

Madsen, C.D., Ferraris, G.M.S., Andolfo, A., Cunningham, O., Sidenius, N., 2007. uPAR-induced cell adhesion and migration: vitronectin provides the key. J. Cell Biol. 177 (5), 927–939, http://dx.doi.org/10.1083/jcb.200612058.

Mitchison, T., Kirschner, M., 1988. Cytoskeletal dynamics and nerve growth. Neuron 1 (9), 761–772.

Moser, M., Legate, K.R., Zent, R., Fässler, R., 2009. The tail of integrins, talin, and kindlins. Science (New York, NY) 324 (5929), 895–899, http://dx.doi.org/10.1126/science.1163865.

Orłowski, A., Kukkurainen, S., Pöyry, A., Rissanen, S., Vattulainen, I., Hytönen, V.P., Tomasz, R., 2015, August. PIP2 and talin join forces to activate integrin. J. Phys. Chem. B, http://dx.doi.org/10.1021/acs.jpcb.5b06457.

Pinon, P., Pärssinen, J., Vazquez, P., Bachmann, M., Rahikainen, R., Jacquier, M.-C., Azizi, L., et al., 2014. Talin-bound NPLY motif recruits integrin-signaling adapters to regulate cell spreading and mechanosensing. J. Cell Biol. 205 (2), 265–281, http://dx.doi.org/10.1083/jcb.201308136.

Pirazzoli, V., Ferraris, G.M.S., Sidenius, N., 2013. Direct evidence of the importance of vitronectin and its interaction with the urokinase receptor in tumor growth. Blood 121 (12), 2316–2323, http://dx.doi.org/10.1182/blood-2012-08-451187.

Puricelli, L., Galluzzi, M., Schulte, C., Podestà, A., Milani, P., 2015. Nanomechanical and topographical imaging of living cells by atomic force microscopy with colloidal probes. Rev. Sci. Instrum. 86 (3), 033705, http://dx.doi.org/10.1063/1.4915896.

Rantala, J.K., Pouwels, J., Pellinen, T., Veltel, S., Laasola, P., Mattila, E., Potter, C.S., et al., 2011. SHARPIN is an endogenous inhibitor of β1-integrin activation. Nat. Cell Biol. 13 (11), 1315–1324, http://dx.doi.org/10.1038/ncb2340.

Raucher, D., Sheetz, M.P., 2000. Cell spreading and lamellipodial extension rate is regulated by membrane tension. J. Cell Biol. 148 (1), 127–136.

Renkawitz, J., Schumann, K., Weber, M., Lämmermann, T., Pflicke, H., Piel, M., Polleux, J., Spatz, J.P., Michael, S., 2009. Adaptive force transmission in amoeboid cell migration. Nat. Cell Biol. 11 (12), 1438–1443, http://dx.doi.org/10.1038/ncb1992.

Ridley, A.J., 2011. Life at the leading edge. Cell 145 (7), 1012–1022, http://dx.doi.org/10.1016/j.cell.2011.06.010.

Riedl, Julia, Crevenna, Alvaro H., Kessenbrock, Kai, Yu, Jerry Haochen, Neukirchen, Dorothee, Bista, Michal, Bradke, Frank, et al., 2008. Lifeact: A Versatile Marker to Visualize F-Actin. Nat. Methods 5 (7), 605–607, http://dx.doi.org/10.1038/nmeth.1220.

Schiller, Herbert B., Fässler, Reinhard, 2013. Mechanosensitivity and Compositional Dynamics of Cell-Matrix Adhesions. EMBO Rep. 14 (6), 509–519, http://dx.doi.org/10.1038/embor.2013.49.

Schwartz, Martin A., Horwitz, Alan Rick, 2006. Integrating Adhesion, Protrusion, and Contraction during Cell Migration. Cell 125 (7), 1223–1225, http://dx.doi.org/10.1016/j.cell.2006.06.015.

Seguin, Laetitia, Desgrosellier, Jay S., Weis, Sara M., Cheresh, David A., 2015, January. Integrins and Cancer: Regulators of Cancer Stemness, Metastasis, and Drug Resistance. Trends Cell Biol., http://dx.doi.org/10.1016/j.tcb.2014.12.006.

Shattil, Sanford J., Kim, Chungho, Ginsberg, Mark H., 2010. The Final Steps of Integrin Activation: The End Game. Nat. Rev. Mol. Cell Biol. 11 (4), 288–300, http://dx.doi.org/10.1038/nrm2871.

Simunovic, Mijo, Voth, Gregory A., 2015. Membrane Tension Controls the Assembly of Curvature-Generating Proteins. Nat. Commun. 6, 7219, http://dx.doi.org/10.1038/ncomms8219.

Smith, H.W., Marra, P., Marshall, C.J., 2008. uPAR promotes formation of the p130Cas–Crk complex to activate Rac through DOCK180. J. Cell Biol. 182 (4), 777–790, http://dx.doi.org/10.1083/jcb.200712050.

Suetsugu, S., Kurisu, S., Takenawa, T., 2014. Dynamic shaping of cellular membranes by phospholipids and membrane-deforming proteins. Physiol. Rev. 94 (4), 1219–1248, http://dx.doi.org/10.1152/physrev.00040.2013.

Suzuki, K., Sterba, R.E., Sheetz, M.P., 2000. Outer membrane monolayer domains from two-dimensional surface scanning resistance measurements. Biophys. J. 79 (1), 448–459.

Svitkina, T.M., Verkhovsky, A.B., McQuade, K.M., Borisy, G.G., 1997. Analysis of the actin–myosin II system in fish epidermal keratocytes: mechanism of cell body translocation. J. Cell Biol. 139 (2), 397–415.

Tadokoro, S., Shattil, S.J., Eto, K., Tai, V., Liddington, R.C., de Pereda, J.M., Ginsberg, M.H., Calderwood, D.A., 2003. Talin binding to integrin beta tails: a final common step in integrin activation. Science (New York, NY) 302 (5642), 103–106, http://dx.doi.org/10.1126/science.1086652.

Takada, Y., Ylänne, J., Mandelman, D., Puzon, W., Ginsberg, M.H., 1992. A point mutation of integrin beta 1 subunit blocks binding of alpha 5 beta 1 to fibronectin and invasin but not recruitment to adhesion plaques. J. Cell Biol. 119 (4), 913–921.

Thapa, N., Choi, S., Hedman, A., Tan, X., Anderson, R.A., 2013. Phosphatidylinositol phosphate 5-kinase Iγi2 in association with Src controls anchorage-independent growth of tumor cells. J. Biol. Chem. 288 (48), 34707–34718, http://dx.doi.org/10.1074/jbc.M113.512848.

Thievessen, I., Thompson, P.M., Berlemont, S., Plevock, K.M., Plotnikov, S.V., Zemljic-Harpf, A., Ross, R.S., et al., 2013. Vinculin–actin interaction couples actin retrograde flow to focal adhesions, but is dispensable for focal adhesion growth. J. Cell Biol. 202 (1), 163–177, http://dx.doi.org/10.1083/jcb.201303129.

Tsujita, K., Takenawa, T., Toshiki, I., 2015. Feedback regulation between plasma membrane tension and membrane-bending proteins organizes cell polarity during leading edge formation. Nat. Cell Biol. 17 (6), 749–758, http://dx.doi.org/10.1038/ncb3162.

Vicente-Manzanares, M., Choi, C.K., Horwitz, A.R., 2009. Integrins in cell migration – the actin connection. J. Cell Sci. 122 (Pt 2), 199–206, http://dx.doi.org/10.1242/jcs.018564.

Vinogradova, O., Velyvis, A., Velyviene, A., Hu, B., Haas, T., Plow, E., Jun, Q., 2002. A structural mechanism of integrin alpha(IIb)beta(3) 'inside-out' activation as regulated by its cytoplasmic face. Cell 110 (5), 587–597.

Wegener, K.L., Partridge, A.W., Han, J., Pickford, A.R., Liddington, R.C., Ginsberg, M.H., Campbell, I.D., 2007. Structural basis of integrin activation by talin. Cell 128 (1), 171–182, http://dx.doi.org/10.1016/j.cell.2006.10.048.

Yao, M., Goult, B.T., Chen, H., Cong, P., Sheetz, M.P., Jie, Y., 2014. Mechanical activation of vinculin binding to talin locks talin in an unfolded conformation. Sci. Rep. 4, 4610, http://dx.doi.org/10.1038/srep04610.

Ye, F., Hu, G., Taylor, D., Ratnikov, B., Bobkov, A.A., McLean, M.A., Sligar, S.G., Taylor, K.A., Ginsberg, M.H., 2010. Recreation of the terminal events in physiological integrin activation. J. Cell Biol. 188 (1), 157–173, http://dx.doi.org/10.1083/jcb.200908045.

Zhang, X., Jiang, G., Cai, Y., Monkley, S.J., Critchley, D.R., Sheetz, M.P., 2008. Talin depletion reveals independence of initial cell spreading from integrin activation and traction. Nat. Cell Biol. 10 (9), 1062–1068, http://dx.doi.org/10.1038/ncb1765.

2.2.1 Additional discussion

Some of the results obtained in the paper reported above deserve a further discussion. First of all, we should keep in mind that an overexpression of talin may not necessarily imply a stiffening of the cytoskeleton or an increase in migration speed as a consequence of the slowdown of the actin retrograde flow. This is due to several reasons:

- AFM-based measurements of cell elasticity provided basically a test of the overall structural and spatial organization of the ensemble plasma membrane-actin cytoskeleton, which may be only weakly impacted by talin overexpression, compared to the endogenous situation: in both cases a similar integrin-cytoskeleton linkage is obtained, the main difference being represented by a different degree of integrin clustering. A missing connection between integrins and the actin cytoskeleton instead, as in the case of talin ΔABS, can imply a more significant rearrangement of the latter and a higher slippage of the actin filaments upon probe indentation, together resulting in the lower measured Young's modulus. From a more physiological perspective, the observed change in the microscopic mechanical properties can be interpreted as a marker of significant alterations at a deeper level, i.e. in the molecular state of the cell.
- Cell migration is a dynamic process, requiring the simultaneous engagement of the molecular clutches and building-up of adhesion complexes at the cell leading edge, and their disruption at the opposite side. This process can be hampered by an excessive integrin clustering and integrin-cytoskeleton linkage, hindering the MC and focal adhesion disengagement and therefore cell translocation, as in the case of TLN overexpressed.
- To enable an effective cell migration, cells need to polarize, promoting lamellipodial spreading mainly on a well-defined direction. An overexpression of talin can lead to an excessive non-polarized lamellipodia formation, in multiple directions or around the whole cell, thus lowering the cellular polarization and its average migration speed, i.e. the overall ability to migrate.

The case of cholesterol depletion in the cellular membrane is a little more tricky. Indeed, we observe a decrease in the measured Young's modulus similar to the case of talin ΔABS, but it is associated to an increase of the retrograde actin flow speed (thus potentially impacting on the migration capability) only when using $\mathrm{VN}^{\mathrm{RAD}}$ substrates. The removal of cholesterol might have a large impact on many membrane proteins and on the thermodynamic phase of the lipid component of the membrane; these changes in turn might be very relevant for the outside-to-inside transmission of mechanical signals, but a clear and comprehensive picture of these processes is still missing. Therefore, the overall effect of cholesterol variation on cellular elasticity is currently controversial and debated [48].

Chapter 3

Mechanics of the cellular microenvironment

3.1 Insight on colorectal carcinoma infiltration

As previously sketched in section 1.2, accumulating evidence suggests that deregulation of biophysical properties of the extracellular matrix (ECM) plays an *active and causative* role in cancer pathogenesis and progression. In particular, ECM stiffening is typically observed in tumoral tissues, compared to the healthy ones [12]. The increase in ECM rigidity is likely the outcome of the overexpression of lysyl-oxidase (LOX), an enzyme responsible for the cross-linking of ECM molecular components, as well as an architectural reorganization of the ECM fine structure into thicker and linearized fibres, often observed in regions characterized by tumor invasion (see refs. [25, 49] and therein cited references). These findings suggest that alterations in ECM mechanics, in association with tumor angiogenesis (i.e. the induced development of new blood vessels) facilitate cell migration and colonization, thus leading to metastasis. A comprehensive overview of these processes is represented in fig. 3.1.

In the following, a paper born within the collaboration with a scientific group from S. Raffaele hospital (Milan, Italy), led by Dr. Massimo Alfano, is reported [26]. The rationale behind this work was provided by a previous publication by Genovese et al. [28]: here, a protocol for the purification of tissue-derived ECMs, aimed at the complete removal of cells and cellular debris, is successfully developed and tested, showing that decellularized ECMs mantain their own

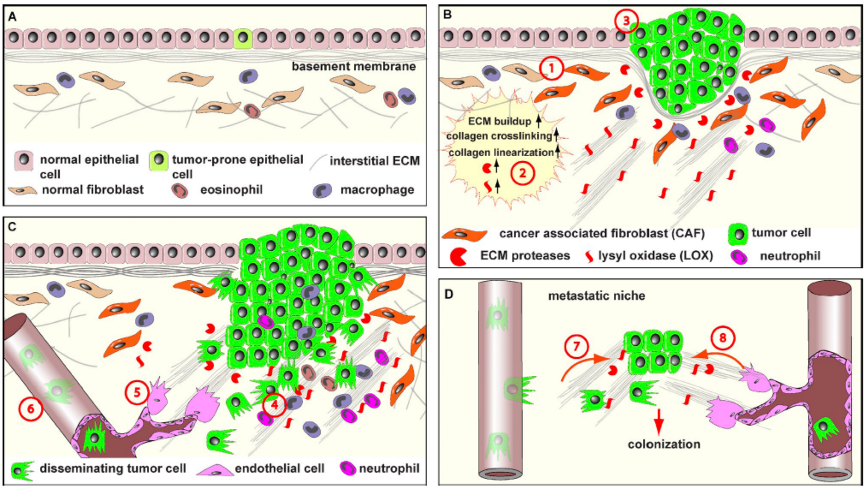
A
basement membrane
normal epithelial cell
tumor-prone epithelial cell
interstitial ECM
normal fibroblast
eosinophil
macrophage
B
3
1
ECM buildup
collagen crosslinking
collagen linearization
2
cancer associated fibroblast (CAF)
tumor cell
ECM proteases
lysyl oxidase (LOX)
neutrophil
C
5
6
4
disseminating tumor cell
endothelial cell
neutrophil
D
metastatic niche
7
8
colonization

Figure 4. **Abnormal ECM promotes cancer progression.** (A) ECM remodeling is tightly controlled to ensure organ homeostasis and functions. Normal ECM dynamics are essential for maintaining tissue integrity and keep rare tumor-prone cells, together with resident fibroblasts, eosinophils, macrophages, and other stromal cells, in check by maintaining an overall healthy microenvironment. (B) With age or under pathological conditions, tissues can enter a series of tumorigenic events. One of the earlier events is the generation of activated fibroblasts or CAFs (stage 1), which contributes to abnormal ECM buildup and deregulated expression of ECM remodeling enzymes (stage 2). Abnormal ECM has profound impacts on surrounding cells, including epithelial, endothelial, and immune cells and other stromal cell types. Deregulated ECM promotes epithelial cellular transformation and hyperplasia (stage 3). (C) In late-stage tumors, immune cells are often recruited to the tumor site to promote cancer progression (stage 4). In addition, deregulated ECM affects various aspects of vascular biology and promotes tumor-associated angiogenesis (stage 5). Creation of a leaky tumor vasculature in turn facilitates tumor cell invasion and metastasis to distant sites (stage 6). (D) At distant sites, cancer cells leave the circulation and take hold of the local tissue. Together with local stromal cells, cancer cells express ECM remodeling enzymes and create a local metastatic niche. Abnormal niche ECM promotes extravasation, survival, and proliferation of cancer cells (stage 7). At later stages when cancer cells awake from dormancy, abnormal ECM turns on the angiogenic switch (stage 8), presumably using a mechanism similar to that used at the primary site (stage 5), and promotes the rapid growth of cancer cells and an expansion of micrometastasis to macrometastasis.

Figure 3.1: Summary of the main steps involved in cancer progression. Reproduced from [25]

starting biochemical properties and three-dimensional structures, thus allowing to study ECM features decoupled from cell interference. The protocol is then applied to investigate the different abilities of tumoral, perilesional and healthy ECMs derived from resection surgery of human patients in sustaining colorectal carcinoma (CRC) progression; healthy and perilesional ECMs are localized respectively more than 10 cm and 1 cm far from tumoral neoplasia and free of lesions and necrotic areas. Remarkably, the three different ECMs display a structural organization characterized by a progressive degree of anisotropy and fibres linearization, moving from healthy to tumoral ECM; in particular, when seeded with CRC-derived malignant cells, healthy ECM shows a noticeable ability in constraining cell infiltration and knocking down proliferation rate, compared to perilesional and neoplastic ECM. Starting from this evidence, the work of Nebuloni et al. aims at investigating at a deeper level the biochemical and mechanical properties of pair-wise healthy, perilesional and tumoral ECMs derived from CRC, trying to unveil the key features of perilesional ECM predisposing a suitable environment for tumor invasion, in order to identify specific prognostic markers or alternative therapeutic strategies targeting the tumor surrounding microenvironment. As we will see, healthy and perilesional ECMs share an *unmodified biochemical composition*, whereas mechanical testing on the microscale by AFM reveals an *increasing gradient of stiffness* from healthy to perilesional and neoplastic ECMs, as the outcome of the increased cross-linking, thickening and linearization of ECM fibres likely associated to enhanced vascularization and subsequent oxygenation. Therefore, AFM-based mechanical measurements turn out to be fundamental in discriminating among different pathological (or even pre-pathological) states, unveiling early changes in biophysical properties of the samples where more conventional clinical tests or biochemical techniques don't detect significant alterations. In this context, AFM measurements have been performed on the basis of the protocol reported in section 2.1, properly adjusted to match the new experimental conditions: in particular, the difficulties faced in preparing "satisfactorily" flat samples, combined with the intrinsic structural heterogeneity of ECMs (see fig. 1.1 A and section 3.3) which places them a little outside of the assumptions at the basis of the classic contact mechanics models, have required the capturing of large data sets, allowing to drop the force curves which fall far apart from the predicted hertzian behavior and still relying on at least some hundreds of independent force curves; eventually, the statistical analysis has been refined, dropping average values in favour of more robust and properly weighted medians and median absolute deviations (MADs). Here below, the whole paper is reported, except for "Supplementary Material 2" which contains proteomics tabulations.

www.nature.com/scientificreports

SCIENTIFIC REPORTS

OPEN

Received: 02 September 2015
Accepted: 15 February 2016
Published: 04 March 2016

Insight On Colorectal Carcinoma Infiltration by Studying Perilesional Extracellular Matrix

Manuela Nebuloni[1], Luca Albarello[2], Annapaola Andolfo[3], Cinzia Magagnotti[3], Luca Genovese[4], Irene Locatelli[4], Giovanni Tonon[5], Erika Longhi[1], Pietro Zerbi[1], Raffaele Allevi[6], Alessandro Podestà[7], Luca Puricelli[7], Paolo Milani[7], Armando Soldarini[8], Andrea Salonia[9,10] & Massimo Alfano[4]

The extracellular matrix (ECM) from perilesional and colorectal carcinoma (CRC), but not healthy colon, sustains proliferation and invasion of tumor cells. We investigated the biochemical and physical diversity of ECM in pair-wised comparisons of healthy, perilesional and CRC specimens. Progressive linearization and degree of organization of fibrils was observed from healthy to perilesional and CRC ECM, and was associated with a steady increase of stiffness and collagen crosslinking. In the perilesional ECM these modifications coincided with increased vascularization, whereas in the neoplastic ECM they were associated with altered modulation of matrisome proteins, increased content of hydroxylated lysine and lysyl oxidase. This study identifies the increased stiffness and crosslinking of the perilesional ECM predisposing an environment suitable for CRC invasion as a phenomenon associated with vascularization. The increased stiffness of colon areas may represent a new predictive marker of desmoplastic region predisposing to invasion, thus offering new potential application for monitoring adenoma with invasive potential.

Tumor pathogenesis is affected by genetic mutations, escape from recognition by the immune system and modifications of the extracellular environment. Among the latter, transformed cells require the existence, generation and recruitment of a microenvironment permissive for tumor growth, the spread of neoplastic cells into the blood vasculature and/or lymphatic system, and seeding in distant organs[1]. Each of these tumorigenic steps is fine-tuned by factors related to the tumor cells and host[2]. As a major component of the local microenvironment, the extracellular matrix (ECM) has emerged as an active participant in major cell behaviors, including developmental processes and various stages of the carcinogenic process. Indeed, certain stroma components (i.e. vasculature) play a tumor promoting role[3] while others (i.e., myofibroblasts) have a tumor-suppressive role[3,4].

Dysregulation of the biochemical and physical features of the extracellular matrix such as composition, architecture, ultrastructural 3D conformation or stiffness of the ECM are associated with a lack of asymmetric division and differentiation of stem cells, epithelial-mesenchymal transition of cancer cells, as well as the modulation of cell migration, differentiation and proliferation sustaining the onset and progression of cancer both at primary and metastatic sites[5–8]. As for other epithelial cancers resulting from aberrant epithelial-mesenchymal interactions[8] the ECM profoundly regulates CRC progression and metastasis. Colon adenoma-carcinoma progression is associated with an overexpression of collagen XII[9], whereas liver metastasis is preceded by an accumulation of collagen IV in the liver where the conditioned hepatic ECM has to mediate mesenchymal-epithelial transition[10,11].

[1]L. Sacco Hospital, Department of Biomedical and Clinical Sciences, University of Milan, 20157 Milan, Italy. [2]Department of Pathology, San Raffaele Scientific Institute, Milan, Italy. [3]ProMiFa, Protein Microsequencing Facility, San Raffaele Scientific Institute, Milan, Italy. [4]Division of Experimental Oncology/Unit of Urology, URI, IRCCS Ospedale San Raffaele, 20132 Milan, Italy. [5]Functional Genomics of Cancer Unit, Division of Experimental Oncology, Istituto di Ricovero e Cura a Carattere Scientifico (IRCCS) San Raffaele Scientific Institute, Milan, Italy. [6]L. Sacco Hospital, Department of Biomedical and Clinical Sciences, Centro di Microscopia Elettronica per lo studio delle Nanotecnologie Applicate alla medicina "C.M.E.N.A.", University of Milan, 20157 Milan, Italy. [7]Interdisciplinary Centre for Nanostructured Materials and Interfaces (CIMaINa) and Dept. of Physics, Università degli Studi di Milano, Milano, Italy. [8]Diagnostica e Ricerca San Raffaele, Milan, Italy. [9]Università Vita-Salute San Raffaele, 20132 Milan, Italy.[10]Research Doctorate Program in Urology, Magna Graecia University, 88100 Catanzaro, Italy. Correspondence and requests for materials should be addressed to M.A. (email: alfano.massimo@hsr.it)

Not just biochemical composition but also increased lysyl oxidase (LOX) dependent crosslinking and stiffness have recently been reported to be responsible for fibrosis enhanced metastatic colonization of breast and colon cancer cells[10–14].

An important area of future cancer research will be to determine whether an abnormal ECM could be an effective cancer therapeutic target. To achieve this goal, we must understand how the ECM composition and organization are normally maintained and regulated and how they may be deregulated in cancer. A daunting task in this regard will be to determine which ECM changes have causative effects on disease progression and how these changes, alone or in combination with others, may affect cancer cells and cells in the stromal compartment[6]. In particular, discriminating which among the many features of the ECM is mandatory for invasion of the surrounding matrix is of priority.

We recently reported that the ECM from healthy colon mucosa constrains the spreading of metastatic cells, thus indicating the contribution of host factors versus the intrinsic capacity of neoplastic cells to invade the matrix. On the contrary the ECM from perilesional mucosa and CRC supported cell infiltration and increased cell proliferation[15]. The aim of this study was to unveil the features of the ECM in the perilesional mucosa mandatory for tumor infiltration. We investigated biochemical and mechanical features of the ECM isolated from pair-wised healthy colon mucosa, perilesional mucosa and infiltrated CRC, and identified a steady increase of crosslinking and stiffness from healthy to perilesional to CRC ECM. This study also identifies two different mechanisms associated with the increased stiffness occurring in the perilesional and CRC ECM, such as increased vascularization in the perilesional area and increased content of hydroxylysine in the CRC ECM.

Methods

Patients and tissue specimens.

Patients that underwent colon surgical resection at Ospedale San Raffaele (Milan, Italy) were included in this study. Matched specimens were collected from the left colon of patients undergoing resection surgery for sporadic CRC and obtained through the Unit of Surgical Pathology (Ospedale San Raffaele, Milan, Italy). All patients that participated in this study provided written informed consent. All experimental protocols were approved by the Institutional Review Board (Authorization protocol 279/DG, Ethic Committee Ospedale San Raffaele, Milan, Italy), and all methods were carried out in accordance with the approved guidelines. All mucosa specimens encompassed the luminal surface, mucosa and upper submucosa. Neoplastic, peritumoral and healthy areas were collected from fresh and unfixed surgical specimen within one hour after surgery.

Neoplastic tissue was obtained at the edge of infiltrating neoplasia, and healthy colon mucosa was from the resection margins (>10 cm far from the CRC).

We classified perilesional tissue based on lack of epithelial dysplasia, mild architectural abnormalities and blood vessels with elongated and dilated shape. All the perilesional areas used in the study were in a range of 0.5–1 cm far from the edge of the neoplastic lesion.

Each specimen was divided in two parts for evaluation of histology and preparation of ECM.

Histological report with tumor histotype, staging and grading was performed by pathologists on the original surgical specimen (Supplementary Material 1) according to TNM Classification of Malignant Tumours, 7th Edition (2009).

ECM purification and protein identification using nanoLiquid-Chromatography MS/MS.

Tissues were collected from paired healthy colon, perilesional area and CRC, and tissue-derived ECM prepared as previously described[15]. ECMs were weighed, cut in small pieces and dissolved (1/5 weight/volume) in a buffer containing 5 M urea, 2M thiourea, 2% CHAPS, 2% Zwittergent and 10 μl/ml protease inhibitors using a plastic potter. After 24 h shaking at 1400 rpm at room temperature, the samples were centrifuged at 14000 rpm at 4 °C for 15 minutes. The recovered supernatant was analyzed to determine total protein concentration using BioRad protein assay and BSA as standard. Forty μg of total protein from each sample were in-solution digested using Filter Aided Sample Preparation (FASP) protocol as reported in literature[16]. Samples were desalted using Stage tips C18 columns (ThermoScientific) and injected in a capillary chromatographic system (EasyLC, Proxeon Biosystem). Peptide separations occurred on a home-made 25 cm reverse phase spraying fused silica capillary column, packed with 3-μm ReproSil 120 Å C18 AQ. A gradient of eluents A (pure water with 2% v/v ACN, 0.5% v/v acetic acid) and B (ACN with 20% v/v pure water with 0.5% v/v acetic acid) was used to achieve separation (0.15 μL/min flow rate) (from 10 to 35% B in 230 minutes, from 35 to 50% B in 5 minutes and from 50 to 70% B in 30 minutes). MS analysis was performed using an LTQ-Orbitrap mass spectrometer (ThermoScientific) equipped with a nanoelectrospray ion source (Proxeon Biosystems). Full scan mass spectra were acquired with the lock-mass option and resolution set to 60,000. The acquisition mass range for each sample was from m/z 300 to 1750 Da. The ten most intense doubly and triply charged ions were selected and fragmented in the ion trap using normalized collision energy 37%. Target ions already selected for the MS/MS were dynamically excluded for 120 seconds. All MS/MS samples were analyzed using Mascot (v.2.2.07, Matrix Science, London, UK) search engine to search the UniProt_ Human Complete Proteome_ cp_hum_2015_01. Searches were performed with trypsin specificity, two missed cleavages allowed, cysteine carbamidomethylation as fixed modification, acetylation at protein N-terminus, oxidation of methionine and lysine as variable modifications. Mass tolerance was set to 5 ppm and 0.6 Da for precursor and fragment ions, respectively. To quantify proteins, the raw data were loaded into the MaxQuant[17] software version 1.3.0.5: label-free protein quantification was based on the intensities of precursors, both as protein intensities and normalized protein intensities (LFQ intensities). Peptides and proteins were accepted with a FDR less than 1%, two minimum peptides per protein with one unique. The experiments were performed in technical triplicates, with technical reproducibility among replicates (both as number of unique peptides and LFQ intensities for each protein) >0.98. The proteins identified by proteomic analysis were compared to the "*Total Human*

Matrisome" database (http://web.mit.edu/hyneslab/matrisome/)[18] in October 2013, when the database comprised 1065 genes coding for human proteins in the extra-cellular matrix.

Histological and immunohistochemistry analysis. Cells and nuclei in the tissues and ECMs were evaluated by hematoxylin-eosin, and cellular antigens (Tenascin and ER-b) by immunohistochemistry, as reported[15,19]. Antibody against ER-b receptor was the clone EME02 (Novocastra, Leica Biosystems Newcastle, UK), as reported[20]. Goat anti-human Matrilin-2 Ab was the clone 3044-MN from, R&D Systems (MN, USA). Mouse monoclonal anti-tenascin Ab (clone ab58954) and rabbit monoclonal anti-LOX (clone EPR4025) were from Abcam; anti-CD34 mAb (clone QBEnd/10 from Ventana Medical Systems, Arizona, USA) was used for blood vessels. Number and width of capillaries were measured by using the plug-in "cell counter" and the function "measure" in the Image J software (version 1.5)[21] on high magnification images.

Western blot. Tissues and ECMs were weighed, cut in small pieces and dissolved (1/5 weight/volume) in a buffer containing 5 M urea, 2 M thiourea, 2% CHAPS, 2% Zwittergent and 10 µl/ml protease inhibitors using a plastic potter. After 24 h shaking at 1400 rpm at room temperature, the samples were centrifuged at 14000 rpm at 4 °C for 15 minutes. From recovered supernatant the buffer was exchanged against PBS by using the Amicon Ultra-0.5 ml device (Merck Millipore, Darmstadt, Germany), and total protein concentration estimated using BioRad protein assay and BSA as standard.

Level of Matrilin-2 expression was evaluated in pair-wised ECMs and tissues; 20 µg of ECM and 50 µg of tissue lysates were loaded onto 8% SDS-PAGE and Matrilin-2 revealed by goat-anti human Matrilin-2 (clone 3044-MN, R&D Systems, MN, USA).

Level of LOX expression was evaluated in pair-wised ECMs. Fifteen µg of lysate were loaded onto 12% SDS-PAGE and LOX revealed by mouse monoclonal anti lysyl oxidase Ab (clone 8G5, Lifespan Biosciences, Seattle WA, USA). Mouse monoclonal anti-collagen III antibody (clone FH-7A) was from Abcam.

Nanoindentation measurements by atomic force microscopy (AFM). The AFM analysis was carried out on ECMs derived from healthy colon, perilesional area and CRC of three patients. ECMs were grossly dried and attached to glass coverslips (diameter 15 mm) by means of a thin bi-adhesive tape. ECMs were then attached to the bottom of Petri dishes (Greiner Bio-One) and left overnight in an evacuated desiccator in order to dry out and improve spreading and adhesion on the substrate. Prior to AFM measurements, the Petri dish hosting the ECM sample was filled with PBS buffer and the ECM was allowed to rehydrate for 30 minutes at room temperature. Measurements were carried out at room temperature. Hydration-dehydration processes could in principle modify the pristine rigidity of ECMs; with this in mind, we have strictly followed the same protocol for the preparation of each ECM sample, in order to be sure that the results obtained on different samples could be compared.

For the measurement of the Young's modulus of ECM samples, a Bioscope Catalyst AFM (Bruker) was used to collect series of force vs distance curves[22,23]. We have used monolithic borosilicate glass probes consisting in micrometer-sized spherical glass beads with radius R = 8–10 µm attached to silicon cantilevers with force constant k = 0.2–0.3 N/m. Probes were produced according to an established custom protocol[24]. The probes' diameter was chosen in order to have a reliable and robust mechanical readout, capturing the overall elastic behavior of ECM on a scale comparable to the size of its characteristic micro-structural domains, as observed in scanning electron microscopy images reported in this manuscript.

Each set of force curves (a force volume) consisted of a 16 × 16 array of curves acquired on a 70µm × 70μm area. Ten force volumes were typically recorded on each ECM sample, on macroscopically separated regions, with the exception of patient #1, where only a few hundreds force curves were acquired as a preliminary test.

All the measurements were performed with the following parameters: 4096 points per curve, ramp length L = 10 µm, maximum applied force F = 60–70 nN, and ramp frequency f = 1.1 Hz. Typically, indentations up to 2–3 µm were obtained. Data processing of force volumes was carried out in Matlab environment according to the published protocol[23]. The values of the Young's modulus were extracted by fitting the Hertz model to each indentation curve. A first very soft indentation region (0–35% of total indentation) was excluded, in order to separate the possible contribution of loosely-bound superficial layers.

The cumulative distributions of Young's modulus values of the ECMs from the three donors turned out to be the envelop of several nearly lognormal modes, representing the major contributions to the overall ECM rigidity and originating from micro-scale domains that the AFM probe was able to resolve. Multi-Gaussian fit in semi-log10 scale allowed identifying the peak value E' and the geometric standard deviation σ_g^{10} of each lognormal mode; from these values the median value E_{med} and the standard deviation of the median σ_{med} were evaluated for all modes[25] as

$$\mathrm{E}_{\mathrm{med}} = 10^{E'} \text{ and } \sigma_{\mathrm{med}} = \sqrt{\pi/2}\,\mathrm{E}_{\mathrm{med}}\sigma_g^{10}/\sqrt{N}. \tag{1}$$

N being the number of force curves in each mode (typically N = 1000–2000). The effective rigidity of each ECM sample was characterized by the weighted average of median values

$$\mathrm{E} = \sum_i f_i E_{med,i}, \tag{2}$$

using the fraction $f = N/N_{tot}$ of force curves in the mode as weight; the total error σ_E associated to E was calculated by summing in quadrature the propagated error of the medians

$$\sigma = \sqrt{\sum_i f_i^2 \, \sigma_{med,i}^2} \tag{3}$$

and an effective instrumental relative error

$$\sigma_{\text{instr}} = 4.4\%\text{: } \sigma_E = \sqrt{\sigma_{instrum}^2 E^2 + \sigma^2}\,. \tag{4}$$

The average median values of the Young's modulus of the healthy, perilesional and CRC ECM of all donors have also been evaluated; the corresponding error has been calculated as the standard deviation of the mean.

Collagen and crosslinking. ECM was hydrolysed in 1 ml of 6 M HCl for 20 h at 110 °C, and the acid lysate added of internal standard control and assayed for hydroxyproline content by HPLC (Hydroxyproline reagent kit #195–9501, Biorad); the amount of collagen was estimated based on the level of hydroxyproline accounting for 13.5% of the collagen amino acid composition[26]. Hydroxylysylpyridinoline (HP) and Lysylpyridinoline (LP) were measured by HPLC, in ECM hydrolised in 0.5 ml of 6 M HCl for 20 h at 110 °C, and added of internal standard (Crosslinks, pyridinolin and deoxypyridinolin kit, Chromsystem kit #48000).

Scanning electron microscopy. Pair-wised tissues were collected from CRC patients, selecting areas of mucosa, submucosa, muscularis propria and subserosa from healthy colon and neoplasia. Pieces of tissue were obtained by performing punch biopsy using a sterile cork borer into tissue, producing a cylindrical core of tissue (2 mm diameter and 5 mm length). ECMs were prepared as previously described[15]. Briefly, ECM were fixed with 2.5% glutaraldehyde (25% solution, electron microscopy grade) in PBS for 24 hours, then dewaxed, dehydrated in an ascending degree of ethanol (10–25–50–75–90–100%) and dried overnight in hexamethyldisilizane. ECMs were coated with gold-palladium after evaporation of hexamethyldisilizane and examined in a Leica S420 scanning electron microscopy.

Three researchers (M.N, R.A., and P.Z.) independently evaluated electron micrographs. Number and width of capillaries were estimated by using the plug-in "cell counter" and the function "measure" in the Image J software (version 1.5)[21]; 3 electron micrographs were evaluated for each donor. Fibrils width and degree of organization of fibrils (anisotropy) were estimated by using the function "measure" and the plug-in FibrilTool[27] in the Image J software; 3 electron micrographs were evaluated for each donor. Anisotropy was measured on the entire area of electron micrographs, in order to avoid any bias due to the selection of areas excluding or over-representing certain fibers in the outputs. The degree of alignment of fibrils in pair-wised ECMs was estimated on images with the same magnification.

Statistical analysis and data mining. Three to 10 surgical specimens were used for each investigative technique, and from each specimen paired healthy-perilesional-tumor area were used. Sample size for each investigative technique is reported in Supplementary Material 1. Difference among groups was evaluated by using ANOVA followed by post-test analysis. MeV software (version 4_9_0)[28] was used for data from proteomic analysis to generate hierarchical clustering heat-map. Data mining was performed using Ingenuity Pathway Analysis (IPA)[29].

Results

Morphology of healthy colon, perilesional area and CRC tissue. Healthy colon mucosa came from the resection margins and was >10 cm from the CRC, whereas the neoplastic tissue was obtained at the edge of the infiltrating neoplasia. The choice of perilesional tissue was based on the lack of epithelial dysplasia, mild architectural abnormalities, and blood vessels with elongated and dilated shape and in a range of 0.5–1 cm from the edge of the neoplastic lesion.

Hematoxylin-eosin staining (Fig. 1A), the size and shape of blood vessels (Fig. 1B) and collagen distribution (Fig. 1C) were used to establish morphology of surgical specimens (Supplementary Material 1).

The left colon from the resection margin showed normal architecture, a homogeneous distribution of blood vessels, homogeneous size and distribution of crypts and short wavy bundles of collagen fibres.

Compared to healthy tissue, perilesional mucosa showed mild hyperplastic crypts, increased thickness of the lamina propria and an increased number of blood vessels of larger size (median number of capillaries for 100 crypts was 16 vs 38, and median capillary width of 13 vs 35 μm in the healthy colon mucosa vs peritumoral tissue, Supplementary Fig. S1), associated with straight bundles of collagen fibres in the submucosa. Colorectal carcinoma was characterized by neoplastic glands infiltrating desmoplastic stroma, disorganized architecture, and increased number of enlarged (Supplementary Fig. S1) ectatic vessels and collagen fibres organized in thick straight bundles.

Differential composition of core matrisome and matrix-associated components in CRC but not perilesional ECM. To assess whether modification of tissue architecture was caused by different protein composition a quantitative proteomic analysis was performed on ECM purified from 5 pairwised tissues obtained from CRC patients (Supplementary Material 1). A total of 1139 non-redundant proteins were measured among the three types of ECMs (Supplementary Material 2.1). Based on the human matrisome database[18], 128 proteins out of 1139 were ascribed to the human matrisome, with 76 proteins belonging to the core matrisome (Fig. 2A) and 52 proteins being matrix-associated components (Fig. 2B). In the core matrisome group we identified 12 proteoglycans, 18 collagens and 46 glycoproteins out of 36 proteoglycans, 45 collagens and 200 glycoprotiens reported in the human matrisome database (red circles in Fig. 2A, and Supplementary Material 2.2 and 2.3). In the matrix-associated components we identified 16 ECM-affiliated components out of 176, 24 ECM regulators

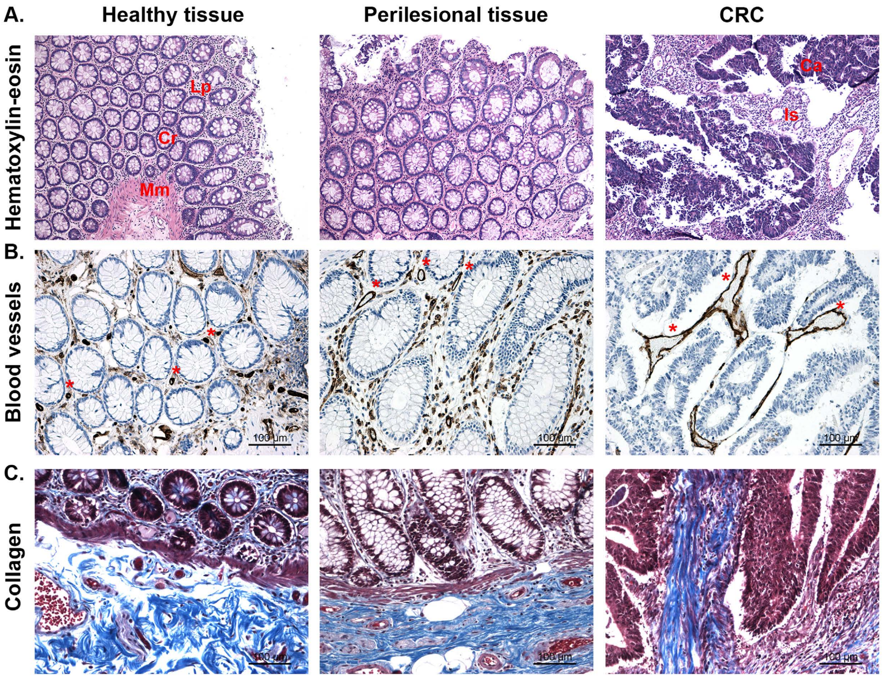

Figure 1. Tissue selection. Pair-wised healthy colon, perilesional area and CRC were evaluated by means of hematoxylin-eosin staining (**A**), CD34+ blood vessels (**B**) and collagen (blue staining) by means of Masson Trichrome stain (**C**). Cr; cryptae. Lp; lamina propria. Mm; muscularis mucosae. Ca; carcinoma. Is; intratumoral stroma. *blood vessels. Pictures are representative of pair-wised tissues from one of the six patients tested and listed in Supplementary Material 1.

out of 254, and 12 secreted factors out of 353 reported in the human matrisome database (red circles in Fig. 2B and Supplementary Material 2.2 and 2.3).

Unsupervised hierarchical clustering of the 128 ECM proteins showed dysregulation of ECM composition in the CRC-ECM (13 core matrisome and 1 matrix affiliated protein, $p < 0.01$) vs. the healthy and perilesional ECM, while the healthy vs perilesional ECMs showed no difference (Fig. 2C and Supplementary Material 2.4).

CRC ECM was characterized by a down-modulation of i) basal membrane proteins such as Laminin subunit beta-2 and Nidogen-1, and ii) interstitial matrix proteins (Matrilin-2, full-lenght and isoform 4 of Collagen 6A3, and Mimecan), for some of which (Decorin and Dermatopontin) anti-proliferative activity was previously demonstrated (described in section 4 of Supplementary Material 1). Six interstitial matrix proteins (Fibronectin, Collagen 12A1, Fibulin-1, Galectin-3, Microfibrillar associated protein-2 and Tenascin) were over-expressed in the CRC ECM. A drastic shift in the ratio between collagen 12A1 and collagen 6A3 was observed, with 50–200 fold accumulation of collagen 12 vs collagen 6 in the CRC ECM (Fig. 2D).

To confirm the differential expression of proteins identified by the proteomic analysis, representative down and up modulated proteins such as Matrilin-2 and Tenascin were evaluated on pair-wised samples. Decreased level of Matrilin-2 in CRC, but not in the perilesional area, was confirmed in both ECMs and tissues by western blot (Fig. 2E) and immunohistochemistry (Fig. 2F) analysis. Increased level of Tenascin in CRC was confirmed by immunohistochemistry analysis of ECMs (Fig. 2G).

Other proteins not reported in the matrisome database were also identified in the ECMs. Tumoral antigens (eg, CEACAM5 and OCIAD2) and tumor-associated proteins CD97 were present and overexpressed in the CRC ECM ($p < 0.01$) and, as for the matrisome proteins, no difference was observed between healthy and perilesional ECMs. In addition, two tumor-associated proteins FAP (fibroblast activation protein/seprase) and DPEP1 (dipeptidase 1) were absent from healthy and perilesional ECM (Supplementary Material 2.5).

An Ingenuity Pathway Analysis (IPA) based on all dysregulated proteins (Supplementary Material 2.6) identified mono-(2-ethylhexyl)phthalate ($p = 10^{-7}$) and beta-estradiol ($p = 10^{-5}$) as the top and activated upstream regulators that could explain the observed differences. The oestrogen pathway was validated on surgical specimens for the expression of estradiol receptor-beta (ER-β). As reported[20,30,31], the neoplastic tissue was characterized by i) low numbers of epithelial cells expressing ER-β and ii) low intensity of ER-β, whereas all epithelial cells in the healthy and perilesional tissue were positive for ER-β (Supplementary Fig. S2). All stromal cells expressed ER-β irrespectively of their localization in the healthy tissue, peritumoral area or CRC, with comparable level of ER-β expression (Supplementary Fig. S2).

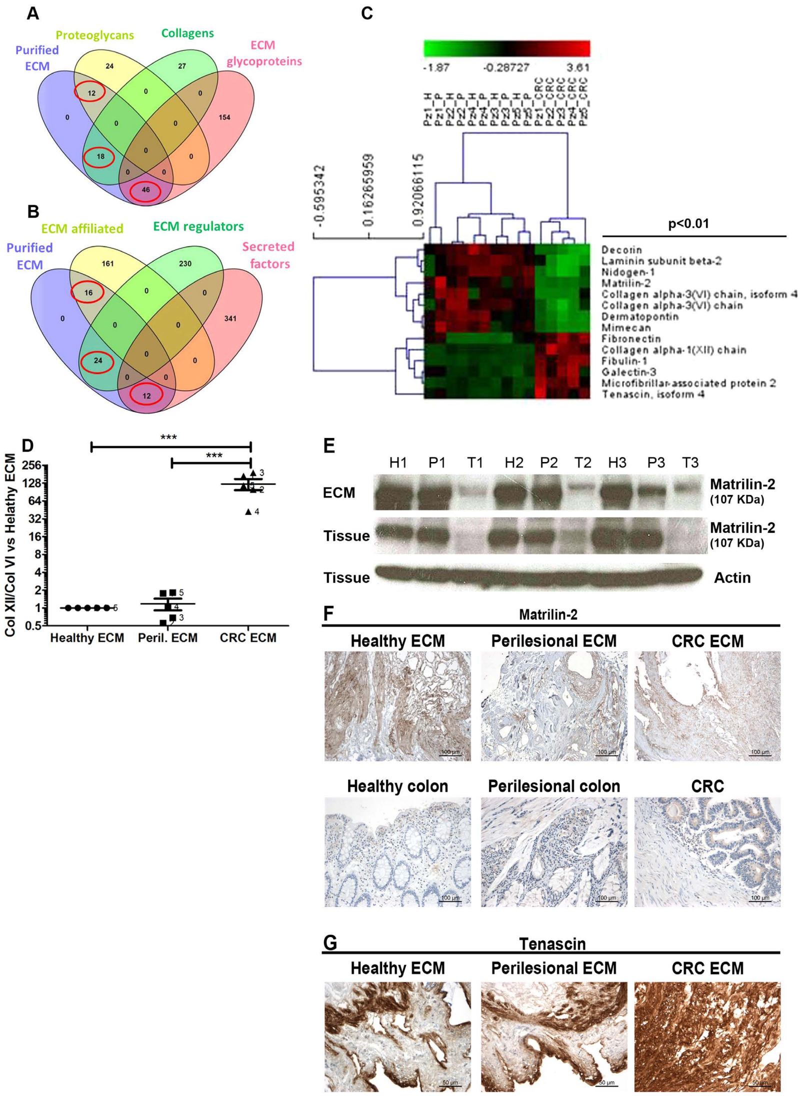

Figure 2. Protein composition of ECMs. ECM was purified from pair-wised colon resection margins (healthy, H), perilesional areas (P) and colorectal carcinomas (CRC) from 5 patients listed in Supplementary Material 1, and proteomic analysis was performed as described in Methods. Comparison of purified ECMs (purple ellipse in the Venn's diagrams) with the matrisome database[18] revealed identification of 128 matrisome proteins; 76 structural components (12 proteoglycans, 18 collagens and 46 ECM glycoproteins, as highlighted by red circles in panel (**A**) and 52 matrix-associated components (16 ECM affiliated, 24 ECM regulators and 12 Secreted factors, as highlighted by red circles in panel (**B**) such as i) ECM-affiliated, as annexin, mucin, complement, calcium binding proteins S100; ii) ECM-regulators, as metallo-proteases, metallo-protease inhibitors; iii) Secreted factors bound to ECM, as latent TGF-b, growth factors, chemokines. Unsupervised hierarchical cluster analysis of LFQ intensities as derived from MaxQuant elaboration (Suppl. file 2.1) was performed upon parametric ANOVA test: the heatmap shows significantly differentially expressed ECM proteins with p-value < 0.01 (**C**). The ratio between collagen XII and the sum of the two forms of collagen VI reported in the above heat-map was estimated in all 5 ECMs and fold of expression was calculated vs healthy ECM (**D**). Western blot analysis for Matrilin-2 expression in ECMs and tissues from 3 surgical specimens; level of actin expression in tissue was used as loading control (**E**). Expression of Matrilin-2 was further evaluated by IHC, in pair-wised ECMs (one representative patient is shown) (**F**). Expression of Tenascin was evaluated by IHC (pair-wised tissues from one representative patient are shown) (**G**). (**H**) P and T in panel C and panel E indicate healthy, perilesional and tumor area, respectively. P value in panel C and asterisks in panel D indicate statistical significance.

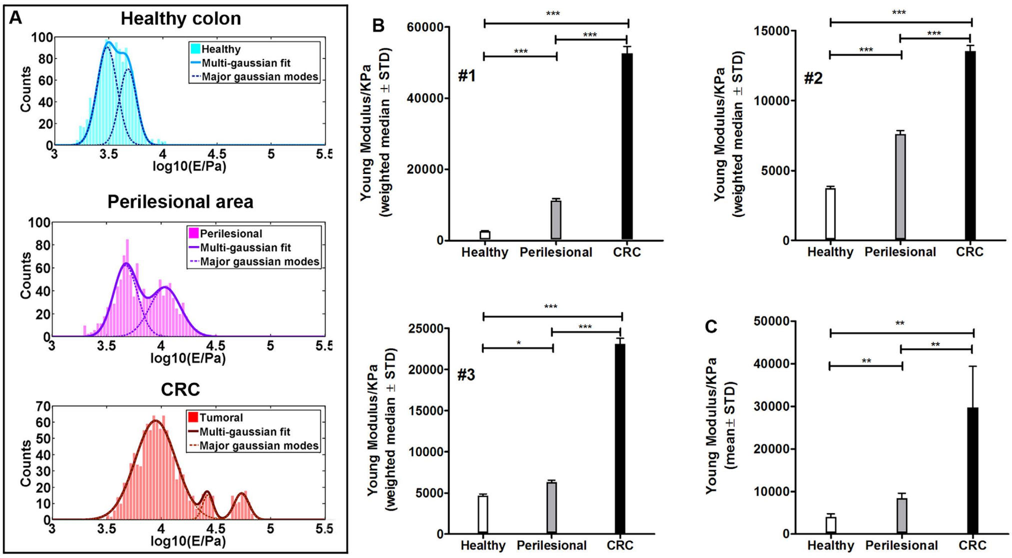

Figure 3. Elastic Young's modulus of ECM from healthy, perilesional and CRC area. Cumulative distributions of Young's modulus (E) values in Pa units (semilog10 scale) of the three ECMs derived from 1 representative patient (out of 3 tested and listed in the Supplementary Material 1; multi-gaussian fit representative of the cumulative distribution (solid line) and the contribution of major Gaussian modes (dotted line) were estimated (**A**). Median value for each ECM was estimated by weighting the relative contribution of each mode, and showed for all 3 donors (**B**). Mean value of Young's modulus of healthy, perilesional and CRC ECM (**C**). Error bars are calculated as standard deviation of the median. Statistical significance was evaluated by means of ANOVA followed by Tukey post-test analysis. E; elasticity. Pa; pascal.

Gradient of increasing stiffness in healthy to perilesional and colorectal carcinoma extracellular matrix. Despite the perilesional area is showing altered architecture and its ECM is susceptible to infiltration by invasive cancer cells[15], the perilesional ECM components, the amount of FAP bound to the ECM and the number of ER-β+ cells did not differ from the healthy environment. Thus, the physical feature of the ECM was assessed. Stiffness of the ECM derived from the healthy colon, perilesional area and CRC of three donors was measured by atomic force microscopy (AFM) indentation measurements. Broad distributions of the elastic modulus values (Fig. 3A, solid line) was represented by major modes contributing to the cumulative distribution (Fig. 3A, dotted line), suggesting a strong diversity of elastic properties within the same sample. A remarkable overlap of some of the major modes within ECM was always present, although the relative contribution of single modes to the cumulative stiffness was different in the healthy, perilesional and CRC ECM. To take in account the relative contribution of each modes a weighted median was estimated for each ECM (Fig. 3B). Indeed, a common trend was observed for all patients, showing a softer healthy ECM and a stiffer tumoral one, with the perilesional ECM sharing features with both healthy and tumoral cases (Fig. 3C and Supplementary Fig. S3).

The average median value of the Young's modulus of ECMs from different regions shows similar pattern in each donor. This suggests that, even within the large patient-to-patient and even tissue-to-tissue variability, there are common characteristics related to the physio-pathological state of the tissues that are statistically conserved. Indentation measurements were thus representative of the collective contributions of nanoscale molecular components organized in micrometer-sized structural and functional domains in the ECMs; adjusting the probe diameter[23,24] to the size of these domains allowed detecting and resolving ECMs mechanical responses, monitoring them in relation to the degree of pathology progression.

Gradient of increasing collagen crosslinking in healthy, perilesional and colorectal carcinoma extracellular matrix. In order to investigate the steady increase of ECM stiffness, independent of protein composition, post-translational modifications of the ECM such as collagen crosslinking was assessed. We measured hydroxylysyl-pyridinoline (HP) and lysyl-pyridinoline (LP) crosslinking, which are formed from oxidative de-amination of hydroxylysine and lysine, respectively, upon the action of the lysyl oxidase (LOX) in the presence of oxygen[32].

An enhanced amount of crosslinking was present in the perilesional vs healthy ECM, and this increase was even more substantial in the CRC ECM (Fig. 4A). The ratio between HP and LP was identical for healthy and perilesional ECM and ca. 2 times greater in CRC (Fig. 4B). Comparable HP/LP ratios in healthy and perilesional ECMs confirmed findings from proteomic analysis, suggesting that both ECMs show similar protein composition, primary structure and post-transcriptional modification. On the other hand, the increased HP/

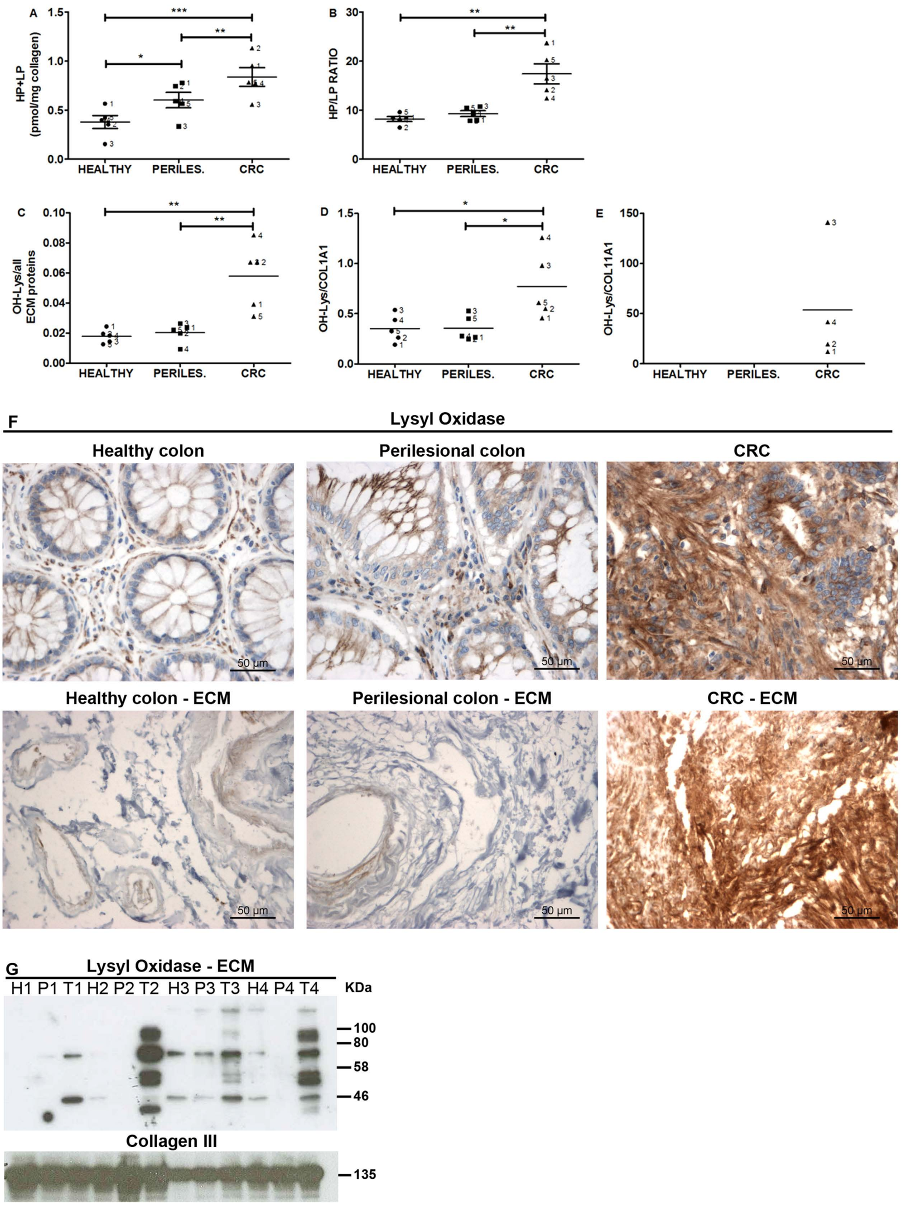

Figure 4. Level of collagen crosslinking, OH-Lys content of ECM proteins and lysyl oxidase in healthy, perilesional area and CRC ECMs. Pair-wised ECMs from tissue of 5 donors (Supplementary Material 1) were evaluated for the content of collagen crosslinking HP and LP (**A**) and the ratio between HP/LP (**B**). Level of OH-lysine was estimated for all ECM proteins: sum of peak intensities, as estimated by MaxQuant software, for all OH-lysine-containing peptides was normalized to sum of ECM protein intensities in each ECM derived from 5 patients (Supplementary Material 2.7) (**C**). Sum of peak intensities, as estimated by MaxQuant software, for all OH-lysine-containing peptides was normalized to each protein intensity in each ECM derived from 5 patients (Supplementary Material 2.8) (**D**, Collagen 1A1; (**E**), Collagen 11A1). Asterisks indicate statistical significance evaluated by means of ANOVA. Immunohistochemistry (40× magnification) of LOX on pair-wised tissues (healthy colon, perilesional area and CRC) and the derived ECMs; data from one representative surgical sample out of 4 tested (**F**). Level of lysyl oxidase was evaluated by western blot using pair-wised ECMs from 4 donors (**G**); the molecular masses (kDa) are indicated on the right side of the panel. H, P and T in panel G indicate that ECM was isolated from pair-wised healthy, perilesional and tumor area, respectively, from 4 different surgical specimens.

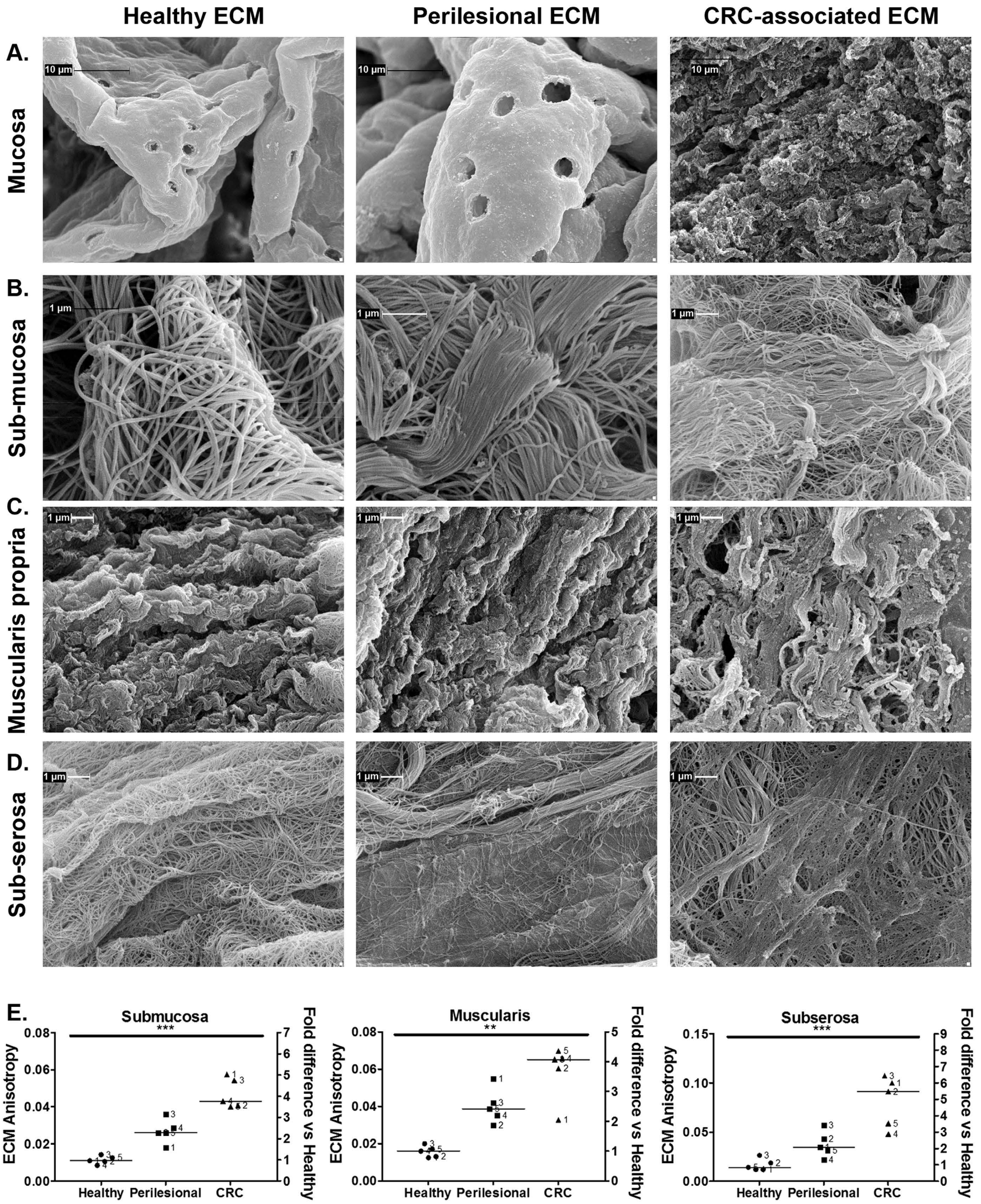
Healthy ECM
Perilesional ECM
CRC-associated ECM
A.
Mucosa
10 µm
B.
Sub-mucosa
1 µm
C.
Muscularis propria
D.
Sub-serosa
E.
Submucosa
***
Muscularis
**
Subserosa
ECM Anisotropy
Fold difference vs Healthy
0.00
0.02
0.04
0.06
0.08
0.05
0.10
0.15
0
1
2
3
4
5
6
7
8
9
Healthy
Perilesional
CRC

Figure 5. Ultrastructural analysis of ECMs. ECMs from mucosa (**A**), submucosa (**B**), muscularis propria (**C**) and subserosa (**D**) of pair-wised healthy colon, perilesional area and CRC were evaluated by means of scanning electron microscopy. Lower magnifications are reported in the Supplementary Fig. S5. Pictures show ultrastructure of pair-wised ECMs from one representative patient (#2 listed in Supplementary Material 1). Degree of organization of fibrils (anisotropy) was evaluated in pair-wised ECMs from 5 donors (**E**); horizontal bars indicate median value, and asterisks show statistical significance evaluated by means of Anova. Representative scanning electron micrographs used for establishing anisotropy are reported in the Supplementary Fig. S6.

LP ratio in the CRC ECM (Fig. 4B) was associated with an increased level of hydroxylated lysine (Fig. 4C and Supplementary Material 2.7), and among all ECM proteins carrying hydroxylated lysine (Supplementary Material 2.8 and Supplementary Fig. S4) only COL1A1 showed increased content of hydroxylated lysine vs healthy and perilesional ECMs (Fig. 4D). Moreover, COL11A1 with a high level of OH-Lys was expressed only in CRC ECM (Fig. 4E), in agreement with a report showing COL11A1 to be produced by cancer-associated myofibroblasts and not expressed in the healthy colon[33].

Among collagens, the fibrillar collagen-I is the main substrate for LOX[10], inducing post-translational modification of hydroxylysine and lysine. To address the increased amount of HP crosslinking with the increased amount of OH-Lysine content in collagen-I, we evaluated distribution and level of expression of LOX. The extracellular enzyme LOX was detected both in the tissues and ECMs by IHC. Distribution and level of expression of LOX was similar between healthy colon and perilesional tissue, and a drastic increase was evident in the CRC; similar profile was evident in the derived ECMs (Fig. 4F). Comparable level of LOX expression between healthy colon and perilesional ECMs, and increased amount of LOX associated to the CRC ECM was also confirmed by western blot analysis (Fig. 4G). This finding was in agreement with previous report[18]. Moreover, different forms of LOX were evident from the western blot analysis, corresponding to the non-glycosylated LOX (molecular weight 47 kDa) and the glycosylated forms (upper bands at 54 and 57 kDa), as already described[34].

Ultrastructural analysis of human colon layers ECM. Scanning electron microscopy was used to establish how the biochemical composition and physical modifications were associated with ECM ultrastructure of colon mucosa. The same analysis was further extended to the underlying tissue layers, such as muscularis propria and subserosa.

In the ECM derived from healthy mucosa, regular morphology of crypts with homogeneous distribution, honeycomb-like shape and size (50–80 μm width) of empty crypts and homogeneous thickness of the lamina propria between crypts was observed. In the lamina propria of healthy ECM "holes" left from the removal of endothelial cells (i.e., capillaries) were present (Fig. 5A and Supplementary Fig. S5A). Perilesional mucosa ECM showed an irregular topography of lamina propria, highlighting the heterogeneous shape and diameter of crypts (Fig. 5A and Supplementary Fig. S5A). In addition, the lamina propria of perilesional ECM was characterized by an increased number of capillaries (262 ± 14 vs. 146 ± 16 per mm^2, ECMs from 3 different surgical specimens, $p = 0.002$) and increased capillary width (5.3 ± 0.1 vs. 2.9 ± 0.05 μm, $n = 3$ for a total of 146 capillaries, $p = 0.0001$) (Fig. 5A and Supplementary Fig. S5A) compared to healthy ECM, with a fold of increase of 1.8 in agreement with the fold of increase observed by immunohistochemical analysis of tissues (Supplementary Fig. S1). Mucosa associated with CRC ECM was characterized by an irregular and indistinct morphology (Fig. 5A and Supplementary Fig. S5A); dilated/ectatic vessels in the CRC ECM were not evaluated because not distinguishable from empty spaces present in the neoplastic stroma.

In the submucosa of healthy and perilesional ECM, morphology with a wavy pattern was observed (Fig. 5B and Supplementary Fig. S5B). Both healthy and perilesional ECMs were constituted by thousands of fibers, though organization and thickness were very different. Fibrils in healthy ECM (Fig. 5B) mainly intersected each other to form a random network. The random network of relaxed and crosslinked fibrils in the healthy ECM become progressively linearized in the perilesional ECM, forming tight and organized in bundles (Fig. 5B). Submucosa ECM associated with CRC was characterized by a loss of tissue morphology, as reported for human adenocarcinoma[35], with fibrils organized in tight bundles and thinner than that observed in the healthy and perilesional ECM (Fig. 5B and Supplementary Fig. S5B) (fibrils width; 40 ± 8 vs 90 ± 26 nm, $p < 0.0001$, 52 measurements in pair-wised ECMs from 3 donors).

The ECM from the healthy colon muscularis propria showed a structure with a regular morphology of crests and clefts and a well-oriented direction of fibers constituted by parallel fibrils organized in intertwisted bundles (Fig. 5C and Supplementary Fig. S5C). Crests and clefts were less evident in the perilesional muscularis propria ECM due to fibrils being condensed in a denser matrix (Fig. 5C and Supplementary Fig. S5C). Loss of organized bundles and architecture was evident in the CRC-associated muscularis propria ECM, with the fibrils organized to form a heterogeneous structure characterized by irregular spaces (Fig. 5C and Supplementary Fig. S5C).

The healthy subserosa ECM was composed of many homogeneous and well-separated fibrils forming a mesh with regular spaces in the network (Fig. 5D and Supplementary Fig. S5D). In the perilesional subserosa ECM fibrils were of the same width as in the healthy ECM (60 ± 0.9 vs 62 ± 1.3 nm) but were linearized and mainly organized in bundles (Fig. 5D and Supplementary Fig. S5D). In the CRC-associated subserosa ECM fibrils were thinner (55 ± 1.2 nm, $p < 0.001$ vs healthy and perilesional), linearized and mainly organized to form a mesh of heterogeneous structure, characterized by irregular spaces among the bundles (Fig. 5D and Supplementary Fig. S5D).

The ultrastructural modifications were quantified by assessing the degree of alignment of fibrils (anisotropy). Increased anisotropy was observed in both perilesional and CRC ECMs vs healthy ECM, and the gradient was common to the submucosa, muscularis propria and subserosa (Fig. 5E).

Discussion

We recently reported that perilesional, but not healthy, ECM supports cell invasion[15]. This study provides an in-depth investigation of both physical and biochemical features of healthy, perilesional and neoplastic ECMs and identifies stiffness and crosslinking of the perilesional ECM as the main parameters associated with infiltration of cancer cells (Table 1). In agreement with the gradient of stiffness and amount of crosslinking from healthy to perilesional and CRC area, we also report a gradient in the modification of the ultrastructure characterized by increased degree of fibril organization and disorganized architecture common to all colon tissue layers. Moreover, the broad distribution of the elastic modulus reflected ultrastructural changes in the perilesional and CRC areas indicating that nanomechanical measurements using colloidal probes[22,23] may potentially be a predictive tool for assessing the modification of ultrastructural changes associated with CRC progression.

	PERILESIONAL	CRC
Morphology	Irregular	Loss of morphology
Ultrastructure	Organized and linearized	Fibrils fused in tight bundles
Anisotropy	Increased (2×)	Increased (4×)
Vascularization	Increased (2×)	Ectatic vessels
Stiffness	Increased (2.5×)	Increased (9.4×)
Proteomic	No difference	Different, and increased OH-Lys
Crosslinking	Increased (1.5×)	Increased (2×), with 2× increased HP/LP ratio
Cell proliferation[15]	Increased	Increased
Cell apoptosis[15]	As in healthy	Delayed
Invasion[15]	Present	Present

Table 1. Modification of the features of perilesional and CRC ECMs vs healthy ECM. Fold difference vs healthy ECM was calculated using median values. Cell proliferation, apoptosis and invasion by metastatic cells seeded on healthy colon, perilesional and CRC derived ECM was recently reported[15].

In the CRC we confirmed the modulation of the oestrogen pathway at the level of neoplastic cells and the presence of a poorly organized vascular network[35] composed by ectatic vessels, previously reported to be associated with a hypoxic condition[35–37]. Analysis of ECM protein content confirmed the invasive pattern of CRC, as previously described on tissues (down-modulated decorin[38,39], nidogen-1[40], laminin subunit beta-2[40–42], dermatopontin[43], mimecan[44] and up-modulated fibronectin[45], tenascin[46] and collagen 12[9,47]).

Lysyl oxidase (LOX) in the presence of oxygen catalyzes an oxidative de-amination of lysine and hydroxylysine residues, spontaneously condensing to form LP and HP crosslinks in collagen and elastin[32]. In line with our data, the increased stiffness of tissues has previously been correlated with an enhanced i) amount of lysine-derived crosslinks and ii) HP/LP ratio[48–50], and an increased level of HP was associated with irreversible fibrosis[51]. We also detected an increased level of LOX in the CRC ECM, previously reported to be enhanced in hypoxic environments[52,53]. Concomitantly the CRC ECM was also highly enriched in LOX substrate[10] as revealed by the increased amount of OH-lysine content in in COL1A1.

Neoplasia-associated ECM was deeply re-arranged in terms of both biochemical and physical features. The physical and biochemical diversity of CRC ECM was evident from the formation of bundles composed by linearized and organized fibrils, the increased stiffness and number of collagen crosslinking, change in the matrisome composition and an increased hydroxylation of lysine. In this study we associate the modified ultrastructure and increased stiffness of CRC desmoplastic stroma to the i) enhanced amount of OH-Lysine-derived hydroxylysyl-pyridinoline (HP) crosslinking, and ii) dys-regulated composition of ECM.

The perilesional area of CRC has been described as a histologically normal appearing epithelium with elongated crypts, with thicker lamina propria than normal mucosa and the presence of vessels with elongated and dilated shape[35].

We confirm the increased vascular density and wider capillary diameter in the perilesional mucosa, despite the fact that tumor-associated pathways were absent in the perilesional ECM (eg, decreased number of ER-β+ epithelial cells, dysmodulation of ECM proteins, CEACAM5, OCIAD2 and FAP bound to neoplastic ECM). Compared to the healthy ECM, perilesional ECM was characterized by increased vascularization, linearized fibrils organized in bundles and increased crosslinking and stiffness, and those modifications were independent of modified protein composition.

Despite the unchanged level of collagens, OH-Lysine content in ECM proteins and LOX, the amount of crosslinking in the perilesional ECM was higher than in normal ECM and its ultrastructure recapitulated the neoplastic ECM. LOXs' activity depends on the amount of substrates as collagen/elastin and molecular oxygen, suggesting that the increased vascularization/oxygenation of the perilesional area likely represents the responsible factor for the increased crosslinking and stiffness of perilesional ECM.

Moreover, we provide findings here indicative of different mechanisms sustaining an increased level of collagen crosslinking and stiffness of the perilesional and CRC ECMs. The desmoplastic tumoral stroma is composed by dysregulated composition of ECM proteins, with a change in the ratio among collagen XII/VI, increased HP crosslinking consequent to enhanced hydroxylation of lysine in COL1A1. In the perilesional area the desmoplastic stroma is independent of altered i) composition of ECM, ii) level of LOX or iii) OH-lysine level in the ECM protein. The increased vascularization/oxygenation of the perilesional area accounts for the increased HP and LP levels in the perilesional desmoplastic stroma.

Increased crosslinking, stiffness and differently organized ECM fibrils of the perilesional area provide an extracellular environment suitable for tumor invasion and progression. These findings underlie two mechanisms in the CRC pathogenesis. First, cancer cells instruct surrounding tissues to undergo changes that promote malignancy, for example by endorsing neo-angiogenesis or mechanically-induced over-expression of proteins involved in epithelial cell-cell adhesion and gene transcription, as β-catenin[54]. Indeed, mechanical loading has also recently been reported to increase LOX-mediated crosslinking[55]. Modifications in the vascularized and stiffer perilesional area might represent a feed-forward loop which spreads features of the neoplastic ECM.

Second, our results also suggest that mechanical pre-strain of the ECM might predispose a soil needed for the onset of CRC. We observed that in the perilesional area the level of LOX was unchanged vs the healthy tissue.

The pre-strain of perilesional ECM is likely supported by the enhanced vascularization of the tissue, providing increased amount of oxygen which is one of the substrate of the enzymatic reaction mediated by LOX. This interpretation is supported by epidemiological studies reporting that patients with Crohn's disease are characterized by enhanced intestinal vascularization and matrix stiffness and experience an increased incidence of CRC[56]. Similarly, a study from an animal model showed that microvascular blood content increased very early in colon carcinogenesis prior to the development of adenomas[57].

These findings provide a framework for alternative therapeutic strategies against CRC progression, as chemoresistance may be overcome by targeting the tumor surrounding microenvironment[58] and level of pyridinoline crosslinking might be controlled by anti-oxidant agents[59], anti-fibrotic agents[60] or through normalization of vasculature[36].

This study identifies stiffness and crosslinking of the ECM as the main parameters responsible for the "soil effect" of the perilesional area, such as increased proliferation and turn-over of cancer cells and permissiveness to infiltration[15]. Furthermore, relative increased stiffness of colon areas, within the same patient, may represent a new predictive marker of desmoplastic region, predisposing to invasion, thus offering new potential application for monitoring adenoma with invasive potential.

References

1. Folkman, J. & Kalluri, R. Cancer without disease. *Nature* **427,** 787 (2004).
2. Kalluri, R. & Zeisberg, M. Fibroblasts in cancer. *Nat Rev Cancer* **6,** 392–401 (2006).
3. Rhim, A. D. *et al.* Stromal elements act to restrain, rather than support, pancreatic ductal adenocarcinoma. *Cancer Cell* **25,** 735–747 (2014).
4. Ozdemir, B. C. *et al.* Depletion of carcinoma-associated fibroblasts and fibrosis induces immunosuppression and accelerates pancreas cancer with reduced survival. *Cancer Cell* **25,** 719–734 (2014).
5. Jaalouk, D. E. & Lammerding, J. Mechanotransduction gone awry. *Nat Rev Mol Cell Biol* **10,** 63–73 (2009).
6. Lu, P., Weaver, V. M. & Werb, Z. The extracellular matrix: a dynamic niche in cancer progression. *J Cell Biol* **196,** 395–406 (2012).
7. Brabletz, T., Jung, A., Spaderna, S., Hlubek, F. & Kirchner, T. Opinion: migrating cancer stem cells—an integrated concept of malignant tumour progression. *Nat Rev Cancer* **5,** 744–749 (2005).
8. Ingber, D. E. Can cancer be reversed by engineering the tumor microenvironment? *Semin Cancer Biol* **18,** 356–364 (2008).
9. Mikula, M. *et al.* Integrating proteomic and transcriptomic high-throughput surveys for search of new biomarkers of colon tumors. *Funct Integr Genomics* **11,** 215–224 (2011).
10. Cox, T. R. *et al.* LOX-mediated collagen crosslinking is responsible for fibrosis-enhanced metastasis. *Cancer research* **73,** 1721–1732 (2013).
11. Nishioka, T., Eustace, A. & West, C. Lysyl oxidase: from basic science to future cancer treatment. *Cell Struct Funct* **37,** 75–80 (2012).
12. Baker, A. M. *et al.* The role of lysyl oxidase in SRC-dependent proliferation and metastasis of colorectal cancer. *J Natl Cancer Inst* **103,** 407–424 (2011).
13. Fong, S. F. *et al.* Lysyl oxidase-like 2 expression is increased in colon and esophageal tumors and associated with less differentiated colon tumors. *Genes Chromosomes Cancer* **46,** 644–655 (2007).
14. Paszek, M. J. *et al.* Tensional homeostasis and the malignant phenotype. *Cancer Cell* **8,** 241–254 (2005).
15. Genovese, L. *et al.* Cellular localization, invasion, and turnover are differently influenced by healthy and tumor-derived extracellular matrix. *Tissue Eng Part A* **20,** 2005–2018 (2014).
16. Wisniewski, J. R., Zougman, A., Nagaraj, N. & Mann, M. Universal sample preparation method for proteome analysis. *Nat Methods* **6,** 359–362 (2009).
17. Cox, J. *et al.* Andromeda: a peptide search engine integrated into the MaxQuant environment. *J Proteome Res* **10,** 1794–1805 (2011).
18. Naba, A. *et al.* The matrisome: in silico definition and *in vivo* characterization by proteomics of normal and tumor extracellular matrices. *Mol Cell Proteomics* **11,** 1–18 (2012).
19. Nebuloni, M. *et al.* HIV-1 Infected Lymphoid Organs Upregulate Expression and Release of the Cleaved Form of uPAR That Modulates Chemotaxis and Virus Expression. *PLoS One* **8,** e70606 (2013).
20. Barone, M. *et al.* ERbeta expression in normal, adenomatous and carcinomatous tissues of patients with familial adenomatous polyposis. *Scand J Gastroenterol* **45,** 1320–1328 (2010).
21. Schneider, C. A., Rasband, W. S. & Eliceiri, K. W. NIH Image to ImageJ: 25 years of image analysis. *Nat Methods* **9**, 671–675 (2012).
22. Butt, H. J., Cappella B. & Kappl, M. Force measurements with the atomic force microscope: Technique, interpretation and applications. *Surface Science Reports* **59,** 1–152 (2005).
23. Puricelli, L., Galluzzi, M., Schulte, C., Podestà, A. & Milani, P. Nanomechanical and topographical imaging of living cells by Atomic Force Microscopy with colloidal probes. *Rev Sci Instrum* **86,** 033705, doi: 10.1063/1.4915896 (2015).
24. Indrieri, M., Podesta, A., Bongiorno, G., Marchesi, D. & Milani, P. Adhesive-free colloidal probes for nanoscale force measurements: production and characterization. *Rev Sci Instrum* **82,** 023708, doi: 10.1063/1.3553499 (2011).
25. Cramer, H. Mathematical Methods of Statistics. *Princeton University Press* (1999).
26. Gonzalez, G. E. *et al.* N-acetyl-seryl-aspartyl-lysyl-proline reduces cardiac collagen cross-linking and inflammation in angiotensin II-induced hypertensive rats. *Clinical science* **126,** 85–94 (2014).
27. Boudaoud, A. *et al.* FibrilTool, an ImageJ plug-in to quantify fibrillar structures in raw microscopy images. *Nat Protoc* **9,** 457–463 (2014).
28. Saeed, A. I. *et al.* TM4: a free, open-source system for microarray data management and analysis. *Biotechniques* **34,** 374–378 (2003).
29. Kramer, A., Green, J., Pollard, J. Jr. & Tugendreich, S. Causal analysis approaches in Ingenuity Pathway Analysis. *Bioinformatics* **30,** 523–530 (2014).
30. Hasson, R. M. *et al.* Estrogen receptor alpha or beta loss in the colon of Min/+ mice promotes crypt expansion and impairs TGFbeta and HNF3beta signaling. *Carcinogenesis* **35,** 96–102 (2014).
31. He, Y. Q. *et al.* Estradiol regulates miR-135b and mismatch repair gene expressions via estrogen receptor-beta in colorectal cells. *Exp Mol Med* **44,** 723–732 (2012).
32. Rodriguez, C. *et al.* Regulation of lysyl oxidase in vascular cells: lysyl oxidase as a new player in cardiovascular diseases. *Cardiovasc Res* **79,** 7–13 (2008).
33. Galvan, J. A. *et al.* Validation of COL11A1/procollagen 11A1 expression in TGF-beta1-activated immortalised human mesenchymal cells and in stromal cells of human colon adenocarcinoma. *BMC Cancer* **14,** 867, doi: 10.1186/1471-2407-14-867 (2014).
34. Grimsby, J. L., Lucero, H. A., Trackman, P. C., Ravid, K. & Kagan, H. M. Role of lysyl oxidase propeptide in secretion and enzyme activity. *J Cell Biochem* **111,** 1231–1243 (2010).
35. Sun, X. F. *et al.* Microvascular corrosion casting of normal tissue, transitional mucosa and adenocarcinoma in the human colon. *Acta Oncol* **31,** 37–40 (1992).
36. Jain, R. K. Normalizing tumor vasculature with anti-angiogenic therapy: a new paradigm for combination therapy. *Nat Med* **7,** 987–989 (2001).

37. Khong, T. L. *et al.* Identification of the angiogenic gene signature induced by EGF and hypoxia in colorectal cancer. *BMC Cancer* **13,** 518, doi: 10.1186/1471-2407-13-518 (2013).
38. Augoff, K. *et al.* Immunohistochemical study of decorin expression in polyps and carcinomas of the colon. *Med Sci Monit* **14,** CR530–535 (2008).
39. Bi, X. *et al.* Genetic deficiency of decorin causes intestinal tumor formation through disruption of intestinal cell maturation. *Carcinogenesis* **29,** 1435–1440 (2008).
40. Delektorskaya, V. V., Golovkov, D. A. & Kushlinskii, N. E. Clinical significance of levels of molecular biological markers in zones of invasive front-line of colorectal cancer. *Bull Exp Biol Med* **146,** 616–619 (2008).
41. Lazaris, A. *et al.* Immunohistochemical assessment of basement membrane components in colorectal cancer: prognostic implications. *J Exp Clin Cancer Res* **22,** 599–606 (2003).
42. Ulazzi, L. *et al.* Nidogen 1 and 2 gene promoters are aberrantly methylated in human gastrointestinal cancer. *Mol Cancer* **6,** 17, doi: 1476-4598-6-17 (2007).
43. Pesson, M. *et al.* A gene expression and pre-mRNA splicing signature that marks the adenoma-adenocarcinoma progression in colorectal cancer. *PLoS One* **9,** e87761 (2014).
44. Wang, Y. *et al.* Differential expression of mimecan and thioredoxin domain-containing protein 5 in colorectal adenoma and cancer: a proteomic study. *Exp Biol Med* **232,** 1152–1159 (2007).
45. Saito, N., Nishimura, H. & Kameoka, S. Clinical significance of fibronectin expression in colorectal cancer. *Mol Med Rep* **1,** 77–81 (2008).
46. Midwood, K. S., Hussenet, T., Langlois, B. & Orend, G. Advances in tenascin-C biology. *Cell Mol Life Sci* **68,** 3175–3199 (2011).
47. Karagiannis, G. S. *et al.* Proteomic signatures of the desmoplastic invasion front reveal collagen type XII as a marker of myofibroblastic differentiation during colorectal cancer metastasis. *Oncotarget* **3,** 267–285 (2012).
48. Banse, X., Sims, T. J. & Bailey, A. J. Mechanical properties of adult vertebral cancellous bone: correlation with collagen intermolecular cross-links. *J Bone Miner Res* **17,** 1621–1628 (2002).
49. Leppert, P. C., Jayes, F. L. & Segars, J. H. The extracellular matrix contributes to mechanotransduction in uterine fibroids. *Obstet Gynecol Int* **2014,** 783289, doi: 10.1155/2014/783289 (2014).
50. Wan, K. C. & Evans, J. H. Free radical involvement in hypertrophic scar formation. *Free Radic Biol Med* **26,** 603–608 (1999).
51. van der Slot-Verhoeven, A. J. *et al.* The type of collagen cross-link determines the reversibility of experimental skin fibrosis. *Biochim Biophys Acta* **1740,** 60–67 (2005).
52. Higgins, D. F. *et al.* Hypoxia promotes fibrogenesis *in vivo* via HIF-1 stimulation of epithelial-to-mesenchymal transition. *J Clin Invest* **117,** 3810–3820 (2007).
53. Barker, H. E., Cox, T. R. & Erler, J. T. The rationale for targeting the LOX family in cancer. *Nat Rev Cancer* **12,** 540–552 (2012).
54. Fernandez-Sanchez, M. E. *et al.* Mechanical induction of the tumorigenic beta-catenin pathway by tumour growth pressure. *Nature* **523,** 92–95 (2015).
55. Kaku, M. *et al.* Mechanical Loading Stimulates Expression of Collagen Cross-Linking Associated Enzymes in Periodontal Ligament. *J Cell Physiol* **231,** 926–933 (2015).
56. von Roon, A. C. *et al.* The risk of cancer in patients with Crohn's disease. *Dis Colon Rectum* **50,** 839–855 (2007).
57. Wali, R. K. *et al.* Increased microvascular blood content is an early event in colon carcinogenesis. *Gut* **54,** 654–660 (2005).
58. Egeblad, M., Nakasone, E. S. & Werb, Z. Tumors as organs: complex tissues that interface with the entire organism. *Dev Cell* **18,** 884–901 (2010).
59. Wan, K. C., Wu, H. T., Chan, H. P. & Hung, L. K. Effects of antioxidants on pyridinoline cross-link formation in culture supernatants of fibroblasts from normal skin and hypertrophic scars. *Clin Exp Dermatol* **27,** 507–512 (2002).
60. Johnson, L. A. *et al.* Novel Rho/MRTF/SRF inhibitors block matrix-stiffness and TGF-beta-induced fibrogenesis in human colonic myofibroblasts. *Inflamm Bowel Dis* **20,** 154–165 (2014).

Acknowledgements

The authors wish to thank Dr. Dana Kuefner (San Raffaele Scientific Institute) for reviewing the language in this manuscript, Dr. Vincenzo Russo for professional reading (San Raffaele Scientific Institute), Dr. Fernanda Dorigatti (San Raffaele Scientific Institute) and Dr. Francesco Puppi (Università degli Studi di Milano) for support in crosslinking and AFM measurements, respectively.

Author Contributions

M.N., L.A., A.A., C.M., L.G., I.L., E.L., P.Z., R.A., A.P., L.P., A.S. and M.A. performed experiments and analysis. M.N., A.A., C.M., A.P., L.P. and M.A. prepared Figs M.N., L.A., A.A., G.T., A.P., L.P., P.M., A.S. and M.A. contributed to write the manuscript text. M.N., L.A. and M.A. designed the study. All authors contributed to data interpretation and reviewed the manuscript.

Additional Information

Supplementary information accompanies this paper at http://www.nature.com/srep

Competing financial interests: The authors declare no competing financial interests.

How to cite this article: Nebuloni, M. *et al.* Insight On Colorectal Carcinoma Infiltration by Studying Perilesional Extracellular Matrix. *Sci. Rep.* **6**, 22522; doi: 10.1038/srep22522 (2016).

This work is licensed under a Creative Commons Attribution 4.0 International License. The images or other third party material in this article are included in the article's Creative Commons license, unless indicated otherwise in the credit line; if the material is not included under the Creative Commons license, users will need to obtain permission from the license holder to reproduce the material. To view a copy of this license, visit http://creativecommons.org/licenses/by/4.0/

INSIGHT ON COLORECTAL CARCINOMA INFILTRATION BY STUDYING PERILESIONAL EXTRACELLULAR MATRIX

List of investigators: Manuela Nebuloni, Luca Albarello, Annapaola Andolfo, Cinzia Magagnotti, Luca Genovese, Irene Locatelli, Giovanni Tonon, Erika Longhi, Pietro Zerbi, Raffaele Allevi, Alessandro Podestà, Luca Puricelli, Paolo Milani, Armando Soldarini, Andrea Salonia, Massimo Alfano.

ADDITIONAL INFORMATION

Table of contents:

1. Supplementary Figures
2. Supplementary Table S1. Clinico-pathological features of left colon cancer patients and investigative techniques used on each surgical sample.
3. Supplementary Figure Legends
4. Significance of down and up regulated proteins in CRC ECM
5. References

1. SUPPLEMENTARY FIGURES

SUPPLEMENTARY FIGURE S1

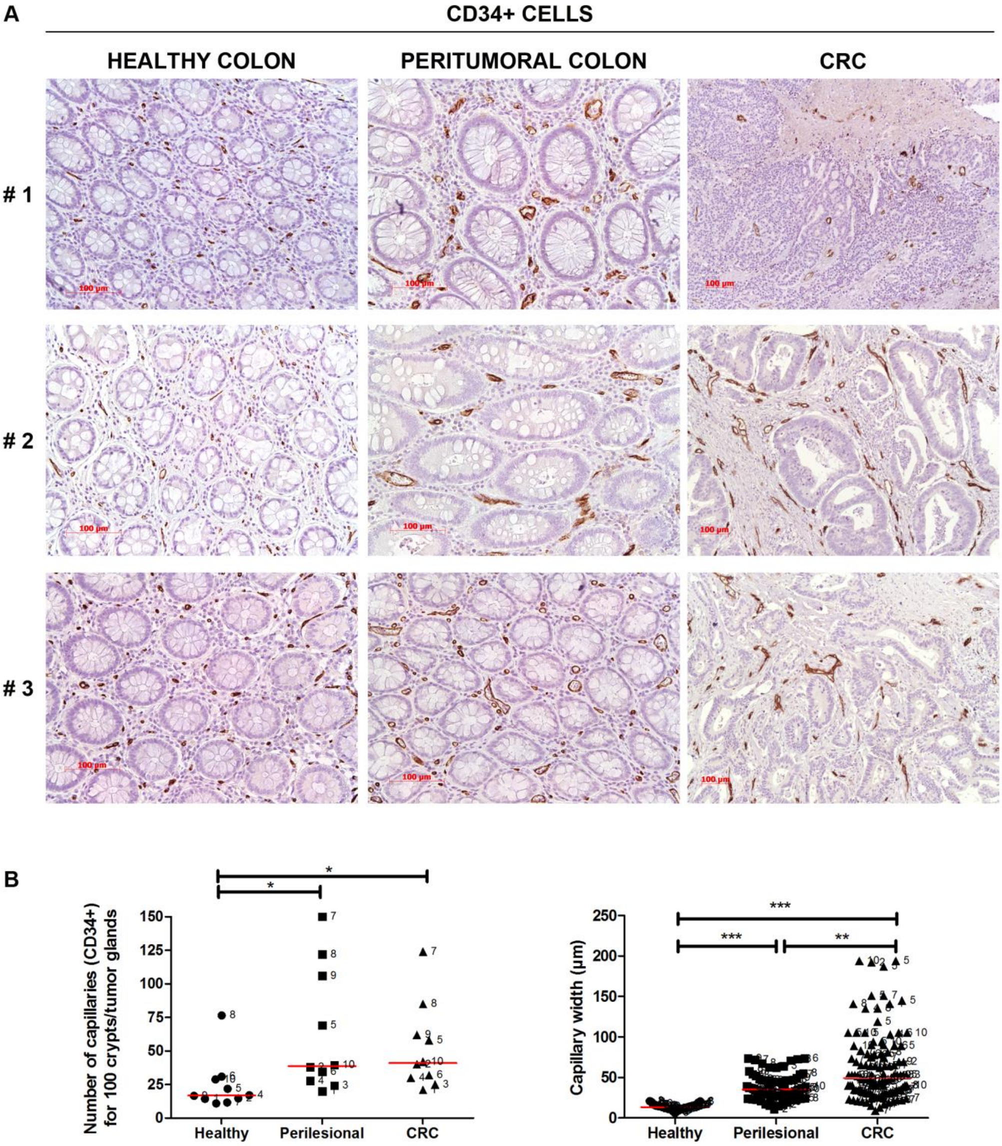
A
CD34+ CELLS
HEALTHY COLON
PERITUMORAL COLON
CRC
# 1
# 2
# 3
100 μm
B
Number of capillaries (CD34+) for 100 crypts/tumor glands
0
25
50
75
100
125
150
Healthy
Perilesional
CRC
*
*
Capillary width (μm)
0
50
100
150
200
250
Healthy
Perilesional
CRC
***
***
**

SUPPLEMENTARY FIGURE S2

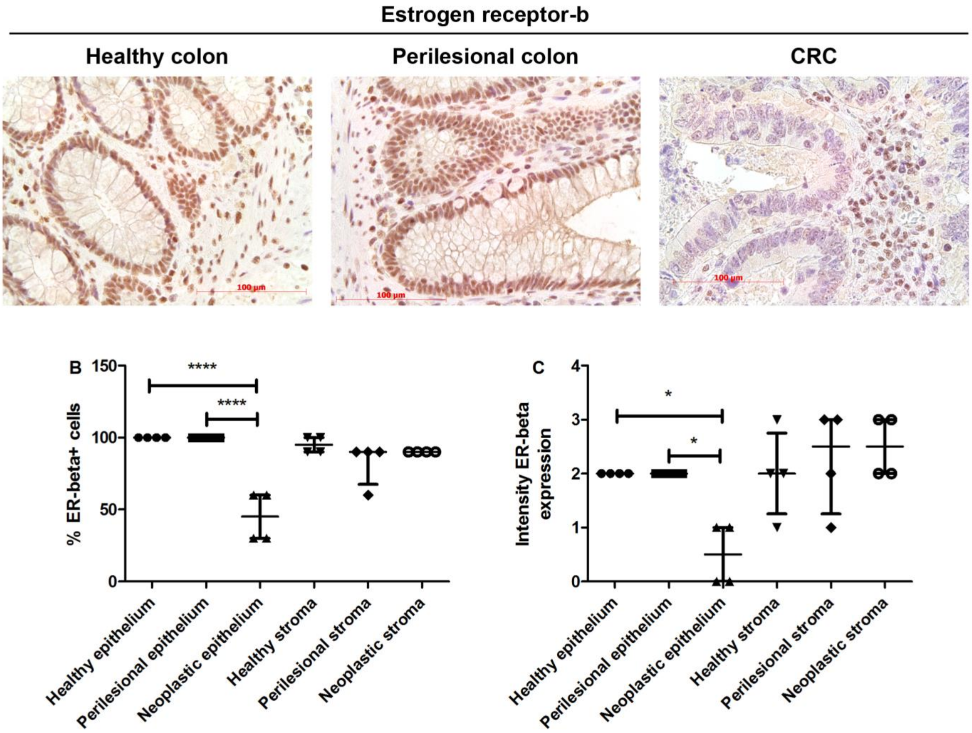
Estrogen receptor-b
Healthy colon
Perilesional colon
CRC
100 µm
100 µm
100 µm
B
% ER-beta+ cells
150
100
50
0
****
****
Healthy epithelium
Perilesional epithelium
Neoplastic epithelium
Healthy stroma
Perilesional stroma
Neoplastic stroma
C
Intensity ER-beta expression
4
3
2
1
0
*
*
Healthy epithelium
Perilesional epithelium
Neoplastic epithelium
Healthy stroma
Perilesional stroma
Neoplastic stroma

SUPPLEMENTARY FIGURE S3

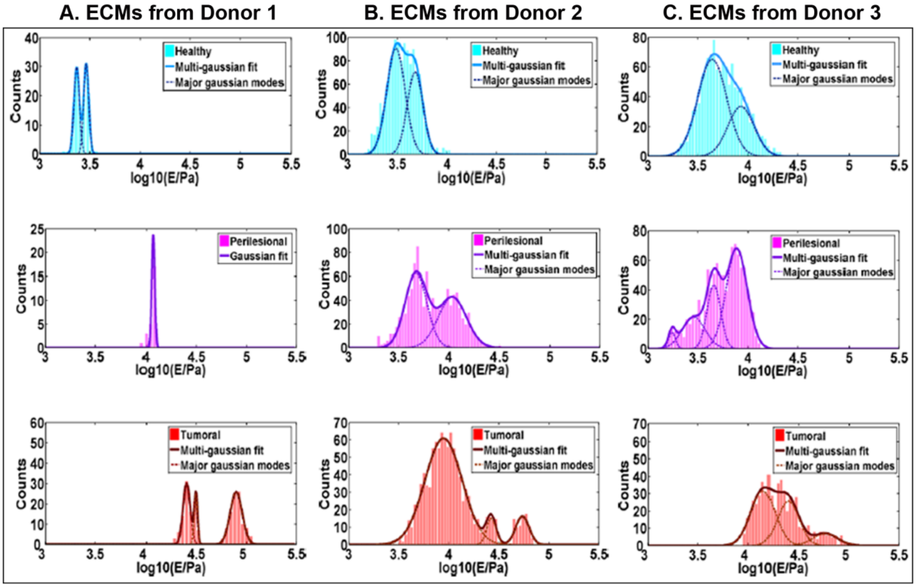

SUPPLEMENTARY FIGURE S4

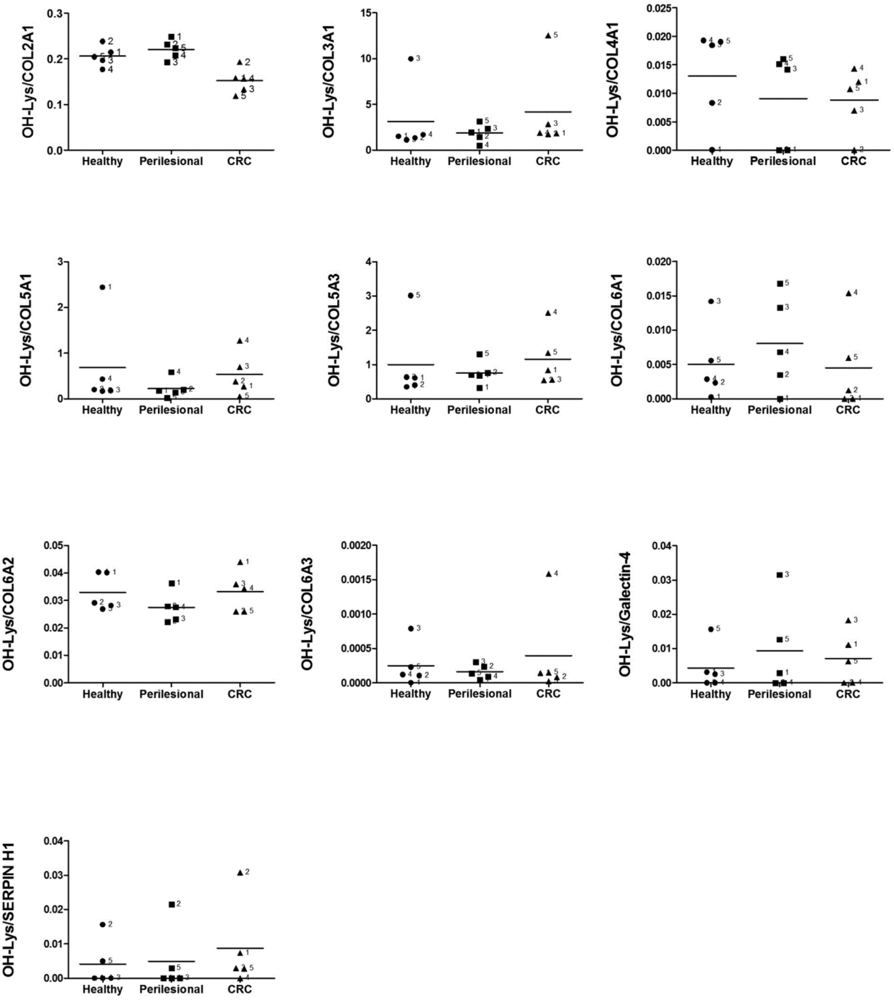

SUPPLEMENTARY FIGURE S5

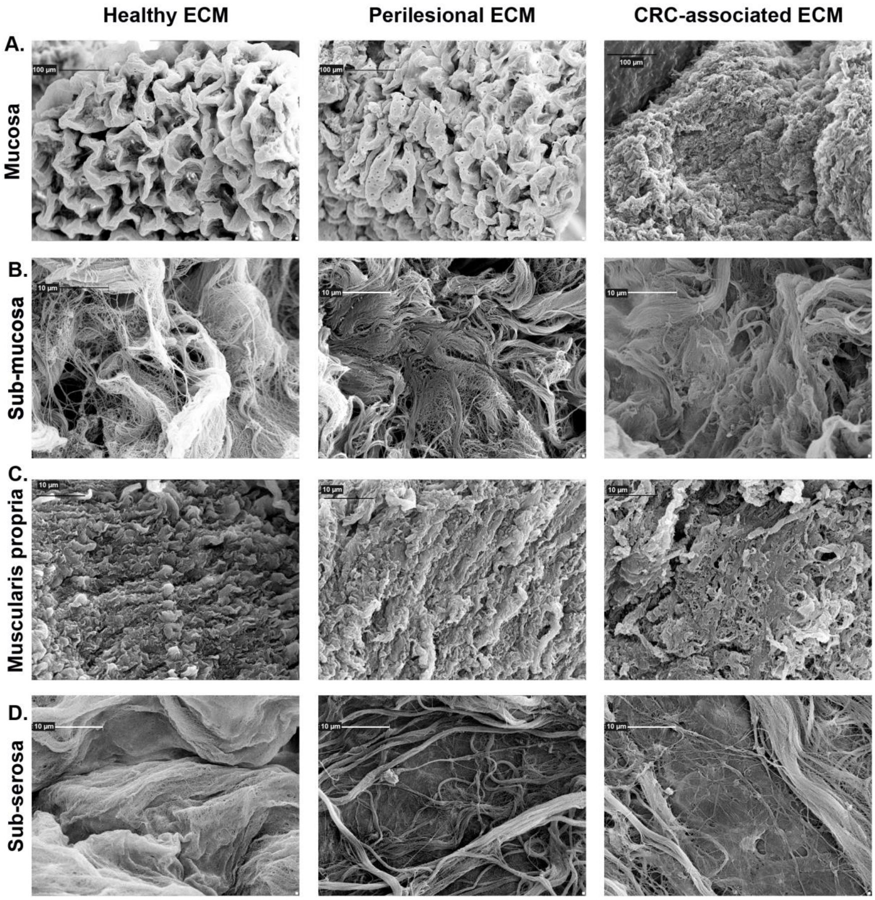
Healthy ECM
Perilesional ECM
CRC-associated ECM
A.
Mucosa
100 µm
100 µm
100 µm
B.
Sub-mucosa
10 µm
10 µm
10 µm
C.
Muscularis propria
10 µm
10 µm
10 µm
D.
Sub-serosa
10 µm
10 µm
10 µm

Supplementary Figure S6

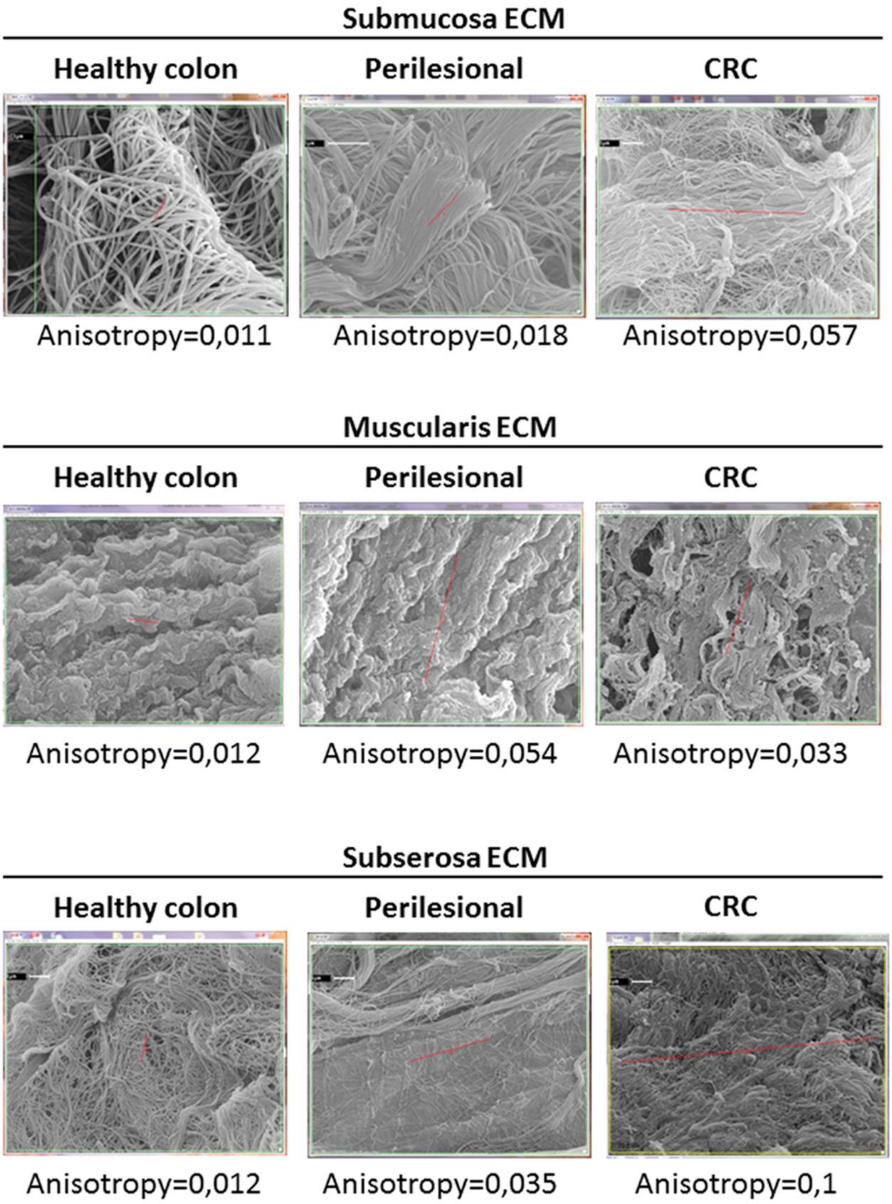
Submucosa ECM
Healthy colon
Perilesional
CRC
Anisotropy=0,011
Anisotropy=0,018
Anisotropy=0,057
Muscularis ECM
Healthy colon
Perilesional
CRC
Anisotropy=0,012
Anisotropy=0,054
Anisotropy=0,033
Subserosa ECM
Healthy colon
Perilesional
CRC
Anisotropy=0,012
Anisotropy=0,035
Anisotropy=0,1

2. Supplementary Table S1. Clinico-pathological features of left colon cancer patients and investigative techniques used on each surgical sample.

#[a]	**Age**	**Sex**[b]	**TNM, Grade**[c]	**Morphology and structural study**	**CD34+ cells**	**Proteomic analysis**	**Matrilin-2, Tenascin Validation**	**ER-b**	**Stiffness**	**Crosslinking**	**LOX analysis**
1	75	F	pT2N0, G2	x							
2	74	M	pT3N1a, G2	x	x						
3	71	F	pT2N1a, G2	x	x						
4	74	M	pT3N0, G2	x	x						
5	82	M	pT3N0, G2	x	x						
6	77	F	pT3N1b, G3	x	x						
7	78	M	pT4aN1b, G2		x						
8	58	M	pT3N0, G2		x				x	x	x
9	79	M	pT3N0, G3		x	x	x	x			
10	68	M	pT3N0, G3		x	x	x	x			
11	55	F	pT3N0, G2		x	x	x	x			
12	72	F	pT3N1a, G2			x	x	x			
13	66	M	pT3N0, G3			x	x				
14	92	M	pT4aN2a, G3							x	
15	73	F	pT3N0, G2						x	x	
16	63	F	pT3N0, G2						x	x	
17	71	M	pT3N1a, G2							x	
18	65	M	pT3N0, G2								x
19	76	M	pT3N1b, G2								x
20	68	M	pT4aN1a, G2								x

[a] Anonymized code. [b] Male/Female. [c] TNM classification (7th Edition, 2009).

3. SUPPLEMENTARY FIGURE LEGENDS

Supplementary Figure S1. Increased number and capillary width in the perilesional colon mucosa. Ten pair-wised tissues were investigated for the level of CD34+ cells (Supplementary Table S1). Representative pair-wised pictures from three donors are shown (A). Number of capillaries was evaluated on all 10 pair-wised tissues and expressed for 100 crypts or neoplastic glands, and capillary width estimated on all counted capillaries (B); median values are shown by red bar. Statistical significance, indicated by asterisks, was evaluated by two-tailed paired t-test. Selection of capillaries was based on CD34+ staining and presence of lumen. Healthy and perilesional tissues are shown at 20x magnification, whereas CRC at 10x magnification.

Supplementary Figure S2. Down-modulation of ER-b receptor in neoplastic epithelial cells. The oestrogen pathway identified through IPA, based on all differentially expressed ECM proteins, was validated by means of immunohistochemistry for estrogen receptor-b on healthy, perilesional and CRC tissue (A). Number of ER-b+ cells (B) and levels of ER-b expression (C) in pair-wised healthy colon, perilesional area and CRC were evaluated on pair-wised tissues from 4 patients (representative images are from pair-wised tissues of patient #9 listed in Supplementary Table S1). Intensity of ER-b expression was evaluated on a scale from 0 to 3.

Supplementary Figure S3. Elastic Young’s modulus of ECM from healthy, perilesional and CRC area. The cumulative distributions of Young’s modulus values of ECMs derived from 3 patients listed in Supplementary Table S1 were assessed. From distributions of Young’s modulus values in semilog10 scale (A-C, bold line), the median values of the broad distributions as well as of their major modes (A-C, dotted lines) were estimated.

Supplementary Figure S4. Level of OH-lysine in ECM proteins. Sum of peak intensities was estimated by MaxQuant software for all OH-lysine-containing peptides, and normalized to each protein intensity in each ECM derived from 5 patients.

Supplementary Figure S5. Ultrastructural analysis of ECMs. Lower magnification of pictures reported in Figure 5, representing broader field of ECMs. Pictures from representative pair-wised ECMs are shown.

Supplementary Figure S6. Anisotropy of ECMs. The degree of organization of fibrils was established by means of the plug-in FibriTool in the ImageJ software. The output from FibrilTool is represented by a red line, the angle of which represents the average orientation and the length of which is proportional to the array of anisotropy. Representative images are shown. The colored box (green or yellow) within the electron micrographs represents the area selected for the measure,

4. Significance of down and up regulated proteins in CRC ECM

Down-regulated proteins in CRC.

Decorin: Connective tissue, interstitial matrix. Extracellular proteoglycan which acts as an important regulator of collagen fibrillogenesis, and inhibitor of cellular proliferation[1] via sequestration of TGF-b and other growth factors[2]. Loss of Decorin has been associated with tumor aggressiveness and unfavorable prognosis[3,4] in urothelial bladder cancer[5].

Laminin subunit beta 2: Laminins, a family of extracellular matrix glycoproteins, are the major noncollagenous constituent of basement membranes. They have been implicated in a wide variety of biological processes including cell adhesion, differentiation, migration, signaling, neurite outgrowth and metastasis (http://www.ncbi.nlm.nih.gov/gene?Db=gene&Cmd=ShowDetailView&TermToSearch=3913).

Nidogen 1: *Nidogen*-1/entactin-1[6] and *nidogen*-2/entactin-2[7] are basement membrane (BM) glycoproteins mainly expressed by mesenchymal cells and deposited into the epithelial and endothelial BMs during development[8]. Nidogen-1 and nidogen-2 have similar structures and abilities to bind to ECM proteins. Nidogens are reported to be highly sensitive to proteolytic cleavage, although the binding of nidogen-1 to laminin-γ1 decreases susceptibility to proteolysis [9]. Similarly, the binding of nidogen-1 to laminin-γ1 also protects laminins from proteolysis, therefore contributing to BM stability, whereas the removal of nidogens contributes to BM disintegration, thus favoring epithelial-mesenchymal transition and metastasis[8].

Matrilin 2: This gene encodes a member of the von Willebrand factor A domain containing protein family. This family of proteins is thought to be involved in the formation of filamentous networks in the extracellular matrices of various tissues. This protein contains five von Willebrand factor A domains. The specific function of this gene has not yet been determined. (http://www.ncbi.nlm.nih.gov/gene/4147). Lack of Matrilin-2 Favors Liver Tumor Development via Erk1/2 and GSK-3β Pathways i*n Vivo*[10].

Col 6A3 and isoform 4: Connective tissue, interstitial matrix. The alpha-3 chain is one of the three alpha chains of type VI collagen, a beaded filament collagen found in most connective tissues. The alpha-3 chain of type VI collagen is much larger than the alpha-1 and -2 chains. This difference in size is largely due to an increase in the number of subdomains, similar to von Willebrand Factor type A domains, that are found in the amino terminal globular domain of all the alpha chains. These domains have been shown to bind extracellular matrix proteins, an interaction that explains the importance of this collagen in organizing matrix components. (http://www.ncbi.nlm.nih.gov/gene?Db=gene&Cmd=ShowDetailView&TermToSearch=1293).
Growth Promoting Activities of Collagen 6A3[11].

Dermatopontin: Seems to mediate adhesion by cell surface integrin binding. May serve as a communication link between the dermal fibroblast cell surface and its extracellular matrix environment. Enhances TGFB1 activity. Inhibits cell proliferation. Accelerates collagen fibril formation, and stabilizes collagen fibrils against low-temperature dissociation (http://www.uniprot.org/uniprot/Q07507). Down-regulated in colorectal adenoma and CRC[12].

Mimecan: Induces bone formation in conjunction with TGF-beta-1 or TGF-beta-2. This protein is a small proteoglycan which contains tandem leucine-rich repeats (LRR). Gene ontology annotations related to this gene include growth factor activity (http://www.uniprot.org/uniprot/P20774). Down-regulated in colorectal adenoma and CRC[13].

Up-regulated proteins in CRC.

Fibronectin: A multifunctional and adhesive glycoprotein widely distributed in connective tissues and subendothelial matrices, as well as in many cell types. Fibronectin is present in a soluble form in body fluids and in an insoluble form in the ECM where it interacts with many other matrix components as well as collagen, fibrin, several integrins and syndecans[14]. Fibronectin originates from a primary transcript, which can be alternatively spliced generating at least 20 different variants.

Fibronectins are involved in cell adhesion, cell motility, opsonization, wound healing, and maintenance of cell shape. Involved in osteoblast compaction through the fibronectin fibrillogenesis cell-mediated matrix assembly process, essential for osteoblast mineralization. Anastellin binds fibronectin and induces fibril formation. This fibronectin polymer, named superfibronectin, exhibits enhanced adhesive properties. Both anastellin and superfibronectin inhibit tumor growth, angiogenesis and metastasis (http://www.uniprot.org/uniprot/P02751).

Fibronectin has been implicated in carcinoma development[15]. In lung carcinoma, fibronectin expression is increased, especially in non-small cell lung carcinoma. The adhesion of lung carcinoma cells to fibronectin enhances tumorigenicity and confers resistance to apoptosis-inducing chemotherapeutic agents. Fibronectin has been shown to stimulate the gonadal steroids that interact with vertebrate androgen receptors, which are capable of controlling the expression of cyclin D and related genes involved in cell cycle control. These observations suggest that fibronectin may promote lung tumor growth/survival and resistance to therapy, and it could represent a novel target for the development of new anticancer drugs.

Collagen 12A1: Connective tissue, interstitial matrix. The alpha chain of type XII collagen, a member of the FACIT (fibril-associated collagens with interrupted triple helices) collagen family. Type XII collagen is a homotrimer found in association with type I collagen, an association that is thought to modify the interactions between collagen I fibrils and the surrounding matrix (http://www.uniprot.org/uniprot/Q99715). Colon adenoma-adenocarcinoma progression is associated with overexpression of collagen XII[16].

Fibulin 1: Incorporated into fibronectin-containing matrix fibers. May play a role in cell adhesion and migration along protein fibers within the extracellular matrix (ECM). Homomultimerizes and interacts with various extracellular matrix components such as FN1, LAMA1, LAMA2, and contribute to the supramolecular organization of ECM architecture, in particular to those of basement membranes through its binding to laminin, nidogen and collagen IV. Widely expressed during embryonic development. Four splice variants which differ in the 3' end have been identified. Each variant encodes a different isoform, but no functional distinctions have been identified among the four variants (http://www.genecards.org/cgi-bin/carddisp.pl?gene=FBLN1).

Has been implicated in a role in cellular transformation and tumor invasion, it appears to be a tumor suppressor. May play a role in haemostasis and thrombosis owing to its ability to bind fibrinogen and incorporate into clots (http://www.uniprot.org/uniprot/P23142).

Galectin 3: This gene encodes a member of the galectin family of carbohydrate binding proteins. Members of this protein family have an affinity for beta-galactosides. The encoded protein is characterized by an N-terminal proline-rich tandem repeat domain and a single C-terminal carbohydrate recognition domain. This protein can self-associate through the N-terminal domain allowing it to bind to multivalent saccharide ligands. This protein localizes to the extracellular matrix, the cytoplasm and the nucleus. This protein plays a role in numerous cellular functions including apoptosis, innate immunity, cell adhesion and T-cell regulation. Alternate splicing results in multiple transcript variants (http://www.genecards.org/cgi-bin/carddisp.pl?gene=LGALS3).

Galectin-3 is a galactose-specific lectin which binds IgE. May mediate with the alpha-3, beta-1 integrin the stimulation by CSPG4 of endothelial cells migration. Together with DMBT1, required for terminal differentiation of columnar epithelial cells during early embryogenesis (By similarity). In the nucleus: acts as a pre-mRNA splicing factor. Involved in acute inflammatory responses including neutrophil activation and adhesion, chemoattraction of monocytes macrophages, opsonization of apoptotic neutrophils, and activation of mast cells (http://www.uniprot.org/uniprot/P17931#section_comments).

Microfibrillar associated protein 2: Microfibrillar-associated protein 2 is a major component of elastin-associated microfibrils and a candidate for involvement in the etiology of inherited connective tissue diseases. Four transcript variants encoding two different isoforms have been found for this gene. GO annotations related to this gene include *fibronectin binding* and *fibrinogen binding*. An important paralog of this gene is MFAP5 (http://www.genecards.org/cgi-bin/carddisp.pl?gene=MFAP2).

Through $\alpha_V\beta_3$ integrin-mediated signaling, MAGP2 promotes tumor and endothelial cell survival, and its overexpression associated with poor prognosis in ovarian cancer patients[17].

Tenascin: Extracellular matrix protein with a spatially and temporally restricted tissue distribution. This protein is homohexameric with disulfide-linked subunits, and contains multiple EGF-like and fibronectin type-III domains (http://www.genecards.org/cgi-bin/carddisp.pl?gene=TNC). TNC is as an extracellular matrix protein of stem cell niches and component of the metastatic niche. Cancer cell–

derived TNC promotes the survival and outgrowth of pulmonary micrometastases, until the tumor stroma takes over as a source of TNC[18].

5. REFERENCES

1. Stander, M., Naumann, U., Wick, W. & Weller, M. Transforming growth factor-beta and p-21: multiple molecular targets of decorin-mediated suppression of neoplastic growth. *Cell Tissue Res* **296**, 221-227 (1999).
2. Neill, T., Schaefer, L. & Iozzo, R.V. Decorin: a guardian from the matrix. *Am J Pathol* **181**, 380-387 (2012).
3. Iozzo, R.V., *et al.* Decorin antagonizes IGF receptor I (IGF-IR) function by interfering with IGF-IR activity and attenuating downstream signaling. *J Biol Chem* **286**, 34712-34721.
4. Niedworok, C., *et al.* Inhibitory role of the small leucine-rich proteoglycan biglycan in bladder cancer. *PLoS One* **8**, e80084.
5. Sainio, A., *et al.* Lack of decorin expression by human bladder cancer cells offers new tools in the therapy of urothelial malignancies. *PLoS One* **8**, e76190.
6. Timpl, R., Dziadek, M., Fujiwara, S., Nowack, H. & Wick, G. Nidogen: a new, self-aggregating basement membrane protein. *Eur J Biochem* **137**, 455-465 (1983).
7. Kohfeldt, E., Sasaki, T., Gohring, W. & Timpl, R. Nidogen-2: a new basement membrane protein with diverse binding properties. *J Mol Biol* **282**, 99-109 (1998).
8. Dziadek, M. Role of laminin-nidogen complexes in basement membrane formation during embryonic development. *Experientia* **51**, 901-913 (1995).
9. Mayer, U., *et al.* Binding properties and protease stability of recombinant human nidogen. *Eur J Biochem* **227**, 681-686 (1995).
10. Fullar, A., *et al.* Lack of Matrilin-2 favors liver tumor development via Erk1/2 and GSK-3beta pathways in vivo. *PLoS One* **9**, e93469 (2014).

11. Martianov, I., *et al.* TAF4 inactivation reveals the 3 dimensional growth promoting activities of collagen 6A3. *PLoS One* **9**, e87365 (2014).

12. Pesson, M., *et al.* A gene expression and pre-mRNA splicing signature that marks the adenoma-adenocarcinoma progression in colorectal cancer. *PLoS One* **9**, e87761 (2014).

13. Wang, Y., *et al.* Differential expression of mimecan and thioredoxin domain-containing protein 5 in colorectal adenoma and cancer: a proteomic study. *Experimental biology and medicine* **232**, 1152-1159 (2007).

14. Midwood, K.S., Mao, Y., Hsia, H.C., Valenick, L.V. & Schwarzbauer, J.E. Modulation of cell-fibronectin matrix interactions during tissue repair. *J Investig Dermatol Symp Proc* **11**, 73-78 (2006).

15. Han, S., Khuri, F.R. & Roman, J. Fibronectin stimulates non-small cell lung carcinoma cell growth through activation of Akt/mammalian target of rapamycin/S6 kinase and inactivation of LKB1/AMP-activated protein kinase signal pathways. *Cancer research* **66**, 315-323 (2006).

16. Mikula, M., *et al.* Integrating proteomic and transcriptomic high-throughput surveys for search of new biomarkers of colon tumors. *Functional & integrative genomics* (2010).

17. Spivey, K.A. & Banyard, J. A prognostic gene signature in advanced ovarian cancer reveals a microfibril-associated protein (MAGP2) as a promoter of tumor cell survival and angiogenesis. *Cell adhesion & migration* **4**, 169-171 (2010).

18. Oskarsson, T., *et al.* Breast cancer cells produce tenascin C as a metastatic niche component to colonize the lungs. *Nature medicine* **17**, 867-874 (2011).

3.2 Inflammatory bowel disease : a murine model

An approach similar to the one discussed in section 3.1 has driven the collaboration with a scientific group from Weizmann Institute (Rehovot, Israel), led by Prof. Irit Sagi. In this case, the inflammatory bowel disease (IBD), a group of colon and upper intestine inflammations including also ulcerative colitis and Crohn's disease, has been investigated through mice-derived samples. The importance of this research relies on the increasing concern which IBD is raising inside the medical community, as well as its debilitating character and still unknown exact etiology. Moreover, tissue damage associated with IBD is yet considered more as a secondary outcome than a contributing factor. By contrast, a previous work [15] has recently provided preliminary evidence suggesting that the ECM plays an active role in intestinal inflammation. Indeed, we will see once again how changes in ECM morphology, composition and stiffness may represent the markers of disease onset, thus showing potential for early IBD diagnostics or therapeutic strategies targeting the ensemble cell-ECM as a whole. In this specific context, AFM-based mechanical measurements have revealed a decrease in ECM stiffness, along with the pathology progression; this finding is well supported by topographic images highlighting a progressive weakening and deterioration of the ECM fine structure.

Here below, an extract of the work by Shimshoni et al. [27], mainly related to AFM measurements, is reported; this material must be considered as confidential, since the paper is actually unpublished. Two different models, the transient acute colitis and the persistent chronic colitis are analyzed. Acute colitis was induced in wild type (WT) C57BL/6 mice via addition of DSS (dextran sodium solfate) into the drinking water, whereas to gain insight on chronic intestinal inflammation, C57BL/6 IL-10-/- mice that spontaneously develop chronic colon inflammation have been used. The latter indeed is not chemically induced, but rather a result of a dysregulated immune system. The two models also allow us to identify two pre-symptomatic states, i.e. day 4 of the DSS model and the healthy naïve IL-10-/- mouse.

Decoding omics: unsupervised tissue composition-to-structure translation reveals silent pathological states

Authors: Elee Shimshoni[1]†, Ran Afik[1]†, Anjana Shenoy[2], Miri Adler[3], Luca Puricelli[4], Alessandro Podestà[4], Tamar Geiger[2], Paolo Milani[4], Uri Alon[3] and Irit Sagi[1*]

Affiliations:

[1]Department of Biological Regulation, Weizmann Institute of Science, Rehovot, Israel

[2] Department of Human Molecular Genetics and Biochemistry, Sackler Faculty of Medicine, Tel Aviv University, Tel Aviv-Yafo, Israel

[3]Department of Molecular Cell Biology, Weizmann Institute of Science, Rehovot, Israel

[4]CIMAINA and Department of Physics, Università degli Studi di Milano, Milano, Italy

*Correspondence to: irit.sagi@weizmann.ac.il

†These authors contributed equally to this work.

One Sentence Summary: Intestinal inflammation can be predicted by linking extracellular matrix structure and composition.

Main Text:

Results

Colitis is associated by a gradual loss of colonic ECM rigidity

Biomechanical properties of decellularized ECM scaffolds derived from colons of WT and IL-10$^{-/-}$ C57BL/6 mice were analyzed using mesoscale atomic-force microscopy (AFM). Colons from all five states, i.e., healthy WT, day 4 of DSS, day 10 of DSS, healthy IL-10$^{-/-}$ and chronically ill IL-10$^{-/-}$ were used. The use of micrometer-sized probes instead of the classical sharp AFM tips (characterized by a radius of curvature of a few nm) allowed acquirement of mesoscopically averaged, statistically robust Young's Modulus (YM) values of the ECM scaffolds (*1*,*2*), which are representative of the collective contributions of nanoscale molecular components organized in micrometer-sized structural and functional domains in the ECM. Cumulative distributions of the measured YM values of colonic ECM samples are broad (**Fig. S1**), demonstrating a strong diversity of elastic properties within the same sample, which can be attributed to the complex structure and composition of the ECM. Each mode in the cumulative distributions (**Fig. S1** and **Table S2**) represents the elastic properties of a region of the ECM with lateral dimensions (and thickness) of several microns, what we may define a structural and functional domain of the ECM. The corresponding single-mode median values and average median values of the YM are reported in **Fig. 2D-E**.

A general trend is observed in all cases: the ECM of inflamed colons are overall softer than those of healthy colons, as portrayed by the median YM (**Fig. 2D-E** and **Tables S1**). Noticeably, the structurally modified ECM in the pre-symptomatic state (day 4) of the DSS model shows an intermediate behavior, between the healthy and acutely inflamed states. The trend observed in the acute model is augmented in the chronic model, as the ECM of the chronically ill IL-10$^{-/-}$ is much softer than that of the healthy IL-10$^{-/-}$, portrayed by the median YM (**Fig. 2E** and **Table S1**). Moreover, it appears that the rigidity of the ECM, as opposed to its structure, is similar in healthy colons across the two mouse strains, namely both healthy IL-10$^{-/-}$ and healthy WT mice have a relatively stiff colonic ECM, with median YM values of 11.00 kPa and 10.55 kPa respectively. Nevertheless, the ECM of the chronically inflamed colon is much softer than any other ECM, with a YM value of approximately two-fold less than that of the acutely inflamed colon (**Tables S1**). Altogether, the analysis indicates a gradual softening of the ECM over the course of acute colitis development, peaking in concordance with the acute symptoms. This loss of rigidity is even more pronounced in the chronic colitis model. This softening is most likely occurring due to the structural deterioration and perforation of the matrix, as observed in the imaging modalities (**Fig. 2A-C**).

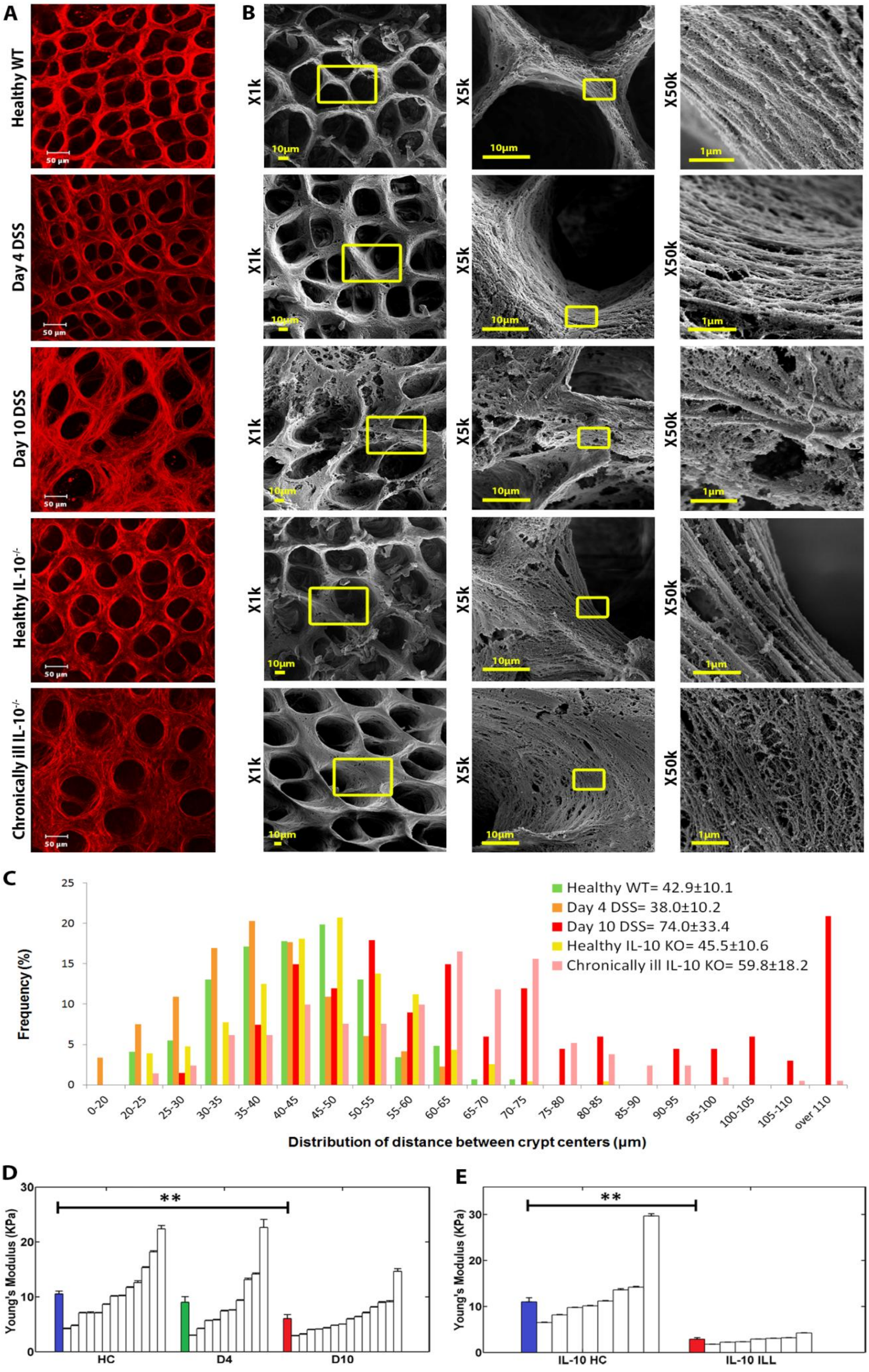
A
Healthy WT
Day 4 DSS
Day 10 DSS
Healthy IL-10-/-
Chronically ill IL-10-/-
50 µm
B
X1k
X5k
X50k
10µm
1µm
C
Healthy WT= 42.9±10.1
Day 4 DSS= 38.0±10.2
Day 10 DSS= 74.0±33.4
Healthy IL-10 KO= 45.5±10.6
Chronically ill IL-10 KO= 59.8±18.2
Frequency (%)
0
5
10
15
20
25
0-20
20-25
25-30
30-35
35-40
40-45
45-50
50-55
55-60
60-65
65-70
70-75
75-80
80-85
85-90
90-95
95-100
100-105
105-110
over 110
Distribution of distance between crypt centers (µm)
D
Young's Modulus (KPa)
0
10
20
30
**
HC
D4
D10
E
Young's Modulus (KPa)
0
10
20
30
**
IL-10 HC
IL-10 ILL

Fig. 2. Structural and mechanical damaging of the ECM during colitis.

(A) Second-harmonic imaging of mouse colon on the indicated time points over the course of the disease, corresponding to distinct states: healthy WT, pre-symptomatic (day 4 of DSS and healthy IL-$10^{-/-}$), acute inflammation (day 10 of DSS) and chronic inflammation (Chronically ill IL-$10^{-/-}$, 14 days after piroxicam discontinuation). Mice were sacrificed on the indicated time point, and colon was snap frozen in liquid nitrogen. On day of imaging, all samples were thawed in PBS and immediately imaged under a two-photon microscope (X20 objective). Vast ECM structural changes occur in acute inflammation, as indicated in the comparison between day 0 and day 10. Remarkably, some reorganization of the ECM is apparent from day 4, before clinical symptoms are evident. Healthy IL-$10^{-/-}$ display different ECM structure than that of WT mice, with ECM condensation similar to that of day 4. Chronic illness leads to an overall maintained crypt architecture, but with loosely packed ECM. **(B)** Scanning electron microscope (SEM) images of decellularized colonic ECM at the corresponding states, at three different magnifications. Note the damage and crypt size heterogeneity apparent on day 10 compared to Healthy WT colon. Also note, that the ECM under chronic illness is characterized by perforated crypt walls with thin fibrils. Most remarkably, the two pre-symptomatic states (day 4 and healthy IL-$10^{-/-}$) show a common feature of exposure of fibrillar ECM proteins on the crypt walls. **(C)** Distribution of distances between two adjacent crypt centers ($n>30$) at the different states as measured in different SEM images. Means ± standard deviation are denoted in legend. Means are significantly different from one another ($p<0.001$). Note that crypt size variance is increased in states of illness. **(D+E)** Properly weighted median values and associated errors, for both the cumulative distributions (filled colored bars in each group) and the underlying single-mode contributions (empty bars in each group) represented in Fig. S1. The statistical significance of differences between the various states of inflammation has been evaluated by applying a two-tailed student's t-test. The results show a significant ($p<0.01$) reduction in ECM rigidity between the healthy and acutely inflamed samples, as well as between the healthy and chronically inflamed states ($p<0.002$). The differences between the pairs HC-D4 and D4-D10 are not statistically significant ($p<0.30$ and $p<0.10$, respectively); nevertheless, pre-symptomatic ECMs (D4) show an intermediate behavior with respect to the healthy and acutely inflamed cases.

Supplementary Materials

Materials and Methods

Testing elastic properties of ECM samples by Atomic Force Microscopy

The AFM analysis was carried out on ECM samples derived from mouse colon tissues. Typically, three-four samples were analyzed for each inflammatory condition. ECM samples were grossly dried and attached to glass coverslips (diameter 15 mm) by means of a thin bi-adhesive tape. Samples were then attached to the bottom of Petri dishes (Greiner Bio-One) and left overnight in an evacuated desiccator in order to dry out, so to improve spreading and adhesion of ECM on tape. Prior to AFM measurements, the Petri dish hosting the ECM sample was filled with ddH_2O and the ECM was allowed to rehydrate for 30 minutes at room temperature. Measurements were carried out at room temperature.To accomplish the nanomechanical characterization of the ECM samples, a Bioscope Catalyst AFM (Bruker) was used to collect series of force vs distance curves (*3*), recording the local deformation of the sample induced by the AFM probe. According to a recently published protocol (*2*), we used monolithic borosilicate glass probes consisting in micrometer-sized spherical glass beads with radius R=9-10 µm attached to silicon cantilevers with a force constant k=0.25-0.35 N/m. The probes were produced and characterized as previously described (*1*). Each set of force curves (a force volume) consisted of a 16x16 array of curves acquired on a 70µm × 70µm area. Ten force volumes were typically recorded on each ECM on macroscopically separated regions. All measurements were performed with the following parameters: 4096 points per curve, ramp length $L=10\ \mu m$, maximum applied force $F = 60\text{-}70nN$, and ramp frequency $f=1.10\ Hz$. Typically, indentations up to 2-3 µm were obtained. Data processing of force volumes was carried out in Matlab according to the general protocol described previously (*2*). The values of the Young's Modulus (YM) were extracted by fitting the Hertz model to the experimental data (*3*). A first very soft indentation region (0-40% of total indentation) was excluded, in order to separate the possible contribution of loosely-bound superficial layers from those of the bulk ECM. Artifacts deriving from an ill-defined contact area between sample and probe, like boundaries of colonic crypts or more generally crypts with characteristic dimensions comparable to, or larger than the probe diameter, were identified and discarded.

The cumulative distributions of YM values of the ECMs from mice turned out to be the envelope of several nearly lognormal modes, representing the major contributions to the overall ECM rigidity and originating from micro-scale domains that the AFM probe was able to resolve. Each mode in the cumulative distributions represents the elastic properties of a region of the ECM with lateral dimensions (and thickness) of several microns, which may define a structural and functional domain of the ECM. Multi-Gaussian fit in semilog10 scale allowed identification of the peak value E' and the geometric standard deviation σ_g^{10} of each lognormal mode; from these values the median value E_{med} and the standard deviation of the median σ_{med} were evaluated for all modes as $E_{med} = 10^{E'}$ and $\sigma_{med} = \sqrt{\pi/2} E_{med} \sigma_g^{10} / \sqrt{N}$ (*4*), N being the number of force curves in each mode.

The effective rigidity of each ECM sample was characterized by the weighted average of median values $E = \sum_i f_i E_{med,i}$, using the fraction $f_i = N_i/N_{tot}$ of force curves in the mode as the weight; the total error σ_E associated to E was calculated by summing in quadrature the propagated error of the medians $\sigma = \sqrt{\sum_i f_i^2 \sigma_{med,i}^2}$ and an effective instrumental relative error $\sigma_{instr} = 3\ \%$: $\sigma_E = \sqrt{\sigma_{instrum}^2 E^2 + \sigma^2}$. The average median values of the YM of the different states of inflammation have also been evaluated; the corresponding error has been calculated as the standard deviation of the mean summed in quadrature with the propagated σ_E. The statistical significance of differences between YM values of different states of inflammation has been evaluated applying a two-tailed student's t-test.

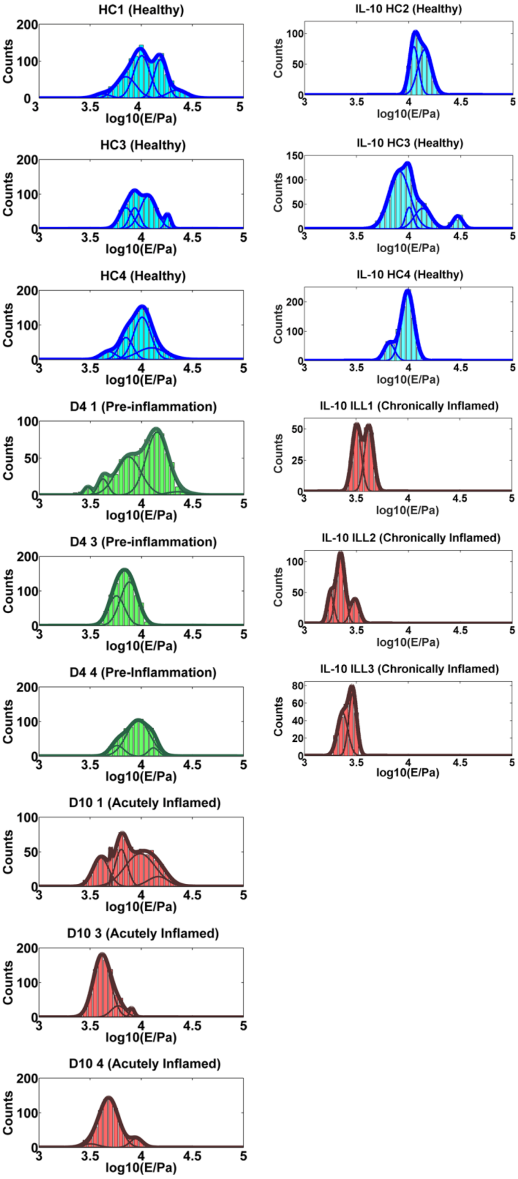

Fig. S1.

Cumulative distributions of Young’s Modulus values (E) measured on ECMs derived from colons of mice at three different states of the DSS-induced colitis model and two states of the PAC IL-10$^{-/-}$ model (HC: healthy colon; D4: pre-symptomatic; D10: acutely inflamed; IL-10 HC: healthy naïve IL-10$^{-\backslash-}$; IL-10 ILL: chronically inflamed IL-10$^{-/-}$). The numbers next to each condition name stand for different samples. Thick lines represent the result of the superposition of the underlying major contributions, highlighted by thin continuous lines. Single contributions are detected by fitting the envelope of several Gaussian profiles to data in semilog10 scale. Under the hypothesis that the underlying distributions are log-normal, the peaks of the Gaussians represent the median values of the Young’s Modulus. Different contributions arise from the fact that each ECM is tested in different locations, therefore multiple modes witness the mechanical and structural heterogeneity of ECMs.

Sample		Young’s Modulus / kPa (weighted median ± propagated errors)	Young’s Modulus / kPa (average median ± effective STD of the mean)
Healthy WT (day 0)	**HC 1**	11.61 ± 0.25	10.55 ± 0.49
	HC 3	10.39 ± 0.26	
	HC 4	9.65 ± 0.25	
Pre-Symptomatic (day 4)	**D4 1**	11.07 ± 0.39	9.03 ± 1.01
	D4 3	6.86 ± 0.25	
	D4 4	9.15 ± 0.36	
Acutely inflamed (day 10)	**D10 1**	8.23 ± 0.24	6.04 ± 0.72
	D10 2	6.31 ± 0.24	
	D10 3	4.47 ± 0.15	
	D10 4	5.14 ± 0.18	
Healthy IL-10$^{-/-}$	**IL-10 HC2**	12.94 ± 0.30	11.00 ± 0.90
	IL-10 HC3	10.84 ± 0.20	
	IL-10 HC4	9.21 ± 0.24	
Chronically ill IL-10$^{-/-}$	**IL-10 ILL1**	3.71 ± 0.06	2.89 ± 0.34
	IL-10 ILL2	2.32 ± 0.03	
	IL-10 ILL3	2.64 ± 0.04	

Table S1.
Statistical indicators and associated errors derived from the single-mode analysis for the cumulative distributions of Young’s Modulus values of ECMs represented in Figure 2D and 2E. STD- standard deviation. The numbers next to each condition name stand for different samples. All data are expressed in kPa units.

Sample	**Young's Modulus / kPa** **(median ± STD of the median)**					
Healthy WT 1		4.17 ± 0.14	7.08 ± 0.12	10.12 ± 0.11	15.33 ± 0.15	22.40 ± 0.60
Healthy WT 3			7.08 ± 0.19	8.63 ± 0.10	18.20 ± 0.21	
Healthy WT 4		4.76 ± 0.11	7.08 ± 0.09	10.20 ± 0.11 12.60 ± 0.33		
Day 4 1	2.98 ± 0.07	4.21 ± 0.08	7.42 ± 0.15		14.16 ± 0.20	22.66 ± 1.46
Day 4 3			5.68 ± 0.07 7.59 ± 0.08			
Day 4 4			5.80 ± 0.11	9.35 ± 0.13	13.16 ± 0.24	
Day 10 1		4.02 ± 0.07	5.03 ± 0.03 6.38 ± 0.09	9.76 ± 0.22	14.64 ± 0.50	
Day 10 2	2.89 ± 0.07	4.31 ± 0.12	7.08 ± 0.15			
Day 10 3		4.11 ± 0.04	5.96 ± 0.11	8.12 ± 0.11		
Day 10 4	3.19 ± 0.11	4.81 ± 0.05			8.96 ± 0.18	
IL-10 Healthy 2				11.19 ± 0.11 14.20 ± 0.17		
IL-10 Healthy 3			8.17 ±0.10	10.13 ± 0.12 13.62 ± 0.24	29.66 ± 0.51	
IL-10 Healthy 4			6.52 ± 0.08	9.77 ± 0.06		
IL-10 Ill 1		3.20 ± 0.04 4.23 ± 0.05				
IL-10 Ill 2	1.78 ± 0.02 2.23 ± 0.02	3.07 ± 0.04				
IL-10 Ill 3	2.33 ± 0.03	2.91 ± 0.03				

Table S2.

Major contributions to the broad statistical distributions (see Materials and Methods section for details). The numbers next to each condition name stand for different samples. STD - standard deviation. All data are expressed in kPa units.

References

1. M. Indrieri, A. Podestà, G. Bongiorno, D. Marchesi, P. Milani, Adhesive-free colloidal probes for nanoscale force measurements: production and characterization. *Rev. Sci. Instrum.* **82**, 023708 (2011).
2. L. Puricelli, M. Galluzzi, C. Schulte, A. Podestà, P. Milani, Nanomechanical and topographical imaging of living cells by atomic force microscopy with colloidal probes. *Rev. Sci. Instrum.* **86**, 033705 (2015).
3. H.-J. Butt, B. Cappella, M. Kappl, Force measurements with the atomic force microscope: Technique, interpretation and applications. *Surf. Sci. Rep.* **59**, 1–152 (2005).
4. H. Cramér, Mathematical Methods of Statistics. *Princet. Univ. Press* (1999).

3.3 Additional discussion

ECMs may be classified among the most challenging biological samples from the experimental point of view. As discussed in the papers reported in sections 3.1 and 3.2 (refs. [26, 27]), they require a detailed and fine-tuned biochemical protocol in order to be decellularized, i.e. get rid of cells and cellular debris, without losing their own structural and compositional properties; moreover, a careful preparation is needed too for AFM-based measurements (see also Chapter 5). Alongside this, ECMs typically show an enhanced topographical heterogeneity, compared to other biological samples (e.g. cells), even on the microscale and on both horizontal and vertical directions. This is particularly marked in the case of colon ECMs, which display large and deep holes (the cellular crypts), with dimensions comparable to or even bigger (see fig. 1.1) than the radii of the colloidal probes employed so far in this work ($R \leq 10\,\mu m$). Luckily, not all the possible types of tissue-derived ECMs exhibit crypts or such an extreme heterogeneity (e.g. bladder-derived ECMs, ref. [49]); in any case, these features hardly match with the classic contact mechanics models (see section 2.1, ref. [16]) which describe the deformation of continuous bodies, thus implying that the typical dimensions of discrete, step-like topographical features of the analyzed samples are much smaller than the characteristic dimensions of the probe.

Consequently, many force curves acquired on colon ECMs by AFM had to be dropped, as mentioned in section 3.1, due to a bad agreement with the theoretical behavior described by the Hertz model. This has led to the idea of moving towards very big colloidal probes, characterized by radii $R \geq 30\,\mu m$. If, on the one hand, these large probes should satisfy with greater accuracy the requirements at the basis of contact mechanics models, even in the case of complex samples such as ECMs, on the other hand this choice brings along some intrinsic drawbacks. Indeed, according to the Hertz model, for a fixed applied force F and sample elastic properties (Young's modulus E , Poisson ratio ν), the indentation δ is inversely proportional to the cube root of the probe radius [16]:

$$\delta = \left[\frac{3}{4}\left(\frac{1-\nu^2}{E}\right)F\right]^{\frac{2}{3}}\frac{1}{\sqrt[3]{R}} \tag{3.1}$$

Therefore, we need to apply larger forces, i.e. move towards stiffer cantilevers, since $F = Kd$, where d stands for the cantilever deflection and K represent its force constant. In turn, this implies the use of shorter cantilevers, since

$K \sim 1/L^3$ [43], where L stands for the cantilever length. Summarizing, the typical dimensions and masses of probes and cantilevers become comparable, along with increasing probe radii (fig. 3.2). This can determine nontrivial calibration issues for two fundamental parameters in the framework of AFM-based mechanics, i.e. cantilever force constant and deflection sensitivity, as extensively discussed in Appendix A.

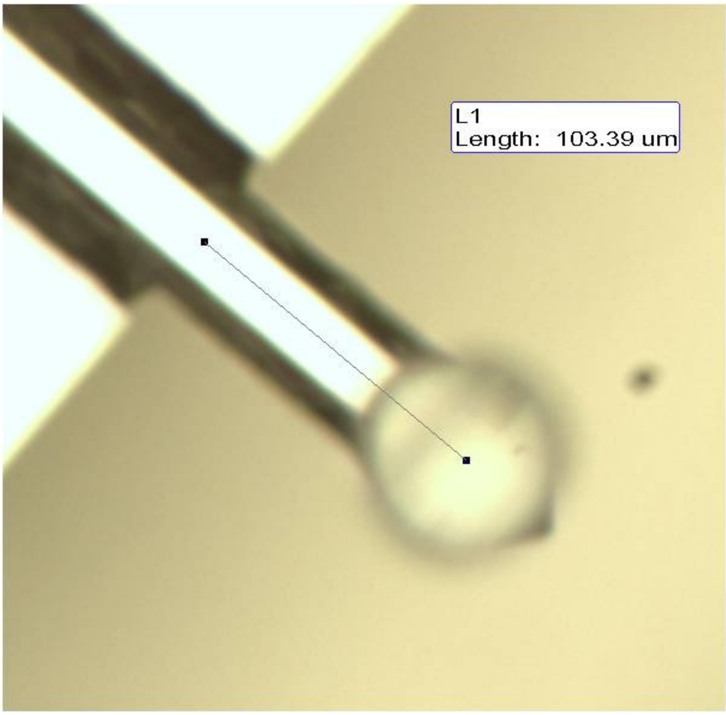

Figure 3.2: Optical microscope image of a colloidal probe with radius $R \sim 30\,\mu m$, attached to a tapping-mode cantilever characterized by $K \sim 50\,N/m$. The measured distance between the probe center and the cantilever base is reported. The sphere appears out of focus with respect to the cantilever profile due to its dimensions.

Chapter 4

Mimicking the ECM: engineering nanostructured biocompatible substrates

4.1 Differentiation of PC12 cells induced by nanostructured zirconia surfaces

As outlined in section 1.2, a better understanding of the interplay between ECMs and cells can be useful to improve the efficacy of in-vitro systems, mainly aimed at a controlled stimulation of given cellular behaviors. This can provide a significant breakthrough in the biomedical field, from the point of view of both basic and applied research, allowing us to develop specific cell culturing devices or to greatly improve the potency and functionality of implants and interfaces in general. Nevertheless, it appears to be a daunting task, requiring a deep quantitative comprehension of cell-microenvironment interactions starting from the nanoscale: this, in turn, is fundamental to achieve control and reproducibility, key features to translate basic knowledge into effective applications. Among the many possible pathways linking ECM with cellular behavior and fate (fig. 1.3), in the last decades lot of efforts have been dedicated to the mimicking of the main topographical and architectural features of ECMs on the nanoscale; however, only a partial and qualitative understanding of the mechanotransductive process, linking topographical and mechanical cues on the nanoscale to the cellular response on the microscale, has been obtained so far. Moreover, the design of ordered patterns by means of top-down approaches [32] doesn't look able to capture the true ECM features, which usually appear rough yet disordered on the nanoscale (fig. 1.4 A).

In the following, a paper by Schulte et al., to which I contributed as a co-author, is reported. This work aims at overcoming the main aforementioned limitations in the framework of mechanotransduction, with specific regard to the differentiation process induced on a neuron-like cell model (PC12) by nanostructured zirconia surfaces. These goals are achieved through the employment of a bottom-up technique like Supersonic Cluster Beam Deposition (SCBD) on the one hand, and the AFM-based analysis of both surface morfological properties and cell mechanics, joined to different types of microscopy and biochemical approaches, on the other. The working principles of SCBD are explained in detail in refs. [36, 37], [50]. Basically, this technique allows for the synthesis of nanostructured thin films starting from the generation and deposition of low-energy clusters on a selected substrate (fig. 4.1). The obtained morphology appears disordered (fig. 1.4 B); yet, it has been demonstrated [38] that SCBD enables to gain a very good control and reproducibility over several morphological "averaged" properties, like roughness, porosity, correlation length, and cluster size distribution. Therefore, this morphology enables us to mimic the "hierarchically ordered" disorder of the ECMs (see fig. 1.4). At the same time, AFM versatility allowed to characterize the main morphological properties of surfaces *on the nanoscale* by means of conventional sharp tips, as well as to show the combined topographic/mechanical response of cells *on the microscale* through colloidal probes, according to the protocol described in section 2.1. In any case, the knowledge of averaged properties like roughness is not enough by itself to achieve a deep understanding of the mechanotransductive process at the basis of PC12 differentiation, thus requiring a detailed analysis of the finer morphological features of the surfaces, like "asperities" distribution and dimensions. This, combined with important evidence provided by diverse experimental techniques, has let us to define a *quantitative* model underlying this specific mechanotransductive phenomenon, linking the information perceived by cells on the nanoscale to the global cellular response on the microscale in a *causal* way. In this framework, modulation of the cellular mechanical properties probed by AFM turned out to be, once again, an important biophysical marker, representing the key *integrating* signal for the onset of the differentiation process. Recently, the capability of disordered nanostructured surfaces to induce cellular differentiation has been demonstrated also for primary (ex-vivo) cells, like hippocampal neurons [40].

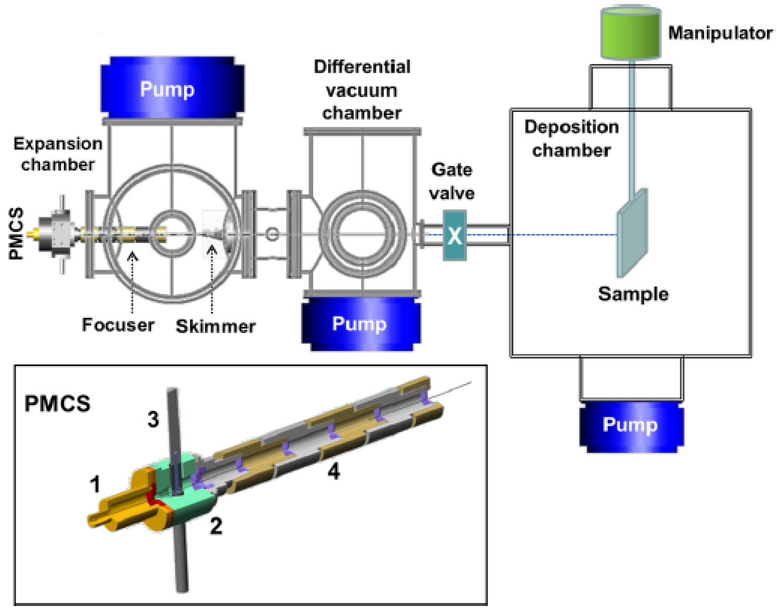
Manipulator
Pump
Differential vacuum chamber
Expansion chamber
Deposition chamber
Gate valve
PMCS
X
Sample
Focuser
Skimmer
Pump
Pump
PMCS
3
1
4
2

FIG. 1. The SCBD apparatus. The mixture of gas and clusters is accelerated by a difference of pressure between the interior of the cluster source (higher pressure) and the expansion chamber (lower pressure and high vacuum), and collimated through the aerodynamic focuser. A skimmer selects the central portion of the beam. Eventually, nanoparticles enter the deposition chamber and are deposited on a substrate to form a film with thickness in the 1–1000 nm range. The details of the PMCS are shown in the inset: the pulsed valve (1) injects the carrier gas into the ceramic body (2) of the source, hosting the Ti rod (3); the focuser (4) containing the aerodynamic lenses concentrates the nanoparticles along the beam axis.

Figure 4.1: Schematics of the SCBD experimental apparatus, joined to a pulsed Micro-plasma Cluster Source. Reproduced from [38].

Schulte *et al. J Nanobiotechnol (2016) 14:18*
DOI 10.1186/s12951-016-0171-3

Journal of Nanobiotechnology

RESEARCH

Open Access

Conversion of nanoscale topographical information of cluster-assembled zirconia surfaces into mechanotransductive events promotes neuronal differentiation

Carsten Schulte[1*†], Simona Rodighiero[4], Martino Alfredo Cappelluti[2,4], Luca Puricelli[1], Elisa Maffioli[3,4], Francesca Borghi[1], Armando Negri[3,4], Elisa Sogne[2,4], Massimiliano Galluzzi[1], Claudio Piazzoni[1], Margherita Tamplenizza[4], Alessandro Podestà[1], Gabriella Tedeschi[3,4], Cristina Lenardi[1] and Paolo Milani[1*†]

Abstract

Background: Thanks to mechanotransductive components cells are competent to perceive nanoscale topographical features of their environment and to convert the immanent information into corresponding physiological responses. Due to its complex configuration, unraveling the role of the extracellular matrix is particularly challenging. Cell substrates with simplified topographical cues, fabricated by top-down micro- and nanofabrication approaches, have been useful in order to identify basic principles. However, the underlying molecular mechanisms of this conversion remain only partially understood.

Results: Here we present the results of a broad, systematic and quantitative approach aimed at understanding how the surface nanoscale information is converted into cell response providing a profound causal link between mechanotransductive events, proceeding from the cell/nanostructure interface to the nucleus. We produced nanostructured ZrO_2 substrates with disordered yet controlled topographic features by the bottom-up technique supersonic cluster beam deposition, i.e. the assembling of zirconia nanoparticles from the gas phase on a flat substrate through a supersonic expansion. We used PC12 cells, a well-established model in the context of neuronal differentiation. We found that the cell/nanotopography interaction enforces a nanoscopic architecture of the adhesion regions that affects the focal adhesion dynamics and the cytoskeletal organization, which thereby modulates the general biomechanical properties by decreasing the rigidity of the cell. The mechanotransduction impacts furthermore on transcription factors relevant for neuronal differentiation (e.g. CREB), and eventually the protein expression profile. Detailed proteomic data validated the observed differentiation. In particular, the abundance of proteins that are involved in adhesome and/or cytoskeletal organization is striking, and their up- or downregulation is in line with their demonstrated functions in neuronal differentiation processes.

Conclusion: Our work provides a deep insight into the molecular mechanotransductive mechanisms that realize the conversion of the nanoscale topographical information of SCBD-fabricated surfaces into cellular responses, in this case neuronal differentiation. The results lay a profound cell biological foundation indicating the strong potential of these surfaces in promoting neuronal differentiation events which could be exploited for the development of prospective research and/or biomedical applications. These applications could be e.g. tools to study mechanotransductive processes, improved neural interfaces and circuits, or cell culture devices supporting neurogenic processes.

---

*Correspondence: carsten.schulte@unimi.it; paolo.milani@mi.infn.it
†Carsten Schulte and Paolo Milani are co-last authors
[1] CIMAINA, Dipartimento di Fisica, Università degli Studi di Milano, via Celoria 16, Milan 20133, Italy
Full list of author information is available at the end of the article

© 2016 Schulte et al. This article is distributed under the terms of the Creative Commons Attribution 4.0 International License (http://creativecommons.org/licenses/by/4.0/), which permits unrestricted use, distribution, and reproduction in any medium, provided you give appropriate credit to the original author(s) and the source, provide a link to the Creative Commons license, and indicate if changes were made. The Creative Commons Public Domain Dedication waiver (http://creativecommons.org/publicdomain/zero/1.0/) applies to the data made available in this article, unless otherwise stated.

Keywords: Mechanotransduction, Focal adhesion, Biomaterial, Integrin, Atomic force microscopy, Biophysics, Cell adhesion, Proteomics

Background

Cells are capable of sensing, in a surprisingly precise manner, nanoscale topographical features and mechanical characteristics of the microenvironment they interact with, mainly via integrin-mediated adhesion sites which serve as mechanoreceptors [1–4].

The conversion of these physical signals (structural and mechanical cues) into a modulation of the cellular (biochemical) responses is defined as mechanotransduction [5, 6]. The general meaning of this concept is that the stiffness and the topography of the extracellular matrix (ECM) [2, 4, 7] influence the architecture and composition of adhesions sites (e.g. integrin clustering) which feedbacks on the force transmission, cytoskeletal organization and mechanical properties (e.g. actomyosin network configuration) of the cell. The variation of the cellular biophysical state impacts on the nuclear architecture and mechanosensitive transcription factors which eventually modulate the cellular program or even the cell fate [1–6]. Mechanotransduction involves different molecules and/or cellular components, i.e. the ECM, channels, focal complexes/adhesions (FC or FA), the actomyosin network, transcription factors and the nucleus [1–9]. Cellular mechanosensing and mechanotransduction have been shown to play an important role in differentiation processes [2, 6, 9, 10], in particular also in a neuronal context. Especially the growth cones of neuronal cells constantly explore the status of their microenvironmental surroundings which in turn has a strong impact on the behavior (growth cone advancement or retraction/guidance) and differentiation/maturation events of these cells [11].

Many aspects, in particular the role of the ECM nanoscale topography and architecture in determining the mechanotransductive signaling, are still poorly understood due to the extremely high structural and functional complexity [2, 4, 7].

In order to dissect the fundamental factors concurring to the building of ECM nanotopographic complexity and to identify the structural ingredients for the mimicking of the in vivo ECM characteristics, a huge effort has been concentrated on the fabrication of artificial substrates where micron- and nanoscale features can be precisely controlled and mixed [2, 4, 9, 12].

In the case of neuronal cells, it has been demonstrated that they have a nanoscale sensitivity for environmental surface features and that their cellular activities are strongly affected by the interaction with these features [11–15]. Several studies suggest that the nanoscale topography obtained e.g. by the use of electrospun fibers [16], or ordered nanopatterns [17–20] can contribute to a modulation of neuronal differentiation processes.

Gaining a reliable and reproducible control of the topographic surface features on the nanoscale level to mimic the complex structure of the ECM is a daunting challenge: in the last decades a reductionist approach has been adopted consisting in the micro- and nanofabrication of simple basic motifs such as grooves, pillars, dots with different dimensions and pitches in order to reproduce and to recapitulate the elemental topographical cues that may influence the cell behavior [2, 4, 9, 12]. This approach has also been dictated by the fact that the vast majority of micro- and nanofabrication techniques were taken from the microelectronic or from the molecular electronic world (top-down lithographic approaches, micromolding, nanoimprint, etc.). This restricted also the choice of the substrate materials to those typically used in these contexts. In general these high-precision fabrication methods are quite expensive and difficult to scale-up [4, 12]. Most importantly it is yet to be demonstrated that starting from simple topographical motifs one can reconstruct realistically the ECM complexity [2].

As an alternative, methods exploiting chemical or physical etching are largely used in the production of implants since they provide the possibility of obtaining disordered surfaces at the nano- and microscale over large surfaces of different metallic materials [4, 12], however the tuning to the best performing surface topography in terms of cell adhesion and differentiation is based essentially on a trial-and-error approach with no predictive quantitative evaluation of the topographical features inducing the observed cell behavior [2, 4, 12].

There is still an eminent need for an in-depth insight of the proposed molecular mechanisms of mechanotransduction, even more in the context of biomaterials highlighted in this work, to realize a reliable, efficient and intelligent development of potential research and/or medical applications [2, 4, 9, 12]. Here we present the results of a broad, systematic and quantitative interdisciplinary approach aimed at capturing the complexity of the mechanotransductive signaling cascade provoked by cellular interaction with nanostructured zirconia substrates with tailored and reproducible nanoscale topography. Zirconia is a biocompatible material used in various clinical applications (i.e. for dental and orthopaedic prostheses), especially due to its favorable chemical and structural properties [21].

In this work the approach for the production of nanostructured ZrO_2 substrates with disordered yet controlled topographic features is based on the assembling of zirconia nanoparticles, produced in the gas phase and accelerated in a supersonic expansion, on a flat substrate (Supersonic Cluster Beam Deposition, SCBD) [22]. This bottom-up assembling technique produces nanostructured films obtained by randomly distributed clusters, thus creating a nanoscale topography whose roughness can be accurately controlled and varied in a reproducible manner [23]. This very precise and reproducible control over nanoscale topography can be easily obtained over macroscopic areas which is a necessary requirement for the large number of experiments performed in this study.

As cell model to study the neuronal differentiation we utilized PC12 cells, a well-established cell model to address biological questions regarding this subject (also presented in various publications throughout this manuscript).

Starting from an ultrastructural characterization of the cell/nanostructure interface, we followed intracellular physiological conditions (i.e. FA dynamics, cytoskeletal organization, nanomechanical properties, CREB phosphorylation) that eventually influence and alter the cellular program and activities. Taken together, our data enable a causal link of the nanoscale topography-induced mechanotransductive events and emphasize the significant potential of nanostructured cluster-assembled substrates in influencing essential cellular functions, in particular in inducing (neuronal) differentiation processes. This potential could be utilized e.g. for the rational design of enhanced neural interfaces and circuits, devices promoting neurogenic events or tools for mechanotransduction studies.

Results and discussion

Cluster-assembled zirconia surface induces neuritogenesis

In a previous study we have shown that the nanoscale topographic cues of cluster-assembled titania surfaces produced by SCBD trigger neuritogenesis in the neuron-like PC12 cells in the absence of a biochemical stimulus [15]. An involvement of processes associated with cell adhesion and the cytoskeleton was broached but the detailed molecular mechanisms were not investigated.

This phenomenon occurs also for cluster-assembled zirconia substrates with different nanoscale roughnesses. Figure 1a displays the biological response of PC12 cells after 24 h of interaction with different substrates, including flat zirconia (flat-Zr), nanostructured cluster-assembled surfaces with different roughness parameter R_q of 15 nm (ns-Zr15) and 25 nm (ns-Zr25), and as canonical control poly-L-lysine (PLL)-coated glass, with and without the nerve growth factor (NGF). As criterion for differentiation the presence of at least one neurite (cell projections growing from the soma of a neuronal cell during the initial phase of neuronal differentiation) with a length > 10 μm was imposed (some prominent examples are indicated with arrows in Fig. 1a and in a close-up in Additional file 1: Figure S1 the features of differentiated PC12 are illustrated).

Nanostructured zirconia induced differentiation and therewith neuritogenesis even in the absence of NGF, with the strongest effect on ns-Zr15 surfaces. Here, the differentiation and neurite outgrowth was in the range of the canonical condition achieved by NGF stimulation of PC12 cells plated on PLL (Fig. 1b). Also the rougher ns-Zr25 surfaces triggered differentiation, yet to a lower extent, which could be complemented, though, by the addition of NGF. Cells on flat-Zr surfaces instead did not show any sign of neuritogenesis, not even if they were exposed to the NGF stimulus (Fig. 1b). The potential of zirconia surfaces to induce NGF-independent neuritogenesis are thus correlated to their nanoscale morphological properties.

Characterization of surface nanoscale morphology of cluster-assembled ZrO_2 films

Figure 2a, b show typical AFM topographic maps (Fig. 2a: top- and Fig. 2b: 3-dimensional views) of PLL-coated glass, flat-Zr, ns-Zr15 and ns-Zr25 surfaces. PLL-coated glass and flat-Zr are very smooth (R_q < 1 nm) compared to the nanostructured ZrO_2 films of different nanoscale roughnesses, as evident from the comparison of representative surface profiles shown in Fig. 2c.

The surface profiles of cluster-assembled zirconia films show peaks and valleys defining complex random patterns with features whose size and spatial distribution resemble those of the ECM [7]. The structure and morphology of cluster-assembled films are characterized by the random hierarchical self-organization of nanometer-sized building blocks (the clusters) in larger and larger units (statistical scale invariance). This is substantially different from the highly regularly patterned nano- and micro-fabricated surfaces (i.e. pillars, gratings, holes) usually employed in the vast majority of nanotopography-related studies of biomaterials [2, 4, 12]. Although the presence of topographic disorder at the nanoscale has been shown to have a large influence on cell adhesion, integrin clustering and differentiation [2, 24], no systematic characterization of the influence of disordered substrates with different nanoscale features has been reported so far.

The complexity of the cluster-assembled zirconia morphology is the result of the growth mechanism of interfaces produced under the ballistic deposition regime (BDR), this regime is typical of the SCBD technique [23,

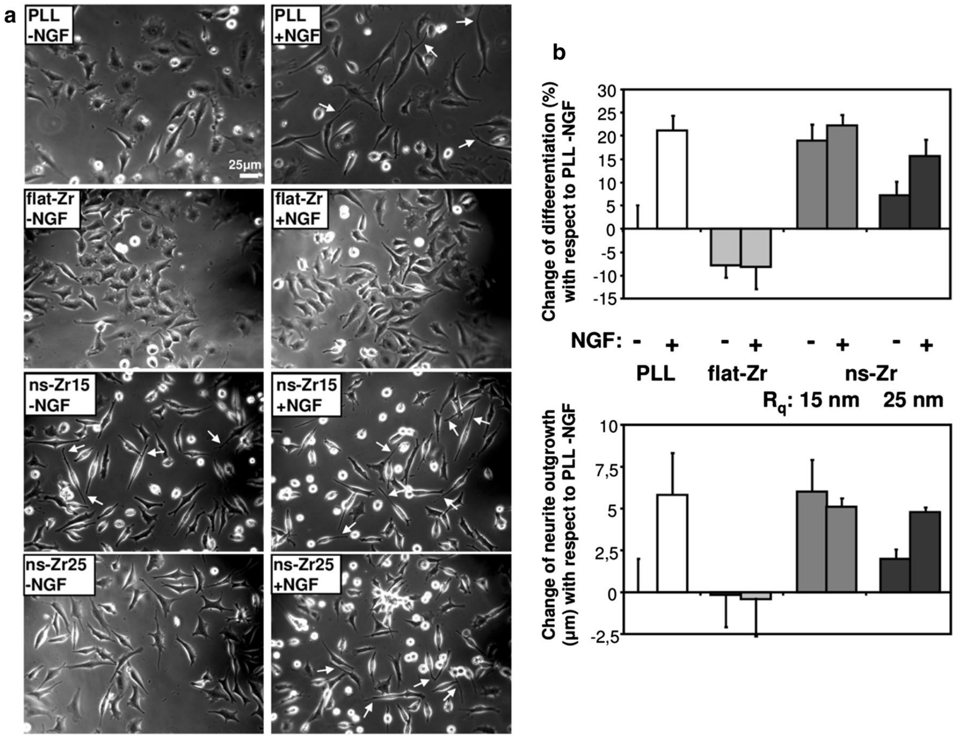

Fig. 1 SCBD-produced nanostructured zirconia induces neuronal differentiation in PC12 cells. **a** The phase contrast images demonstrate the biological responses of neuron-like PC12 cells after 24 h interaction with the different surfaces presented in Fig. 2 in the absence or presence of nerve growth factor (NGF). *White arrows* indicated typical examples of neurite outgrowth of differentiated PC12 cells (in Additional file 1: Figure S1, **a** close up image of representative differentiated cells on ns-Zr15 is shown to illustrate more detailed the features of differentiated PC12 cells). **b** On the right the corresponding statistical quantification of the differentiation rate (*top*) and neurite outgrowth (*bottom*) is shown. A cell that developed at least one neurite with a length >10 µm was counted as differentiated, the quantification of neurite outgrowth are detailed in the "Methods" section. The *bars* represent the change of differentiation and neurite outgrowth compared to the PLL condition in the absence of NGF. The *bars* represent the average and are shown with the SD, representing the global statistics of five independent experiments (n: >500 cells, >150 neurites)

25]. In BDR, elemental building blocks (atom clusters in our case) produced in the gas phase land on a substrate sticking without significant mobility; fragmentation of the clusters upon landing is inhibited due to their low kinetic energy [22]. In the framework of BDR regime, the nanoscale roughness of cluster-assembled surfaces can be quantitatively analysed and precisely reproduced, since it depends on simple scaling laws [23, 25]. This means that the topographical features and the evolution of disordered cluster-assembled substrates can be described by simple mathematical models [25]. In particular, the surface roughness R_q and other morphological parameters (e.g. specific area, slope, lateral correlation length) in the BDR regime depend on the film thickness and typically increase with it [23]. By carefully characterizing the evolution of the nanoscale surface parameters with film thickness it is thus possible to obtain a calibration allowing the precise and reproducible control over the surface morphology evolution by controlling the SCBD deposition parameters [23].

Potential of nanostructured zirconia surfaces in modulating cell adhesion-related processes

Nanoscale roughness is an important parameter influencing the interaction of surfaces with proteins and cells [2, 4, 7, 26, 27], however, it does not provide details about the precise surface nanoscale information relevant for the cell and hidden in the configuration of the random layout of asperities. Yet, it is this configuration which is likely to impact on mechanotransductive processes in cells via the

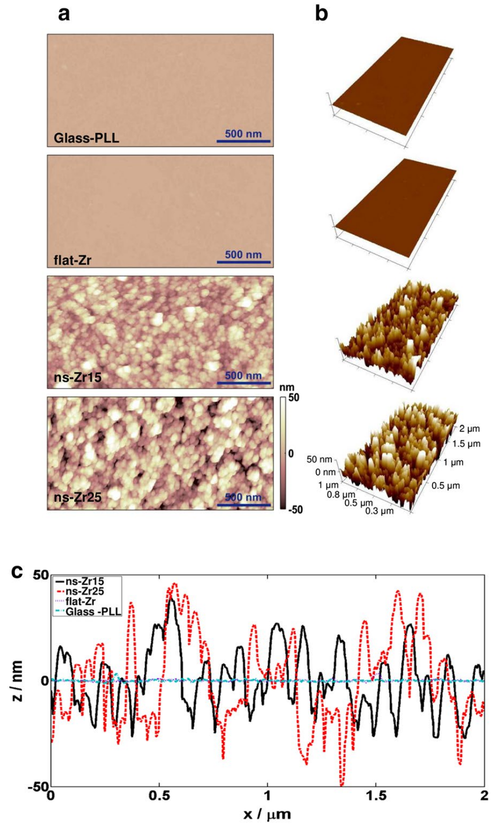

Fig. 2 AFM morphological analysis of control and nanostructured surfaces produced by SCBD. The images show representative **a** *top views* and **b** *3-dimensional views* of the surfaces morphology of glass coated with poly-L-lysine (PLL), flat zirconia (flat-Zr) produced by e-beam evaporation, and nanostructured zirconia (ns-Zr) produced by SCBD with $R_q = 15$ (ns-Zr15), or 25 nm (ns-Zr25), respectively. **c** The *graphs* display a comparison of representative topographic profiles of different substrates

modulation of cell adhesion-related processes, in particular regarding integrin clustering and FA maturation/composition [2, 4, 24].

It was therefore important to study the asperity layout to understand profoundly what kind of nanoscale information is potentially perceived by cells interacting with the cluster-assembled zirconia surfaces. As a first step, we visualized and analyzed the actual cell/substrate interface. We achieved the visualization via ultrathin section images of the interaction interface recorded by transmission electron microscopy (TEM).

An exemplary illustration of the cellular interaction with flat-Zr and ns-Zr15 substrates is shown in Fig. 3a–c. A first important observation is that the cell membrane does not follow strictly the topographical profile of the surfaces; the cell instead interacts with the substrate at isolated locations, separated by regions where contact is not established. Figure 3b, and in particular the close-up in Fig. 3c, show that contact between the cell and the nanostructured substrate is achieved in correspondence of the apical part of the most protruding surface asperities. From the TEM sections contact regions have been quantitatively characterized and the results are reported in Table 1; Fig. 3d,e. While the spatial occurrence of contact regions (the average distance between nanoscopic adhesion regions) is statistically similar on the two surfaces, contact regions on flat-Zr (average diameter: 90 nm) are highly significantly (p value = 0.0002, Wilcoxon–Mann–Whitney test) larger than those on ns-Zr15 (average diameter: 53 nm) (Table 1).

Based on this initial observation, we determined from AFM topographic maps the characteristics of the potential individual nanoscopic contact sites provided to the cells by the nanostructured surface, which represent the actual nanoscale information sensed by the cells (for details on the approach, see “Methods” section and Additional file 2: Figure S2). Figure 4a, b shows representative asperity maps for ns-Zr15 and ns-Zr25 surfaces and Table 2 reports the median values and median absolute deviations (MADs) of the relevant parameters of surface asperities. The distributions of asperity diameters and contact areas are shown in Fig. 4e, f. The asperity diameters and the potential contact area for cells provided by the individual asperities are significantly smaller for the ns-Zr15 sample (diameter: −9 % but still significant with p value = 0.01, as the sample size (>2000) is large, area: −25 % p value = 0.001, double-sided t-test). Remarkably, the distributions of surface asperity diameters determined by AFM (Fig. 4e) and of adhesion contact widths from TEM sections (Fig. 3e) are quite similar (median values are 43 and 40 nm, respectively).

Together with intrinsic cellular conditions (discussed in detail in the following section “Intracellular processes induced by the cellular interaction with the nanoscale roughness of zirconia substrates: focal adhesion dynamics and cytoskeletal organization”), there are several pivotal features of extracellular microenvironment configuration which are decisive for the formation of superior adhesion structures, such as nanoclusters or even FC/As realized by integrin clustering and adhesome complex assembly [2, 3].

One of them is the available nanoscale adhesion area as there seems to exist a minimal adhesion unit (>4–9 integrins)

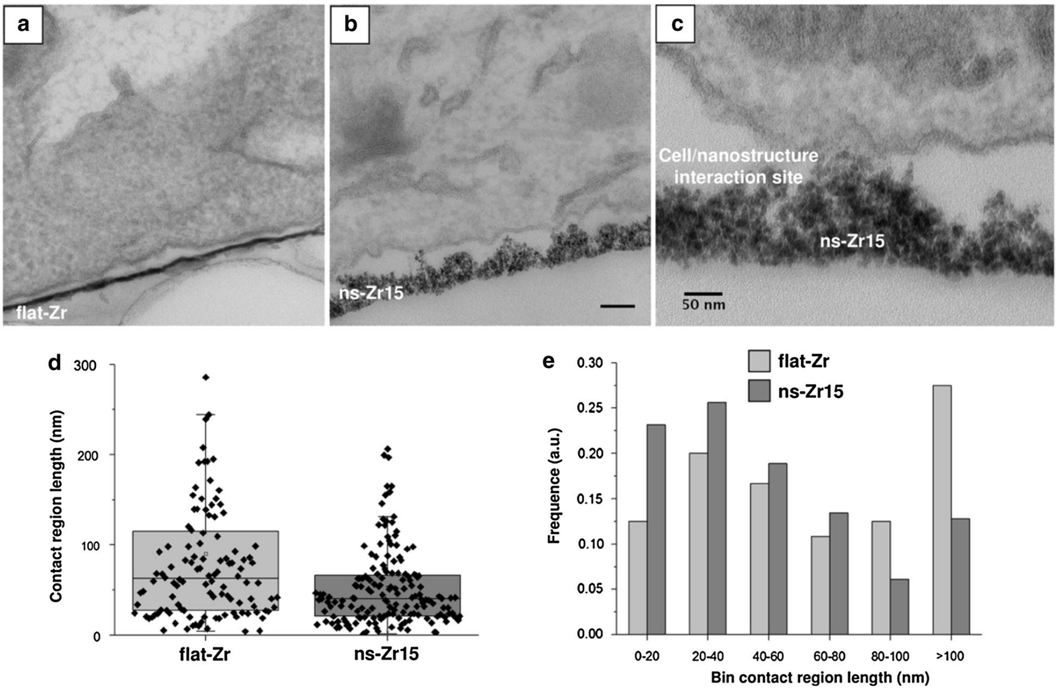

Fig. 3 Nanostructured zirconia surfaces alter the nanoscale adhesion site architecture. Representative TEM images of the cell/substrate interface on **a** flat-Zr, and **b** ns-Zr15 substrates. The *scale bars* equal 100 nm. **c** This image shows a close-up of a representative interaction zone between a PC12 cell and the ns-Zr15 surface. The cells interacted with the surfaces for 24 h. A description of experimental setting and quantification can be found in the "Methods" section. In d, e the corresponding analysis of the width of the adhesion sites at the nanoscale are summarized. **d** The absolute values of all measurements for both substrates are shown. **e** The *histogram* of measured widths of adhesion sites are displayed here. The *graphs* represent the global statistics of images obtained from two independent experiments (fl-Zr: n = 120, ns-Zr15 = 164)

Table 1 Characterization of the contact regions from TEM analysis

	Flat-Zr	ns-Zr15
Width of contact regions (nm)	Av.: 90.2 ± 93.2	Av.: 53.2 ± 48.0
	(SD) ± 16.9 (95 % CI)	(SD) ± 7.4 (95 % CI)
	Median: 62.8 ± 37.5	Median: 40.4 ± 21.6
Distance between contact regions (nm)	Av.: 108.6 ± 101.9	Av.: 99.1 ± 101.4
	(SD) ± 21.9 (95 % CI)	(SD) ± 18.6 (95 % CI)
	Median: 73.7 ± 38.6	Median: 60.4 ± 33.4

[2, 28], but considering the size of integrins (~15–20 nm in height and width of the extracellular domain) [29], most of the individual asperities offer large enough contact area dimensions to establish this minimal adhesion unit.

Moreover, critical ligand spacing thresholds between adhesion sites have been identified to influence the cellular capability to establish FAs [1, 2, 30], force transmission and mechanoregulation [31]. Interestingly, with a value of ~60–70 nm these thresholds are in the range of what was determined as the median of the asperity separation of our tested surfaces.

To get a visual prediction of how the asperity layout and the distances between the asperities might impact on integrin clustering and FA formation, we have grouped neighboring asperities applying a spacing threshold of 60 nm. This procedure enabled us to define potential asperity clusters which might permit the intracellular formation of the aforementioned superior adhesion structures (Fig. 4c, d). It can be recognized that the ns-Zr surface features set spatial constraints for the asperity clusters, in a manner that they remain mostly of small dimensions, actually in the range of nanoclusters or FCs [32]. For further maturation of the nascent adhesions into FCs or even into FAs, though, the surface characteristics might be quite restrictive. This is true in particular for ns-Zr15, whereas for ns-Zr25 these effects are mitigated because the

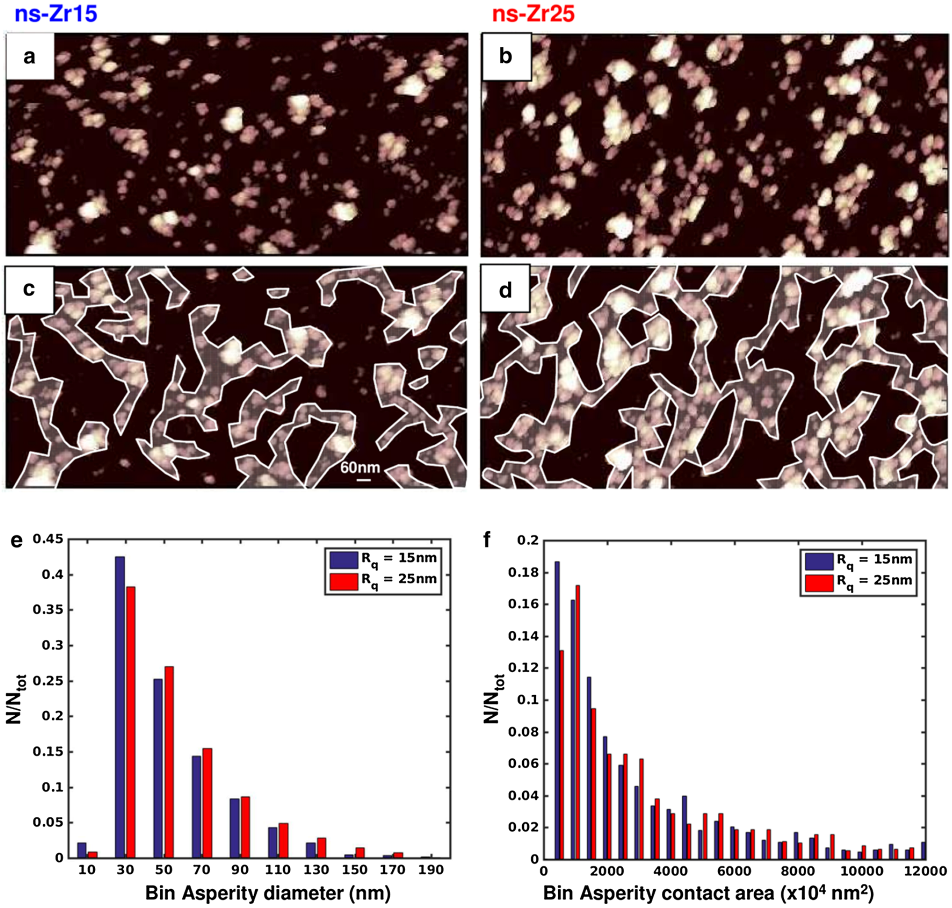

Fig. 4 SCBD-produced nanostructured zirconia surfaces have the potential to modulate adhesion-related processes. **a, b** Representative asperity maps of ns-Zr substrates with different roughness ($R_q = 15, 25$ nm, respectively). For details, see Additional file 2: Figure S2 and "Methods" section. **c, d** Asperity clusters highlighted from the asperity maps shown in panels **a, b** after grouping asperities separated by less than 60 nm (a reference *bar* with length 60 nm is shown). **e, f** The *graphs* show cumulative distribution of (**e**) asperity diameters and (**f**) the asperity area of ns-Zr15 and ns-Zr25 substrates

Table 2 Characterization of the contact asperities from AFM analysis

	ns-Zr15	ns-Zr25
Distance between asperities (nm)	72 ± 8	87 ± 10
Asperity diameter (nm)	43 ± 15	47 ± 17
Asperity contact area (nm^2)	1954 ± 1268	2596 ± 1766

asperity clusters are of notably larger dimensions (compare Fig. 4c,d), probably also as a consequence of the larger contact area and diameter of single asperities (Fig. 4f). On glass-PLL or flat-Zr apparently no such substrate-induced topological constraints exist.

Summarizing, our analysis suggests that nanostructured surfaces produced by SCBD possess a significant potential in modulating cell adhesion-related processes, e.g. by restricting integrin clustering and FA maturation [2, 4], and that the conditions for expressing this potential are better satisfied in the case of ns-Zr15, the sample with lower roughness. In the proceedings of our study we have therefore focused our attention only on ns-Zr15 samples, which also induced the strongest biological effect; using flat-Zr and the canonical PLL-coated glass surfaces (±NGF) as references.

Intracellular processes induced by the cellular interaction with the nanoscale roughness of zirconia substrates: focal adhesion dynamics and cytoskeletal organization

The analysis of the cell/substrate interface predicted hence a possible impact of the nanoscale roughness on integrin clustering and FA formation, which prompts a deeper examination of these processes and the receptors and signaling cascades effectively involved in mediating the observed morphological effects.

The canonical neuritogenesis in PC12 is typically activated by binding of NGF to TrkA (which represents the principal NGF receptor of these cells) [33] and predominantly mediated via the MAPK/Erk signaling cascade [34] (Fig. 5a). Consequently, the inhibitor GW441756 (a selective inhibitor of TrkA) diminished this kind of NGF-induced differentiation, whereas it was interesting to notice that it was ineffective for the nanostructure-induced differentiation (Fig. 5b), thus excluding that the nanotopography activates TrkA.

As aforementioned, the receptor family of integrins plays an eminent and essential role in FA-mediated cell adhesion and also (in particular β1 subunit-containing integrins) in the regulation of neuronal differentiation, neurite/axon outgrowth and pathfinding [35–37]. An involvement of FA-related processes in nanotopography-promoted cellular differentiation is likely [2, 4, 9] and has been addressed recently by Yang et al. in a neuronal context [20], but nevertheless many aspects are still unclear [2, 4, 9, 10]. In contrast to the TrkA inhibition, an allosteric inhibitor of β1 integrin activity (antibody 4B4) strongly impaired the growth of neurites in both conditions (Fig. 5c). K20, a β1 integrin-binding, but activity-neutral antibody instead interfered only moderately (Fig. 5c).

Moreover, also the inhibition of further prominent mediators and structural compoments in the integrin/FA signaling cascade (lipid rafts, FAK, RhoGTPases, cytoskeleton, actomyosin) confirmed the involvement of this signaling pathway (Additional file 3: Figure S3A, B). Interestingly, despite the dispensability of NGF (Fig. 1) and TrkA activation (Fig. 5b), the induction of the MAPK pathway was necessary also in nanostructure-induced neuritogenesis as inhibition experiments with U-0126 (an inhibitor against MEK1/2) demonstrated (Fig. 5d). In fact, it is well-known that the integrin and MAPK signaling pathways are interlaced [38] (Fig. 5a) and that MAPK pathway activation by β1 integrin plays an important role in neural stem cells [35].

Our results show that NGF and TrkA activation are not required for the nanostructure-induced PC12

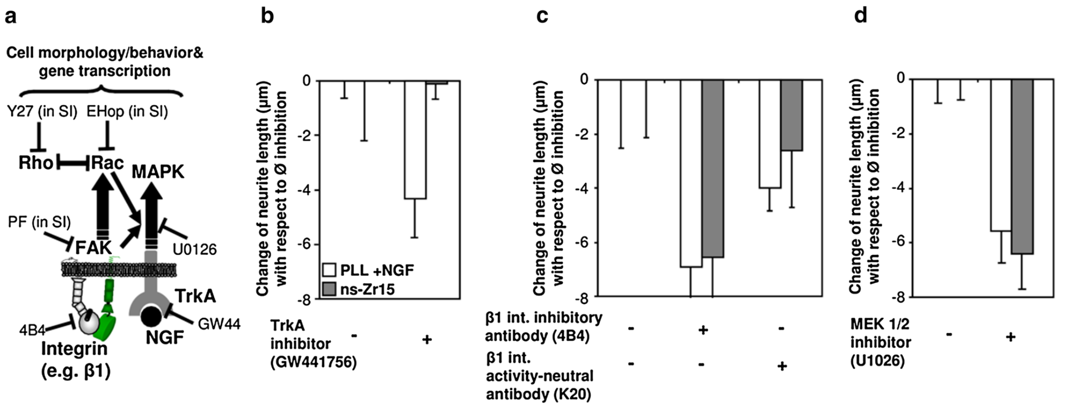

Fig. 5 NGF and TrkA activation are dispensable in nanostructure-induced neuritogenesis whereas β1 integrin activation/signaling are essential. **a** The *scheme* illustrates the interference points of the various inhibitors of proteins involved in the integrin and RTK signaling cascade which were used in the experiments. **b–d** The PC12 cells were plated on PLL (+NGF) or surfaces with a roughness R_q of 15 nm rms. In case of inhibitor treatment, the inhibitors were preincubated for 15 min prior to cell plating and then present for the whole ongoing experimental period. The cell morphology was recorded by phase contrast microscopy 24 h after plating the cells. As biological read-out for the differentiation the quantification of the neurite outgrowth is shown (obtained with the help of ImageJ); representative images can be found in Additional file 1: Figure S1. The *bars* display the change of neurite outgrowth compared to the situation without treatment on the corresponding substrate. The *bars* are flanked by SD. The *graph* displays the results of an inhibitor treatment against **b** TrkA (GW441756 1 µM, from two independent experiments), **c** the incubation with the 4B4 inhibitory antibody (2.5 µg/ml) (or activity-neutral antibody K20 (2.5 µg/ml) as control) against β1 integrin (from three independent experiments) or **d** the inhibition of MEK 1/2 (U1026 10 µM, from two independent experiments), always both in the canonical (NGF-induced) and the nanostructure-induced condition (n: >500 cells, >150 neurites). Further inhibitions of major mediators and processes involved in integrin signaling and cytoskeletal organization are displayed in Additional file 3: Figure S3

differentiation. However, the same biomechanical, cytoskeletal and FA-related structural and signaling components are essential to realize the outgrowth of neurites, independent of whether the given neuritogenesis-inducing stimulus is NGF or triggered by the cellular interaction with a nanostructure providing the adequate roughness.

Apart from this general involvement of the same structural and cell adhesion signaling components, the combined TEM and AFM analysis (Fig. 3, respectively 4) suggested that differences in FA formation might arise between the flat and nanostructured surfaces. In particular for the neuritogenesis-inducing ns-Zr15 surface a partially frustrated potential in permitting the formation of superior adhesion structures, especially mature FA, was predicted (Fig. 4c, d). We have discussed in the precedent section "Potential of nanostructured zirconia surfaces in modulating cell adhesion-related processes" that FA formation depends on extracellular microenvironmental features such as area, geometry, ligand spacing and nanotopography of the adhesion sites [1, 2, 4, 30, 39]. Intracellularly, FA signal transduction is regulated by the nanoscale architecture/composition of the adhesion complex, the force and tension development between integrins and the actomyosin network [2, 3, 10, 32, 40–42] (Fig. 6a). However, the exact mechanism of this cellular environmental (mechano) sensing and especially its impact on differentiation processes is intricate and still only partially understood [1–4, 6, 10, 11].

We therefore investigated the impact of cellular interaction with the different surfaces on the spatiotemporal dynamics of FA formation. Vinculin staining at different time points recorded by TIRF microscopy confirmed that the FA dynamics and the extent of their maturation clearly vary between flat and nanostructured surfaces (Fig. 6b–d). In the canonical condition on glass-PLL we observed an evident formation of small FC-like structures and also more mature FAs after a few hours. Without NGF the presence of these structures remained high, whereas in the case of NGF stimulus they reduced in number towards the 24 h time point and became smaller. On flat-Zr the FC/A formation was accelerated and clearly enhanced. Already after half an hour apparent accumulations of vinculin were detectable. After 1 h and later on distinct and numerous FAs were detectable, mainly at the cell border.

On ns-Zr15 substrates the situation was instead quite different. Diffuse punctate staining, indicating nanoclusters or FCs, was visible starting from the 4 h time point but FAs basically did not form, not even at later time points (Fig. 6b–d). For the correlated formation of high order actin filament structures (e.g. stress fibers) the situation was similar. They were mainly established on the flat substrates Glass-PLL and flat-Zr, but to a much lower extent on the neuritogenesis-inducing ns-Zr15 (Fig. 6e).

We demonstrated the indispensability of β1 integrin activation and the alteration of the FA configuration, but it remained unclear whether direct integrin/nanostructure interaction is taking place. It can be speculated, though, that the interaction is mediated with involvement of adhesome complexes. Moreover, it has been shown recently that cell adhesion mediated by non-integrin anchoring receptors can trigger integrin activation/signaling via membrane tension also independently of actual integrin/ligand binding [43].

We further investigated whether this modulation of the FAs and the cytoskeleton was causally involved in the nanostructure-driven induction of neuritogenesis. To contrast the altered FA dynamics and cytoskeletal organization on ns-Zr15 we chose to treat cells with lysophosphatic acid (LPA). LPA is long-known for its ability to remodel the actin cytoskeleton by inducing Rho signaling-dependent formation of FA and stress fibers, and to cause therefore subsequently neurite retraction in PC12 [44]. Congruently, the treatment reduced both, the NGF- or nanostructure-induced neurite outgrowth, at higher LPA concentration. In the nanostructure-induced neuronal differentiation, though, already lower concentrations of LPA had an inhibiting impact on the neurite outgrowth (Additional file 3: Figure S3C).

Neuritogenesis is a complex case of cellular morphogenesis. Neurite budding requires a concerted interplay between the neuronal actin and tubulin cytoskeleton components in order to break the neuronal sphere [45]. Furthermore, once a neurite is initiated the processes driving neuritogenesis and in particular the growth cone advancement [36] are very similar to the ones in mesenchymal cell migration and depend therefore on a highly regulated crosstalk between Rac1 and RhoA orchestrating the turnover of contact points [36, 46] and mediating thereby an appropriate, balanced ECM/integrin/actin cytoskeleton linkage [36, 41, 42, 47–49] and force generation by the molecular clutch [11, 41, 50, 51]. In fact, growth cones itself have been determined as rather soft cellular structures [50] requiring small point contacts with a dynamic turnover for efficient motility [36, 52]. It can be speculated that on flat-Zr the adhesion might be utterly enhanced to a point that leads to more stable/less dynamic focal adhesions imposing an overall anti-differentiation biomechanical condition, which makes it difficult to break the neuronal sphere in the initial phase of neurite budding and/or to promote efficiently the growth cone advancement, thereby even contrasting the NGF stimulus. On the contrary, ns-Zr15 surfaces seem to set an ideal cellular status of adhesion and cytoskeletal organization to favor neuritogenesis, even in the absence

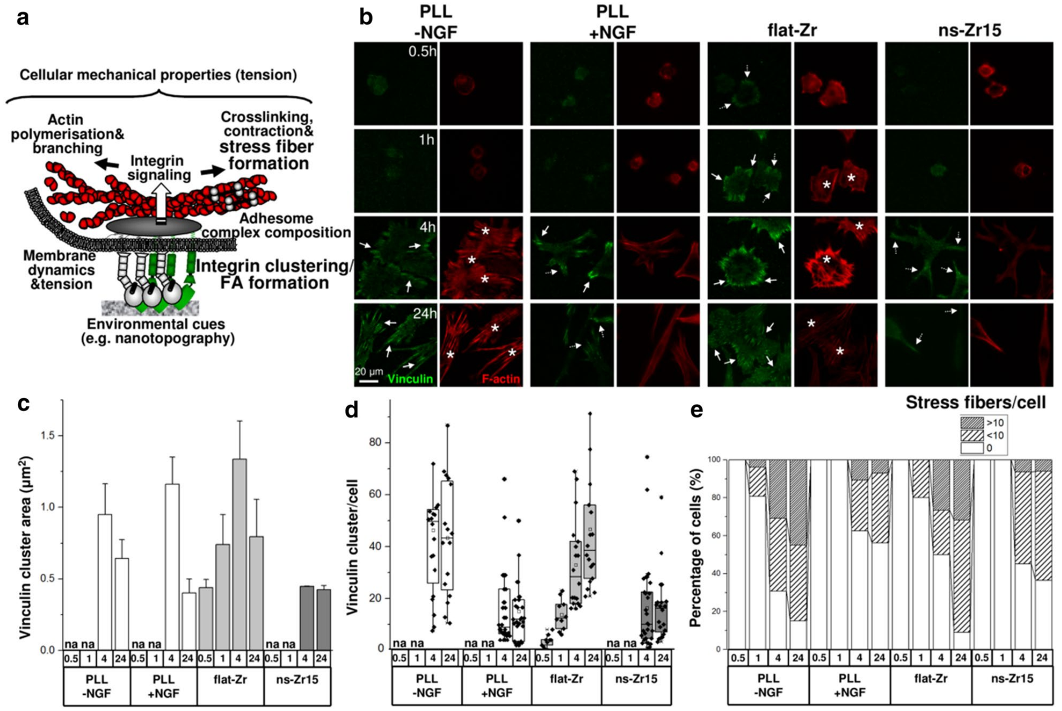

Fig. 6 Focal adhesion formation/dynamics and cytoskeletal organisation differ on flat or neuritogenesis-inducing nanostructured surfaces. **a** The *graphic* visualizes and summarizes the cytoskeletal and mechanobiological processes which are influenced by FA organization and dynamics. **b** In the *panel* representative images of the PC12 cells fixed with 4 % PFA after the indicated time periods on the different surfaces are demonstrated (vinculin staining recorded by TIRF microscopy, f-actin in epifluorescence). The *white arrows* indicate exemplary areas with focal complex (*pointed line*) or focal adhesion (*continuous line*) structures. The *asterisks* pinpoint to exemplary areas with strong actin fiber formation. **c**–**e** The *graphs* summarize the corresponding results (representing the global statistics of three independent experiments, vinculin clusters: n = 722–3678, cells: n = 16–34) of the quantifications (obtained with ImageJ) of **c, d** FA dynamics; **c** Vinculin cluster area, **d** Number of vinculin clusters per cell, and **e** cytoskeletal actin fiber organization. *na* not analyzable

of a biochemical stimulus. Further experiments are necessary to eventually elucidate these aspects.

However, together the presented complex of data on FA dynamics/signaling and the cytoskeleton propose a particular importance of the mechanotransductive aspect in the nanostructure-induced condition.

Modulation of the cellular mechanical properties is the key signal integration for the nanostructure-induced neuronal differentiation processes

In fact, cell/substrate interactions, the integrin engagement to the actomyosin network and correlated FA signaling strongly impact on the organization and the biomechanical, tensional state of the cytoskeleton [3, 6, 41, 42]. Effectively, cellular mechanics have been suggested to be by themselves a signal integrator which potentially not only affect the cell morphology [53] but also essential cell functions and eventually the cell's fate [5, 6, 10, 41] (Fig. 6a), in particular also in neuronal cells [11]. In mesenchymal stem cells it was hypothesized that effects on FAs, the cytoskeleton and cellular mechanics were provoked by adding nanogratings (350 or 500 nm width) to the substrate [54].

As described above, our experiments demonstrate that integrin signaling and cytoskeletal dynamics are essential for both canonical and nanostructure-induced neuritogenesis (Fig. 5; Additional file 3: Figure S3A, B). The data also accentuated, though, decisive differences in the nanoarchitecture of the cell/substrate interface (Figs. 3, 4), FA dynamics and actin filament organization (Fig. 6b–e) between cells on flat-Zr and neuritogenesis-inducing ns-Zr15 surfaces. Therefore it was important to understand whether different cell/substrate interactions might have an effect on the overall cellular mechanical properties.

We performed AFM-based nanomechanical measurements of living PC12 interacting with PLL ±NGF, flat-Zr and ns-Zr15 surfaces (Fig. 7). Interestingly, in the latter case the membrane/cytoskeletal layer of the somas of the cells were characterized by a highly significantly lower rigidity (−51 % in the Young's modulus, p value < 0.01, double-sided t test) compared to the cells on flat-Zr (Fig. 7b). Similarly, in the cells on glass-PLL a decrease of the rigidity was notable between the undifferentiated cells without NGF stimulus and the differentiated cells in the presence of NGF (−28 % in Young's modulus, p value < 0.1), arriving at a level comparable to the one of the cells on ns-Zr15 (Fig. 7b). The fact that the cells in the flat-Zr condition demonstrate the highest absolute rigidity value of all tested conditions (p value PLL −NGF vs flat-Zr < 0.02) is furthermore congruent with the aspects of enhanced cell adhesion and neuritogenesis-unfavorable biomechanical state in this condition, discussed in the section "Intracellular processes induced by the cellular interaction with the nanoscale roughness of zirconia substrates: focal adhesion dynamics and cytoskeletal organization".

Taken together, the data strongly suggest that the status of the FA architecture/dynamics and the cytoskeletal organization—enforced by the specific characteristics of the neuritogenesis-inducing substrate—might be the reason for the decrease of the rigidity/tension in the somal membrane/cytoskeletal layer.

Keeping in mind the hypothesis of the mechanotransduction concept, these results on the impact of the

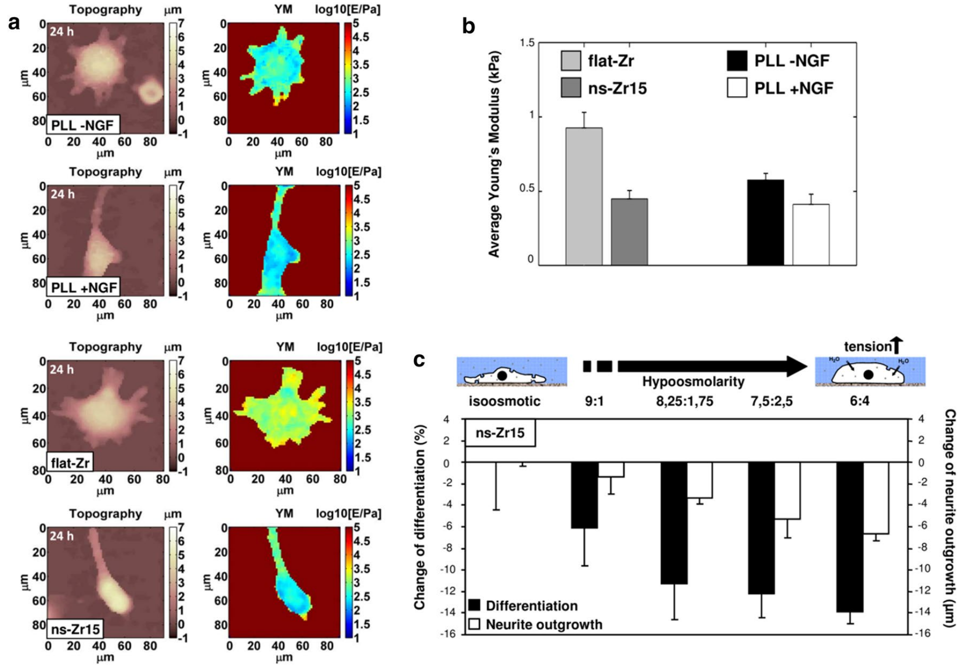

Fig. 7 Cellular rigidity is decreased on the neuritogenesis-inducing surface, being the decisive signal for the differentiation. **a** Representative morphological images (*left images*) and maps of the Young's modulus of elasticity (*right images*) of living PC12 cells interacting with PLL (in the presence or absence of NGF), or with flat or the nanostructured neuritogenesis-inducing zirconia surfaces. **b** On the *upper right*, the *graph* displays the summary of the corresponding analysis of the biomechanical properties of the membrane/cytoskeletal layer. The *bar* represents the average of the global statistics obtained from two (flat-Zr, Glass-PLL ±NGF), respectively three (ns-Zr15) independent experiments (number of measured cells: flat-Zr: n = 6, ns-Zr15: n = 7, PLL −NGF: n = 8; Glass-PLL +NGF: n = 8), flanked with the error which was calculated as described in the "Methods" section. YM young's modulus. **c** Differentiation rate and neurite outgrowth of PC12 cells plated for 24 h on the neuritogenesis-inducing ns-Zr15 surface in the presence of isoosmotic medium or in medium with the indicated hypoosmolarity. The *bars* represent the average of two independent experiments and are flanked with the SD (n: >500 cells, >150 neurites). Representative images of all conditions can be found in Additional file 3: Figure S3

ns-Zr15 surface on cellular FA formation, cytoskeletal organization and nanomechanics evoked the question concerning the role of the causal signal integration as the effective driving force of the nanostructure-induced neuronal differentiation.

To address this issue, we compensated the reduced rigidity/tension of cells plated on the neuritogenesis-inducing surfaces by hypoosmotic swelling. We observed that upon increasing of hypoosmolarity, the nanostructure-induced effects gradually decreased (Fig. 7c). Congruently, low hyperosmolarity even slightly increased the percentage of differentiated PC12. Higher hyperosmolarity levels had a slightly decreasing effect on differentiation due to general rounding up of the cells, but neurite length was basically unaffected (Additional file 3: Figure S3D).

We therefore conclude that the alteration of the cellular biomechanical properties—caused by the interaction with a neuritogenesis-inducing nanostructured surface and the subsequent induction of mechanotransductive events—is the decisive integrating signal permitting the promotion of neuronal differentiation. Altogether, to our best knowledge, this is the first robust evidence of a strong causal link between mechanotransductive processes and nanotopography-based biomaterial-induced biological effects.

Dynamics of transcription factors controlling neurogenic processes induced by surface nanostructure

Our experiments demonstrate the pivotal significance of mechanotransductive signaling pathways for the nanostructure-induced neuronal differentiation. Typically signaling cascades are finalized by the activation of transcription factors (TF) and their binding to specific sequences of the DNA. Thereby they eventually realize the necessary change of the gene expression profile and cellular program.

CREB is a prominent TF which can be the endpoint of versatile signal inputs arriving from cAMP-, integrin-, RTK/MAPK/Erk-, NO-, calcium- or mechanical force-mediated signaling cascades or, very often, also a combination of them [55–57]. Consequently it functions as a signal integrator with a strong impact on the expression level of a wide range of genes [58], notably also in the control of early neurogenesis [56–58]. For these reasons CREB was a good first candidate in our context to examine downstream events on the level of transcription control relevant for early neuronal differentiation processes.

We performed a confocal imaging analysis of nuclear CREB phosphorylation (which activates this TF) (Fig. 8a). On flat-Zr there was no detectable phosphorylation of the nuclear CREB. For the canonical NGF stimulation a slight, but significant nuclear p-CREB signal was visible after 1 h which further increased at the 24 h time point. Interestingly, in the nanostructure-induced neuritogenesis a strong nuclear phosphorylation of CREB (significantly stronger than the one of the canonical condition) was already present after 1 h. After 24 h this signal was reduced compared to the 1 h time point but remained still in the range of the canonical signal.

Another interesting TF candidate in this context is JNK/c-jun which is known to be downstream of integrin signaling and susceptible to geometric cues [39] and involved in neurogenic processes, e.g. neurite/axon development [59]. In keratinocytes reduced FA/stress fiber formation on soft hydrogels coincides with augmented JNK phosphorylation [60].

Congruently to the described biological effects of this TF, indeed a higher inhibitor concentration against c-jun is needed to completely block the differentiation induced by the biomaterial (indicating a higher c-jun activity) compared to the canonical NGF-stimulated condition (Fig. 8b). An interesting fact to mention is that this result is opposite to the result obtained with LPA which displays the reversed biological effect on FAs and the cytoskeleton (Additional file 3: Figure S3C) and in fact realized its inhibitory impact on nanostructure-induced neuritogenesis already at lower concentration compared to the NGF-induced one.

The results for CREB and JNK/c-jun indicate that TFs, known to be susceptible to mechanotransductive pathways and with substantial roles in neuronal differentiation, are effectively modulated by the cellular interaction with nanostructured zirconia interaction.

Proteomic profile of nanostructure-induced neuritogenesis and mechanotransduction

In order to confirm the neuronal differentiation and to further characterize the mechanotransductive mechanism at the molecular level we performed a shotgun proteomic analysis comparing the proteome of PC12 cells grown on neuritogenesis-inducing ns-Zr15 substrates with the one of cells grown on flat-Zr and PLL (in the presence of NGF) (after 24 h cell/substrate interaction). Based on the analysis detailed in the "Methods", 52 proteins were found upregulated or present only in cells grown on ns-Zr15, while 54 proteins were downregulated in cells on ns-Zr15 or were present only in cells on flat-Zr (Fig. 9a; Additional file 4: Table S1, Additonal file 5: Table S2).

Analyzing in detail the proteins differentially expressed, several of them reflect also at the protein level the morphologically observed differentiation processes induced by the nanostructure. In particular, the upregulation of β2-tubulin is in line with the observed induction of neuritogenesis as it represents one of the main structural components of the neurite/axon and its knockdown

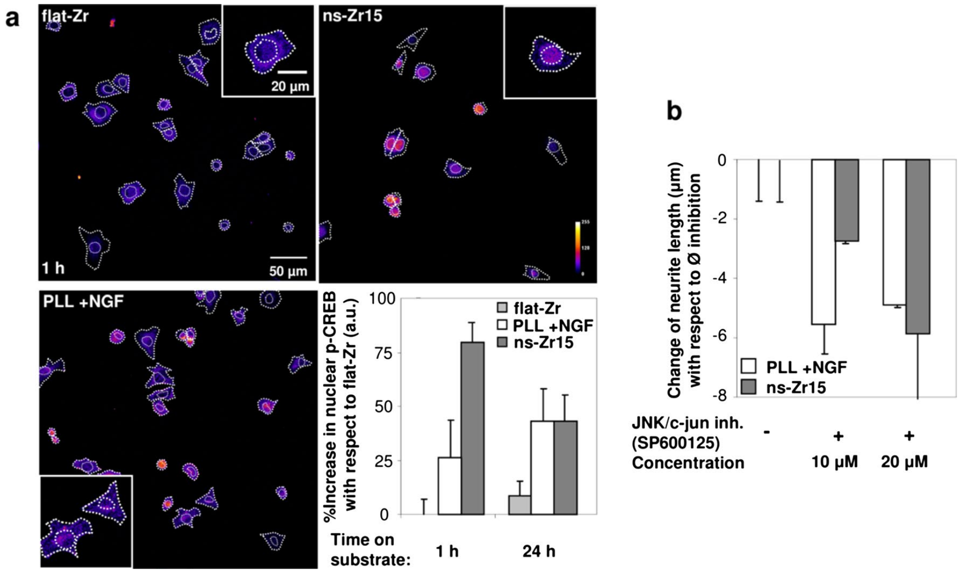

Fig. 8 The interaction with the neuritogenesis-inducing surface has an impact on transcription factor dynamics relevant for neuronal differentiation. **a** The confocal images show the average stack projection of p-CREB stainings of cells in the indicated experimental conditions. The cells were fixed with 4 % PFA 60 min or 24 h after in the indicated conditions and stained for the nucleus (HOECHST), f-actin and p-CREB. The outer dashed lines represent the outlines of the cells obtained from the f-actin staining and the inner dashed line the nuclear area determined from the HOECHST staining. The *graph* (representing the global statistics of two independent experiments, n = 33–76 cells) summarizes the corresponding quantification performed with the help of ImageJ (see also "Methods"). **b** The same experimental procedure and quantification (from three independent experiments, n: > 500 cells, >150 neurites) as in Additional file 2: Figure S2A–C, but with an inhibitor against JNK/c-jun (SP600125 10 and 20 µM). Representative images of the conditions can be found in Additional file 3: Figure S3

decreases neurite outgrowth and neuronal differentiation [61]. UCH-L1 is long-known to be upregulated in differentiated PC12 [62] and enhances neurogenesis in NPC by regulating their morphology and differentiation [63]. In congruency with the data on CREB phosphorylation (Fig. 8a), we have found several genes whose expression is known to be potentially modulated by CREB [58] and which are indeed differentially expressed in ns-Zr compared to flat-Zr (marked with crosses in Additional file 4: Tables S1, Additonal file 5: Table S2). Considering the fact that PC12 are also a neurosecretion model [64], the upregulation of the aldehyde dehydrogenase ALDH4A1 and the aspartate aminotransferase Got1, which play a role in the metabolism of the neurotransmitter glutamate (Reactome: DOI: 10.3180/REACT_13.4), is an indication of potential beginning neurosecretory activity. Moreover, also in the section below highlighting mechanotransductively relevant proteins (Fig. 9b), further proteins with prominent well-documented functions in neuronal differentiation are broadly present.

Regarding adhesion and integrin signaling, there is an evident abundance of integrin adhesome-related proteins among the up- or downregulated proteins in the PC12 cells interacting with the ns-Zr15. 7 out of 63 proteins concordantly found in three proteomic adhesome analyses [65] are highly significantly altered in their expression level. Furthermore, eight proteins are in the integrin adhesome list defined by Winograd-Katz et al. [66] (these adhesome proteins are marked in the Additional file 4: Tables S1 and Additonal file 5: Table S2 in dark grey, further proteins with roles in mechanobiological processes mentioned below are marked in light grey).

Among the adhesome proteins the downregulated protein testin is of eminent significance, taking into account the results regarding FA dynamics and actin filament bundling on the different surfaces reported in this study. Testin is a FA protein known to interact with several cytoskeletal and FA proteins, such as actin, MENA, talin, VASP and zyxin, and plays an important role in the regulation of cell spreading and migration [67]. Its downregulation causes the loss of stress fibers and a decrease in RhoA activity [68]. Furthermore, in a proteomic analysis testin was found to be one of the LIM domain proteins whose recruitment to the adhesome is

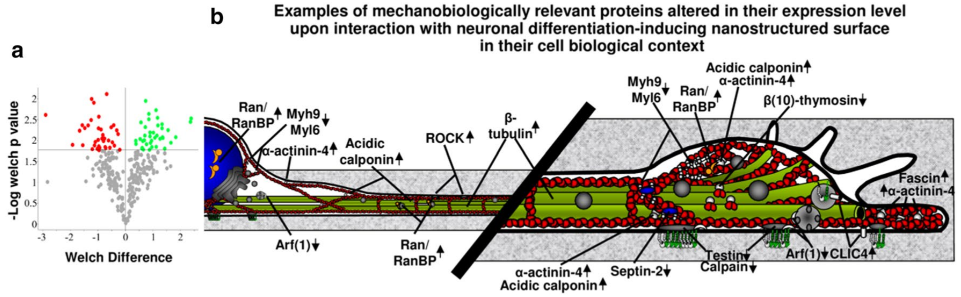

Fig. 9 Proteomic analysis confirms the differentiation and reveals alterations of the mechanotransductive cellular status upon nanostructure/cell interaction. **a** A shotgun proteomic analysis was carried out on PC12 cells on neuritogenesis-inducing ns-Zr15 or on flat-Zr or PLL in the presence of NGF (after 24 h cell/substrate interaction). An ANOVA test was performed in order to identify the proteins that were differentially expressed. In this report, only the data comparing ns-Zr15 and flat-Zr are presented. The *colored* data points in the *volcano plot* that are located above the p value line (t test value cut off is 0.0167) correspond to the proteins that were differentially expressed in these two conditions upon treatment with large magnitude fold changes and high statistical significance. In *green* are indicated proteins that are up regulated, in *red* are the down regulated. The proteins having a fold-change less than 1.5 are shown in gray. A complete list of these proteins can be found in Additional file 4: Table S1, Additional file 5: Table S2 in the supplementaries. **b** The cartoon summarizes and visualizes the sites of action and functions of adhesome- and mechanobiologically-relevant proteins found to be altered in their expression level upon interaction with the neuritogenesis-inducing nanostructured surface (for further details see text). *Arrows* indicate up- or downregulation compared to the flat zirconia condition

myosin II-dependent and essential in the process of FA maturation. In general, LIM domain-containing proteins are emerging as key players in actin cytoskeletal- and FA-dependent cellular mechanotransductive responses [3]. In this context also the downregulation of the Class IIA myosin component MYH9 and the myosin light chain regulatory protein MYL6 are quite interesting. A decrease in their expression level is accompanied by long process formation, e.g. in fibroblasts [69].

Also the downregulated GTPase Arf1 can be found associated with FA proteins and the membrane and is thus known to be involved in FA maturation and cytoskeletal organization. In fact, it regulates the recruitment of paxillin and β1 integrin-binding partners (e.g. talin, vinculin, FAK) to the FA [70]. In addition, in the neuronal context it is also involved in the modulation of actin polymerization for synaptic plasticity [71].

Another interesting example is the upregulated α-actinin-4, a member of an actin-binding protein family which serve as protein interaction platforms and as such have versatile, in particular cytoskeleton-related functions [72], e.g. in the initial maturation phase of nascent adhesions [73]. Interestingly, in developing neurons it is involved in the distribution of f-actin [74]. Its activity is regulated by MAPK/calpain-dependent processes [72].

Calpain again can be found among the downregulated adhesome proteins. Indeed, this protease has various substrates among adhesome proteins and many tasks [75]. In the neuronal context it has a vital role in a number of axon/neurite growth cone-related processes, e.g. growth cone collapse and neurite consolidation. Its inhibition enhances neurite budding and stimulates cortactin-dependent actin polymerization [76].

In addition, there are further up- or downregulated proteins which may not be direct integrin adhesome members but nevertheless quite intriguing from the cytoskeletal and mechanotransductive perspective (and often function in close relation to integrin adhesome proteins).

The upregulated acidic calponin (calponin-3), for example, is a protein that is found to be upregulated in postmitotic neurons, localised mainly in the growth cones [77]. Acidic calponin inhibits actomyosin activity [78] and indeed its overexpression causes a re-adjustment of the organization and force balance between microtubules and actin filaments, which leads to long process formation, even in non-neuronal cells (like HEK293) [79], or elongated dendrites in hippocampal neurons [80].

Another interesting result is the upregulation of CLIC4 and fascin. CLIC4 orchestrates Rab35-dependent trafficking of β1 integrin and thereby cell adhesion [81]. Rab35 has been shown to regulate neurite outgrowth in PC12 cells, by Cdc42-dependent modulation of the actin cytoskeletal organization and cell shape [82]. It was also demonstrated that Rab35 triggers actin bundling by recruiting fascin to the plasma membrane [83]. Fascin itself is known to be a decisive factor in FA and stress fiber dynamics by inhibiting myosin II activity and slowing down FA turnover [84]. Furthermore it is an essential key protein for filopodia formation, due to its localized tight actin bundling capacity, which drives growth cone advancement [85]. In our context, CLIC4 could balance the Rab35/fascin-dependent actin bundling activity necessary for accurate neurite formation.

Four further proteins with prominent demonstrated functions in cytoskeletal organization are altered in their expression level. The upregulation of ROCK might be confusing at a first glance because the inhibitory function of ROCK/RhoA activity for the necessary reorganization of the actin cytoskeleton and membrane exocytosis for neurite budding and growth cone advancement is well-established [86, 87]. The role of ROCK/RhoA in neuritogenesis is more complex, though, its moderate and local activation is necessary to stabilize actin filaments and growth cone point contacts [46]. Furthermore it suppresses lamellipodial protrusions during axon/neurite consolidation which maintains the growth cone polarity [88]. Its actomyosin contraction-promoting activity could instead be locally controlled and diminished by the altered presence of calponin-3 and testin that both as aforementioned counteract this function. In addition, it might be reminded in this context that myosin II components are downregulated, too. Also septin-2 is downregulated, which is known to interact with myosin II serving thereby as a sort of regulatory hub to scaffold and recruit proteins that control the contractility of actomyosin [89]. In this context the downregulation of β10-thymosin is in accordance. β-thymosins bind globular monomeric actin and are therefore pivotal for the control of actin cytoskeleton dynamics and in the regulation of neuritogenesis. Indeed, their knockdown increases the outgrowth of neurites [90]. Also the upregulated Ran and RanBP1/3 are involved in cytoskeletal processes at distant sites from the nucleus. In fact, Ran knockdown results in abnormal neurite morphology because of augmented branching. Furthermore these proteins are crucial for axonal retrograde signaling [91].

Altogether, this proteomic profile of proteins altered in their expression level reflects, broadly and in a congruent manner, the differentiation events and cell biological effects described throughout the precedent paragraphs. In particular, the abundance of proteins that are involved in adhesome, cytoskeletal organization and/or cellular biomechanics is striking (Fig. 9b) and their up- or down-regulation in line with their demonstrated functions in neuronal differentiation processes. Furthermore, the results have revealed some interesting otherwise maybe unrecognized or underestimated candidates for more detailed future analysis of mechanotransductive processes induced by nanoscale topography of substrates.

Conclusions

We have characterized, in the context of neuronal differentiation, the sequence of the mechanotransductive events starting from the cell interaction with nanoscale topography and we have followed the triggered intracellular cytoskeletal/biomechanical dynamics and signaling cascades to the activation of transcription factors, eventually addressing the consequences on the cellular program.

The data were obtained with the cell line PC12 as a widely accepted and studied model for neuronal differentiation processes. The use of the PC12 cell line allowed us a broad experimental freedom whereby we were able to build a rationale picture of nanoscale topography-induced mechanotransductive processes leading to cell differentiation, and to connect them causally. This provided an in-depth understanding of how nanoscale topography induces complex mechanotransductive, molecular mechanisms that eventually modulate cell biological functions.

Taken together, our results show that an adequate nanoscale surface structure, produced by SCBD of zirconia nanoparticles, has the potential to limit integrin clustering and the grade of FA formation. This alteration of the FA architecture and dynamics, enforced by the nanoscale information provided by an appropriate surface topography, feedbacks on the correlated adhesome architecture/composition and the biomechanical properties of the cell. These mechanotransductive pathways modify the activation dynamics of TFs susceptible to mechanosensitive inputs. Furthermore, the change of the cellular protein profile sets an overall cellular status eventually promoting, in this case, neuronal differentiation equivalent to the canonical NGF-induced one (summarized in Fig. 10). The indicated mechanotransductive signal integration initiated by the interaction of the cells with the neuritogenesis-inducing nanostructured surfaces was linked to the induced differentiation.

It can be speculated that the interaction of PC12 cells with a suitable nanostructured surface resembles more closely the in vivo physiological ECM configuration where neuronal cells naturally differentiate (compared to the flat PLL-coated glass or zirconia). Therefore, by the demonstrated mechanotransductive events, a biomechanical status might be set that lowers the threshold for the induction of neuronal differentiation and favors neurite budding and neurite growth cone advancement on the ns-Zr15, in this model even in the absence of a biochemical stimulus. On the flat, from a nanotopographical point of view more unnatural anti-differentiation glass-PLL surface instead the right biomechanical status has to be implemented by a cumbersome reorganization

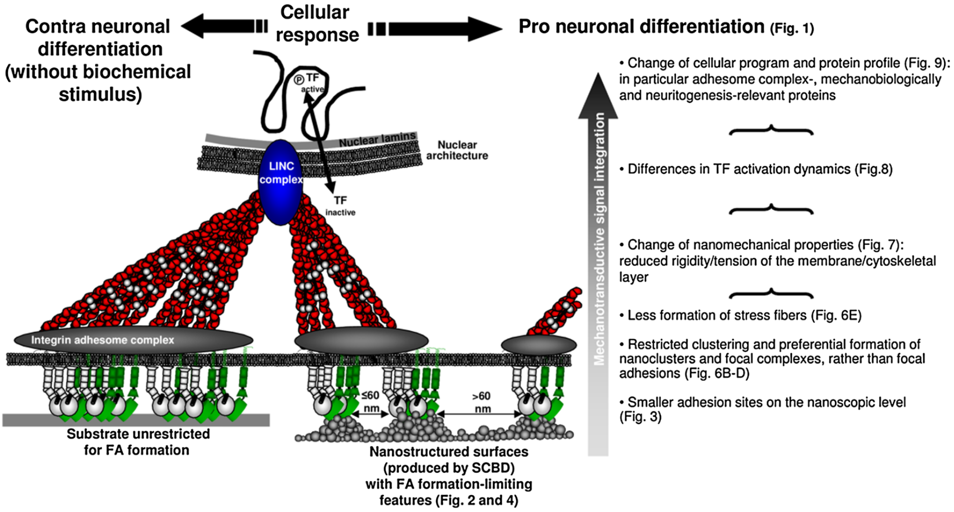
Contra neuronal differentiation (without biochemical stimulus)
Cellular response
Pro neuronal differentiation (Fig. 1)
• Change of cellular program and protein profile (Fig. 9): in particular adhesome complex-, mechanobiologically and neuritogenesis-relevant proteins
• Differences in TF activation dynamics (Fig.8)
• Change of nanomechanical properties (Fig. 7): reduced rigidity/tension of the membrane/cytoskeletal layer
• Less formation of stress fibers (Fig. 6E)
• Restricted clustering and preferential formation of nanoclusters and focal complexes, rather than focal adhesions (Fig. 6B-D)
• Smaller adhesion sites on the nanoscopic level (Fig. 3)
Mechanotransductive signal integration
Ⓟ TF active
Nuclear lamins
Nuclear architecture
LINC complex
TF inactive
Integrin adhesome complex
≤60 nm
>60 nm
Substrate unrestricted for FA formation
Nanostructured surfaces (produced by SCBD) with FA formation-limiting features (Fig. 2 and 4)

Fig. 10 Summary and model of the molecular mechanism of SCBD-induced cell biological responses

of the cytoskeleton induced by a sufficient biochemical input. The still large vinculin clusters in the PLL +NGF condition after 4 h (compared to the ns-Zr15 condition, see Fig. 6b, c) are an indication for this hypothesis. On flat-Zr not even this biochemical stimulus is sufficient, possibly due to the enhanced FA formation and cellular rigidity. Future experimentations will further address these aspects.

We are aware of the fact that results obtained with cell lines should be handled with care and that details might differ for other (neuronal/primary) cells, depending e.g. on their cell adhesion receptor profile/density and intrinsic intracellular cytoskeletal/signaling dynamics [3, 41]. These factors might also have influence on the appropriate roughness to obtain the desired biological responses. It is very likely, though, that the basics of the nanostructure-induced effects presented here, are comparable in equivalent cells. In fact, the neuronal differentiation-promoting capacity of these nanostructured zirconia surfaces is not restricted to the PC12 cell line, but is broadly confirmed by preliminary studies with the clinically more relevant cell model dissociated primary hippocampal neurons (unpublished data). Also a recent publication by Sun et al. has shown that soft biomaterials support YAP-mediated neuronal differentiation of human pluripotent stem cells into motor neurons by mechanotransductive ROCK signalling-dependent processes impacting on actomyosin contractility [92].

Altogether, this work lays a substantial cell biological foundation for the intelligent design of substrates for cell culturing based on nanostructured surfaces produced by cluster assembling that mimic more closely physiological 3D extracellular microenvironmental features. Our data suggest that the nanoscale information provided by these surfaces could have a strong potential in favoring neurogenic processes by mechanotransductive processes also in adequate primary or stem cell systems [2, 4, 9, 10]. Biophysical cues that can improve neuroinduction protocols would indeed have a significant relevance for neuroscience research (e.g. for the development of in vitro disease models [93] or neural interfaces and circuits [94]) and cell replacement strategies in neurodegenerative diseases [93].

We demonstrated that SCBD is a robust bottom-up technology for the reproducible and high-throughput fabrication of zirconia substrates with controlled nanoscale topography constituting a very effective tool to study mechanotransductive signaling. It is important to underline that the experiments reported here required a huge number of substrates (~150 Ø13 mm glass cover slips, dozens of Ø24 mm glass cover slips, several Ø40 mm glass-bottomed dishes and 76 × 26 mm microscope slides) with reproducible nanoscale roughness over a large macroscopic area. This is a serious obstacle for most of the top-down nanofabrication technologies usually employed for surface nanostructuring, in terms of fabrication time, costs and reproducibility [4, 12].

Methods

Substrate fabrication

Nanostructured zirconia films with controlled and reproducible nanoscale morphology were produced by supersonic cluster beam deposition (SCBD) using a deposition apparatus equipped with a pulsed microplasma cluster source (PMCS) [22].

In the PMCS an argon plasma jet ignited by a pulsed electric discharge ablates a zirconium rod. Zr atoms and ions sputtered from the target thermalize with the argon and traces of oxygen present in the condensation chamber and aggregate to form ZrO_x clusters. The mixture of clusters and inert gas then expands into a vacuum, through a nozzle, to form a seeded supersonic beam. The clusters carried by the seeded supersonic beam are collected on a substrate intersecting the beam trajectory (deposition rate of about 0.5–2.5 nm/min) and placed in a second vacuum chamber, thus forming a cluster-assembled film. Further oxidation of ZrO_x clusters takes place upon exposure to ambient atmosphere thus forming a ZrO_2 film.

Two different batches of cluster-assembled ZrO_2 films (called ns-Zr, hereafter) with roughness R_q of 15 nm (ns-Zr15) and 25 nm (ns-Zr25) were produced on round glass coverslips (Ø13 mm), microscope glass slides (76 × 26 mm area), glass-bottomed cell culture dishes (Ø40 mm) or Aclar® films. As a reference we also produced flat ZrO_2 films ($R_q = 0.4$ nm) by electron beam evaporation of a solid Zr target (flat-Zr). For the experiments, the samples with zirconia surfaces were sterilized with UV light for 10 min directly before seeding the cells on them.

Glass coverslips coated with poly-L-lysine (PLL) (Sigma-Aldrich, St. Louis, USA, Missouri) with a roughness $R_q < 1$ nm were used as standard reference substrates. For this condition, the PLL was incubated for 30 min at RT on clean glass coverslips. The coated glass was then washed twice with PBS and sterilized with UV light for 10 min. The coating procedure was performed directly before plating the cells.

Atomic Force Microscopy characterization of substrates surface morphology

The surface morphology of cluster-assembled zirconia films and other substrates was characterized by atomic force microscopy (AFM) in air using a Multimode AFM equipped with a Nanoscope IV controller (Bruker, Billerica, USA, Massachusetts), operated in Tapping Mode. Rigid silicon cantilevers ($k \approx 40$ N/m, $f_0 \approx 300$ kHz) mounting single crystal silicon tips with nominal radius 5–10 nm have been used. On each samples several 2 μm × 1 μm images were acquired with scan rate of 1 Hz and sampling resolution of 2048 × 512 points. The images were flattened by line-by-line subtraction of first and second order polynomials in order to remove artefacts due to sample tilt and scanner bow. From flattened AFM images root-mean-square surface roughness R_q was calculated as the standard deviation of surface heights.

In order to recognize the main asperities of the surface where cell adhesion contact points are likely to develop, we have applied to AFM topographical maps suitable thresholds on heights in order to segment the image and identify the more relevant morphological protruding features; to this purpose, height thresholds were determined for each image as the z values which maximized the number of isolated topographic features (the asperities) surviving above-threshold (details on this procedure are provided in the Additional file 2: Figure S2A–C). This choice is aimed at identifying the maximum number of asperities that a surface can offer as potential contact sites for cells. The geometrical properties of single asperities (diameter, height, radius of curvature and contact area) were determined by custom image-processing routines written in Matlab (Mathworks, Natick, USA, Massachusetts), based on the Image Processing Toolbox (details in the caption of Additional file 2: Figure S2). In particular, we assumed that each asperity can be approximately described as a spherical cap, with a given diameter at the base, height and curved area (the contact area). Eventually, we identified the potential of the asperity features to enable intracellular clustering of the adhesion spots to superior adhesion structures (such as nanoclusters, focal complexes and adhesions), applying the criterion that the separation between asperities should not exceed 60 nm, and grouping the selected asperities into clusters. This criterion is based on the ligand spacing value found to be critical for focal adhesion formation [30].

Cell culture

PC12 (PC-12 Adh ATCC Catalog no.CRL-1721.1TM) were cultured in RPMI-1640 Medium (Sigma-Aldrich) supplemented with 10 % horse serum (HS; Sigma-Aldrich), 5 % fetal bovine serum (FBS; Sigma-Aldrich), 2 mM L-glutamine, 100 units/ml penicillin, 100 μg/ml streptomycin, 1 mM pyruvic acid (sodium salt) and 10 mM HEPES. The culture condition in the incubator (Galaxy S, RS Biotech, Irvine, UK) were maintained at 5 % CO_2, 98 % air-humidified. For subculturing (routinely performed every 2nd–3rd day) the cells were detached from culture dishes using a 1 mM EDTA solution in HBSS (Sigma-Aldrich) or a trypsin solution (Sigma-Aldrich), centrifuged at 1000×*g* for 5 min, and re-suspended in culture medium.

Preparation of the PC12 cells for the diverse cell biological experiments and analysis of differentiation

PC12 cells were detached with 1 mM EDTA in HBSS, centrifuged at 1000×*g* for 5 min and washed with low serum differentiation medium (RPMI plus supplements but with 1 % HS only and no FBS). Then the cells were counted with an improved Neubauer chamber and plated at a concentration of 7500 cells/ml (~4000 cells/cm^2 in a well of a 24 well plate). If a NGF stimulus (human NGF-β from Sigma-Aldrich) was scheduled, it was added to the medium at a concentration of 50 ng/ml. In the case of a treatment with inhibitors, antibodies or other reagents, the cells were always pre-incubated in suspension for 15 min with the reagent in the indicated concentration (see figure legends) before plating. The treatment was then continued, either for the whole period of the experiment or for 1 h in the initial phase of cell/substrate interaction (as indicated in the figure legends of the single experiments). For the gradual hypoosmotic compensation experiment the cells (after 15 min preincubation in suspension) were plated on ns-Zr15 in the presence of RPMI diluted 9/1; 8,25/1,75; 7,5/2,5 and 6/4 with deionized water (always supplemented with 1 % HS). The hyperosmotic gradient ranged from 25–150 mM sucrose in 1 % HS differentiation medium. To document and quantify the morphological changes, phase contrast images were recorded with an inverted Axiovert 40 CFL microscope (Zeiss, Oberkochen, Germany) equipped with a LD A-Plan 20x/0.3 Ph1 objective (Zeiss), and then analyzed with ImageJ (NIH, New York, USA, New York).

For the differentiation rate only cells with neurites >10 µm were considered as differentiated. For the neurite length measurement, only neurites >10 µm were quantified, in case of more than one neurite, only the two longest were considered for the quantification and if the neurite branched only the longest branch was measured. Each morphological analysis comprised >500 cells for the differentiation rates and >150 neurites for the neurite outgrowth, from 2–5 independent experiments.

Antibodies, reagents and inhibitors for cell biological experiments

The reagents used in work were the following. Antibodies or fluorescence reagents: 4B4 (Beckman Coulter) and K20 (Santa Cruz Biotechnology, Santa Cruz, USA, California) against β1 integrin, 87G3 antibody against p-CREB (Cell signaling, Danvers, USA, Massachusetts), hVin-1 antibody against vinculin (Sigma-Aldrich), HOECHST 33342 (Molecular Probes (Thermo Fischer Scientific), Waltham, USA, Massachusetts), TRITC-Phalloidin (Sigma-Aldrich). Inhibitors: blebbistatin, cytochalasin D, EHop-016, GW441756, lysophosphatidic acid, methyl-β-cyclodextrin, nocodazole, PF-573228, SP600125, U1026, Y27632 (all Sigma-Aldrich).

Transmission electron microscopy analysis of nanoscopic adhesion regions

Flat and cluster-assembled zirconia films have been produced on Aclar® films. 24 h post seeding, cells were fixed in 0.1 M Na cacodylate buffer with 1.2 % glutaraldehyde for 1 h at RT and heavy metal stained as described in Deerinck et al. [95], with minor modifications. Briefly, cells were incubated for 1 h on ice in a solution containing 1.5 % potassium ferrocyanide, 2 % osmium tertroxide and 2 mM $CaCl_2$ in 0.1 M Na cacodylate buffer, rinsed with ddH_2O and incubated with a thiocarbohydrazide solution (10 mg/ml in ddH_2O) for 20 min at RT. Cells were rinsed again in ddH_2O and exposed to 2 % osmium tetroxide in ddH2O for 30 min, rinsed and stained by a saturated solution of uranyl acetate in ddH_2O for 45 min. Cells were then dehydrated by an EtOH series and embedded in Epon resin.

Ultrathin sections were cut using an UltraCut6 ultramicrotome (Leica Microsystems GmbH, Wetzlar, Germany), collected on Formvar coated copper slot grids and imaged with a Tecnai G2 transmission electron microscope (FEI, Hillsboro, USA, Oregon). The images were analyzed with ImageJ (NIH). In order to define the dimension of nanoscopic adhesion sites, profiles of the cell membranes and the substrates were manually traced and both converted into collection of XY coordinates. Using the coordinates, the distance between of every membrane point and the substrate was defined as the shortest segment connecting that point to substrate profile out of all the possible ones. Taking into account the structure and extracellular length of extended integrins and the position of their ligand interaction site [29], we defined the adhesion sites of the cell with the substrate as sections of the membrane where the distance with the substrate is equal or below 15 nm. Respecting this criterion, we eventually measured the length of the adhesion contact regions. In total, for global statistics 164 adhesion regions on cluster-assembled zirconia and 120 on flat zirconia were analyzed surfaces, obtained from images deriving from two independent experiments.

Immunofluorescence imaging

Cells were fixed with 4 % PFA/PBS, permeabilized with 0.2 % Triton X-100/PBS, blocked with 3 % BSA/PBS and incubated with the primary antibody for at least 1 h at RT (or alternatively overnight at 4 °C) and in humid conditions, the secondary antibody was incubated at RT for maximum 1 h. The actin cytoskeleton was stained with TRITC-phalloidin (Sigma-Aldrich) which was added to the secondary antibody. Optionally HOECHST (Molecular Probes) staining was performed to mark the nucleus. If the samples were mounted, this was done with ProLong® Gold antifade (Molecular probes).

Analysis of focal adhesions and actin filaments by Total Internal Reflection Fluorescence (TIRF) microscopy

PC12 cells were seeded on the different substrates (on Ø24 mm glass cover slips). At the indicated time points (30 min, 1, 4 and 24 h) the cells were fixed and labeled for vinculin and f-actin following the immunofluorescence imaging protocol described above. The images were recorded with a Leica AM TIRF MC system using a Leica HCX PL APO 63X NA 1.47 objective (Leica). To visualize the vinculin clusters, integrated 488 nm laser lines and Andor iXon DU-885 camera (Andor Technology, Belfast, UK) was used. The image recording was done with a laser incident angle of 74° allowing a penetration depth of almost 250 nm. The images were elaborated with ImageJ following a recently described method [96] to analyze the area and number of clusters per cell. In total, for global statistics 722-3678 clusters from 16–34 cells were analyzed from three independent experiments. The f-actin instead was imaged in epifluorescence mode. Here the cytoskeletal organization of the cells was categorized in three categories: (1) no detectable presence of actin bundles/stress fibers, (2) 1–10 distinct actin bundles/stress fibers and (3) >10 distinct actin bundles/stress fibers.

Analysis of the mechanical properties of living PC12 cells by AFM

Cells were plated in the standard experimental conditions on Ø40 mm glass-bottom cell culture dishes (Willco Wells, Amsterdam, Netherlands), covered either with flat or cluster-assembled zirconia films or coated with PLL. During the AFM measurements the temperature of the medium was maintained at 37 °C by a custom built thermostatic fluid cell (for details see Fig. 12 and Appendix C1 of Ref. [97]). 25 mM HEPES buffer was added to keep the physiological pH of the medium.

Combined topographical and mechanical AFM imaging was performed with a Bioscope Catalyst AFM (Bruker) operated in *force volume* mode by collecting series of force vs distance curves, according to established protocols [97, 98]. We used a monolithic borosilicate glass probe consisting in a micrometer-sized spherical glass bead with radii R in the range of 4500–5500 nm attached to silicon cantilevers with elastic constant $k = 0.2$–0.3 N/m [99]. Each force volume consists in an array of 64 × 64 force vs distance curves recorded across the region occupied by a single cell. All measurements were performed with the following parameters: ramp length $L = 5$ μm; approaching speed $v_{appr} = 43.4$ μm/s; ramp frequency $f = 7.1$ Hz; 2048 points per curve. The lateral scan size varied between 50 × 50 μm and 100 × 100 μm, depending on the dimension of the cell.

Data processing of force volumes was carried out in Matlab (Mathworks) environment using custom-built routines [97]. The local height of the sample and the local effective Young's modulus can be extracted by single force curves; by these means topographic and elastic maps of the sample can be acquired in one-to-one correspondence. The values of the Young's moduli were extracted by fitting the Hertz model to experimental data [97]. A finite-thickness correction was applied and the force curves linearized in order to identify the presence of multiple elastic regimes inside the cell, and more generally the upper limit of validity of the Hertz model. Following this procedure, the effective Young's modulus of the cell was typically evaluated by fitting the 0–40 % range of the total local indentation. The cumulative distributions of Young's moduli of the cells turned out to be the envelope of a few (typically two–three) lognormal modes, originating from micro-scale domains that the AFM probe was able to resolve. Multi-Gaussian fit in semilog10 scale allowed identifying the peak value E' and the geometric standard deviation σ_g^{10} of each lognormal mode; from these values the median value E_{med} and the standard deviation of the median σ_{med} were calculated for all modes as $E_{med} = 10^{E'}$ and $\sigma_{med} = \sqrt{\pi/2}E_{med}\sigma_g^{10}/\sqrt{N}$ [100], N being the number of force curves in each mode. The effective rigidity of cells was obtained as the weighted average of median values: $E = \sum_i f_i E_{med,i}$, using the fraction $f_i = N_i/N_{tot}$ of force curves in each mode as weight; the total error σ_E associated to E was calculated by summing in quadrature the propagated error of the medians $\sigma = \sqrt{\sum_i f_i^2 \sigma_{med,i}^2}$ and an effective instrumental relative error $\sigma_{instr} = 10$ %: $\sigma_E = \sqrt{\sigma_{instrum}^2 E^2 + \sigma^2}$. Finally, the average median values of the Young's Modulus of all cells belonging to the same condition have been evaluated; the corresponding error has been calculated as the standard deviation of the mean summed in quadrature with the propagated σ_E. The statistical significance of differences between Young's moduli of cells from different culture conditions has been evaluated applying the two-tails t Test. 6–8 cells have been measured for each condition derived from two to three independent experiments.

Analysis of CREB phosphorylation by confocal microscopy

PC12 cells were plated on the indicated substrates and fixed with 4 % PFA at the different time points. The immunofluorescence staining was done as described above. For this experiment it was stained for Ser 133-phosphorylated CREB (antibody 87G3 from Cell signaling), f-actin (Phalloidin) and the nucleus (HOECHST). To quantify the specific nuclear Ser133 phospho-CREB signal, the average-projection signal of the nuclear Ser133 p-CREB (the nuclear region was determined from the max-projection of the HOECHST staining) was set in relation to the average-projection signal of the total cell (total cell region was determined from the outlines of max-projection of f-actin staining). The confocal images were recorded with a Leica confocal microscopy TCS SP2 (Leica). In total, for global statistics the signals of 33–76 cells were analyzed from two independent experiments.

Proteomic analysis

After 24 h on the indicated substrates the cells were scratched from the substrates with a cell scraper (TPP, Trasadingen, Switzerland) (on ice) in the presence of icecold PBS supplemented with protease inhibitor (Roche, Basel, Switzerland).

After reduction and derivatization, the proteins were digested with trypsin sequence grade trypsin (Roche) for 16 h at 37 °C using a protein:trypsin ratio of 1:20. LC-ESI-MS/MS analysis was performed on a Dionex UltiMate 3000 HPLC System with a PicoFrit ProteoPrep C18 column (200 mm, internal diameter of 75 μm) (New Objective, Woburn, USA, Massachusetts). Gradient: 1 % ACN in 0.1 % formic acid for 10 min, 1–4 % ACN in 0.1 % formic acid for 6 min, 4–30 % ACN in 0.1 % formic acid for 147 min and 30–50 % ACN in 0.1 % formic for 3 min at a flow rate of 0.3 μl/min. The eluate was electrosprayed into an LTQ Orbitrap Velos (Thermo Fisher Scientific) through a Proxeon nanoelectrospray ion source (Thermo Fisher Scientific). The LTQ-Orbitrap was operated in positive mode in data-dependent acquisition mode to automatically alternate between a full scan (m/z 350–2000) in the Orbitrap (at resolution 60,000, AGC target 1,000,000) and subsequent CID MS/MS in the linear ion trap of the 20 most intense peaks from full scan (normalized collision energy of 35 %, 10 ms activation). Isolation window: 3 Da, unassigned charge states: rejected, charge state 1: rejected, charge states 2+, 3+, 4+: not rejected; dynamic exclusion enabled (60 s, exclusion list size: 200). Four technical replicate analyses of each sample were performed. Data acquisition was controlled by Xcalibur 2.0 and Tune 2.4 software (Thermo Fisher Scientific).

Mass spectra were analyzed using MaxQuant software (version 1.3.0.5). The initial maximum allowed mass deviation was set to 6 ppm for monoisotopic precursor ions and 0.5 Da for MS/MS peaks. Enzyme specificity was set to trypsin, defined as C-terminal to arginine and lysine excluding proline, and a maximum of two missed cleavages were allowed. Carbamidomethylcysteine was set as a fixed modification, N-terminal acetylation and methionine oxidation as variable modifications. The spectra were searched by the Andromeda search engine against the rat Uniprot sequence database (release 29.05.2013). Protein identification required at least one unique or razor peptide per protein group. Quantification in MaxQuant was performed using the built-in XIC-based label free quantification (LFQ) algorithm using fast LFQ [101]. The required false positive rate was set to 1 % at the peptide and 1 % at the protein level against a concatenated target decoy database, and the minimum required peptide length was set to six amino acids. Statistical analyses were performed using the Perseus software (version 1.4.0.6, www.biochem.mpg.de/mann/tools/). Only proteins present and quantified in at least 3 out of 4 technical repeats were considered as positively identified; 748, 720 and 764 proteins were identified in ns-Zr15, flat-Zr and PLL +NGF, respectively; 18 proteins were exclusively expressed in ns-Zr15, 14 proteins in flat-Zr, and 26 proteins in PLL +NGF. An ANOVA test (false discovery rate 0.05) was carried out to identify proteins differentially expressed among the three conditions: 286 out of 666 common proteins differ with statistical significance and were selected for further analyses. In particular, for the purpose of the present report, we focused only on the differential proteomics between cells on ns-Zr15 in comparison to cells on flat-Zr in order to better understand the effect of the surface nanotopography. Differential expression was considered as significant if (1) a protein was present only in ns-Zr15 or flat-Zr or (2) its normalized (according to the LFQ algorithm) intensity resulted statistical different as calculated by Post Hoc Bonferroni test (t test cut-off at p value = 0.0167) (Fig. 9a).

Additional files

Additional file 1: Figure S1. In this panel representative phase contrast images of cells after the different, indicated treatments are shown (examples of the condition without any treatment are shown in Fig. 1a). Furthermore a close-up from differentiated cells in the ns-Zr15 (-NGF) condition, taken from Fig. 1a, is shown to illustrate the typical features of neuritogenesis.

Additional file 2: Figure S2. Procedure for the identification of asperity pattern from AFM images and data analysis. Height thresholds (**B**) are set for each topographic map (**A** for a representative one) and the points in the image with heights above threshold are retained. Each threshold value therefore determines a pattern of isolated nano-islands (asperities) consisting in connected sets of pixels (**C**). The best asperity pattern is determined by the threshold value maximizing the number of asperities. This choice is based on the objective to identify the maximum number of asperities that a surface can offer as potential contact sites for cells. For this purpose we adopted a statistical approach based on the observation that, as the height threshold is lowered from the topmost level, the number of above-threshold asperities tends to increase, then at a critical threshold it stabilizes, then it decreases again since asperities start merging at their bases. The optimal threshold is therefore the one that selects the more numerous and larger asperities. The asperities can be identified and labeled one by one, and their morphological parameters (diameter, height, radius of curvature, contact area, volume) are calculated. In particular, assuming that asperities are described with good accuracy by the spherical cap geometry [99], the contact area A of the asperity is calculated as $A = \pi[(D/2)^2 + h^2]$, where D and h are the asperity diameter and height, respectively. The mean separation d between asperities is estimated based on the calculated average area per asperity, assuming each asperity occupies a square of area d^2, so that the centers of two adjacent asperities are separated by d (we have detected about 2000–3000 asperities on both ns-ZrO_2 samples).

Additional file 3: Figure S3. Inhibition of principal mediators and cellular structures/processes involved in integrin signaling. Considering the importance of integrin signaling in both, the canonical and the nanostructure-induced neuritogenesis, we further examined prominent mediators and cellular structures/processes involved in the integrin pathway, cytoskeletal organization and neuritogenesis. The experimental set-up is the same as in Fig. 5, with the difference that here, the cells were incubated with the inhibitor only for the 1st h after plating. This treatment turned out to be sufficient for efficient inhibition but minimized collateral, cytotoxic effects of the inhibitors. The impact of these inhibitors on canonical and nanostructure-induced neuritogenesis is summarized in the graphs (representing the global statistics of two or three independent experiments, n: >500 cells, >150 neurites). **A** The graph displays the impact of inhibitors against prominent mediators of the integrin signaling; FAK (PF-573228 50 μM), Rac1 (EHop-016 2.5 μM), and ROCK (Y27632 10 μM). **B** In this graph the results for treatments with cytochalasin D (10 μM), nocodazole (1 mM), blebbistatin (50 μM) and methyl-β-cyclodextrin (5 mM) are shown. **C** The graph summarizes the impact of different concentrations (5 and 10 μM) of lysophosphatic acid (LPA) on canonical or nanostructure-induced neuritogenesis. **D** The graph displays the impact of a hyperosmotic gradient on the nanostructure-induced neuritogenesis (the same experimental set-up as in Fig. 7c). Focal adhesion kinase (FAK) and Rac1 are known to be crucial in the regulation of cytoskeletal dynamics which drive neurite outgrowth [37, 46, 49]. Indeed, the impairment of FAK and Rac1 function abolished the nanostructure-induced neuritogenesis to a similar extent as the canonical one (Additional file 2: Figure S2D). Also the disintegration of lipid rafts (cholesterol-rich membrane compartments involved in signaling events and cytoskeletal organization, particularly also in the context of neuritogenesis [102]) by methyl-β-cyclodextrin impeded both, canonical and nanostructure-induced neurite outgrowth (Additional file 2: Figure S2B). The same was true for the inhibition of actin and tubulin polymerization by cytochalasin D, or respectively nocodazole (Additional file 2: Figure S2B). The latter one even impaired the low basal differentiation congruent with the importance of tubulin polymerization for neurite budding [103]. Blocking of ROCK (inh.: Y27632) instead did not alter the eventual formation of neurites (or even slightly increased it) (Additional file 2: Figure S2A) but at the contrary clearly accelerated the initial budding in both cases (not shown). The negative regulation of neurite budding by the RhoA/ROCK pathway has been shown in many publications (e.g. [46, 86, 87]). Congruently, also reducing the affinity of myosin II to actin via blebbistatin had the same effect (**B**). Representative images of all conditions can be found in Additional file 1: Figure S1.

Additional file 4: Table S1. Proteomic data for upregulated proteins. Proteins upregulated (compared to flat-Zr) or present only in cells grown on ns-Zr15. Adhesome proteins and proteins with roles in mechanobiological processes are marked in dark and light grey, respectively.

Additional file 5: Table S2. Proteomic data for downregulated proteins. Proteins downregulated in cells on ns-Zr15 or were present only in cells on flat-Zr. Adhesome proteins and proteins with roles in mechanobiological processes are marked in dark and light grey, respectively.

Abbreviations

AFM: atomic force microscopy; a.u.: arbitrary units; av: average; BDR: ballistic deposition regime; CREB: cAMP response element-binding protein; ECM: extracellular matrix; Erk: extracellular-signal-regulated kinase; FA: focal adhesion; f-actin: filamentous actin; FBS: fetal bovine serum; FC: focal complex; flat-Zr: flat zirconia; h: hour; HS: horse serum; JNK: c-Jun N-terminal kinases; kPa: kilo pascal; LPA: lysophosphatidic acid; MAD: median absolute deviation; MAPK: mitogen-activated protein kinase; MBC: methyl-β-cyclodextrin; mM: millimolar; na: not analyzable; NGF: nerve growth factor; NO: nitric oxide; ns-Zr: nanostructured zirconia; p-CREB: phosphorylated CREB; PLL: poly-L-lysine; PMCS: pulsed microplasma cluster source; SCBD: supersonic cluster beam deposition; SD: standard deviation; stdev: standard deviation; TEM: transmission electron microscopy; TF: transcription factor; TIRF: total internal reflection fluorescence (microscopy); TrkA: tropomyosin receptor kinase A, also known as high affinity nerve growth factor receptor; ROCK: Rho-associated protein kinase; Rq: root-mean-square surface roughness; RTK: receptor tyrosine kinase.

Authors' contributions

The project was mostly conceived by CS, who performed also many of the cell biological experiments and corresponding quantifications. CS wrote also the principal part of the manuscript and designed most of the figures. SR performed the TEM imaging. MAC did the quantification of the TEM images and performed the TIRF microscopy experiments and corresponding quantifications. FB, LP and AP designed and performed the AFM surface analysis. LP, MG, and AP designed and performed the live cell AFM measurements and corresponding data analysis. EM, AN, CS and GT conceived and realized the proteomic approach and the corresponding data analysis. CP and ES did the supersonic cluster beam depositions. MT was involved in the initial part of the project conception. AP, GT, CL and PM were involved in conceiving and creating the project and the realization of the manuscript, furthermore they contributed reagents, materials and analysis tools. All authors read and approved the final manuscript.

Author details

[1] CIMAINA, Dipartimento di Fisica, Università degli Studi di Milano, via Celoria 16, Milan 20133, Italy. [2] SEMM European School of Molecular Medicine, Via Adamello 16, Milan 20139, Italy. [3] DIVET, Università degli Studi di Milano, via Celoria 10, Milan 20133, Italy. [4] Fondazione Filarete, via le Ortles 22/4, Milan 20139, Italy.

Acknowledgements

This work has been supported by the Italian Ministry of University and Research, MIUR, through the "National Funding for Basic Research" (FIRB) with a project entitled "Oxides at the nanoscale: functionalities and applications" (FIRB RBA-P11AYN) and by the European project FutureNanoNeeds "Framework to respond to regulatory needs of future nanomaterials and markets" (FP7-NMP-2013-LARGE-7). COST Action TD1002 is acknowledged for providing a stimulating scientific environment for the discussion of AFM-based nanomechanics of cells and soft matter. We are very grateful for the work of Andrea Notarnicola and Davide Alessandro Martella who provided a valuable contribution for some of the cell biological experiments and their quantifications. We are also thankful for the help of Massimiliano Garrè from the Imaging Unit of IFOM (The FIRC Institute of Molecular Oncology) in the TIRF microscopy experiments.

Competing interests

The authors declare that they have no competing interests.

Received: 27 December 2015 Accepted: 25 February 2016
Published online: 09 March 2016

References

1. Geiger B, Spatz JP, Bershadsky AD. Environmental sensing through focal adhesions. Nat Rev Mol Cell Biol. 2009;10:21–33. doi:10.1038/nrm2593.
2. Dalby MJ, Gadegaard N, Oreffo ROC. Harnessing nanotopography and integrin-matrix interactions to influence stem cell fate. Nat Mater. 2014;13:558–69. doi:10.1038/nmat3980.
3. Humphries JD, Paul NR, Humphries MJ, Morgan MR. Emerging properties of adhesion complexes: what are they and what do they do? Trends Cell Biol. 2015. doi:10.1016/j.tcb.2015.02.008.
4. Chen W, Shao Y, Li X, Zhao G, Fu J. Nanotopographical surfaces for stem cell fate control: Engineering mechanobiology from the bottom. Nano Today. 2014. doi:10.1016/j.nantod.2014.12.002.
5. Wang N, Tytell JD, Ingber DE. Mechanotransduction at a distance: mechanically coupling the extracellular matrix with the nucleus. Nat Rev Mol Cell Biol. 2009;10:75–82. doi:10.1038/nrm2594.

6. Iskratsch T, Wolfenson H, Sheetz MP. Appreciating force and shape - the rise of mechanotransduction in cell biology. Nat Rev Mol Cell Biol. 2014. doi:10.1038/nrm3903.
7. Gasiorowski JZ, Murphy CJ, Nealey PF. Biophysical Cues and Cell Behavior: the Big Impact of Little Things. Annu Rev Biomed Eng. 2013;15:155–76. doi:10.1146/annurev-bioeng-071811-150021.
8. Sukharev S, Sachs F. Molecular force transduction by ion channels—diversity and unifying principles. J Cell Sci. 2012;125:3075–83. doi:10.1242/jcs.092353.
9. Murphy WL, McDevitt TC, Engler AJ. Materials as stem cell regulators. Nat Mater. 2014;13:547–57. doi:10.1038/nmat3937.
10. Yim EKF, Sheetz MP. Force-dependent cell signaling in stem cell differentiation. Stem Cell Res. Ther. 2012;3:41. doi:10.1186/scrt132.
11. Franze K, Janmey PA, Guck J. Mechanics in neuronal development and repair. Annu Rev Biomed Eng. 2013;15:227–51. doi:10.1146/annurev-bioeng-071811-150045.
12. Mendes PM. Cellular nanotechnology: making biological interfaces smarter. Chem Soc Rev. 2013;42:9207–18. doi:10.1039/c3cs60198f.
13. Brunetti V, Maiorano G, Rizzello L, Sorce B, Sabella S, Cingolani R, et al. Neurons sense nanoscale roughness with nanometer sensitivity. Proc Natl Acad Sci. 2010;107:6264–9. doi:10.1073/pnas.0914456107.
14. Chua JS, Chng C-P, Moe AAK, Tann JY, Goh ELK, Chiam K-H, et al. Extending neurites sense the depth of the underlying topography during neuronal differentiation and contact guidance. Biomaterials. 2014;35:7750–61. doi:10.1016/j.biomaterials.2014.06.008.
15. Tamplenizza M, Lenardi C, Maffioli E, Nonnis S, Negri A, Forti S, et al. Nitric oxide synthase mediates PC12 differentiation induced by the surface topography of nanostructured TiO2. J Nanobiotechnology. 2013;11:35. doi:10.1186/1477-3155-11-35.
16. Christopherson GT, Song H, Mao H-Q. The influence of fiber diameter of electrospun substrates on neural stem cell differentiation and proliferation. Biomaterials. 2009;30:556–64. doi:10.1016/j.biomaterials.2008.10.004.
17. Foley JD, Grunwald EW, Nealey PF, Murphy CJ. Cooperative modulation of neuritogenesis by PC12 cells by topography and nerve growth factor. Biomaterials. 2005;26:3639–44. doi:10.1016/j.biomaterials.2004.09.048.
18. Lee MR, Kwon KW, Jung H, Kim HN, Suh KY, Kim K, et al. Direct differentiation of human embryonic stem cells into selective neurons on nanoscale ridge/groove pattern arrays. Biomaterials. 2010;31:4360–6. doi:10.1016/j.biomaterials.2010.02.012.
19. Migliorini E, Grenci G, Ban J, Pozzato A, Tormen M, Lazzarino M, et al. Acceleration of neuronal precursors differentiation induced by substrate nanotopography. Biotechnol Bioeng. 2011;108:2736–46. doi:10.1002/bit.23232.
20. Yang K, Jung H, Lee H-R, Lee JS, Kim SR, Song KY, et al. Multiscale, hierarchically patterned topography for directing human neural stem cells into functional neurons. ACS Nano. 2014. doi:10.1021/nn501182f.
21. Manicone PF, Iommetti, PR, Raffaelli L. An overview of zirconia ceramics: basic properties and clinical applications. J Dent. 2007;35:819–26. doi:10.1016/j.jdent.2007.07.008.
22. Wegner K, Piseri P, Tafreshi HV, Milani P. Cluster beam deposition: a tool for nanoscale science and technology. J Phys Appl Phys. 2006;39:R439. doi:10.1088/0022-3727/39/22/R02.
23. Podestà A, Borghi F, Indrieri M, Bovio S, Piazzoni C, Milani P. Nanomanufacturing of titania interfaces with controlled structural and functional properties by supersonic cluster beam deposition. J Appl Phys. 2015;118:234309. doi:10.1063/1.4937549.
24. Huang J, Gräter SV, Corbellini F, Rinck S, Bock E, Kemkemer R, et al. Impact of order and disorder in RGD nanopatterns on cell adhesion. Nano Lett. 2009;9:1111–6. doi:10.1021/nl803548b.
25. Barabási A-L, Stanley HE. Fractal concepts in surface growth. Cambridge: Cambridge University Press; 1995. doi:10.1017/CB09780511599798.
26. Scopelliti PE, Borgonovo A, Indrieri M, Giorgetti L, Bongiorno G, Carbone R, et al. The effect of surface nanometre-scale morphology on protein adsorption. PLoS One. 2010;5:e11862. doi:10.1371/journal.pone.0011862.
27. Singh AV, Ferri M, Tamplenizza M, Borghi F, Divitini G, Ducati C, et al. Bottom-up engineering of the surface roughness of nanostructured cubic zirconia to control cell adhesion. Nanotechnology. 2012;23:475101. doi:10.1088/0957-4484/23/47/475101.
28. Schvartzman M, Palma M, Sable J, Abramson J, Hu X, Sheetz MP, et al. Nanolithographic control of the spatial organization of cellular adhesion receptors at the single-molecule level. Nano Lett. 2011;11:1306–12. doi:10.1021/nl104378f.
29. Anthis NJ, Campbell ID. The tail of integrin activation. Trends Biochem Sci. 2011;36:191–8. doi:10.1016/j.tibs.2010.11.002.
30. Cavalcanti-Adam EA, Volberg T, Micoulet A, Kessler H, Geiger B, Spatz JP. Cell spreading and focal adhesion dynamics are regulated by spacing of integrin ligands. Biophys J. 2007;92:2964–74. doi:10.1529/biophysj.106.089730.
31. Liu Y, Medda R, Liu Z, Galior K, Yehl K, Spatz JP, et al. Nanoparticle tension probes patterned at the nanoscale: impact of integrin clustering on force transmission. Nano Lett. 2014. doi:10.1021/nl501912g.
32. Gardel ML, Schneider IC, Aratyn-Schaus Y, Waterman CM. Mechanical integration of actin and adhesion dynamics in cell migration. Annu Rev Cell Dev Biol. 2010;26:315–33. doi:10.1146/annurev.cellbio.011209.122036.
33. Klein R, Jing SQ, Nanduri V, O'Rourke E, Barbacid M. The trk proto-oncogene encodes a receptor for nerve growth factor. Cell. 1991;65:189–97.
34. Vaudry D, Stork PJS, Lazarovici P, Eiden LE. Signaling pathways for PC12 cell differentiation: making the right connections. Science. 2002;296:1648–9. doi:10.1126/science.1071552.
35. Campos LS, Leone DP, Relvas JB, Brakebusch C, Fässler R, Suter U, et al. Beta1 integrins activate a MAPK signalling pathway in neural stem cells that contributes to their maintenance. Dev. Camb. Engl. 2004;131:3433–44. doi:10.1242/dev.01199.
36. Myers JP, Santiago-Medina M, Gomez TM. Regulation of axonal outgrowth and pathfinding by integrin-ECM interactions. Dev. Neurobiol. 2011;71:901–23. doi:10.1002/dneu.20931.
37. Ivankovic-Dikic I, Grönroos E, Blaukat A, Barth BU, Dikic I. Pyk2 and FAK regulate neurite outgrowth induced by growth factors and integrins. Nat Cell Biol. 2000;2:574–81. doi:10.1038/35023515.
38. Miyamoto S, Teramoto H, Gutkind JS, Yamada KM. Integrins can collaborate with growth factors for phosphorylation of receptor tyrosine kinases and MAP kinase activation: roles of integrin aggregation and occupancy of receptors. J Cell Biol. 1996;135:1633–42.
39. Kilian KA, Bugarija B, Lahn BT, Mrksich M. Geometric cues for directing the differentiation of mesenchymal stem cells. Proc Natl Acad Sci. 2010;107:4872–7. doi:10.1073/pnas.0903269107.
40. Galbraith CG, Yamada KM, Sheetz MP. The relationship between force and focal complex development. J Cell Biol. 2002;159:695–705. doi:10.1083/jcb.200204153.
41. Ciobanasu C, Faivre B, Le Clainche C. Integrating actin dynamics, mechanotransduction and integrin activation: the multiple functions of actin binding proteins in focal adhesions. Eur J Cell Biol. 2013;92:339–48. doi:10.1016/j.ejcb.2013.10.009.
42. Schulte C, Ferraris GMS, Oldani A, Galluzzi M, Podestà A, Puricelli L, et al. Lamellipodial tension, not integrin/ligand binding, is the crucial factor to realise integrin activation and migration. Eur J Cell Biol. 2015;. doi:10.1016/j.ejcb.2015.10.002.
43. Ferraris GMS, Schulte C, Buttiglione V, Lorenzi VD, Piontini A, Galluzzi M, et al. The interaction between uPAR and vitronectin triggers ligand-independent adhesion signalling by integrins. EMBO J. 2014;. doi:10.15252/embj.201387611.
44. Tigyi G, Fischer DJ, Sebök Á, Yang C, Dyer DL, Miledi R. Lysophosphatidic acid-induced neurite retraction in PC12 Cells: control by phosphoinositide-Ca2 + signaling and Rho. J Neurochem. 1996;66:537–48. doi:10.1046/j.1471-4159.1996.66020537.x.
45. Flynn KC. The cytoskeleton and neurite initiation. Bioarchitecture. 2013;3:86–109. doi:10.4161/bioa.26259.
46. Woo S, Gomez TM. Rac1 and RhoA promote neurite outgrowth through formation and stabilization of growth cone point contacts. J Neurosci. 2006;26:1418–28. doi:10.1523/JNEUROSCI.4209-05.2006.
47. Huttenlocher A, Ginsberg MH, Horwitz AF. Modulation of cell migration by integrin-mediated cytoskeletal linkages and ligand-binding affinity. J Cell Biol. 1996;134:1551–62. doi:10.1083/jcb.134.6.1551.
48. Schense JC, Hubbell JA. Three-dimensional migration of neurites is mediated by adhesion site density and affinity. J Biol Chem. 2000;275:6813–8. doi:10.1074/jbc.275.10.6813.
49. Schaefer AW, Schoonderwoert VTG, Ji L, Mederios N, Danuser G, Forscher P. Coordination of actin filament and microtubule dynamics

during neurite outgrowth. Dev Cell. 2008;15:146–62. doi:10.1016/j.devcel.2008.05.003.
50. Betz T, Koch D, Lu Y-B, Franze K, Käs JA. Growth cones as soft and weak force generators. Proc Natl Acad Sci. 2011;108:13420–5. doi:10.1073/pnas.1106145108.
51. O'Toole M, Lamoureux P, Miller KE. Measurement of subcellular force generation in neurons. Biophys J. 2015;108:1027–37. doi:10.1016/j.bpj.2015.01.021.
52. Santiago-Medina M, Gregus KA, Gomez TM. PAK-PIX interactions regulate adhesion dynamics and membrane protrusion to control neurite outgrowth. J Cell Sci. 2013;126:1122–33. doi:10.1242/jcs.112607.
53. Diz-Muñoz A, Fletcher DA, Weiner OD. Use the force: membrane tension as an organizer of cell shape and motility. Trends Cell Biol. 2013;23:47–53. doi:10.1016/j.tcb.2012.09.006.
54. Yim EKF, Darling EM, Kulangara K, Guilak F, Leong KW. Nanotopography-induced changes in focal adhesions, cytoskeletal organization, and mechanical properties of human mesenchymal stem cells. Biomaterials. 2010;31:1299–306. doi:10.1016/j.biomaterials.2009.10.037.
55. Meyer CJ, Alenghat FJ, Rim P, Fong JH, Fabry B, Ingber DE. Mechanical control of cyclic AMP signalling and gene transcription through integrins. Nat Cell Biol. 2000;2:666–8. doi:10.1038/35023621.
56. Riccio A. Dynamic epigenetic regulation in neurons: enzymes, stimuli and signaling pathways. Nat Neurosci. 2010;13:1330–7. doi:10.1038/nn.2671.
57. Merz K, Herold S, Lie DC. CREB in adult neurogenesis—master and partner in the development of adult-born neurons? Eur J Neurosci. 2011;33:1078–86. doi:10.1111/j.1460-9568.2011.07606.x.
58. Impey S, McCorkle SR, Cha-Molstad H, Dwyer JM, Yochum GS, Boss JM, et al. Defining the CREB regulon: a genome-wide analysis of transcription factor regulatory regions. Cell. 2004;119:1041–54. doi:10.1016/j.cell.2004.10.032.
59. Barnat M, Enslen H, Propst F, Davis RJ, Soares S, Nothias F. Distinct roles of c-Jun N-terminal kinase isoforms in neurite initiation and elongation during axonal regeneration. J Neurosci. 2010;30:7804–16. doi:10.1523/JNEUROSCI.0372-10.2010.
60. Trappmann B, Gautrot JE, Connelly JT, Strange DGT, Li Y, Oyen ML, et al. Extracellular-matrix tethering regulates stem-cell fate. Nat Mater. 2012;11:642–9. doi:10.1038/nmat3339.
61. Guo J, Walss-Bass C, Ludueña RF. The β isotypes of tubulin in neuronal differentiation. Cytoskeleton. 2010;67:431–41. doi:10.1002/cm.20455.
62. Lee NH, Weinstock KG, Kirkness EF, Earle-Hughes JA, Fuldner RA, Marmaros S, et al. Comparative expressed-sequence-tag analysis of differential gene expression profiles in PC-12 cells before and after nerve growth factor treatment. Proc Natl Acad Sci. 1995;92:8303–7.
63. Sakurai M, Ayukawa K, Setsuie R, Nishikawa K, Hara Y, Ohashi H, et al. Ubiquitin C-terminal hydrolase L1 regulates the morphology of neural progenitor cells and modulates their differentiation. J Cell Sci. 2006;119:162–71. doi:10.1242/jcs.02716.
64. Westerink RHS, Ewing AG. The PC12 cell as model for neurosecretion. Acta Physiol. 2008;192:273–85. doi:10.1111/j.1748-1716.2007.01805.x.
65. Geiger T, Zaidel-Bar R. Opening the floodgates: proteomics and the integrin adhesome. Curr Opin Cell Biol. 2012;24:562–8. doi:10.1016/j.ceb.2012.05.004.
66. Winograd-Katz SE, Fässler R, Geiger B, Legate KR. The integrin adhesome: from genes and proteins to human disease. Nat Rev Mol Cell Biol. 2014;15:273–88. doi:10.1038/nrm3769.
67. Coutts AS, MacKenzie E, Griffith E, Black DM. TES is a novel focal adhesion protein with a role in cell spreading. J Cell Sci. 2003;116:897–906.
68. Griffith E, Coutts AS, Black DM. RNAi knockdown of the focal adhesion protein TES reveals its role in actin stress fibre organisation. Cell Motil. Cytoskeleton. 2005;60:140–52. doi:10.1002/cm.20052.
69. Park I, Han C, Jin S, Lee B, Choi H, Kwon JT, et al. Myosin regulatory light chains are required to maintain the stability of myosin II and cellular integrity. Biochem J. 2011;434:171–80. doi:10.1042/BJ20101473.
70. Schlienger S, Ramirez RAM, Claing A. ARF1 regulates adhesion of MDA-MB-231 invasive breast cancer cells through formation of focal adhesions. Cell Signal. 2015;27:403–15. doi:10.1016/j.cellsig.2014.11.032.
71. Rocca DL, Amici M, Antoniou A, Suarez EB, Halemani N, Murk K, et al. The small GTPase Arf1 modulates Arp2/3-mediated actin polymerization via PICK1 to regulate synaptic plasticity. Neuron. 2013;79:293–307. doi:10.1016/j.neuron.2013.05.003.
72. Otey CA, Carpen O. Alpha-actinin revisited: a fresh look at an old player. Cell Motil. Cytoskeleton. 2004;58:104–11. doi:10.1002/cm.20007.
73. Choi CK, Vicente-Manzanares M, Zareno J, Whitmore LA, Mogilner A, Horwitz AR. Actin and α-actinin orchestrate the assembly and maturation of nascent adhesions in a myosin II motor-independent manner. Nat Cell Biol. 2008;10:1039–50. doi:10.1038/ncb1763.
74. Fu X, Brown KJ, Yap CC, Winckler B, Jaiswal JK, Liu JS. Doublecortin (Dcx) family proteins regulate filamentous actin structure in developing neurons. J Neurosci Off J Soc Neurosci. 2013;33:709–21. doi:10.1523/JNEUROSCI.4603-12.2013.
75. Storr SJ, Carragher NO, Frame MC, Parr T, Martin SG. The calpain system and cancer. Nat Rev Cancer. 2011;11:364–74. doi:10.1038/nrc3050.
76. Mingorance-Le A, Meur TP. O'Connor, neurite consolidation is an active process requiring constant repression of protrusive activity. EMBO J. 2009;28:248–60. doi:10.1038/emboj.2008.265.
77. Plantier M, Fattoum A, Menn B, Ben-Ari Y, Der Terrossian E, Represa A. Acidic calponin immunoreactivity in postnatal rat brain and cultures: subcellular localization in growth cones, under the plasma membrane and along actin and glial filaments. Eur J Neurosci. 1999;11:2801–12. doi:10.1046/j.1460-9568.1999.00702.x.
78. Winder SJ, Sutherland C, Walsh MP. A comparison of the effects of calponin on smooth and skeletal muscle actomyosin systems in the presence and absence of caldesmon. Biochem J. 1992;288(Pt 3):733–9.
79. Ferhat L, Rami G, Medina I, Ben-Ari Y, Represa A. Process formation results from the imbalance between motor-mediated forces. J Cell Sci. 2001;114:3899–904.
80. Rami G, Caillard O, Medina I, Pellegrino C, Fattoum A, Ben-Ari Y, et al. Change in the shape and density of dendritic spines caused by overexpression of acidic calponin in cultured hippocampal neurons. Hippocampus. 2006;16:183–97. doi:10.1002/hipo.20145.
81. Argenzio E, Margadant C, Leyton-Puig D, Janssen H, Jalink K, Sonnenberg A, et al. CLIC4 regulates cell adhesion and β1 integrin trafficking. J Cell Sci. 2014;127:5189–203. doi:10.1242/jcs.150623.
82. Chevallier J, Koop C, Srivastava A, Petrie RJ, Lamarche-Vane N, Presley JF. Rab35 regulates neurite outgrowth and cell shape. FEBS Lett. 2009;583:1096–101. doi:10.1016/j.febslet.2009.03.012.
83. Zhang J, Fonovic M, Suyama K, Bogyo M, Scott MP. Rab35 controls actin bundling by recruiting fascin as an effector protein. Science. 2009;325:1250–4. doi:10.1126/science.1174921.
84. Elkhatib N, Neu MB, Zensen C, Schmoller KM, Louvard D, Bausch AR, et al. Fascin plays a role in stress fiber organization and focal adhesion disassembly. Curr Biol. 2014;24:1492–9. doi:10.1016/j.cub.2014.05.023.
85. Cohan CS, Welnhofer EA, Zhao L, Matsumura F, Yamashiro S. Role of the actin bundling protein fascin in growth cone morphogenesis: localization in filopodia and lamellipodia. Cell Motil. Cytoskeleton. 2001;48:109–20. doi:10.1002/1097-0169(200102)48:2<109:AID-CM1002>3.0.CO;2-G.
86. Yamaguchi Y, Katoh H, Yasui H, Mori K, Negishi M. RhoA inhibits the nerve growth factor-induced Rac1 activation through Rho-associated kinase-dependent pathway. J Biol Chem. 2001;276:18977–83. doi:10.1074/jbc.M100254200.
87. Schulte C, Racchetti G, D'Alessandro R, Meldolesi J. A new form of neurite outgrowth sustained by the exocytosis of enlargeosomes expressed under the control of REST. Traffic. 2010;11:1304–14. doi:10.1111/j.1600-0854.2010.01095.x.
88. Loudon RP, Silver LD, Yee HF, Gallo G. RhoA-kinase and myosin II are required for the maintenance of growth cone polarity and guidance by nerve growth factor. J Neurobiol. 2006;66:847–67. doi:10.1002/neu.20258.
89. Joo E, Surka MC, Trimble WS. Mammalian SEPT2 is required for scaffolding nonmuscle myosin II and its kinases. Dev Cell. 2007;13:677–90. doi:10.1016/j.devcel.2007.09.001.
90. van Kesteren RE, Carter C, Dissel HMG, van Minnen J, Gouwenberg Y, Syed NI, et al. Local synthesis of actin-binding protein beta-thymosin regulates neurite outgrowth. J Neurosci Off J Soc Neurosci. 2006;26:152–7. doi:10.1523/JNEUROSCI.4164-05.2006.
91. Yudin D, Fainzilber M. Ran on tracks–cytoplasmic roles for a nuclear regulator. J Cell Sci. 2009;122:587–93. doi:10.1242/jcs.015289.
92. Sun Y, Yong KMA, Villa-Diaz LG, Zhang X, Chen W, Philson R, et al. Hippo/YAP-mediated rigidity-dependent motor neuron differentiation of human pluripotent stem cells. Nat Mater. 2014;13:599–604. doi:10.1038/nmat3945.
93. Tong Z, Solanki A, Hamilos A, Levy O, Wen K, Yin X, et al. Application of biomaterials to advance induced pluripotent stem cell research and therapy. EMBO J. 2015;. doi:10.15252/embj.201490756.

94. Kotov NA, Winter JO, Clements IP, Jan E, Timko BP, Campidelli S, et al. Nanomaterials for neural interfaces. Adv Mater. 2009;21:3970–4004. doi:10.1002/adma.200801984.
95. Deerinck TJ, Bushong EA, Thor A, Ellisman MH. NCMIR methods for 3D EM: a new protocol for preparation of biological specimens for serial block face scanning electron microscopy. 2010.
96. Horzum U, Ozdil B, Pesen-Okvur D. Step-by-step quantitative analysis of focal adhesions. MethodsX. 2014;1:56–9. doi:10.1016/j.mex.2014.06.004.
97. Puricelli L, Galluzzi M, Schulte C, Podestà A, Milani P. Nanomechanical and topographical imaging of living cells by atomic force microscopy with colloidal probes. Rev Sci Instrum. 2015;86:033705. doi:10.1063/1.4915896.
98. Butt H-J, Cappella B, Kappl M. Force measurements with the atomic force microscope: technique, interpretation and applications. Surf Sci Rep. 2005;59:1–152. doi:10.1016/j.surfrep.2005.08.003.
99. Indrieri M, Podestà A, Bongiorno G, Marchesi D, Milani P. Adhesive-free colloidal probes for nanoscale force measurements: production and characterization. Rev Sci Instrum. 2011;82:023708. doi:10.1063/1.3553499.
100. Cramér H. Mathematical methods of statistics. Princeton University Press. 1945. ISBN 978-0-691-00547-8.
101. Cox J, Mann M. MaxQuant enables high peptide identification rates, individualized p.p.b.—range mass accuracies and proteome-wide protein quantification. Nat Biotechnol. 2008;26:1367–72. doi:10.1038/nbt.1511.
102. Head BP, Patel HH, Insel PA. Interaction of membrane/lipid rafts with the cytoskeleton: impact on signaling and function: Membrane/lipid rafts, mediators of cytoskeletal arrangement and cell signaling. Biochim. Biophys. Acta BBA - Biomembr. 1838;2014:532–45. doi:10.1016/j.bbamem.2013.07.018.
103. Spiegelman BM, Lopata MA, Kirschner MW. Aggregation of microtubule initiation sites preceding neurite outgrowth in mouse neuroblastoma cells. Cell. 1979;16:253–63.

Submit your next manuscript to BioMed Central and we will help you at every step:

- We accept pre-submission inquiries
- Our selector tool helps you to find the most relevant journal
- We provide round the clock customer support
- Convenient online submission
- Thorough peer review
- Inclusion in PubMed and all major indexing services
- Maximum visibility for your research

Submit your manuscript at
www.biomedcentral.com/submit

BioMed Central

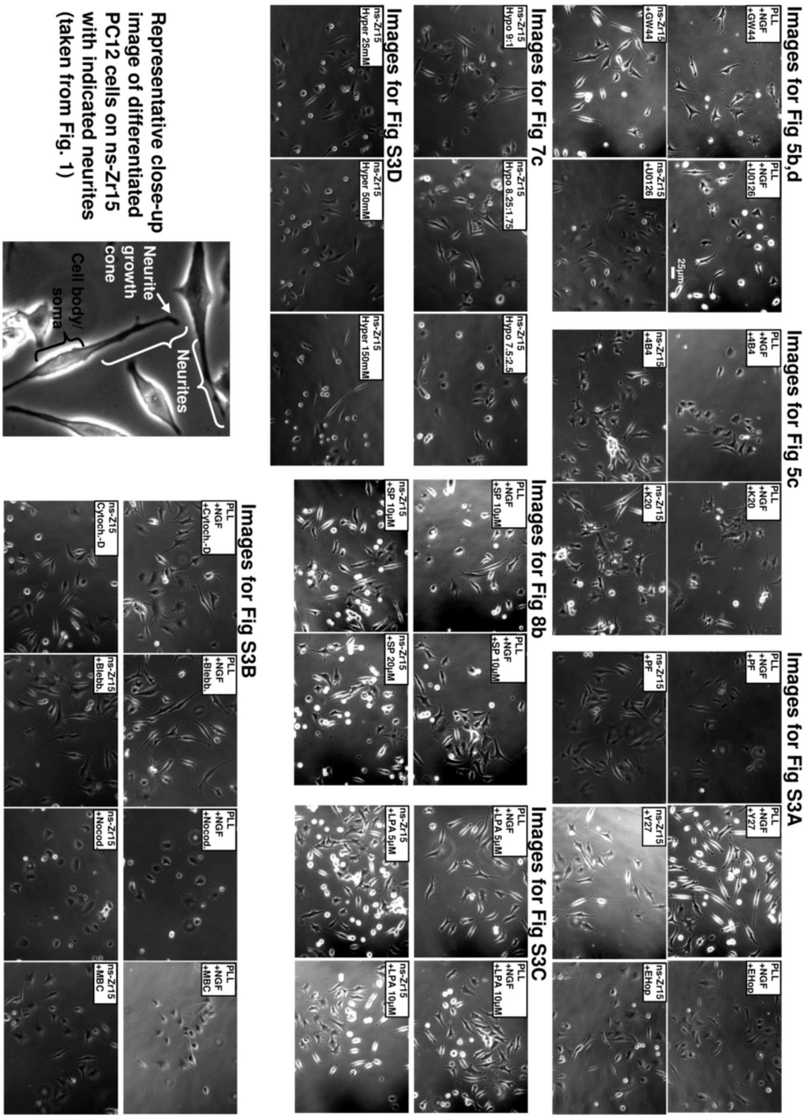
Images for Fig 5b,d
PLL +NGF +GW44
PLL +NGF +U0126
25µm
ns-Zr15 +GW44
ns-Zr15 +U0126
Images for Fig 5c
PLL +NGF +4B4
PLL +NGF +K20
ns-Zr15 +4B4
ns-Zr15 +K20
Images for Fig S3A
PLL +NGF +PF
PLL +NGF +Y27
PLL +NGF +EHop
ns-Zr15 +PF
ns-Zr15 +Y27
ns-Zr15 +EHop
Images for Fig 7c
ns-Zr15 Hypo 9:1
ns-Zr15 Hypo 8.25:1.75
ns-Zr15 Hypo 7.5:2.5
Images for Fig 8b
PLL +NGF +SP 10µM
PLL +NGF +SP 10µM
ns-Zr15 +SP 10µM
ns-Zr15 +SP 20µM
Images for Fig S3C
PLL +NGF +LPA 5µM
PLL +NGF +LPA 10µM
ns-Zr15 +LPA 5µM
ns-Zr15 +LPA 10µM
Images for Fig S3D
ns-Zr15 Hyper 25mM
ns-Zr15 Hyper 50mM
ns-Zr15 Hyper 150mM
Images for Fig S3B
PLL +NGF +Cytoch.-D
PLL +NGF +Blebb.
PLL +NGF +Nocod.
PLL +NGF +MBC
ns-Zr15 Cytoch.-D
ns-Zr15 +Blebb.
ns-Zr15 +Nocod.
ns-Zr15 +MBC
Representative close-up image of differentiated PC12 cells on ns-Zr15 with indicated neurites (taken from Fig. 1)
Neurite growth cone
Cell body/ soma
Neurites

Figure 4.2: Supplementary figure S1

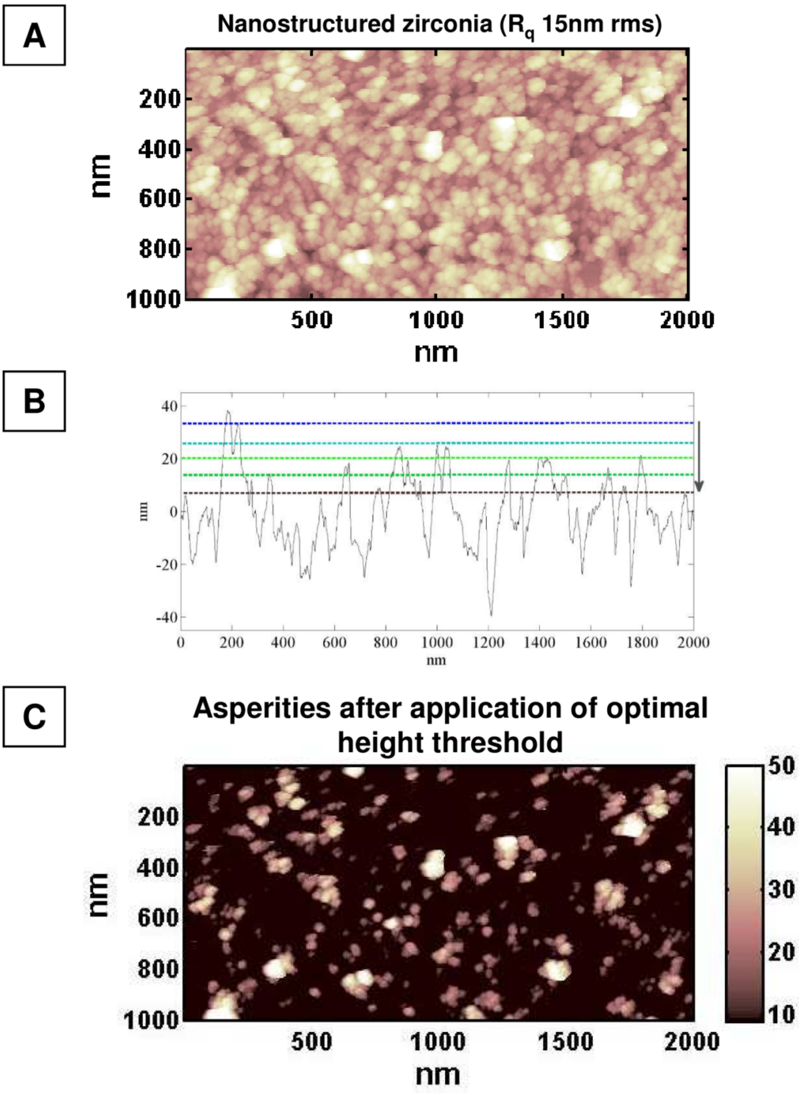

Figure 4.3: Supplementary figure S2

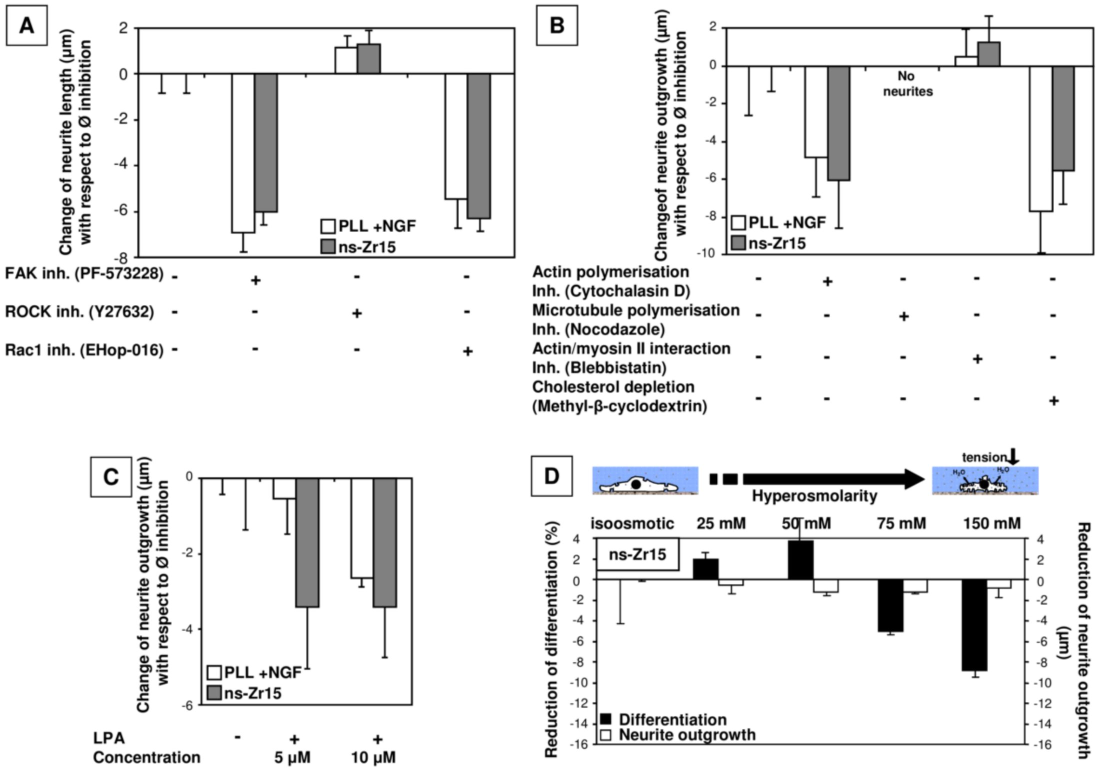

Figure 4.4: Supplementary figure S3

4.1.1 Additional discussion

The definition of "asperity" is worth a more in-depth discussion. Indeed, surface asperities cannot be uniquely and unambiguously defined, leaving some questions still open: Is there an absolute limiting height threshold below which the cell cannot feel further asperities? How could we set this value? Eventually, to what extent is the cell membrane able to adjust to the shape of the underlying surface? Is the latter ability dependent on cell type? The strategy here adopted of selecting surface asperities as those identified by the optimal threshold, different on different surfaces, which maximizes the number of isolated entities surviving above it (see fig. 4.3), is somehow arbitrary, yet statistically robust and intrinsically coherent, i.e. not dependent on specific morphological features of a surface with a given roughness. Let us name it "intrinsic threshold". Nevertheless, there could be other legitimate definitions of asperities potentially leading to different conclusions: e.g., we could set a fixed threshold some nm below the *topmost* asperity of the surface, taking into account only the structures lying above this value. A similar approach has been drafted in the context of a recent work [51], defining a "biological" threshold as the one located 20 nm below the *average* height of the topmost asperities measured on different areas of the same sample. Practically, different topographic maps of the same surface are firstly aligned, i.e. the average height value of each map is set to zero; asperities are then identified through the "intrinsic threshold" method; eventually, the biological threshold is determined as the average value of the topmost asperities (one for each map), downshifted of 20 nm. This definition is based on biological hints such as the knowledge of the average length of integrins (15 nm, ref. [52]) and the observation that the outer membrane of PC12 cells doesn't look particularly prone to bend according to the local shape of the nanostructured surfaces (see fig. 3b inside the paper in section 4.1).

In any case, both these strategies appear too generic and approximate, neglecting several parameters which could be useful to identify a more realistic and specific threshold representative of the effective asperities "seen" by cells: the local slope or curvature radius can determine the amount of energy required to bend the cellular membrane, which in turn may be partially compensated by the adhesion energy at the interface (fig. 4.5, refs. [53, 54]). Apparently, this lack of specificity doesn't let us to accurately estimate a priori the "roughness borders" defining the onset and the ending of the differentiation process, as well as the most performing roughness: indeed, the maturation of hippocampal neurons turns out to be greatly enhanced on nanostructured zirconia surfaces produced by SCBD and characterized by a RMS roughness Rq = 25 nm [40], at variance with the results obtained for the case of PC12 cells, where the differentiation "peak" is reached with Rq = 15 nm. Nonetheless, the "intrinsic threshold" approach adopted inside the paper in section 4.1 is enough to capture the key topographical feature at the basis of the differentiation process induced by nanostructured surfaces, i.e. the spatial constraints manipulating the nanoarchitecture, composition and development of the integrin adhesion complexes.

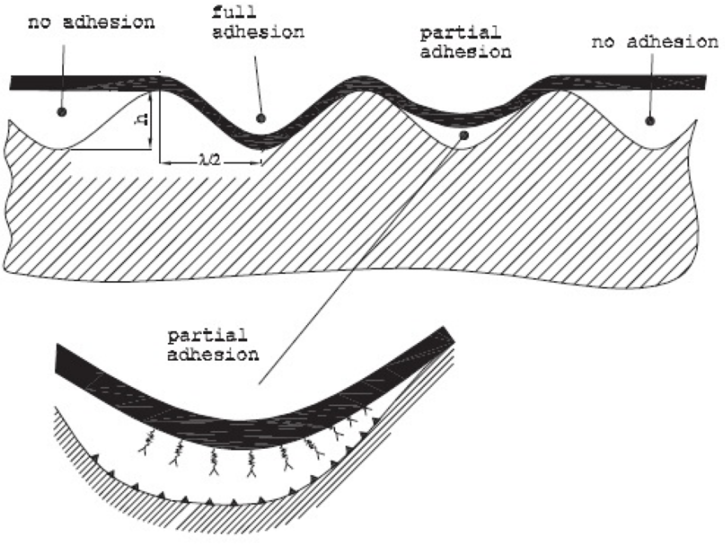

Figure 4.5: Schematic diagram of the potential "adhesion pathways" of the cellular membrane on a rough surface, actually dependent on the balance between the free surface energy of the substrate and the amount of elastic energy needed to bend the membrane. Reproduced from [53].

Chapter 5

Conclusions and perspectives

It is clear that biological samples (cells and ECMs among all) display an intrinsically high degree of complexity, which manifests itself on multiple levels, from the nano- to the microscale. Therefore, a multidisciplinary approach, based on the integration of diverse expertise and the collaboration among scientists from different fields, is indispensable for the achievement of concrete and useful results, as it has been demonstrated throughout this Thesis. AFM alone is often not enough to provide an exhaustive and detailed picture of biophysical topics. Nevertheless, it can offer a strong support to many other experimental techniques, mainly thanks to its great versatility, which allows to match the desired physical dimensions by modulating probe and cantilever properties. We have seen, indeed, how cellular or tissue elasticity, properly investigated on the microscale by means of colloidal probes, turns out to be an important biophysical marker of hidden and fine-tuned molecular processes (Chapter 2), witnessing for example the onset or the progression of specific diseases (Chapter 3) or evolutionary states (Chapter 4); on the other hand, conventional sharp tips can be useful to unveil and analyze important topographic cues on the nanoscale at the basis of complex mechanotransductive processes (Chapter 4).

The complexity of biological samples also requires the development of a robust operational protocol, commonly accepted inside the scientific community, which could allow a quantitative and reliable comparison of the results obtained by independent laboratories. The huge variety of approaches adopted so far has added a further source of uncertainty, thus hampering the way towards an effective application of the collected data. In this context the paper presented in section 2.1 finds its natural place, as well as the collective work born from the activity of the European network "COST Action TD1002" [17]. Here, the critical analysis of mechanical tests performed on a set of polyacrylamide gels and confluent MDCK-C11 cells, shared among eleven different European laboratories, has identified uncertainties in the calibration of the deflection sensitivity *invOLS*, and consequently in the cantilever force constant by thermal noise (see eq. A.6 in Appendix A.2), as one of the main source of errors in the evaluation of samples elasticity. The development of a proper protocol for the accurate calibration of these two fundamental parameters for AFM-based mechanics has led to the decrease of the final discrepancies in gel measurements down to 1%, and a parallel increase of the accuracy in cell measurements by a factor of two. These results, combined with the issues discussed in Appendix A and C, as well as in the paper reported in section 2.1, can provide a significant step towards the effective standardization of AFM-based mechanical measurements on soft and biological samples.

In any case, some work must still be done in order to improve and further expand the results presented so far, both from an experimental and theoretical point of view. We can summarize it as follows.

EXPERIMENTAL SET-UP A novel design of the thermostatic cell illustrated in Appendix C of the paper reported in section 2.1 is needed: a fine control of local temperature, as well as of the evaporation rate, which in turn influences the pH of the culture medium, could be essential to probe more delicate cellular types, whose stability relies on the accurate control of the global physiological conditions. On the side of ECMs, the employment of a two-component epoxy glue, properly hardened to avoid infiltration into the samples (see Chapter 14 in ref. [55]), could replace bi-adhesive tapes, whose efficacy is weakened after a few hours in fluid environments. Eventually, the integration of fluorescence microscopy components could allow more in-depth and oriented experiments.

DATA PROCESSING Typically, a relatively large amount of data is gathered during AFM-based measurements of cells and tissues. Therefore, a look for new algorithms and alternative approaches able to improve the automatization degree of data analysis could be helpful, even though the characteristic heterogeneity of the collected data makes it a quite difficult task. The employment of artificial neural networks [56] in order to discriminate among "good" and "bad" force curves is worth a try; yet, a very careful training of these networks is needed in order to avoid high false positive rates. Segmentation algorithms can be useful to perform a fine analysis of force curves, aimed at the identification of multiple elastic regimes, as discussed in the presented protocol (section 2.1). Their application to a whole Force Volume map may be questionable, being iterative and time-consuming algorithms; nevertheless, small data subsets could be analyzed following this kind of approach. On the other hand, if a whole-set matrical approach like the one described in the paper in section 2.1 is applied, a properly weighted fit should be implemented, since the linearization procedure tends to underestimate the errors associated to high applied forces compared to the smaller ones.

FINITE THICKNESS EFFECT As outlined in subsection 2.1.1, the corrected Hertzian model developed by Dimitriadis et al. [44], accounting for the influence of a rigid substrate on the measured Young's modulus of soft samples, is based on a linear elastic theory, where strains are assumed to be small ($\delta/h \lesssim 0.1$), and directly proportional to stresses. A more recent work by Long et al. [57] further extend these results in the field of nonlinear elasticity, for moderate to large indentations (up to $\delta/h \sim 0.8$), and should be kept into consideration.

INTRACELLULAR MECHANICS MODELING The presence of multiple elastic regimes inside a single force curve may be seen as a further marker of the heterogeneity of biological samples, which manifests itself also on the vertical axis. At the same time, it also rises the question about the possibility of developing an equivalent physical model, able to capture the key features of the complex intracellular mechanics. This is probably one of the most challenging and unresolved tasks in the field of cell mechanics. A relatively simple bilayer model has been proposed by Kaushik et al. [58], in the framework of a biological case of interest; in any case, its applicability to a generic cellular system appears questionable. A good review of the results obtained so far can be found in ref. [59], which also highlights the extreme complexity of this field. Interestingly, a quite recent work by Guz et al. [60] shows how cells could be approximately described as an homogeneous elastic medium if colloidal probes are used, together with an extension of the Hertz model taking into account the presence of a pericellular brush layer.

CELL & ECM RHEOLOGY In a broad portion of literature, as well as throughout this Thesis, the mechanical behavior of cells and tissues has been described by means of an effective Young's modulus, taking into account both the elastic and the viscous response of the analyzed samples in a convoluted manner. An extension of the Hertz model, corrected for the finite thickness effect, could be implemented following the approach of Mahaffy et al. [61], such as to measure separately the elastic and viscous contribution of biological samples. From the experimental point of view, this is realized by superimposing small amplitude harmonic oscillations to the quasi-static force curve and analyzing the sample response through a lock-in amplifier : the in-phase and out-of-phase components can be directly associated to the elastic storage and loss modulus respectively, i.e. to the purely elastic and viscous behavior of the sample. This kind of approach of course doesn't represent a novelty in the field of cell mechanics (e.g., see refs. [45, 46]); in any case, this improvement should be still conceived in the framework of a commonly accepted and standardized protocol. Recently, a similar method has been developed also for a "ferrule-top" interferometric system like the Piuma nanoindenter described in Appendix B [62], thus providing an effective way for the comparison of independent experimental techniques.

In this context, it is also worth mentioning the so-called biphasic or poroelastic model, which describes the rheology of fluid-saturated porous media such as ECMs (a polymer network filled with liquid buffer) and cellular cytoplasm (cytoskeleton and organelles soaked in cytosol), going beyond the approximation of incompressible samples (i.e. volume conserving, Poisson ratio $\nu = 0.5$) typically assumed for cells or other viscoelastic specimens [63].

INSIGHTS ON MECHANOTRANSDUCTION The analysis of the mechanotransductive processes like the one at the basis of the induced differentiation of neuron-like cells by nanostructured surfaces (Chapter 4) is certainly worth a further in-depth study and development. On the one hand, this can be carried out by refining the statistical analysis of the morphological properties at the nanoscale, e.g. the definition of the effective asperities seen by the cells as discussed in section 4.1.1. On the other hand, the strength of the specific adhesion complexes developed by cells on nanostructured surfaces can be investigated by force spectroscopy experiments like the one described in ref. [64], where a cell attached to a probe is brought into contact with properly functionalized surfaces ; the subsequent analysis of the detachment pattern can provide quantitative information on the adhesion forces developed by cells. In any case, a more realistic approach, which is currently being carried out by a member of our group (Matteo Chighizola), is represented by the building-up of a symmetric system : nanostructured zirconia is deposited by means of Supersonic Cluster Beam Deposition (SCBD) on the surface of colloidal probes (fig. 5.1) , which are then brought into contact with cells cultured on nanostructured surfaces characterized by the same physico-chemical properties. In this way, adhesion structures closely resembling the ones developed by cells on the underlying nanostructured surfaces can be quantitatively characterized from a spectroscopic point of view.

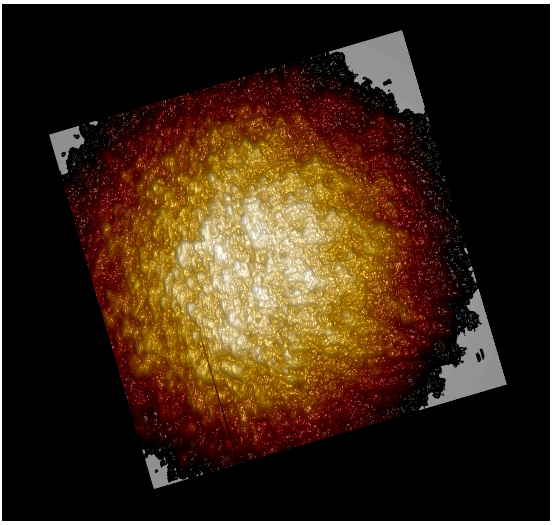

Figure 5.1: AFM-based three dimensional top view image of a spherical cup derived from a borosilicate probe (R = 2.5 μm), covered with nanostructrured zirconia produced by SCBD. A false color scale further highlights higher and lower regions (brighter and darker colors, respectively). Courtesy of Matteo Chighizola & Francesca Borghi.

Appendix A

Calibration issues associated with large colloidal probes

As extensively discussed in section 2.1, colloidal probes provide the best accuracy and reliability in the framework of AFM-based mechanical measurements, compared to conventional sharp tips. Unfortunately, they can also introduce significant complications in the calibration of two fundamental parameters for AFM-based mechanics, i.e. the deflection sensitivity (also known as *invOLS*) and the cantilever force constant K, in particular when reaching dimensions of the order of few tens of µm. Let us analyze both cases in detail.

A.1 Deflection sensitivity : the induced torque effect

The *invOLS* is probably the most delicate parameter, since it affects both the vertical and horizontal axes; indeed, we need to translate the measured voltage differences ΔV into force vs indentation curves according to the following equations [2, 16]:

$$F = Kd \tag{A.1}$$

$$\delta = z + d \tag{A.2}$$

$$d = invOLS \cdot \Delta V \tag{A.3}$$

where d, z and δ represent the cantilever deflection, the z-piezo displacement and the sample's indentation respectively. In eq. A.2, d is positive or negative depending whether the cantilever is deflected upwards or downwards with respect to the sample surface, according to the schematic depicted in fig. A.1.

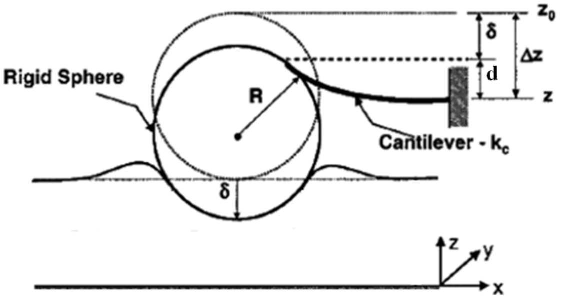

Figure A.1: Schematic of a colloidal probe indenting a deformable sample. Adapted from [44].

The deflection sensitivity can also be needed for the calibration of the cantilever force constant, if carried out through the thermal noise method; indeed, the equipartition theorem at the basis of the thermal noise method implies [42] (see also Appendix A.2):

$$\frac{1}{2}k_B T = \frac{1}{2}K \left\langle d^2 \right\rangle \tag{A.4}$$

The calibration of *invOLS* is typically performed by bringing the probe into contact with a rigid undeformable surface ($\delta \approx 0$), so that the z-piezo displacement is entirely converted into cantilever deflection : this basic assumption allows us to obtain a straight line in the photodiode voltage vs z-piezo displacement curve, and to get the desired *invOLS* parameter as the inverse of its slope. In principle, this should be true for any type of probe or cantilever: indeed, also for relatively big colloidal probes (R ≈ 33 μm) we can observe a linear behavior (fig. A.2), except for a small rounded region near the contact point. Nevertheless, the observed linear behavior could be an artefact. Indeed, the cantilever is typically tilted of an angle $\vartheta \approx 11°$ towards the surface : this determines the appearance of a tangential sliding force component which is due to friction

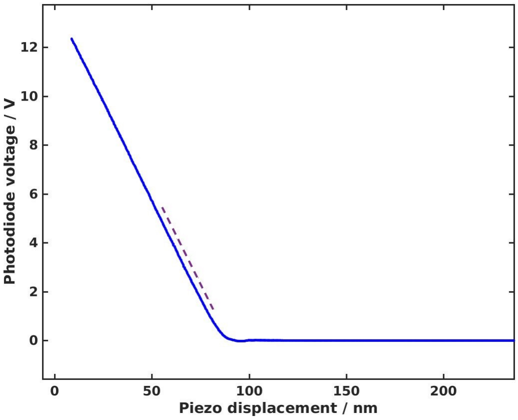

Figure A.2: Approaching force curve on a glass coverslip for a colloidal probe with radius R ≈ 33 µm (blue continuous line). The purple dotted straight line emphasizes the constant slope of curve, in the region where the photodiode response is supposed to be approximately linear (see Appendix C).

$\overrightarrow{F}$. The overall result is a frictionally-driven torque at the loading point of the cantilever, given by :

$$\overrightarrow{\tau} = \overrightarrow{R} \times \overrightarrow{F} \tag{A.5}$$

where $\overrightarrow{R}$ represents the radius of the colloidal probe or the height of a sharp tip (the lever arm) and $\overrightarrow{F}$ the net tangential force, according to the schematic depicted in fig. A.3. Interestingly, a sphere generates the same torque as an "effective" sharp tip with a length equal to the sphere radius, instead of its diameter, as pointed out in ref. [65]. The torque induces a local modification of the cantilever deflection and profile slope, thus impacting on the measured *invOLS*, in a way increasing proportionally to the friction between probe and surface and the lever arm, i.e. to the probe dimensions, at fixed cantilever force constant and geometrical properties. This, in principle, should not represent a real problem, assuming that the position of the laser spot is not changed in between the *invOLS* calibration and the mechanical measurements on the sample of interest, and the latter effects on the cantilever local shape are very similar to those observed on the rigid surface.

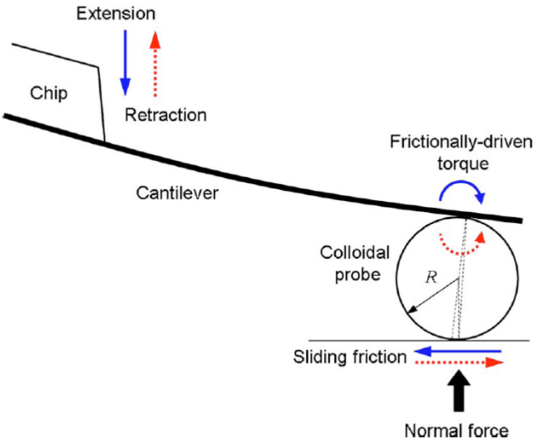
Extension
Retraction
Chip
Cantilever
Frictionally-driven torque
Colloidal probe
R
Sliding friction
Normal force

Figure A.3: Schematic of the net forces acting on a colloidal probe for a cantilever tilted towards the surface. Reproduced from [66]

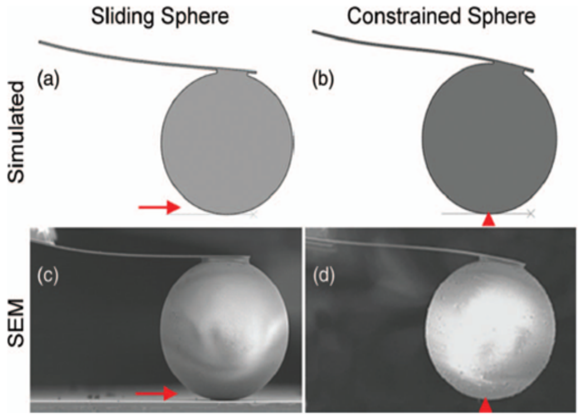
Sliding Sphere
Constrained Sphere
Simulated
SEM
(a)
(b)
(c)
(d)

FIG. 5. Finite element simulations ((a), (b)) and SEM images ((c), (d)) of a cantilever with a sliding and constrained sphere. The cantilever was inclined to 11° in all cases to represent its angle during AFM measurement.

Figure A.4: Cantilever bending profiles of a spherical probe with R $\approx$ 75 µm attached to a cantilever with K $\approx$ 0.65 N/m: the extreme conditions of a free-to-slide and totally constrained sphere. Reproduced from [67].

However, as pointed out by Weafer et al. [67], this last condition may be far away from being satisfied, actually depending on the degree of constraint imposed by a given surface. In fig. A.4 we can see the difference in the cantilever bending profile between the two extreme states, i.e. a probe free to slide on the surface and a totally constrained probe. In fig. A.5 , the side profiling of the same cantilever when the probe is in contact with a glass surface or a compliant silicon sample, reconstructed by confocal microscopy, is shown. At a fixed cantilever deflection (here called δ), the local slope at the loading point is very different, resembling closely the profiles shown in fig. A.4 for a free-to-slide and bound probe, respectively. Unfortunately, the AFM optical lever detection system is not directly sensitive to the cantilever deflection, but rather to its local slope [43]. Therefore, we could have different deflection sensitivities (even in the framework of the same experiment) depending on the net forces acting on the probe (potentially different on different surfaces), as well as the probe dimension, the cantilever force constant and its geometrical parameters. This can lead to significant errors in the final evaluation of the sample's mechanical properties [67]. The root of the problem lies in the fact that we can calibrate *invOLS* when in contact with a rigid undeformable substrate (fig. A.2), whereas we cannot do the same when indenting a deformable sample, since the basic assumption of a complete conversion of piezo displacement into cantilever deflection is no longer statisfied; moreover, it is not easy to define a limiting probe radius beyond which this effect must be taken into consideration, because of the reasons discussed so far. We should keep in mind, in any case, that the probe used in the case of ref. [67] (fig. A.4,A.5) is quite big ($R \approx 75$ µm) and attached to a relatively soft cantilever ($K \approx 0.65$ N/m); furthermore, it is reasonable to think that in the majority of experiments the real cantilever behavior lies somewhere in between the extreme conditions depicted in fig. A.4.
Several practical solutions could be considered to face these problems:

- Aligning the laser spot a bit backward with respect to the loading point, where the slope change is less marked (fig. A.5), since the measured deflection is the same independently of the laser position on the cantilever (i.e., the product $invOLS \cdot \Delta V$ is conserved throughout the cantilever profile, since it corresponds at the deflection at the loading point, or tip apex location);
- If the *invOLS* related to the loading point or the probe center of mass is needed to perform the calibration of the cantilever force constant (see Appendix A.2), we could calibrate two different *invOLS* on a rigid surface: a first one with the laser aligned over the loading point, and a second

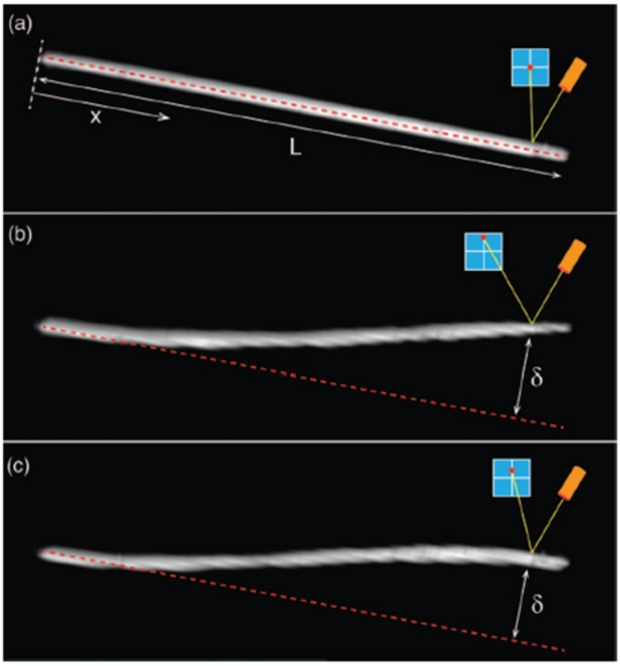

FIG. 6. Side profiling of a cantilever (a) not in contact with a substrate, (b) in contact with glass (sliding sphere profile), and (c) in contact with silicone (constrained sphere profile). Images are created from z-stacks captured using confocal reflection microscopy (attached sphere not visible). This required loading to be performed outside of the AFM using a micromanipulator setup. The superimposed schematic of an AFM laser beam and photodetector illustrates that a larger change in voltage (slope change) would be measured for the sliding sphere profile (b) than for the constrained sphere profile (c) even though deflection (δ) is the same in each case. The cantilever is length L with axial position x.

Figure A.5: Side profiles of the same probe and cantilever of fig. A.4, obtained by confocal microscopy: the local cantilever slope, probed by the optical lever system, can change significantly (at a fixed deflection , here called δ), when switching between different surfaces. Reproduced from [67].

one (for the indentation experiments) with the laser aligned backwards as described previously; alternatively, the method suggested by Slattery et al. [68], where the calibration is performed on an inverted sharp tip which deflects the cantilever at a given distance ΔL from the free end (fig. A.6), could be implemented, even if the determination of ΔL may be not straightforward. In this case, the *invOLS* at the probe position can be related to the one measured loading the cantilever at a distance ΔL through the equation $invOLS_{tip} = invOLS_{\Delta L} L \left(L - \Delta L\right)^{-1}$;

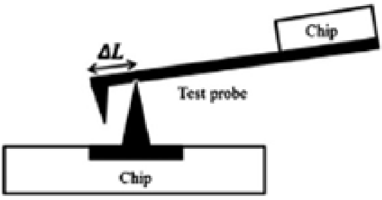

Figure A.6: The "reverse tip" approach. Reproduced from [68]

- Following the approach suggested by Chung et al. [66], we could average the *invOLS* obtained by the approaching and the retracting curves measured on a rigid surface, since the torque due to the friction force acting on the probe changes sign along with the change in sliding direction [69, 70]. In this way we can get an *invOLS* starting value near to the free-to-slide condition, and roughly estimate an error on the *invOLS* related to mechanical tests on deformable samples as two-three times the standard deviation of the approaching and retracting values. Indeed, the hysteresis between the two curves increases with the probe radius, as shown in ref. [69] (fig. A.7), in agreement with eq. A.5. This is further confirmed by a similar experiment which I have performed with two different colloidal probes and a conventional sharp tip (fig. A.8): interestingly, the slope change between approaching and retracting curves appears slightly greater in the case of the sharp tip, compared to the colloidal probe with R $\approx$ 5 µm, probably due to the increased leverage (sharp tip height H $\approx$ 12-15 µm).

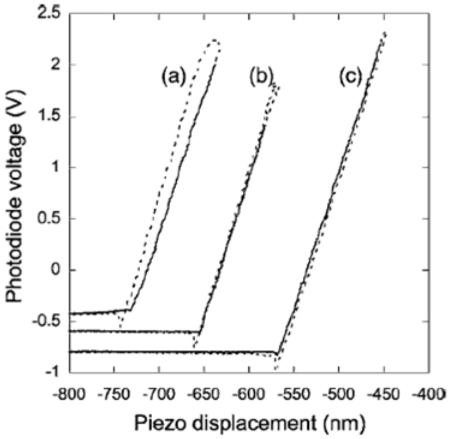

FIG. 2. Cantilever deflection in terms of the photodiode voltage as a function of piezo z position, for three cantilevers with different probe diameters: (a) 36 μm, (b) 16 μm, and (c) without probe. Solid lines refer to loading and dashed lines to unloading traces.

Figure A.7: Approaching and retracting curves for different probes measured on a rigid undeformable surface. The hysteresis disappears in the case of a tipless cantilever. Adapted from [69]

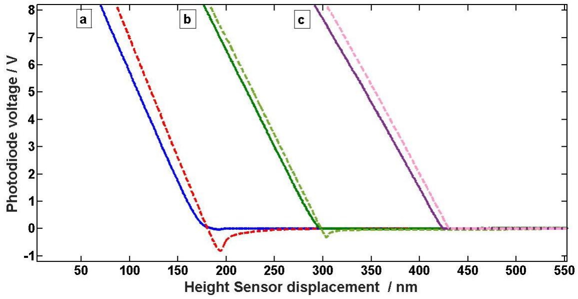

Figure A.8: Approaching (solid lines) and retracting (dashed lines) curves for different probes measured on a glass coverslip. a) Colloidal probe, R ≈ 33 µm. b) Colloidal probe, R ≈ 5 µm. c) Sharp tip, H ≈ 12-15 µm. The vertical axis is cut in order to magnify the differences in the hysteresis between the probes; for the same reason, the curves are artificially shifted on the horizontal axis.

A.2 Cantilever force constant : the added mass effect

Among the several methods developed in the last decades to calibrate the cantilever force constant K [71], one of the most commonly used and included in the commercial AFM software is the so-called thermal noise method. This approach, originally conceived by Hutter and Bechhoefer [42], exploits the energy equipartition theorem to link the cantilever force constant with its thermally-driven mean squared oscillations. Typically, only the first oscillation mode is taken into account (single harmonic oscillator model or SHO); moreover, the optical lever system measures $\partial d/\partial x$, where x is the position along the cantilever profile, rather than deflection d . The final equation can be stated as follows [42, 43, 71, 72, 73]:

$$K_0 = \beta_0 \frac{k_B T}{invOLS^2 P} C_{tilt} C_{piezo} \tag{A.6}$$

where P stands for the area underlying the first resonant mode in the frequency spectrum (the product $invOLS^2P$ is equivalent to $\langle d^2 \rangle$ in eq. A.4), k_B represents the Boltzmann constant, T the absolute temperature, C_{tilt} and C_{piezo} suitable correction factors taking into account the effect of the cantilever tilt angle ϑ and probe dimension, and the error related to a possible z-piezo miscalibration, respectively [43, 71]:

$$C_{tilt} = \left(\frac{1 - \frac{3}{2} \frac{R}{L_{eff}} tan\theta}{1 - 2 \frac{R}{L_{eff}} tan\theta} cos\theta \right)^2 \tag{A.7}$$

$$C_{piezo} = \left(\frac{\frac{\lambda}{2} \left(1 + cos2\theta\right)}{\lambda} \right)^2 \tag{A.8}$$

Here, R represents the sphere radius (or the tip height for a conventional sharp probe), λ the wavelength of the (eventually) observed interference pattern due to reflections of the laser on the cantilever back side and the sample surface, whereas L_{eff} is an effective cantilever length taking into account a possible displacement of the probe loading point from the cantilever free-end, as well as stiffening effects on the final part of the cantilever if a glue is used to stick the probe [74]. However, this last two terms are typically negligible compared to the factor β_0, which can be further expressed as follows:

$$\beta_0 = \frac{\alpha_0}{\chi_0^2} \tag{A.9}$$

Here, χ_0 represents the ratio of the dynamic vs static *invOLS* [43]: in other words, the inverse of the ratio between the *invOLS* calibrated on a rigid surface through a static deflection of the cantilever (see Appendix A.1), which is then inserted in eq. A.6, and the one intrinsically probed by the optical lever system while measuring thermally-driven dynamic oscillations. On the other hand, α_0 corrects for the actual amount of thermal energy stored in the first resonant mode *alone*, in agreement with the SHO model. Indeed, we must keep in mind that during thermal vibrations all the flexural resonant modes of the cantilever are excited : therefore, a small fraction of the area underlying the first mode is due to the next ones, depending on the exact shape of the eigenmodes along the cantilever profile and subsequently on its geometry, as well as on the position of the laser spot, usually placed above the tip. If we further assume that the probe mass is negligible compared to the cantilever mass, as in the case of conventional sharp tips, for rectangular cantilevers we have : $\alpha_0 = 0.971$, $\chi_0 = 1.09$, $\beta_0 = 0.817$ [74, 75].

The latter assumption can become questionable when spherical colloidal probes with large radii (i.e. $R \geq 10\,\mu m$) are used. Laurent et al. [74] have calculated and experimentally measured, by means of a differential interferometer, the exact shape of the first five eigenmodes along the profile of a rectangular cantilever, as a function of the variables $\widetilde{m}$ and $\widetilde{r}$, defined as the ratio of the probe-to-cantilever mass and normalized gyration radius, respectively :

$$\widetilde{m} = \frac{m_{probe}}{m_{cant}} \tag{A.10}$$

$$\widetilde{r} = \sqrt{\frac{7}{5}}\frac{R_{probe}}{L_{eff}} \tag{A.11}$$

The gyration radius basically takes into account the rotational inertia of the sphere and its actual dimensions, i.e. the fact that the mass of the probe is not concentrated in a point, but rather distributed in a finite volume. The results obtained for $\widetilde{m} = 0{-}1$ and $\widetilde{r} = 0{-}0.03$ are reported in fig. A.9 . Interestingly, for increasing $\widetilde{m}$ and $\widetilde{r}$ values, the first mode is weakly impacted, whereas the nodes of the higher modes get closer to the cantilever free end; therefore, the dynamic system better approximates the SHO model, in agreement with a progressive shift of the center of mass towards the cantilever free end, where the probe is supposed to be attached. Alternatively, this means that the first resonant mode

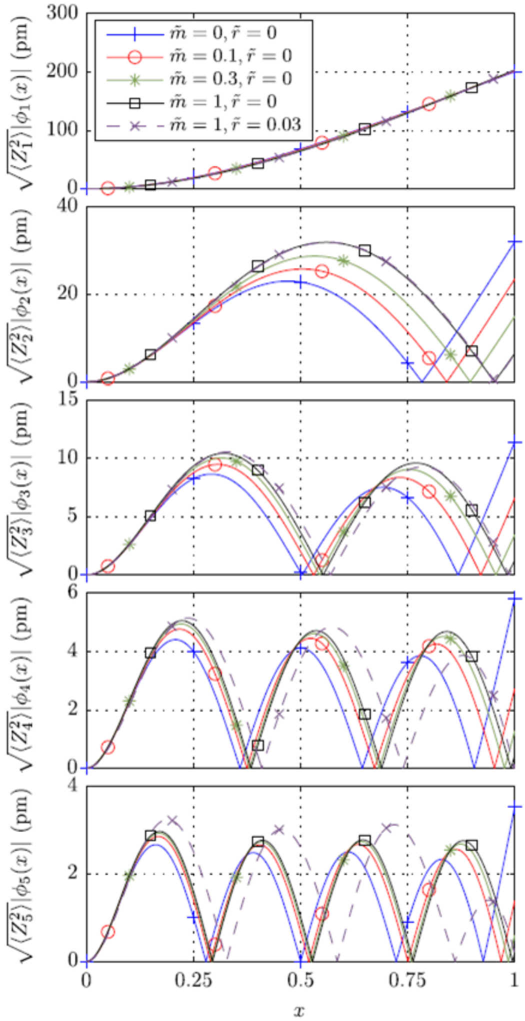

Figure A.9: Rms deflection of the first five modes for a given rectangular cantilever along its normalized profile x, for varying $\widetilde{m}$ and $\widetilde{r}$ values. Reproduced from [74].

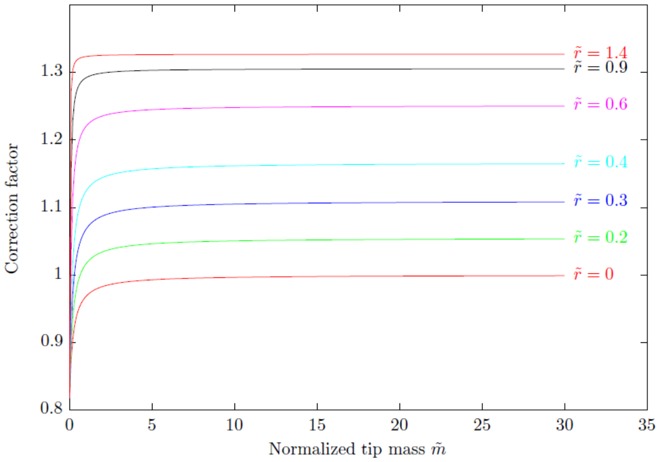

Figure A.10: The correction factor β plotted as a function of the probe-to-cantilever mass ratio, for different values of the normalized gyration radius $\widetilde{r}$. β_0 (eq. A.9) is represented by the common intercept on the vertical axis, for $\widetilde{m} = 0$. Courtesy of L.Bellon [76].

gathers an higher fraction of the thermal energy, for increasing $\widetilde{m}$ values; at the same time, also the previously described χ_0 factor can be influenced by an increase of the normalized gyration radius $\widetilde{r}$. Comprehensively, the factor β_0 (eq. A.9) must be considered as a function of the variables $\widetilde{m}$ and $\widetilde{r}$. This calculation is not straightforward; in any case, Ludovic Bellon has kindly performed the computation for a wide range of $\widetilde{m}$ and $\widetilde{r}$ values [76], extending the results already presented in ref. [74]. As we can see in fig. A.10 , the correction becomes greatly pronounced for probe masses similar to or greater than the cantilever mass. This is not unusual in the context of colloidal probes, since the volume of the spheres grows proportionally to the third power of the radius; some representative values of $\widetilde{m}$ and $\widetilde{r}$ for standard rectangular contact mode (CM), force modulation (FM) and tapping mode (TM) cantilevers can be found in Table A.1. A partial experimental confirmation of the results obtained by Laurent et al. [74, 76] is provided by the work of Gates et al. [77, 78]: here, the authors show how to calibrate the cantilever force constant K by means of laser Doppler vibrometry (LDV), an experimental interferometric technique which allows to measure *directly* the thermally-driven mean squared deflections of the

Probe radius	**Cantilever type**	$\widetilde{m}$	$\widetilde{r}$
R = 5 µm	CM	0.013	0.013
	FM	0.030	0.026
	TM	0.037	0.047
R = 10 µm	CM	0.100	0.026
	FM	0.238	0.053
	TM	0.300	0.095
R = 30 µm	CM	2.70	0.079
	FM	6.43	0.158
	TM	8.10	0.284
R = 50 µm	CM	12.50	0.131
	FM	29.75	0.263
	TM	37.48	0.473

Table A.1: Representative values of $\widetilde{m}$ and $\widetilde{r}$ for different types of rectangular cantilevers and colloidal probes radii. Cantilevers lengths are 450 µm, 225 µm and 125 µm for CM, FM and TM respectively.

cantilever through the Doppler shift of the reflected laser beam frequency due to the motion of the cantilever surface, with respect to a reference beam; therefore, no direct contact with a rigid surface or preliminary calibration of *invOLS* is needed, thus avoiding the potential torque-induced effects described in Appendix A.1 and achieving a much greater accuracy in the calibration of K, since the main source of error relies on the knowledge of the laser wavelength. In any case, the thermal noise method is still used, thus requiring the determination of a suitable mode correction factor (the previously described β_0 , eq. A.9) taking into account the effect of an increasing probe mass (see fig. 6 in ref. [78]). In this specific case, $\beta_0 = \alpha_0$, since *invOLS* calibration is not needed, implying $\chi_0 = 1$. Noticeably, the parameter α_0 is limited by a physical constraint, i.e. it has to converge to the asymptotic value $\alpha_0 = 1$ in the limit of an infinite probe mass, since the amount of thermal energy stored in the first resonant mode cannot exceed unity; the same argument cannot be imposed a priori on the parameter χ_0 : indeed, the correction factor β shows different asymptotic limits with varying $\widetilde{r}$ values (fig. A.10).

Summarizing, from a practical point of view the cantilever force constant K can still be calibrated by an AFM-based thermal noise method, also for the case of large micrometric probes, following the steps listed here below:

1. Calibrate a static *invOLS* as accurate as possible according to the solutions proposed in Appendix A.1;
2. Calculate a starting force constant according to the eq. $K_0 = \beta_0 \frac{k_B T}{invOLS^2 P}$, which is the one usually implemented in AFM software (actually, α_0 is often assumed equal to unity, such that $\beta_0 = \frac{1}{\chi_0^2}$);
3. Measure the relevant cantilever geometrical parameters (e.g by means of optical microscopy) and the probe radius; for the latter, if the probe is too big compared to the periodicity of the calibration spiked gratings like the ones described in Appendix B of ref. [16], a reverse imaging using a single spike represented by a conventional sharp tip accurately fixed to a substrate (likewise the "Slattery" approach, see fig. A.6) can be performed. Similarly, a direct image of the colloidal probe can be acquired in tapping mode. In this case, the large statistics provided by a spiked grating are lost, since a single reverse image of the probe is acquired; in any case, the obtained spherical cap can reach heights of the order of several µm, compared to a maximum of a few hundreds of nm for the gratings, thus reducing potential error sources.
4. Evaluate the normalized mass and gyration radius parameters $\widetilde{m}$ and $\widetilde{r}$ according to eq. A.10 and A.11, as well as the C_{tilt} and C_{piezo} correction factors according to eq. A.7 and A.8;
5. Extrapolate the corresponding correction factor β on the basis of the graph represented in fig. A.10, suitably digitalized;
6. Calculate the actual force constant as $K = K_0 \frac{\beta}{\beta_0} C_{tilt} C_{piezo}$

It is worth remembering, in any case, that the correction factor β is actually a function of the position of the laser spot on the cantilever profile, as well as of its geometrical properties; the results plotted in fig. A.10 are valid *only* for a rectangular cantilever and a laser spot located at the cantilever effective length L_{eff}, approximately given by the probe loading point (if the spheres are not attached by glues [74]). Of course, a more direct and accurate approach is represented by interferometric techniques like the aforementioned LDV, if available. Interestingly, the knowledge of an accurately pre-calibrated value of the cantilever force constant can provide a further solution to correct the static *invOLS* value, measured on a rigid undeformable surface, for potential induced-torque effects, as discussed in [17]: if K_{AFM} represents the force constant obtained by AFM-based thermal noise, and K_{REF} stands for the force constant accurately pre-calibrated by an independent technique like interferometry, we can calculate an *invOLS* correction factor $\lambda = \sqrt{(cos\theta)^2 \frac{K_{AFM}}{K_{REF}}}$, where ϑ is the cantilever tilt angle, such that we obtain the "true" deflection sensitivity as $invOLS^* = \lambda invOLS$ (see also Chapter 5). We must keep in mind that the factor $(cos\theta)^2$ is due to the typical tilt of the cantilever towards the sample surface by an angle ϑ in the AFM setup, whereas the reference elastic constant K_{REF} is usually evaluated in a planar configuration; therefore, if the same tilt in present in both cases (K_{AFM} and K_{REF}) , the correction factor is simply given by $\lambda = \sqrt{\frac{K_{AFM}}{K_{REF}}}$. Moreover, the employment of a reference elastic constant K_{REF} can be useful even in the case it is not greatly accurate, since this method can lead at worst to a systematic error, insignificant if the desired measurements are performed relatively to a control sample and using the same probe throughout the experiment.

Eventually, it is important to underline that, with regard to the AFM-based mechanical measurements performed throughout the papers reported inside this Thesis, corrections of the cantilever force constants according to the above described procedure have not been applied, neither are needed, since we have used colloidal probes attached to CM cantilevers and characterized by radii up to 10 µm (see Table A.1); therefore, the calibrated force constants turn out to be underestimated only up to about 6%, whereas the typical error associated to the thermal noise method amounts to 10%. Moreover, most of the measurements have been performed relatively to a control sample, and using the same probe: this can help in minimizing eventual systematic errors and preserving the general trend, as discussed in sub-section 2.1.1.

Appendix B

AFM & Piuma Nanoindenter

An experimental validation of the results provided by L. Bellon (fig. A.10, Appendix A.2) can be found in the framework of a one-week internship carried out at the facilities of Optics11, a spin-off company from the Vrije Universiteit of Amsterdam (`http://www.optics11.com/`). This collaboration aimed at the comparison of two different techniques, namely AFM and an interferometric nanoindenter called “Piuma” (developed by Optics11; see also refs. [41, 79, 80, 81, 82]), by means of indentation experiments performed on a thick homogeneous PDMS sample using probes of varying dimension, from the nano- to the microscale, eventually compared to the results of macroscopic compressive and tensile mechanical tests.

Piuma nanoindenter is a quite compact and user-friendly instrument (fig. B.1) based on a Fabry-Perot interferometric detection system: basically, a photodiode measures the intensity of the interference pattern produced by the difference in the optical path between the light reflected at the cleaved end of an optical fiber and the light reflected on the back side of the cantilever (fig. B.2). The voltage detector output is given by :

$$W\left(d\right)=W_0\left[1+Vcos\left(\frac{4\pi d}{\lambda}+\varphi_0\right)\right] \tag{B.1}$$

where d represents the gap size between the cantilever and optical fiber, φ_0 is a constant phase shift dependent on the probe geometry, λ is the wavelength of the laser, W_0 and V stand for the midpoint interference signal and fringe visibility, respectively [41]. At variance with other interferometric techniques like LDV, briefly described in Appendix A.2, the derivation of the cantilever deflection

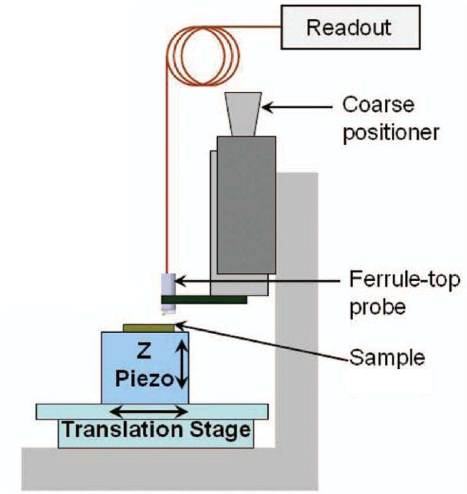
Readout
Coarse positioner
Ferrule-top probe
Sample
Z Piezo
Translation Stage

Figure B.1: Schematic of the “ferrule-top” Piuma nanoindenter setup. Adapted from [41]

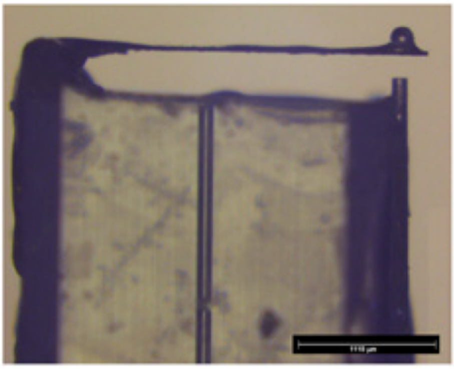

Figure B.2: Optical microscope image of a “ferrule-top” cantilever (scalebar = 1110 µm). A single-mode fiber is attached at the edge of a borosilicate glass ferrule to form an interferometric cavity of approximately 200 µm over which cantilever deflection is measured. Reproduced from [81].

from eq. B.1 requires a suitable pre-calibration procedure based on the static cantilever deflection against a rigid undeformable surface, like in the case of AFM [62]. Nevertheless, this design allows to overcome some limitations intrinsically associated to the optical lever detection system typically implemented for an AFM: the tilt between cantilever and sample surface is removed, thus getting rid of all the problems connected to the calibration of a static *invOLS* , i.e. the induced-torque effect (see Appendix A.1), since only a *normal* force is applied to the probe; moreover, this completely "vertical" approach let us to detect quite large cantilever deflections (over 20 μm, ref. [62]), and subsequently to perform deep indentations also on relatively stiff samples like PDMS, in contrast with AFM where the maximum achievable indentation is strongly constrained by the geometrical features of the optical lever system, for a fixed cantilever force constant and probe radius. Indeed, the operational voltage range of an AFM is typically limited to a given interval ($\Delta V = [-12\,V, +12\,V]$ for Bioscope Catalyst - Bruker), outside which the photodiode response saturates alternatively on the top or bottom-half quadrants (fig. B.3); moreover, the photodiode response is linear approximately on a specific sub-interval (e.g.,$\Delta V = [-5\,V, +5\,V]$), outside which the non-linear behavior must be carefully characterized (see Appendix C).

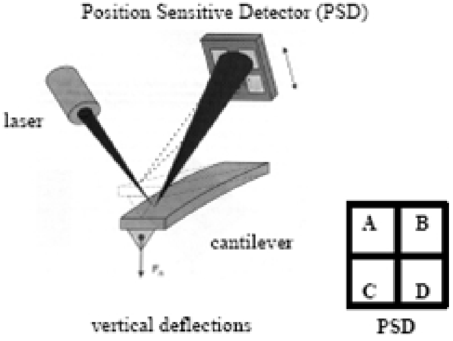

Figure B.3: Schematic of a typical optical lever detection system employed for an AFM. The vertical deflection is given by the normalized difference of the intensities measured in the top and bottom quadrants: $\Delta V = [A + B - (C + D)] \,/\, (A + B + C + D)$. Adapted from Nanoscope AFM manuals.

The results of the combined AFM & Piuma mechanical tests on a thick PDMS sample are summarized in fig. B.4 . All the measurements and the statistical analysis have been performed following the method described in the

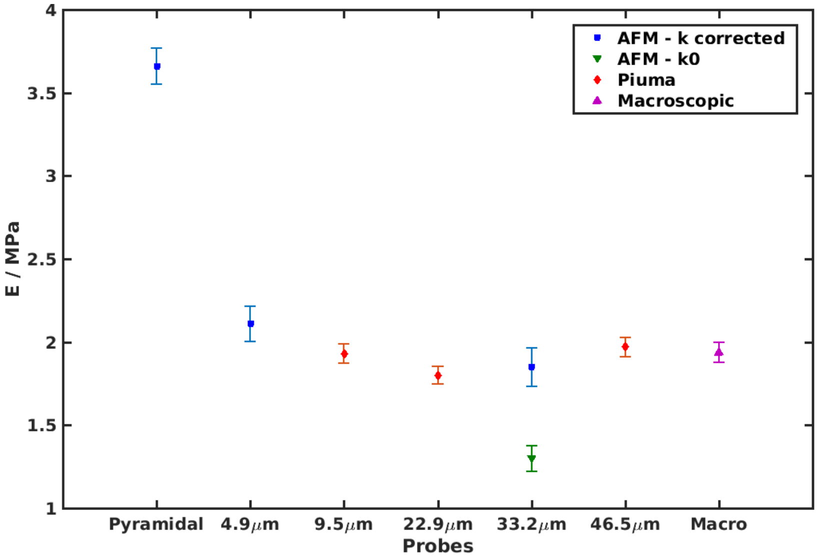

Figure B.4: Median Young's modulus values (E) of a thick PDMS sample, measured with different types of probes and instruments (AFM and Piuma nanoindenter). The terms "pyramidal" and "macro" refer to a conventional AFM sharp probe with pyramidal shape (apical curvature radius R ≈ 10-15 nm) and to macroscopic stress-strain tests, respectively. All the remaining terms indicate spherical probes radii. The agreement with the macroscopic result is good for all cases except for the pyramidal sharp probe and the colloidal probe with radius R = 33.2 µm, without correction of the cantilever force constant ($p < 0.001$, double sided Student's t-test).

papers reported in sections 3.1 and 3.2 (refs. [26, 27]). Basically, few hundreds of independent force curves have been acquired sampling the PDMS specimen, immersed in distilled water, on macroscopically separated regions. The values of the Young's modulus have been extracted by fitting the Hertz model to each indentation curve up to approximately 1.2 µm, since it was the maximum indentation achievable by AFM with micrometric colloidal probes. All the cantilevers used, both from AFM and Piuma, are characterized by force constants in the range $K = 40 - 100\,N/m$. AFM sharp probe (Bruker, RTESP model) and the tipless cantilever (Nanosensors, TL-NCH model) used to produce the colloidal probe with radius R = 33.2 µm are characterized by physical properties and dimensions typical of standard tapping-mode cantilevers: resonant frequency

$f_0 \approx 300\,kHz$, nominal length $L \approx 120 - 130\,\mu m$, width $W \approx 30 - 40\,\mu m$, thickness $T \approx 3-4\,\mu m$; Piuma cantilevers are produced in situ by Optics11 and can reach millimetric dimensions (see fig. B.2 and ref. [81]). As previously outlined, the correction to K values provided by L. Bellon turns out to be relevant, improving significantly the otherwise poor agreement between the macroscopic Young's modulus and the one related to the colloidal probe with radius R $=$ 33.2 µm (in this specific case, $\widetilde{m} \approx 12$ and $\widetilde{r} \approx 0.4$, implying $\beta \approx 1.13$, see fig. A.10 and Appendix A.2). The static *invOLS* value has been corrected for potential torque-induced effects by averaging the results obtained from approaching and retracting curves acquired on a glass substrate, according to one of the possible solutions discussed in Appendix A.1. Interestingly, the conventional sharp tip (curvature radius R $\approx$ 10 nm) provides a significant overestimation of the actual Young's modulus, in agreement with previously obtained results on softer PVA gels [44]. Piuma measurements are associated to a lower global error with respect to the ones performed by AFM : this is mainly due to the peculiar calibration method for the cantilever force constant employed by Optics11, which, combining the readout of the interferometer and the forces measured by a microbalance brought into contact with the probe, is able to provide an estimate of K whose accuracy only relies on the knowledge of weights and laser wavelengths [81]. In addition, this calibration procedure does not require corrections for the added mass effect, at variance with the thermal noise method, since it measures directly the desired *static* cantilever force constant.

Appendix C

Photodetector nonlinearity

As outlined in Appendix B, in some cases the whole operational voltage range allowed by the AFM photodetector could be needed, e.g. when performing mechanical tests on stiff samples and/or using large colloidal probes. If not, it could happen in any case to fall outside the typical interval where the photodetector provides a linear response. Linearity is essential to calibrate the deflection sensitivity, which is defined as the proportionality *constant* needed to translate voltage differences into the desired metric units (see Appendix A.1); therefore, if a non-linear behavior in the photodiode response is observed, it must be properly corrected. In principle, nonlinearity should be a property dependent solely on the technical specifications of the photodiode, so that we could measure a *universal* correction function, valid for every kind of probe, cantilever, buffer, laser spot location, and so on. Actually, this is not the case, as we can see in fig. C.1; here, the error function is computed as:

$$V_{err} = \Delta V_{\langle fit \rangle} - \langle \Delta V_{exp} \rangle \tag{C.1}$$

where $\Delta V_{\langle fit \rangle}$ represents the linear fit of the average vertical deflection $\langle \Delta V_{exp} \rangle$ obtained from *invOLS* calibration measurements (see fig. C.2 and Appendix A.1). Photodetector nonlinearity thus appears to be dependent on the effective experimental conditions, such as the type of environment or the laser location along the cantilever profile, even for the same probe. This effect could be due to the fact that the exact shape and size of the laser spot hitting the photodiode, and subsequently also the *local* energy profile and distribution inside it [83], may change as a function of the overall geometrical features of the detection system (optical path, reflection angles, refractive indexes, etc.), for a fixed

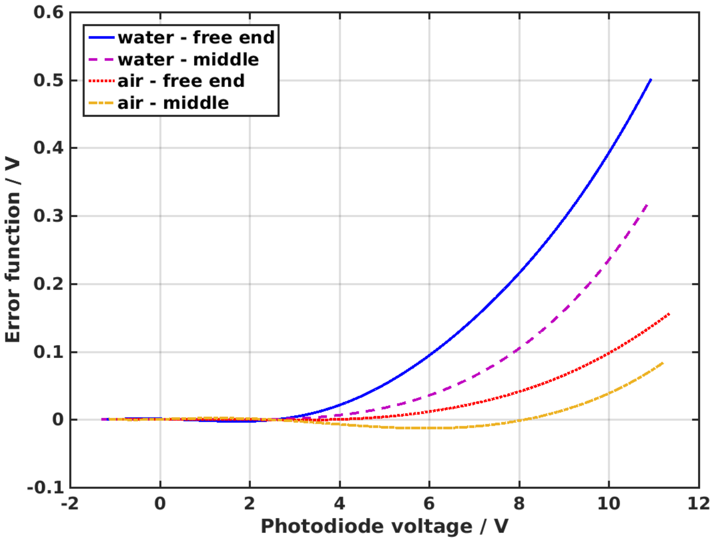

Figure C.1: Characterization of the photodiode deviations from linear behavior as a function of the measured voltage, under different experimental conditions: air or water, laser spot located at the cantilever free-end or middle point. The same probe (a conventional sharp tip) is used throughout the experiment. The error function is evaluated according to eq. C.1.

voltage difference ΔV (fig. B.3).

In the light of these considerations, a calibration of the photodetector non-linearity should be performed (if needed) before every experiment or after any change in the experimental conditions, in a way similar to that shown in fig. C.1, and subsequently applied to the measured force curves before any other data-processing procedure; alternatively, if possible, the average value of the non-contact region of force curves should be manually regulated during measurements, such that the contact region would fall entirely in the interval where the photodiode response is approximately linear (in this specific case, up to about 4-5 Volts for positive detections).

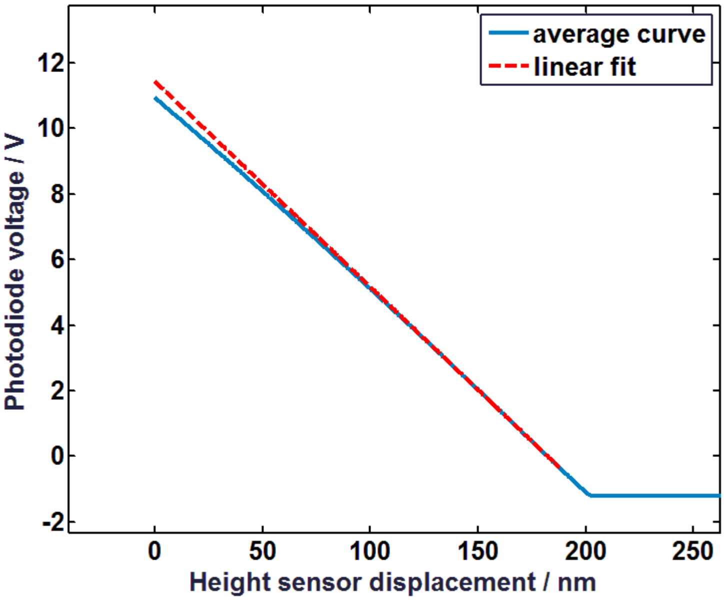

Figure C.2: Evaluation of the photodiode nonlinearity: a linear fit (red dashed line) is computed on the average of the force curves (blue continuous line) acquired on a rigid undeformable surface. The fitting interval is selected in the region where the photodiode response is supposed to be approximately linear (0-4 V). The difference between the two curves provides the error function plotted in fig. C.1.

Bibliography

[1] G. Binnig, C. F. Quate, and C. Gerber, “Atomic force microscope,” *Physical Review Letters*, vol. 56, no. 9, pp. 930–933, 1986.

[2] H.-J. Butt, B. Cappella, and M. Kappl, “Force measurements with the atomic force microscope: Technique, interpretation and applications,” *Surface Science Reports*, vol. 59, no. 1-6, pp. 1–152, 2005.

[3] A. Alessandrini and P. Facci, “AFM: a versatile tool in biophysics,” *Measurement Science and Technology*, vol. 16, no. 6, pp. R65–R92, 2005.

[4] T. G. Kuznetsova, M. N. Starodubtseva, N. I. Yegorenkov, S. A. Chizhik, and R. I. Zhdanov, “Atomic force microscopy probing of cell elasticity,” *Micron*, vol. 38, no. 8, pp. 824–833, 2007.

[5] S. SURESH, “Biomechanics and biophysics of cancer cells,” *Acta Biomaterialia*, vol. 3, no. 4, pp. 413–438, 2007.

[6] K. Haase and A. E. Pelling, “Investigating cell mechanics with atomic force microscopy,” *Journal of The Royal Society Interface*, vol. 12, no. 104, pp. 20140970–20140970, 2015.

[7] E. L. Elson, “Cellular mechanics as an indicator of cytoskeletal structure and function,” *Annual Review of Biophysics and Biophysical Chemistry*, vol. 17, no. 1, pp. 397–430, 1988.

[8] J. Stricker, T. Falzone, and M. L. Gardel, “Mechanics of the f-actin cytoskeleton,” *Journal of Biomechanics*, vol. 43, no. 1, pp. 9–14, 2010.

[9] D. A. Fletcher and R. D. Mullins, “Cell mechanics and the cytoskeleton,” *Nature*, vol. 463, no. 7280, pp. 485–492, 2010.

[10] S. E. Cross, Y.-S. Jin, J. Rao, and J. K. Gimzewski, "Nanomechanical analysis of cells from cancer patients," *Nature Nanotechnology*, vol. 2, no. 12, pp. 780–783, 2007.

[11] M. Lekka, K. Pogoda, J. Gostek, O. Klymenko, S. Prauzner-Bechcicki, J. Wiltowska-Zuber, J. Jaczewska, J. Lekki, and Z. Stachura, "Cancer cell recognition – mechanical phenotype," *Micron*, vol. 43, no. 12, pp. 1259–1266, 2012.

[12] M. Plodinec, M. Loparic, C. A. Monnier, E. C. Obermann, R. Zanetti-Dallenbach, P. Oertle, J. T. Hyotyla, U. Aebi, M. Bentires-Alj, R. Y. H. Lim, and C.-A. Schoenenberger, "The nanomechanical signature of breast cancer," *Nature Nanotechnology*, vol. 7, no. 11, pp. 757–765, 2012.

[13] T. Ludwig, R. Kirmse, K. Poole, and U. S. Schwarz, "Probing cellular microenvironments and tissue remodeling by atomic force microscopy," *Pflügers Archiv - European Journal of Physiology*, vol. 456, no. 1, pp. 29–49, 2007.

[14] M. Lekka, "Discrimination between normal and cancerous cells using AFM," *BioNanoScience*, vol. 6, no. 1, pp. 65–80, 2016.

[15] E. Shimshoni, D. Yablecovitch, L. Baram, I. Dotan, and I. Sagi, "ECM remodelling in IBD: innocent bystander or partner in crime? the emerging role of extracellular molecular events in sustaining intestinal inflammation," *Gut*, vol. 64, no. 3, pp. 367–372, 2014.

[16] L. Puricelli, M. Galluzzi, C. Schulte, A. Podestà, and P. Milani, "Nanomechanical and topographical imaging of living cells by atomic force microscopy with colloidal probes," *Review of Scientific Instruments*, vol. 86, no. 3, p. 033705, 2015.

[17] H. Schillers, C. Rianna, J. Schäpe, T. Luque, H. Doschke, M. Wälte, J. J. Uriarte, N. Campillo, G. P. Michanetzis, J. Bobrowska, A. Dumitru, E. T. Herruzo, S. Bovio, P. Parot, M. Galluzzi, A. Podestà, L. Puricelli, S. Scheuring, Y. Missirlis, R. Garcia, M. Odorico, J.-M. Teulon, F. Lafont, M. Lekka, F. Rico, A. Rigato, J.-L. Pellequer, H. Oberleithner, D. Navajas, and M. Radmacher, "Standardized nanomechanical atomic force microscopy procedure (snap) for measuring soft and biological samples." Submitted.

[18] T. Mitchison and M. Kirschner, "Cytoskeletal dynamics and nerve growth," *Neuron*, vol. 1, no. 9, pp. 761–772, 1988.

[19] L. B. Case and C. M. Waterman, "Integration of actin dynamics and cell adhesion by a three-dimensional, mechanosensitive molecular clutch," *Nature Cell Biology*, vol. 17, no. 8, pp. 955–963, 2015.

[20] Z. Sun, S. S. Guo, and R. Fässler, "Integrin-mediated mechanotransduction," *The Journal of Cell Biology*, vol. 215, no. 4, pp. 445–456, 2016.

[21] V. Swaminathan and C. M. Waterman, "The molecular clutch model for mechanotransduction evolves," *Nature Cell Biology*, vol. 18, no. 5, pp. 459–461, 2016.

[22] C. Schulte, G. M. S. Ferraris, A. Oldani, M. Galluzzi, A. Podestà, L. Puricelli, V. de Lorenzi, C. Lenardi, P. Milani, and N. Sidenius, "Lamellipodial tension, not integrin/ligand binding, is the crucial factor to realise integrin activation and cell migration," *European Journal of Cell Biology*, vol. 95, no. 1, pp. 1–14, 2016.

[23] R. O. Hynes, "The extracellular matrix: Not just pretty fibrils," *Science*, vol. 326, no. 5957, pp. 1216–1219, 2009.

[24] J. Folkman and R. Kalluri, "Cancer without disease," *Nature*, vol. 427, no. 6977, pp. 787–787, 2004.

[25] P. Lu, V. M. Weaver, and Z. Werb, "The extracellular matrix: A dynamic niche in cancer progression," *The Journal of Cell Biology*, vol. 196, no. 4, pp. 395–406, 2012.

[26] M. Nebuloni, L. Albarello, A. Andolfo, C. Magagnotti, L. Genovese, I. Locatelli, G. Tonon, E. Longhi, P. Zerbi, R. Allevi, A. Podestà, L. Puricelli, P. Milani, A. Soldarini, A. Salonia, and M. Alfano, "Insight on colorectal carcinoma infiltration by studying perilesional extracellular matrix," *Scientific Reports*, vol. 6, p. 22522, 2016.

[27] E. Shimshoni, R. Afik, A. Shenoy, M. Adler, L. Puricelli, A. Podestà, T. Geiger, P. Milani, U. Alon, and I. Sagi, "Decoding omics: unsupervised tissue composition-to-structure translation ?reveals silent pathological states." Submitted.

[28] L. Genovese, L. Zawada, A. Tosoni, A. Ferri, P. Zerbi, R. Allevi, M. Nebuloni, and M. Alfano, "Cellular localization, invasion, and turnover are differently influenced by healthy and tumor-derived extracellular matrix," *Tissue Engineering Part A*, vol. 20, no. 13-14, pp. 2005–2018, 2014.

[29] N. Wang, J. D. Tytell, and D. E. Ingber, “Mechanotransduction at a distance: mechanically coupling the extracellular matrix with the nucleus,” *Nature Reviews Molecular Cell Biology*, vol. 10, no. 1, pp. 75–82, 2009.

[30] J. Z. Gasiorowski, C. J. Murphy, and P. F. Nealey, “Biophysical cues and cell behavior: The big impact of little things,” *Annual Review of Biomedical Engineering*, vol. 15, no. 1, pp. 155–176, 2013.

[31] H. Liu and T. J. Webster, “Nanomedicine for implants: A review of studies and necessary experimental tools,” *Biomaterials*, vol. 28, no. 2, pp. 354–369, 2007.

[32] M. J. Dalby, N. Gadegaard, and R. O. C. Oreffo, “Harnessing nanotopography and integrin–matrix interactions to influence stem cell fate,” *Nature Materials*, vol. 13, no. 6, pp. 558–569, 2014.

[33] W. Chen, Y. Shao, X. Li, G. Zhao, and J. Fu, “Nanotopographical surfaces for stem cell fate control: Engineering mechanobiology from the bottom,” *Nano Today*, vol. 9, no. 6, pp. 759–784, 2014.

[34] M. R. Lee, K. W. Kwon, H. Jung, H. N. Kim, K. Y. Suh, K. Kim, and K.-S. Kim, “Direct differentiation of human embryonic stem cells into selective neurons on nanoscale ridge/groove pattern arrays,” *Biomaterials*, vol. 31, no. 15, pp. 4360–4366, 2010.

[35] E. Barborini, P. Piseri, and P. Milani, “A pulsed microplasma source of high intensity supersonic carbon cluster beams,” *Journal of Physics D: Applied Physics*, vol. 32, no. 21, pp. L105–L109, 1999.

[36] K. Wegner, P. Piseri, H. V. Tafreshi, and P. Milani, “Cluster beam deposition: a tool for nanoscale science and technology,” *Journal of Physics D: Applied Physics*, vol. 39, no. 22, pp. R439–R459, 2006.

[37] H. V. Tafreshi, P. Piseri, G. Benedek, and P. Milani, “The role of gas dynamics in operation conditions of a pulsed microplasma cluster source for nanostructured thin films deposition,” *Journal of Nanoscience and Nanotechnology*, vol. 6, no. 4, pp. 1140–1149, 2006.

[38] A. Podestà, F. Borghi, M. Indrieri, S. Bovio, C. Piazzoni, and P. Milani, “Nanomanufacturing of titania interfaces with controlled structural and functional properties by supersonic cluster beam deposition,” *Journal of Applied Physics*, vol. 118, no. 23, p. 234309, 2015.

[39] C. Schulte, S. Rodighiero, M. A. Cappelluti, L. Puricelli, E. Maffioli, F. Borghi, A. Negri, E. Sogne, M. Galluzzi, C. Piazzoni, M. Tamplenizza, A. Podestà, G. Tedeschi, C. Lenardi, and P. Milani, "Conversion of nanoscale topographical information of cluster-assembled zirconia surfaces into mechanotransductive events promotes neuronal differentiation," *Journal of Nanobiotechnology*, vol. 14, no. 18, pp. 1–24, 2016.

[40] C. Schulte, M. Ripamonti, E. Maffioli, M. A. Cappelluti, S. Nonnis, L. Puricelli, J. Lamanna, C. Piazzoni, A. Podestà, C. Lenardi, G. Tedeschi, A. Malgaroli, and P. Milani, "Scale invariant disordered nanotopography promotes hippocampal neuron development and maturation with involvement of mechanotransductive pathways," *Frontiers in Cellular Neuroscience*, vol. 10, no. 267, pp. 1–22, 2016.

[41] D. Chavan, T. C. van de Watering, G. Gruca, J. H. Rector, K. Heeck, M. Slaman, and D. Iannuzzi, "Ferrule-top nanoindenter: An optomechanical fiber sensor for nanoindentation," *Review of Scientific Instruments*, vol. 83, no. 11, p. 115110, 2012.

[42] J. L. Hutter and J. Bechhoefer, "Calibration of atomic-force microscope tips," *Review of Scientific Instruments*, vol. 64, no. 7, p. 1868, 1993.

[43] H.-J. Butt and M. Jaschke, "Calculation of thermal noise in atomic force microscopy," *Nanotechnology*, vol. 6, 1995.

[44] E. K. Dimitriadis, F. Horkay, J. Maresca, B. Kachar, and R. S. Chadwick, "Determination of elastic moduli of thin layers of soft material using the atomic force microscope," *Biophysical Journal*, vol. 82, no. 5, pp. 2798–2810, 2002.

[45] J. Alcaraz, L. Buscemi, M. Grabulosa, X. Trepat, B. Fabry, R. Farré, and D. Navajas, "Microrheology of human lung epithelial cells measured by atomic force microscopy," *Biophysical Journal*, vol. 84, no. 3, pp. 2071–2079, 2003.

[46] F. Rico, P. Roca-Cusachs, N. Gavara, R. Farré, M. Rotger, and D. Navajas, "Probing mechanical properties of living cells by atomic force microscopy with blunted pyramidal cantilever tips," *Physical Review E*, vol. 72, no. 2, 2005.

[47] G. M. S. Ferraris, C. Schulte, V. Buttiglione, V. D. Lorenzi, A. Piontini, M. Galluzzi, A. Podesta, C. D. Madsen, and N. Sidenius, "The interaction

between uPAR and vitronectin triggers ligand-independent adhesion signalling by integrins," *The EMBO Journal*, vol. 33, no. 21, pp. 2458–2472, 2014.

[48] Z. Hong, M. C. Staiculescu, P. Hampel, I. Levitan, and G. Forgacs, "How cholesterol regulates endothelial biomechanics," *Frontiers in Physiology*, vol. 3, no. 426, pp. 1–6, 2012.

[49] M. Alfano, M. Nebuloni, R. Allevi, P. Zerbi, E. Longhi, R. Lucianò, I. Locatelli, A. Pecoraro, M. Indrieri, C. Speziali, C. Doglioni, P. Milani, F. Montorsi, and A. Salonia, "Linearized texture of three-dimensional extracellular matrix is mandatory for bladder cancer cell invasion," *Scientific Reports*, vol. 6, no. 36128, pp. 1–12, 2016.

[50] F. Borghi, *Engineering the structural and functional properties of transition metal oxide interfaces by cluster assembling.* PhD thesis, PhD School in Physics, Astrophysics and Applied Physics, University of Milan, 2015.

[51] C. Ugolini, "Caratterizzazione del ruolo della struttura nanometrica di una superficie sul fenotipo di cellule neuronali," Master's thesis, University of Milan, Physics Department. Bachelor Thesis, 2016.

[52] N. J. Anthis and I. D. Campbell, "The tail of integrin activation," *Trends in Biochemical Sciences*, vol. 36, no. 4, pp. 191–198, 2011.

[53] P. Decuzzi and M. Ferrari, "Modulating cellular adhesion through nanotopography," *Biomaterials*, vol. 31, no. 1, pp. 173–179, 2010.

[54] F. Gentile, R. Medda, L. Cheng, E. Battista, P. E. Scopelliti, P. Milani, E. A. Cavalcanti-Adam, and P. Decuzzi, "Selective modulation of cell response on engineered fractal silicon substrates," *Scientific Reports*, vol. 3, no. 1461, pp. 1–10, 2013.

[55] M. del Mar Vivanco, ed., *Mammary Stem Cells.* Springer New York, 2015.

[56] C. Braunsmann and T. E. Schäffer, "Note: Artificial neural networks for the automated analysis of force map data in atomic force microscopy," *Review of Scientific Instruments*, vol. 85, no. 5, pp. 056104–1–056104–3, 2014.

[57] R. Long, M. S. Hall, M. Wu, and C.-Y. Hui, "Effects of gel thickness on microscopic indentation measurements of gel modulus," *Biophysical Journal*, vol. 101, no. 3, pp. 643–650, 2011.

[58] G. Kaushik, A. Fuhrmann, A. Cammarato, and A. J. Engler, "In situ mechanical analysis of myofibrillar perturbation and aging on soft, bilayered drosophila myocardium," *Biophysical Journal*, vol. 101, no. 11, pp. 2629–2637, 2011.

[59] M. L. Rodriguez, P. J. McGarry, and N. J. Sniadecki, "Review on cell mechanics: Experimental and modeling approaches," *Applied Mechanics Reviews*, vol. 65, no. 6, p. 060801, 2013.

[60] N. Guz, M. Dokukin, V. Kalaparthi, and I. Sokolov, "If cell mechanics can be described by elastic modulus: Study of different models and probes used in indentation experiments," *Biophysical Journal*, vol. 107, no. 3, pp. 564–575, 2014.

[61] R. Mahaffy, S. Park, E. Gerde, J. Käs, and C. Shih, "Quantitative analysis of the viscoelastic properties of thin regions of fibroblasts using atomic force microscopy," *Biophysical Journal*, vol. 86, no. 3, pp. 1777–1793, 2004.

[62] H. van Hoorn, N. A. Kurniawan, G. H. Koenderink, and D. Iannuzzi, "Local dynamic mechanical analysis for heterogeneous soft matter using ferrule-top indentation," *Soft Matter*, vol. 12, no. 12, pp. 3066–3073, 2016.

[63] E. Moeendarbary, L. Valon, M. Fritzsche, A. R. Harris, D. A. Moulding, A. J. Thrasher, E. Stride, L. Mahadevan, and G. T. Charras, "The cytoplasm of living cells behaves as a poroelastic material," *Nature Materials*, vol. 12, no. 3, pp. 253–261, 2013.

[64] C. Canale, A. Petrelli, M. Salerno, A. Diaspro, and S. Dante, "A new quantitative experimental approach to investigate single cell adhesion on multifunctional substrates," *Biosensors and Bioelectronics*, vol. 48, pp. 172–179, 2013.

[65] S. A. Edwards, W. A. Ducker, and J. E. Sader, "Influence of atomic force microscope cantilever tilt and induced torque on force measurements," *Journal of Applied Physics*, vol. 103, no. 6, p. 064513, 2008.

[66] K.-H. Chung, G. A. Shaw, and J. R. Pratt, "Accurate noncontact calibration of colloidal probe sensitivities in atomic force microscopy," *Review of Scientific Instruments*, vol. 80, no. 6, p. 065107, 2009.

[67] P. P. Weafer, J. P. McGarry, M. H. van Es, J. I. Kilpatrick, W. Ronan, D. R. Nolan, and S. P. Jarvis, "Stability enhancement of an atomic force

microscope for long-term force measurement including cantilever modification for whole cell deformation," *Review of Scientific Instruments*, vol. 83, no. 9, p. 093709, 2012.

[68] A. D. Slattery, A. J. Blanch, J. S. Quinton, and C. T. Gibson, "Accurate measurement of atomic force microscope cantilever deflection excluding tip-surface contact with application to force calibration," *Ultramicroscopy*, vol. 131, pp. 46–55, 2013.

[69] J. Stiernstedt, M. W. Rutland, and P. Attard, "A novel technique for the in situ calibration and measurement of friction with the atomic force microscope," *Review of Scientific Instruments*, vol. 76, no. 8, p. 083710, 2005.

[70] J. Stiernstedt, M. W. Rutland, and P. Attard, "Erratum: "a novel technique for the in situ calibration and measurement of friction with the atomic force microscope" [rev. sci. instrum. 76, 083710 (2005)]," *Review of Scientific Instruments*, vol. 77, no. 1, p. 019901, 2006.

[71] N. A. Burnham, X. Chen, C. S. Hodges, G. A. Matei, E. J. Thoreson, C. J. Roberts, M. C. Davies, and S. J. B. Tendler, "Comparison of calibration methods for atomic-force microscopy cantilevers," *Nanotechnology*, vol. 14, no. 1, pp. 1–6, 2002.

[72] J. L. Hutter, "Comment on tilt of atomic force microscope cantilevers: effect on spring constant and adhesion measurements," *Langmuir*, vol. 21, no. 6, pp. 2630–2632, 2005.

[73] L.-O. Heim, M. Kappl, and H.-J. Butt, "Tilt of atomic force microscope cantilevers: effect on spring constant and adhesion measurements," *Langmuir*, vol. 20, no. 7, pp. 2760–2764, 2004.

[74] J. Laurent, A. Steinberger, and L. Bellon, "Functionalized AFM probes for force spectroscopy: eigenmode shapes and stiffness calibration through thermal noise measurements," *Nanotechnology*, vol. 24, no. 22, p. 225504, 2013.

[75] L.-O. Heim, T. S. Rodrigues, and E. Bonaccurso, "Direct thermal noise calibration of colloidal probe cantilevers," *Colloids and Surfaces A: Physicochemical and Engineering Aspects*, vol. 443, pp. 377–383, 2014.

[76] *L. Bellon. Private Communications*, 2016.

[77] R. S. Gates, W. A. Osborn, and J. R. Pratt, "Experimental determination of mode correction factors for thermal method spring constant calibration of AFM cantilevers using laser doppler vibrometry," *Nanotechnology*, vol. 24, no. 25, p. 255706, 2013.

[78] R. S. Gates, W. A. Osborn, and G. A. Shaw, "Accurate flexural spring constant calibration of colloid probe cantilevers using scanning laser doppler vibrometry," *Nanotechnology*, vol. 26, no. 23, p. 235704, 2015.

[79] D. Chavan, G. Gruca, S. de Man, M. Slaman, J. H. Rector, K. Heeck, and D. Iannuzzi, "Ferrule-top atomic force microscope," *Review of Scientific Instruments*, vol. 81, no. 12, p. 123702, 2010.

[80] D. Chavan, D. Andres, and D. Iannuzzi, "Note: Ferrule-top atomic force microscope. II. imaging in tapping mode and at low temperature," *Review of Scientific Instruments*, vol. 82, no. 4, p. 046107, 2011.

[81] S. V. Beekmans and D. Iannuzzi, "A metrological approach for the calibration of force transducers with interferometric readout," *Surface Topography: Metrology and Properties*, vol. 3, no. 2, p. 025004, 2015.

[82] S. V. Beekmans and D. Iannuzzi, "Characterizing tissue stiffness at the tip of a rigid needle using an opto-mechanical force sensor," *Biomedical Microdevices*, vol. 18, no. 1, 2016.

[83] E. Thormann, T. Pettersson, and P. M. Claesson, "How to measure forces with atomic force microscopy without significant influence from nonlinear optical lever sensitivity," *Review of Scientific Instruments*, vol. 80, no. 9, p. 093701, 2009.

Appendix D

Acknowledgments

I am really grateful to all the authors which contributed to the papers reported in this Thesis. In particular, I'd like to thank the scientific supervisors and main responsible of the different projects: Paolo Milani, Cristina Lenardi and Carsten Schulte from C.I.Ma.I.Na. group here at the Physics Department (University of Milan), Massimo Alfano from S. Raffaele Hospital (Milan, Italy), Irit Sagi & Elee Shimshoni from Weizmann Institute (Rehovot, Israel). These complex yet greatly stimulating interdisciplinary works couldn't have been realized without the diverse expertise and precious experiences provided by all these scientists.
Special thanks goes to Carsten Schulte, responsible of the biological labs inside C.I.Ma.I.Na. facilities, who has directly provided me with all the help and support needed in the biological field, both from the experimental and theoretical point of view, greatly contributing to enrich my knowledge of this complex world.
Many thanks also to Davide Iannuzzi, Niek Rijnveld and all the guys from the Optics11 group who helped me in handling and understanding the working principles of Piuma Nanoindenter during my one-week internship in Amsterdam, which has led to fruitful results.

Last but not least, I'd like to thank all the present or former members of the AFM group : Massimiliano Galluzzi, Francesca Borghi, Alice Meroni, Giulia Donadoni, Matteo Chighizola, Stefania Asperti, Alessandro De Vita, Francesco Puppi, Camilla Ugolini, Bianca Scaparra, Lorenzo Marfori, and many others, for their direct or undirect support to the results obtained so far.

Of course, a special mention is reserved to Alessandro Podestà, who has su-

pervised me throughout these years, since my Bachelor Thesis, teaching me everything he could. I owe him a lot.

Questo lavoro é il frutto di tre anni di attività, più o meno intensa, nei laboratori del gruppo C.I.Ma.I.Na. del Dipartimento di Fisica dell' Università degli Studi di Milano. Ancora non so quale sarà il seguito, o se ci sarà un seguito; comunque sia, sono stati tre anni stimolanti e molto istruttivi, fondamentali per la mia crescita dal punto di vista professionale e scientifico. Ho avuto la possibilità di affacciarmi sul mondo della ricerca, quella vera, e di farlo in prima persona, assistito da un gruppo fantastico di persone (e di scienziati) da cui ho avuto la fortuna di poter imparare.
In questo senso, dei ringraziamenti speciali vanno ad Alessandro Podestà, mio "mentore" e supervisore dai tempi della tesi triennale, passando per la magistrale, sino ad oggi. Non posso che essere orgoglioso dei miglioramenti e dei progressi dimostrati in tutti questi anni, ma il merito non è solo mio. Quando ho deciso di svolgere qui la mia attività come dottorando, l'ho fatto principalmente per un motivo: sapevo che con Alessandro avrei potuto lavorare bene e imparare molto...e così è stato, grazie alle sue eccellenti qualità dal punto di vista professionale ed umano. Altrettanto importanti sono state le persone che ho incontrato e conosciuto anche al di fuori del "box AFM": Paolo e Cristina con i loro preziosi consigli; Carsten con la sua profonda conoscenza della biologia e delle birre; Luca e Claudio con cui ho condiviso molti pranzi e discussioni su calcio e politica, anche se purtroppo continuano a non capirci nulla; Andrea con la sua goliardia a casaccio, che fa sempre bene; mamma Francesca con la sua saggezza e solarità; e infine Alice, Giulia, Bianca, Stefania, Matteo, Tommaso, Massimiliano, Patrizia, e in generale tutti coloro che hanno contribuito a strapparmi qualche sorriso in più. Grazie di cuore.

Ovviamente questi anni non sono stati solo laboratorio e AFM; questi anni sono stati anche le persone che ho incontrato al di fuori dell' Università, prima e durante la mia vita da dottorando, le esperienze e i momenti che ho condiviso con loro e che hanno reso tutto un po' più luminoso, allietando i periodi più difficili e contribuendo in qualche modo a farmi arrivare fin qui.
Un grazie speciale a mio nonno Mario (e mia nonna Luigia). Io ho avuto la fortuna di avere un nonno vero, con tanto tempo libero e la voglia di dedicarlo ai suoi nipoti. Grazie a lui ho imparato ad apprezzare la semplicità, la bellezza della natura, la curiosità di conoscere...e anche come fare le barchette di carta. Non lo dimenticherò mai...nemmeno le barchette.
Grazie a Davide & Eleonora, amici da (quasi) una vita, quella post-liceale.

Abbiamo condiviso il percorso universitario, ci siamo laureati insieme, abbiamo riso insieme, bevuto insieme, abbiamo fatto vacanze un po' pazze ma bellissime, campeggi, escursioni in montagna, bivaccate, serate...abbiamo condiviso gioie e dolori, confidenze, sfoghi, consigli. Non siete mai mancati quando ho avuto bisogno di qualcuno. E mi avete fatto un regalo indimenticabile: la possibilità di poter fare da testimone al vostro matrimonio.
Grazie a Camilla. Per avermi insegnato cosa significa voler bene ad una persona.
Grazie al Corpo Musicale S.Cecilia per i bei momenti passati insieme in questi venti anni di onorata attività. E al Rugby Parabiago per la bella esperienza di questi ultimi tre anni..a volte un po' dolorosa, ma comunque bella.
Grazie alla mia famiglia per avermi sempre sostenuto, pur passando attraverso momenti non semplici. A volte lo diamo per scontato, senza renderci conto che non lo è affatto. E grazie infine agli amici di sempre, per le birre, le serate in compagnia e le splendide vacanze trascorse insieme.